

UNIVERSITÀ
DEGLI STUDI
DI PADOVA

Sede Amministrativa: Università degli Studi di Padova

Centro di Ateneo di Studi e Attività Spaziali "Giuseppe Colombo" - CISAS

CORSO DI DOTTORATO DI RICERCA IN: Sciences, Technologies and Measurements
for Space

CURRICULUM: Sciences and Technologies for Aeronautics and Satellite Applications

CICLO XXXVII

HIGH-FIDELITY SIMULATIONS OF HIGH SPEED FLOWS FOR AEROSPACE PROBLEMS

Tesi redatta con il contributo finanziario della fondazione Cassa di Risparmio di Padova e Rovigo

Coordinatore: Ch.mo Prof. Francesco Picano

Supervisore: Ch.mo Prof. Francesco Picano

Dottorando: Michele Cogo

Abstract

The interest in high-speed flows has considerably risen in the last decades, with the growing push of the space economy in the public and private sectors, and with the aim to provide fast long-range methods for air transportation of goods and passengers around the globe.

Flight systems operating at high speeds can be quite different: aircrafts, rockets or reentry vehicles, but they are all eventually enveloped by turbulent, hot, highly compressible flow. These effects become dominant in a very thin region in the proximity of solid boundaries, called the boundary layer. This is the region where intense mechanical and thermal loads are transferred to the vehicle, significantly affecting its design and the choice of surface materials. At hypersonic speeds, the enormous heat generated in the boundary layer can also lead to chemical dissociation processes, which significantly change the resulting flow dynamics.

The objective of the present thesis is two-fold. On one hand, our aim is to better understand the interplay of controlling flow parameters such as the Reynolds number, the Mach number, the wall temperature, and surface roughness, targeting specific configurations that are not yet well understood by the research community. On the other hand, we work towards improving current engineering models that are used to inform design choices, which are often inspired by a better physical understanding of the underlying process. To this end, Computational Fluid Dynamics (CFD) is leveraged as an invaluable tool to systematically analyze several flow configurations without the need to perform very expensive wind tunnel runs or in flight measurements, often impractical for these applications. Among the plethora of methodologies available in CFD, the present thesis is oriented to high-fidelity simulations, specifically Direct Numerical Simulations (DNS), where all turbulent scales are resolved, and Large Eddy Simulations (LES), where only small scales are modeled, yet maintaining the ability to capture the non-stationary and multiscale nature of turbulence.

The first part of this thesis (Papers I and II) investigates flat-plate turbulent boundary layers under varying Reynolds numbers, Mach numbers, and wall temperature conditions to address gaps in high-speed flow DNS reference data. A detailed study of the interplay between Mach number and wall temperature, Paper II, isolates their individual effects, focusing on their relative impact on coupling between kinetic and thermal fields.

Paper III conducts one of the first numerical studies of compressible turbulent boundary layers transitioning from smooth to rough surfaces using DNS. It provides a high-fidelity analysis of turbulent scales and a direct comparison with subsonic cases, identifying unique compressible flow features, including compression and expansion waves from 3D surface elements.

Papers IV and V focus on modeling high-speed flows. Paper IV presents the URANOS compressible flow solver, ported for running in recent Graphic Processing Units (GPUs) architectures and designed for LES and wall-modeled LES methodologies for calorically-perfect gases. Paper V extends the wall model by Griffin et al. (2023) to incorporate finite-rate chemistry and multi-component diffusion in chemically reacting hypersonic boundary layers, showing improved a priori predictions for velocity and temperature profiles compared to classical models, which are not visible for the wall-normal distribution of mass fractions. This finding highlights the need for refined modeling of chemical reaction terms as a result of their highly nonlinear nature.

Keywords: Compressible flows, compressible boundary layers, turbulence simulations, hypersonic flows.

Preface

This thesis deals with the numerical and theoretical study of high-speed flows for aerospace problems. The ‘Paper Collection’ format is chosen, meaning that a brief introduction on the relevance of the present work and the description of mathematical formulations are presented at the beginning, followed by the results presented in the five appended articles. The format of the papers has been altered to comply with the present thesis, but the contents are the same as their original counterparts.

Paper I Cogo, M., Salvadore, F., Bernardini, M. & Picano, F. (2022). Direct numerical simulation of supersonic and hypersonic turbulent boundary layers at moderate-high Reynolds numbers and isothermal wall condition. *J. Fluid Mech.*, 945, A30.

Paper II Cogo, M., Baù, U., Chinappi, M., Bernardini, M., & Picano, F. (2023). Assessment of heat transfer and Mach number effects on high-speed turbulent boundary layers. *J. Fluid Mech.*, 974, A10.

Paper III Cogo, M., Modesti, D., Bernardini, M., & Picano F. (2024). Direct numerical simulation of compressible turbulent boundary layers over smooth and rough surfaces. *J. Fluid Mech.*, Under revision.

Paper IV De Vanna, F., Avanzi F., Cogo, M., Sandrin, S., Bettencourt, M., Picano, F., & Benini, E. (2023). URANOS: A GPU accelerated Navier-Stokes solver for compressible wall-bounded flows *Comput. Phys. Commun.*, 287, 108717.

Paper V Cogo, M., Williams, C. T., Griffin, K. P., Picano, F., & Moin, P. (2024). Inverse-velocity transformation wall model for reacting turbulent hypersonic boundary layers. *CTR Ann. Res. Briefs*.

September 2024, Padova

Michele Cogo

Division of work between authors

The advisor of this project is Francesco Picano (F.P.). The authors' contributions for each paper are depicted as follows

Paper I M.C. was responsible for preparing the simulation setup, carrying out the simulations, analyzing the results and drafting the manuscript; Support for methodological analysis and code validation was provided by F.S.; F.P. and M.B supervised, performed and designed the research, also revised and edited the paper.

Paper II M.C. was responsible for preparing the simulation setup, carrying out the simulations, analyzing the results and drafting the manuscript; Support for post processing was provided by U.B.; F.P., M.Chi. and M.B supervised, performed and designed the research, also revised and edited the paper.

Paper III M.C. was responsible for preparing the simulation setup, carrying out the simulations, analyzing the results and drafting the manuscript; F.P., D.M. and M.B supervised, performed and designed the research, also revised and edited the paper; D.M. also provided support for code validation.

Paper IV F.D. designed the research, conducted theoretical analysis, analyzed data and drafted the paper; F.A., M.C. and S.S. provided support for simulation setup, methodological analysis and code performances validation. M.B. contributed to the code performances optimization, while F.P. and E.B. supervised and revised the paper.

Paper V M.C. performed the simulations, analyzed data and wrote the original draft; C.W. and K.G. designed the research and provided support for methodological analysis and physical interpretation. F.P. and P.M. supervised and revised the paper.

Conferences

Part of the work in this dissertation has been presented at the following international conferences, some of which have been presented by the candidate (underlined)

Francesco De Vanna, Filippo Avanzi, Michele Cogo, Simone Sandrin, Matt Bettencourt, Francesco Picano & Ernesto Benini. *GPU-acceleration of Navier-Stokes solvers for compressible wall-bounded flows: the case of URANOS*. AIAA SCITECH 2023 Forum. Online, 2023

Michele Cogo, Francesco Salvadore, Francesco Picano and & Matteo Bernardini. *DNS of supersonic and hypersonic turbulent boundary layers at moderate-high Reynolds numbers with heat transfer*.

33rd International Conference on Parallel Computational Fluid Dynamics. Alba (CN), Italy, 2022

Michele Cogo, Mauro Chinappi, Matteo Bernardini, and Francesco Picano, *Compressibility effects in supersonic and hypersonic turbulent boundary layers at high Reynolds numbers*. 14th European Fluid Mechanics Conference. Athens, Greece, 2022

Michele Cogo, Christopher Williams, Kevin Griffin, Francesco Picano, & Parviz Moin. *Development of a wall model for chemically-reacting turbulent hypersonic boundary layers*. APS-DFD, 76th Annual Meeting of the American Physical Society's Division of Fluid Dynamics. Washington, DC, USA, 2023

Michele Cogo, Mauro Chinappi, Matteo Bernardini, & Francesco Picano. *Wall-cooling and compressibility effects on high-speed turbulent boundary layers*. APS-DFD, 76th Annual Meeting of the American Physical Society's Division of Fluid Dynamics. Washington, DC, USA, 2023

Matteo Bernardini, Michele Cogo, Francesco Picano, & Francesco Salvadore. *Supersonic wall turbulence at high Reynolds numbers*. APS-DFD, 76th Annual Meeting of the American Physical Society's Division of Fluid Dynamics. Washington, DC, USA, 2023

Michele Cogo, Mauro Chinappi, Matteo Bernardini, & Francesco Picano. *Compressibility and wall-cooling effects on high-speed turbulent boundary layers* Aerospace Science and Engineering - IV Aerospace PhD-Days. Scopello (TP), Italy, 2024

Michele Cogo, Davide Modesti, Matteo Bernardini, & Francesco Picano. *DNS of supersonic turbulent boundary layers over rough surfaces* Direct and Large-Eddy Simulation 14. Erlangen, Germany, 2024.

Michele Cogo, Davide Modesti, Matteo Bernardini, & Francesco Picano. *Compressibility effects in turbulent boundary layers with three-dimensional roughness* 1st European Fluid Dynamics Conference (EFDC1). Aachen, Germany, 2024

Visiting periods

Part of the work in this dissertation has been carried on during two visiting periods spent in international research centers:

Center for Turbulence Research, Stanford University, California, USA. *Research activity on wall models for hypersonic turbulent boundary layer with chemical reactions.* Host supervisor: Prof. Parviz Moin. Duration: June 1, 2023, November 30, 2023.

Flow Physics and Technology, Faculty of Aerospace Engineering, TU Delft, Delft, The Netherlands. *Research activity on high-fidelity simulations of compressible boundary layers over rough surfaces.* Host supervisor: Prof. Davide Modesti. Duration: October 15, 2022, to February 15, 2023.

I sincerely thank Fondazione Cariparo for supporting me in both visiting periods. The research activity at Stanford was made possible by the Fulbright scholarship, and supported by Zegna Founder's scholarship and Franklin P. and Caroline M. Johnson Fellowship, for which I'm deeply grateful.

Other works

During the Ph.D. there have been other research outputs that were not included in the present thesis given that their scope was not strictly in line with the objectives described here:

Placco, L., Cogo, M., Bernardini, M., Aboudan, A., Ferri, F., & Picano, F. (2023). Large-Eddy Simulation of the unsteady supersonic flow around a Mars entry capsule at different angles of attack. *Aerospace Science and Technology*, 143, 108709.

Contents

| | | |
|----------|--|-----------|
| 1 | Introduction | 1 |
| 1.1 | Background and motivations | 1 |
| 1.2 | The physical characteristics of high-speed flows | 2 |
| 2 | Physics of high-speed boundary layers | 8 |
| 2.1 | Fundamental aspects of high-speed turbulent boundary layers | 8 |
| 2.1.1 | Reynolds averaged Navier-Stokes | 9 |
| 2.1.2 | Boundary layer approximation | 10 |
| 2.1.3 | Turbulent kinetic energy budget | 13 |
| 2.1.4 | Compressibility transformations | 14 |
| 2.1.5 | Reynolds analogy | 17 |
| 2.2 | Roughness effects | 19 |
| 2.2.1 | Variations in the surface topography | 22 |
| 2.2.2 | Compressibility effects | 23 |
| 2.3 | Thermochemical effects in dissociating air | 24 |
| 3 | Near-wall modeling for hypersonic flows | 26 |
| 3.1 | Large Eddy Simulation | 26 |
| 3.2 | Near-wall turbulence modeling | 28 |
| 3.2.1 | Equilibrium wall model | 28 |
| 3.2.2 | Incorporating compressibility effects and strong heat transfer | 30 |
| 3.2.3 | Incorportating thermochemical effects | 32 |
| 4 | Objectives and Methodology | 33 |
| 4.1 | Research objectives | 33 |
| 4.2 | Numerical approach and discretization | 34 |
| 4.2.1 | CFD in the era of GPUs | 34 |
| 4.2.2 | STREAmS solver | 35 |
| 4.2.3 | URANOS solver | 36 |
| 5 | Summary of results | 38 |
| 5.1 | Paper I | 38 |
| 5.2 | Paper II | 39 |
| 5.3 | Paper III | 40 |
| 5.4 | Paper IV | 42 |
| 5.5 | Paper V | 42 |
| 6 | Conclusions | 44 |
| | Bibliography | 48 |
| A | Paper I | 56 |

| | |
|-------------|-----|
| B Paper II | 88 |
| C Paper III | 122 |
| D Paper IV | 150 |
| E Paper V | 187 |

Chapter 1

Introduction

1.1 Background and motivations

In recent years, the design of supersonic and hypersonic vehicles has gained significant attention from public and private institutions due to their potential for revolutionary applications, such as space exploration and high-speed commercial aviation (Leyva, 2017; Bertin and Cummings, 2003).

Despite the world becoming increasingly interconnected, vast distances still separate us, and access to space remains restricted to public agencies and a few private companies. More than a decade has passed since the Space Shuttle's final flight, and over fifty years since the X-15, a manned, powered, winged aircraft, set the still unbroken world record for the highest speed ever achieved (Urzay, 2018). Yet, a renewed interest is recently picking up on the return of high-speed commercial travel for several purposes, such as fast transportation of passengers and goods around the globe or access to Low Earth Orbit (LEO). The development of a new class of high-speed vehicles is driven by recent advances in materials, propulsion, manufacturing techniques, and software, which enabled engineers to face long-standing problems from a different perspective. However, there are still many critical aspects that are subject of research in order to efficiently design flight systems that can withstand huge mechanical and thermal loads (Candler, 2019), along with more advanced propulsion systems (Urzay, 2018).

Figure 1.1 shows different flight trajectories that can be exploited for civil and commercial transportation and space exploration. Here, high-speed flows can be encountered in very different flight envelopes. For example, a hypersonic cruise aircraft trajectory takes place in a relatively dense part of the atmosphere with a powered flight that can be entirely sustained by air-breathing engines, such as scramjets (supersonic combustion ramjets). Examples of experimental aircraft of this kind are the NASA X-15, X-43, and X-51. In this regime, the ratio between inertia and viscous forces, the Reynolds number, is expected to be high enough to promote turbulence in several parts of the vehicle's surface.

On the other hand, if a similar aircraft targets higher altitudes and orbit insertion, a hypersonic spaceplane, there must be a transition from air-breathing engines to a rocket propulsion system, a capability that is still under development and never deployed in operational vehicles (Urzay, 2018).

Supersonic and hypersonic regimes are also experienced by unpowered flight systems reentering the atmosphere from different orbits (Gnoffo, 1999). These vehicles initially fly in a very low-density environment, where the flow is expected to be laminar (low Reynolds numbers), starting from ex-

tremely high Mach numbers (e.g. Mach 25 for the Shuttle orbiter and Mach 36 for Apollo reentry modules). As the vehicle descends through the denser part of the atmosphere, part of its extremely high kinetic energy is converted into heat, while turbulent regions start to arise (Van Driest, 1956). During descent, extremely high temperatures can activate chemical and ionization processes, which in turn can induce structural damage to the surface (Bertin and Cummings, 2006). In order to maintain the structural integrity, reentry vehicles are equipped with tiled or ablative thermal protection systems (TPS), and in both cases the flow may experience a rough surface. Tiled TPS are made up of carbon or ceramic tiles with square, diamond, or hexagonal shapes, and the gaps between the tiles can form a structured pattern. Ablative TPS protects the underlying structure because the material undergoes pyrolysis and the gases that are generated in this process blow the boundary layer away from the surface. The surface ablates with a nonuniform recession rate, resulting in regular or irregular distributed roughness patterns, depending on the type of material (Laganelli and Nestler, 1969). Tiled thermal protection systems are reusable, and typical examples are the TPS of the Space Shuttle and the SpaceX Starship. Instead, ablative TPS are not reusable and ablation often leads to the formation of structured rough surfaces, a process called crosshatching (Stock and Ginoux, 1973; Peltier et al., 2016).

In this scenario, it is not surprising that many major milestones in the design of high-speed vehicles are still ahead of us, particularly in supersonic and hypersonic flight at relatively low altitudes, which is one of the most unexplored research areas due to the inherent complexities. The reader may be familiar with the famous sound barrier, which is associated with the peak of aerodynamic drag that an aircraft encounters when traveling at the speed of sound (Mach 1). Although initially this limit was thought to be extremely difficult to overcome, technical solutions were found in the 1940s and 1950s to design supersonic aircraft for military and commercial purposes. In order to achieve sustained powered flight at higher Mach numbers, we now face another similar challenge, the heat barrier, posing severe constraints in the airframe surface material choice. The study of aerothermodynamics is essential to understand the generated drag and the amount of heat that is transferred to the solid wall as opposed to the part that is dissipated into the environment. The following section aims to discuss some of the effects that are representative of a flight system approaching such extreme conditions.

1.2 The physical characteristics of high-speed flows

As the vehicle moves through the atmosphere at a velocity several times the local speed of sound, aerodynamic drag and heat transfer become determining factors in terms of its structural integrity and aerodynamic performance. These effects start to arise in the supersonic regime, i.e. when the relative freestream velocity v_∞ is higher than the local speed of sound a_∞ , but are really evident when the freestream Mach number is greater than five $M_\infty = v_\infty/a_\infty > 5$, which denotes the lower bound of the hypersonic regime and corresponds to applications of high-speed atmospheric flights at relatively low altitudes. Flows pertaining to supersonic and hypersonic regimes are referred to as *highly compressible*, as opposed to the nearly *incompressible* nature of subsonic flows (Gatski and Bonnet, 2013).

At these speeds, shock waves are formed around the vehicle's surface, which, depending on the slenderness of the body, can form different angles and stand-off distances. For example, in a reentry

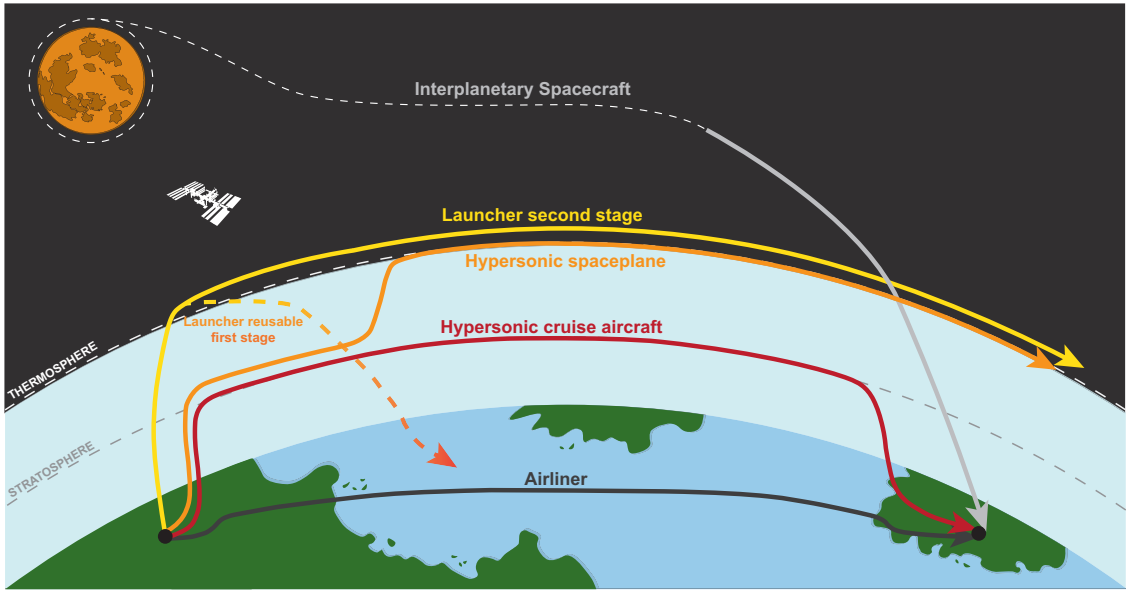


Figure 1.1: Characteristic flight trajectories for different aerospace systems for present and future commercial and space exploration applications.

capsule, which leverages its blunt shape to increase aerodynamic drag, the shock wave that forms on the heat shield is curved and detached from the leading edge, often referred to as a bow shock. In this case, the region between the shock wave and the vehicle's surface, the shock layer, can be quite large, and the post-shock temperature in this region can be enormous at hypersonic speeds, as the flow is nearly stagnating.

On the other hand, a hypersonic cruise aircraft has by design a very sharp nose followed by flat surfaces to minimize drag, which will promote the formation of an oblique shock wave with a very small deflection angle. In this case, the shock layer can be very thin, to the point that viscous effects present near the wall can interact with it (Anderson, 2006).

Shock waves can also directly interact with the flow in the proximity of solid boundaries when they are generated by auxiliary parts of the flight system, e.g. engine inlets. This phenomenon is referred to as a shock wave-boundary layer interaction and can lead to intense and localized mechanical and thermal loads, which may cause structural damage (Gaitonde, 2015).

If we consider the flow dynamics around the flight system as a whole, it is very difficult to discern all the different physical processes that are often coupled with each other. For this reason, researchers often try to simplify the problem, considering very simple configurations that can nevertheless give crucial hints on the flow physics. One of these configurations consists of a flow passing above a flat plate, in which the flow is brought to rest by friction with the wall, generating strong velocity and temperature gradients within the so-called boundary layer. In this section, we highlight some fundamental aspects concerning compressible boundary layers that are relevant to the scope of this thesis. For this reason, other important processes may be left out in order not to overload the discussion.

The main aspect in which high-speed compressible boundary layers fundamentally differ from their incompressible counterparts is that the momentum and thermal fields are strongly coupled through the density. The dependence on the temperature of viscosity and thermal conductivity makes physics even more complex, promoting the exchange of momentum and heat between different

regions of the flow. It can be shown that the square of the Mach number is proportional to the ratio between the kinetic energy $E_{kin} = v_\infty^2/2$ and specific thermal enthalpy $E_{therm} = h_\infty$ of the surrounding flow:

$$M_\infty^2 \propto E_{kin}/E_{therm}. \quad (1.1)$$

As the flow is slowed by viscous effects within the boundary layer, the huge amount of kinetic energy carried by the flow is then converted into thermal energy, resulting in high temperatures and chemical dissociation. A good indicator of this energy conversion is the stagnation enthalpy h_0 , which from the first law of thermodynamics takes the form

$$h_0 = h_\infty + \frac{u_\infty^2}{2}. \quad (1.2)$$

For a calorically perfect gas, this law can be rewritten as

$$T_0 = T_\infty + \frac{u_\infty^2}{2c_p} = T_\infty \left(1 + \frac{\gamma - 1}{2} M_\infty^2 \right), \quad (1.3)$$

where $\gamma = c_p/c_v$ is the ratio of specific heats at constant pressure, c_p , and volume, c_v , respectively ($\gamma_{air} = 1.4$). In compressible boundary layers, although the flow is necessarily brought to rest at the wall, nonisentropic processes are present, and tends to settle to a slightly lower temperature, the adiabatic wall temperaure T_{aw} , determined by a recovery factor, which can be defined as

$$r = \frac{T_{aw} - T_\infty}{T_0 - T_\infty} = \frac{2}{(\gamma - 1)M_\infty^2} \left(\frac{T_{aw}}{T_\infty} - 1 \right). \quad (1.4)$$

For common gases with $Pr \sim 1$ in a laminar flow it is very well approximated by $Pr^{1/2}$, otherwise in turbulent flows it becomes approximated by $Pr^{1/3}$ (Van Driest, 1956). From the recovery factor, we can define a recovery temperature as

$$T_r = T_\infty \left(1 + r \frac{\gamma - 1}{2} M_\infty^2 \right). \quad (1.5)$$

In most practical applications, the solid wall is much colder than the adiabatic wall temperature, particularly at hypersonic speeds (Duan et al., 2010), and thermal equilibrium with the fluid is expected to be reached with much longer time scales than those related to a specific flow regime in the overall flight trajectory. For this reason, a finite flux of heat q_w often exists from the flow to the solid boundary, which is the driving factor in viscous aerodynamic heating (Hirschel and Weiland, 2009). The balance between the tendency of the fluid to reach the adiabatic wall temperature T_{aw} and the local surface temperature T_w results in a local maximum in the static temperature profile, as shown in figure 1.2. The peak temperature in the boundary layer (and therefore the heat exchanged with the wall) increases rapidly with M_∞ . To give a sense of the rate at which this increase occurs, it can be shown that q_w is proportional to the freestream velocity elevated to the cube, as opposed to the quadratic dependence of the aerodynamic drag (Anderson, 2006), which better motivates the 'heat barrier' concept introduced in Section 1.1.

The interplay between the Mach number and the wall temperature condition and their influence on the resulting dynamics of a turbulent boundary layer is at the core of the present dissertation. These effects have been studied mainly in the calorically perfect gas regime, meaning that the

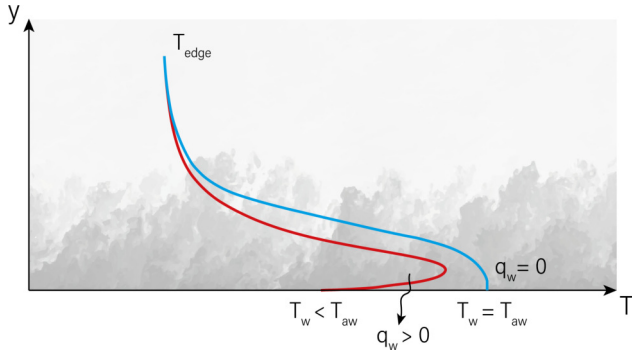


Figure 1.2: Wall-normal temperature profile $T = f(y)$ in the case of cold wall (red line) and adiabatic wall (blue line). The local maximum of the red profile near the wall is associated with strong aerodynamic heating in that region.

specific heat capacity is a constant value $c_p = \text{const}$. This is a good approximation for a large portion of possible flight trajectories of high-speed vehicles in which turbulence is also present, for example, a hypersonic cruise aircraft flying in the stratosphere up to Mach 6.

However, there are specific flight envelopes in which viscous aerodynamic heating can promote temperatures high enough to excite different degrees of freedom of air molecules, creating more complex energy pathways that are not accounted for in the calorically perfect gas regime. For air, after $800K$ the vibrational energy of the molecules starts to become important, such that the specific heat shows a temperature dependence $c_p = f(T)$ (Anderson, 2006). As the gas temperature increases, molecules can be forced to split as dissociation and recombination processes appear. For example, at sea level, oxygen begins to dissociate at $T \approx 2000K$ while nitrogen at $T \approx 4000K$. With higher temperatures reached, dissociation processes are enhanced and eventually lead to ionization ($T \approx 9000K$). These effects change profoundly the flow physics, especially in the prediction of post-shock quantities (Candler, 2019; Urzay and Di Renzo, 2021). In the context of boundary layers, one of the most difficult problems to face when thermochemical effects appear is to assess their interaction with turbulence, which may arise in denser parts of the atmosphere and provide a constant mixing of products and reactants (Di Renzo and Urzay, 2021; Passiatore et al., 2021). Depending on the specific mode that is excited at a particular stage (translational, vibrational, etc.), it is important to take into consideration its relaxation time τ , and how it relates to the characteristic time of the flow τ_{flow} .

When the relaxation time τ is much slower than the flow's characteristic time ($\tau \gg \tau_{\text{flow}}$), the flow is considered frozen, showing minimal response to changes in excitation. If the relaxation time is much faster than the flow's characteristic time ($\tau \ll \tau_{\text{flow}}$), the flow is in equilibrium, adapting quickly to changes. When the excitation time is comparable to the flow's time scale ($\tau \approx \tau_{\text{flow}}$), the flow is in non-equilibrium (Park, 1989a), leading to complex interactions between the flow and excitation dynamics which require advanced computational capabilities to study (Passiatore et al., 2022; Ninni et al., 2022).

Characterizing and modeling these effects is crucial in turbulent hypersonic boundary layers to predict the thermal loads on the surface. Here, the description is limited to the conductive nature of heat transfer $q_w = \lambda_w \partial T / \partial y|_w$ associated with thermal conductivity λ_w and the wall temperature gradient. It is important to note that another source of heat in the body (especially for reentry vehicles) is thermal radiation, which is due to the extreme temperatures that the flow field achieves

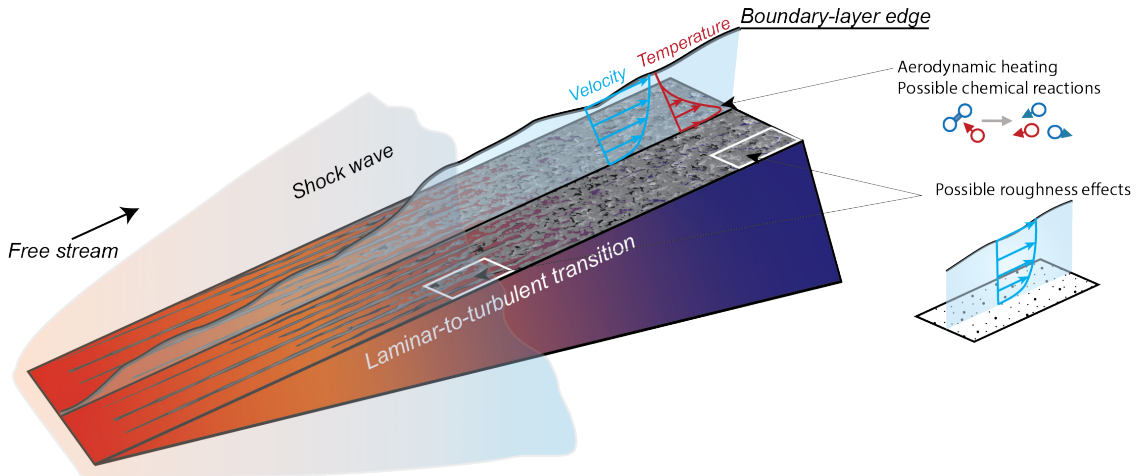


Figure 1.3: Schematic of a hypersonic flow configuration over a wedge and the underlying variation of flow properties in the turbulent region.

(for other details, the reader is referenced to Anderson (2006)).

Predictive models for chemically-reacting flows in the near-wall regions are also crucial to compute the average mass fraction of each species, which may interact with the surface material and possibly alter its geometry. Investigating the physics of catalysis and ablation is beyond the scope of this study, and the reader can refer to (Candler, 2019; Bonelli et al., 2021) for an overview. However, we are interested in studying the response of compressible boundary layers to surface roughness that may be a result of these processes or could be related to the inherent composition of thermal protection systems (Uyanna and Najafi, 2020). Surface erosion or pitting may also occur from localized events such as shock wave-boundary layer interaction (Babinsky and Harvey, 2011). These effects permanently modify the wetted area of the flight system for the remainder of the trajectory and may be the cause for the laminar-to-turbulent transition of a boundary layer or can abruptly change the dynamics of an already turbulent flow coming from a smoother surface by locally increasing drag and heat fluxes (Peltier et al., 2016; Bowersox, 2007). Multiple physical aspects of wall-bounded flows over rough walls have been historically studied for low-speed flows (e.g., flow through pipes) and several geometries have been experimentally characterized in terms of their drag increase, which resulted in standardized tools to guide engineering design (e.g., Moody diagram) (Nikuradse, 1933). One key factor driving the research on this topic is that whether a surface is hydraulically smooth or fully rough depends on the fluid flow that occurs next to it, so that relations between a certain roughness geometry and the expected drag are dominated by empirical correlations (Chung et al., 2021; Flack and Schultz, 2014).

In the context of high-speed flows, it is not clear whether the theories developed for incompressible turbulence apply, and the literature on the subject is scarce (Bowersox, 2007; Kocher et al., 2022). Experimental campaigns are very difficult for these types of flow as it is almost impossible to accurately measure near-wall turbulent structures; for this reason, numerical studies are crucial to drive research.

As mentioned above, several different processes and disciplines are entangled in the study of aerothermodynamics, some of which may have been glossed over in this overview. Figure 1.3 provides a sketch of a simplified geometry, a wedge, that includes some important features that are relevant in the engineering design of high-speed vehicles. Highlighted are the formation and development of

a turbulent boundary layer within the shock layer, which features the onset of viscous aerodynamic heating, high temperature effects, and the possible influence of surface roughness. These are the main aspects investigated in the present thesis, whose mathematical model and classical theories are presented in the next chapter.

Chapter 2

Physics of high-speed boundary layers

In this chapter, we will review the classical theory of compressible turbulent boundary layers, stressing the most important relations and scalings that can be derived from them.

2.1 Fundamental aspects of high-speed turbulent boundary layers

The Navier-Stokes equations provide the mathematical basis for the description of compressible flows, ascribing the conservation of mass, momentum, and energy. In this section, we begin by introducing their formulation in the assumption of a viscous, heat-conducting, calorically-perfect gas (Gatski and Bonnet, 2013):

$$\frac{\partial \rho}{\partial t} + \frac{\partial(\rho u_j)}{\partial x_j} = 0, \quad (2.1a)$$

$$\frac{\partial(\rho u_i)}{\partial t} + \frac{\partial(\rho u_i u_j)}{\partial x_j} + \frac{\partial p}{\partial x_i} - \frac{\partial \sigma_{ij}}{\partial x_j} = 0, \quad (2.1b)$$

$$\frac{\partial(\rho E)}{\partial t} + \frac{\partial(\rho u_j H)}{\partial x_j} - \frac{\partial(\sigma_{ij} u_i - q_j)}{\partial x_j} = 0. \quad (2.1c)$$

where ρ is the density, u_i denotes the velocity component in the i th Cartesian direction ($i = x, y, z$), p is the thermodynamic pressure and

$$\sigma_{ij} = \mu \left(\frac{\partial u_i}{\partial x_j} + \frac{\partial u_j}{\partial x_i} - \frac{2}{3} \frac{\partial u_k}{\partial x_k} \delta_{ij} \right), \quad (2.2)$$

is the viscous stress tensor for a Newtonian fluid. In the energy equation, Eq. (2.1c), q_j is the heat flux in the j -th direction and can be modelled using Fourier's law

$$q_j = -\lambda \frac{\partial T}{\partial x_j}, \quad (2.3)$$

where $k = k(T)$ is the heat transport coefficient of the system and $\partial T / \partial x_j$ is the temperature gradient.

The system is supplemented by the ideal gas equation of state

$$p = \rho R T, \quad (2.4)$$

being R is the specific gas constant, and a caloric equation of state for the total energy

$$E = e + \frac{u_i u_i}{2} = c_v T + \frac{u_i u_i}{2}, \quad (2.5)$$

where e is the internal energy. The total energy is related to the total enthalpy by the relation $H = h + u_i u_i / 2 = E + p/\rho$.

The molecular viscosity μ is assumed to follow Sutherland's law

$$\mu(T) = T^{3/2} \left(\frac{T_0 + S}{T + S} \right), \quad (2.6)$$

where T_0 is a reference free-stream temperature and S is an empirical parameter ($S = 110.4K$ for air). Finally, the thermal conductivity λ is related to the viscosity through the Prandtl number $Pr = 0.72$, $k = c_p \mu / Pr$, where c_p is the specific heat at constant pressure.

2.1.1 Reynolds averaged Navier-Stokes

The statistical analysis of compressible flows involves an averaging process that partitions the flow variables into an averaged part \bar{f} and a fluctuating part f' , such that $f = \bar{f} + f'$, which is called the Reynolds decomposition. In the Reynolds-averaged Navier-Stokes (RANS) framework, the averaged quantity \bar{f} can be evaluated with an ensemble average, which can be represented by a long time average over numerous turbulent time scales in the case of stationary flow (hence ergodicity can be assumed), or a spatial average over many turbulent length scales if the turbulence is statistically homogeneous. In compressible flows, another type of average is frequently used for its convenient properties that simplify the mathematical treatment of N-S averaged equations, the density-weighted average (or Favre) (Gatski and Bonnet, 2013). For a dependent variable f , the Favre average is defined as

$$\tilde{f} = \frac{\overline{\rho f}}{\bar{\rho}}, \quad (2.7)$$

while its fluctuating part is denoted by f'' , such that $f = \tilde{f} + f''$. Note that in both Reynolds and Favre decompositions, the partitioning between averaged and fluctuating quantities can also be substituted by a filtering process, applicable for example to the Large Eddy Simulation; see section 3.1.

Reynolds Averaged Navier-Stokes equations are the result of the averaging process applied to Eqs. (2.1), which is not derived here in order not to overload the discussion. Their final form can be written as Gatski and Bonnet (2013):

$$\frac{\partial \bar{\rho}}{\partial t} + \frac{\partial(\bar{\rho} \bar{u}_j)}{\partial x_j} = 0, \quad (2.8a)$$

$$\frac{\partial(\bar{\rho} \tilde{u}_i)}{\partial t} + \frac{\partial}{\partial x_j} (\bar{\rho} \tilde{u}_i \tilde{u}_j) = -\frac{\partial \bar{p}}{\partial x_i} + \frac{\partial}{\partial x_j} (\bar{\sigma}_{ij} - \bar{R}_{ij}), \quad (2.8b)$$

$$\frac{\partial(\bar{\rho} \tilde{E})}{\partial t} + \frac{\partial}{\partial x_j} (\bar{\rho} \tilde{u}_j \tilde{H}) = \frac{\partial}{\partial x_j} (\bar{u}_i \bar{\sigma}_{ij}) - \frac{\partial \bar{q}_j}{\partial x_j} - \frac{\partial \bar{Q}_j}{\partial x_j}. \quad (2.8c)$$

where terms \bar{R}_{ij} and \bar{Q}_j arise from the decomposition of convective terms in the left hand side of

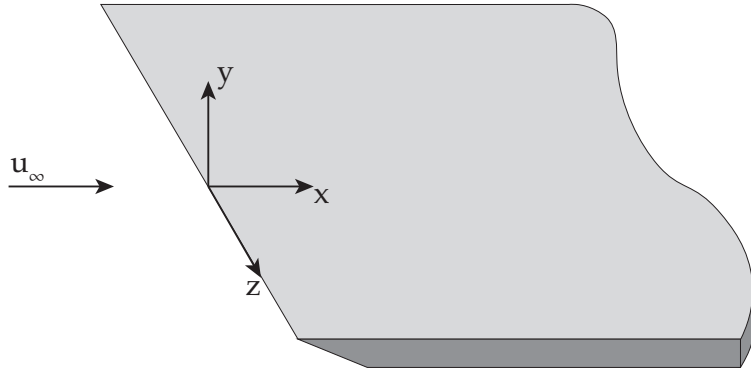


Figure 2.1: Schematic of a flat-plate boundary layer.

equations (2.8b) and (2.8c). The turbulent stress tensor \bar{R}_{ij} takes the form $\bar{R}_{ij} = \bar{\rho}\widetilde{u_i''u_j''}$, while \bar{Q}_j incorporates temperature-velocity turbulent diffusion and higher-order velocity correlations:

$$\bar{Q}_j = \bar{\rho}c_p\widetilde{u_j''T''} + \frac{\bar{\rho}\widetilde{u_i''u_i''u_j''}}{2} + \bar{\rho}\widetilde{u_i}u_i''\widetilde{u_j''}. \quad (2.9)$$

The presence of terms \bar{R}_{ij} and \bar{Q}_j prevents a closed-form solution of the RANS equations and must be modeled or parametrized in some way. One of the possible ways is discussed in Section 3.1.

2.1.2 Boundary layer approximation

We now consider the case of a wall-bounded flow developing over a smooth flat plate along the streamwise coordinate x . The surface of the plate is positioned at the wall-normal location $y = 0$, where the flow velocity is zero (no-slip condition), while it reaches a constant value of u_∞ outside of the boundary layer, assuming a zero-pressure-gradient (ZPG) condition, $dp_\infty/dx = 0$. The flow is statistically homogeneous in the spanwise direction z .

One of the first definitions of the boundary layer thickness $\delta(x)$ that is found in the literature (Pope, 2000) is the wall-normal location at which the average streamwise velocity reaches the 99% of its free-stream value, $\bar{u}(x, y) = 0.99u_\infty$, referred to with the symbol δ_{99} . Integral measures are also often used, such as the displacement thickness

$$\delta^* = \int_0^\infty \left(1 - \frac{\overline{\rho u}}{\rho_\infty u_\infty}\right) dy, \quad (2.10)$$

or the momentum thickness

$$\theta = \int_0^\infty \frac{\overline{\rho u}}{\rho_\infty u_\infty} \left(1 - \frac{\bar{u}}{u_\infty}\right) dy, \quad (2.11)$$

whose ratio is called the shape factor $H = \delta^*/\theta$. From the momentum thickness θ can be defined the classically used Reynolds numbers $Re_\theta = \rho_\infty u_\infty \theta / \mu_\infty$ and $Re_{\delta_2} = \rho_\infty u_\infty \theta / \mu_w$, where the subscript w indicates quantities computed at the wall. Other Reynolds numbers can be formed using different measures, such as displacement thickness δ^* or 99% thickness δ_{99} , which are all indicative of the largest scales of turbulent motions in the boundary layer.

However, these scales are not representative of the inner part of the boundary layer, where viscous effects progressively dominate. This is even more true in compressible boundary layers, where thermodynamic quantities vary considerably from the freestream to the wall. Different layers

can be defined within the main boundary layer by physical considerations on the dominating terms of averaged N-S applied to this problem. In the boundary layer approximation, we can simplify Eqs. (2.8) by considering that a steady-state regime with the flow that is statistically independent in the z direction and develops slowly in the x direction, with axial gradients being small compared with wall-normal ones. This derivation was first made by Van Driest (1951), and is reported here with the use of Favre averages (Gatski and Bonnet, 2013):

$$\frac{\partial \bar{\rho} \bar{u}}{\partial x} + \frac{\partial \bar{\rho} \bar{v}}{\partial y} = 0, \quad (2.12a)$$

$$\bar{\rho} \bar{u} \frac{\partial \bar{u}}{\partial x} + \bar{\rho} \bar{v} \frac{\partial \bar{u}}{\partial y} = \frac{\partial}{\partial y} \left[\bar{\sigma}_{xy} - \widetilde{\bar{\rho} u'' v''} \right], \quad (2.12b)$$

$$\bar{\rho} \bar{u} \frac{\partial \bar{h}}{\partial x} + \bar{\rho} \bar{v} \frac{\partial \bar{h}}{\partial y} = - \frac{\partial}{\partial y} \left[q_y + c_p \bar{\rho} \widetilde{v'' T''} \right] - \frac{\partial}{\partial y} \left[\tilde{u} \left(\bar{\sigma}_{xy} - \widetilde{\bar{\rho} u'' v''} \right) \right]. \quad (2.12c)$$

Here, we note that the momentum equation (2.12b) is only reported for its streamwise component x , since the flow is independent of the spanwise direction and the wall-normal component y reduces to:

$$\frac{\partial \bar{p}}{\partial y} + \frac{\partial (\bar{\rho} \widetilde{v''^2})}{\partial y} = 0, \quad (2.13)$$

The analysis of Eq. (2.12b) is of critical importance in order to grasp the dominant factors that compete within the boundary layer, namely viscous stresses, acting through the term $\sigma_{xy} = \bar{\mu} \partial \bar{u} / \partial y$, and turbulent (or Reynolds) stresses, acting through the term $\widetilde{\bar{\rho} u'' v''}$. If we assume that in the inner layer convective terms can be ignored (left hand side of Eq. (2.12b)), rembembering that we already made the assumption of zero-pressure-gradient, we can derive the existence of a constant stress layer, and Eq. (2.12b) integrates to

$$\bar{\mu} \frac{\partial \bar{u}}{\partial y} - \widetilde{\bar{\rho} u'' v''} \approx const = \tau_w, \quad (2.14)$$

where $\tau_w = \mu_w \partial \bar{u} / \partial y|_w$ is the wall shear stress. In this layer, the sum of viscous and turbulent stresses is approximately constant, yielding several important relations that are universal to wall-bounded flows. Given the dominance of viscous effects close to the wall, we define viscous scales that are representative of the near-wall region, such as the friction velocity

$$u_\tau \equiv \sqrt{\frac{\tau_w}{\rho_w}}, \quad (2.15)$$

and the viscous lengthscale

$$\delta_\nu \equiv \frac{\mu_w}{\rho_w u_\tau}, \quad (2.16)$$

such that a Reynolds number based on these scales is identically unity, $u_\tau \delta_\nu \rho_w / \mu_w = 1$. These scales are essential to define the region where viscous effects are dominant, the viscous layer, as opposed to the scales representative of the whole boundary layer, the outer layer, such as u_∞ , and δ_{99} . With these definitions, we can introduce the friction Reynolds number

$$Re_\tau \equiv \frac{\rho_w u_\tau \delta_{99}}{\mu_w} = \frac{\delta_{99}}{\delta_\nu}, \quad (2.17)$$

which is an important parameter representative of the separation of turbulent scales. Similarly to the definition of Re_τ number, the y coordinate can be rescaled with viscous length to form the so-called wall units, indicated with $y^+ = y/\delta_\nu$, as well as the inner scaled velocity $u^+ = u/u_\tau$.

Other important quantities can be defined, such as the friction Mach number

$$M_\tau = \frac{u_\tau}{a_w}, \quad (2.18)$$

where $a_w = \sqrt{\gamma R T_w}$ is the speed of sound at the wall, and the heat flux parameter

$$B_q = \frac{q_w}{\rho_w c_p u_\tau T_w}. \quad (2.19)$$

Given these definitions, we can introduce the two famous laws of the wall, the linear and log laws (Pope, 2000). In order to obtain a similarity with the incompressible derivation, which is the standard to which even compressible flows aim to compare with, we will make specific assumptions that do not take into account the local variations of thermodynamic and transport quantities such as viscosity and density, by instead taking their value at the wall as constant. Section 2.1.4 will summarize the advancements made so far in order to obtain appropriate scalings for compressible flows that maintain the validity of these laws.

If we consider the first part of the viscous layer, the viscous sublayer (approximately up to $y^+ < 5$), the Reynolds stresses can be neglected from Eq. (2.14), yielding the expression $\tau_w = \bar{\mu} \partial \bar{u} / \partial y$. If we assume that the viscosity in this region remains constant, equal to its value at the wall μ_w , we can reformulate this expression as

$$\mu_w \frac{\partial \bar{u}}{\partial y} = \rho_w u_\tau^2, \quad (2.20)$$

which can be rewritten as $\partial u^+ / \partial y^+ = 1$. Hence, the inner-scaled velocity is linearly dependent to the wall-normal direction in wall units

$$u^+ = y^+, \quad y^+ < 5. \quad (2.21)$$

On the other hand, outside the viscous layer exists a region in which total shear stress is almost entirely composed of Reynolds stresses $\widetilde{\rho u'' v''}$, being viscosity effects negligible. In this region, τ_w is now equal to the Reynolds stresses, which can be viewed through the Boussinesq assumption as the product of an additional 'eddy' viscosity and the mean strain rate

$$\tau_w = -\widetilde{\rho u'' v''} = \mu_T \frac{\partial \bar{u}}{\partial y}, \quad (2.22)$$

where μ_T is defined as $\mu_T = \rho_w l^2 \partial \bar{u} / \partial y$, where $l = \kappa y$ is the mixing length (Pope, 2000). Here, the use of wall density ρ_w is made in accordance with the incompressible literature, assuming that the density is constant in this region. In Section 2.1.4 we will discard this assumption. If the expression of the eddy viscosity is substituted in Eq. (2.22), we arrive to an expression for the mean strain rate

$$\frac{\partial \bar{u}}{\partial y} = \frac{u_\tau}{\kappa y}, \quad (2.23)$$

where κ is the von Kármán constant approximately equal to 0.41. By integrating Eq. (2.23) we

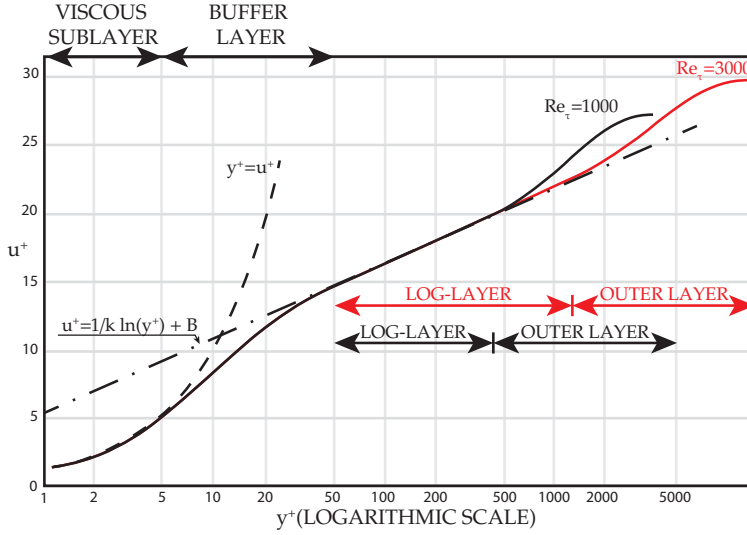


Figure 2.2: Regions of a zero pressure gradient turbulent boundary layer.

obtain the famous log law

$$u^+ = \frac{1}{\kappa} \ln y^+ + B, \quad 30 < y^+ < 0.3 Re_\tau, \quad (2.24)$$

where B is a constant experimentally measured around 5.2. The region between the viscous sublayer ($y^+ < 5$) and the log-law region ($y^+ > 30$) is called the buffer layer. It is the transition region between the viscosity-dominated and turbulence-dominated parts of the flow (Pope, 2000). A summary of the different regions of a boundary layer, with the expected behavior of the mean velocity profile in inner units, is presented in figure 2.2.

2.1.3 Turbulent kinetic energy budget

The importance of defining different regions within a turbulent boundary layer is also apparent in the dynamics of the fluctuating velocity field, defined by the three components $\tilde{u}'', \tilde{v}'', \tilde{w}''$. These three components contribute to the turbulent kinetic energy, defined as $k = 1/2 \tilde{u}_i'' \tilde{u}_i''$, whose transport equation for a compressible boundary layer (according to the derivation of Zhang et al. (2018), which is followed to ease the comparison) is given by

$$\frac{(D\bar{\rho}k)}{Dt} = P + TT + \Pi - \phi + D + ST, \quad (2.25)$$

with

$$P = -\bar{\rho} \widetilde{u_i'' u_j''} \frac{\partial \widetilde{u_i}}{\partial x_j}, \quad (2.26)$$

$$TT = -\frac{\partial}{\partial x_j} \left[\frac{1}{2} \bar{\rho} \widetilde{u_i'' u_i'' u_j''} \right], \quad (2.27)$$

$$\Pi = -\frac{\partial}{\partial x_i} \left(\overline{p' u_i''} \right) + p' \overline{\frac{\partial u_i''}{\partial x_i}}, \quad (2.28)$$

$$\phi = \overline{\sigma'_{ij} \frac{\partial u_i''}{\partial x_j}}, \quad (2.29)$$

$$D = \frac{\partial}{\partial x_j} \left(\overline{\sigma'_{ij} u''_i} \right), \quad (2.30)$$

$$ST = -\bar{\rho} \tilde{k} \frac{\partial \tilde{u}_k}{\partial x_k} + \overline{u''_i} \left(\frac{\partial \bar{\sigma}_{ij}}{\partial x_j} - \frac{\partial \bar{p}}{\partial x_i} \right). \quad (2.31)$$

where P is the production term, TT represents the turbulent transport, Π includes the pressure diffusion and dilatation, $-\phi$ is the viscous dissipation, D is the viscous diffusion, and ST includes all additional terms that arise when density is not constant.

In a turbulent boundary layer, we observe that turbulent production P reaches its maximum in the buffer layer, sustaining the near-wall cycle of turbulence (Pope, 2000). The intensity of this peak, as well as its location, can be affected by compressibility and wall cooling in a way that is currently not clear Zhang et al. (2018), and it is subject of research in the present thesis. Another important fact is that in the log-layer there is approximate self-similarity, which implies, among other things, that production and dissipation are in balance $P/\phi \approx 1$, the viscous and turbulent transport being very small in comparison. This argument yields important consequences for modeling purposes in incompressible flows, while thermodynamic property variations need to be accounted for in compressible ones in order to maintain its validity (Griffin et al., 2023) (see Section 2.1.4).

2.1.4 Compressibility transformations

Compressible flows are characterized by locally variable thermodynamic properties, such as temperature and density, which can alter the applicability of some theoretical laws developed for their incompressible counterparts. In fact, the agreement of a compressible mean velocity profile with the laws depicted in Figure 2.2 would progressively degrade as the Mach number increases, especially in the log-layer. In order to mitigate this effect, the hypothesis from Morkovin (1962) argues that in the absence of shocks, and by accounting for mean density and temperature variations, the mean and turbulent compressible flow variables can be cast to a behavior similar to their incompressible counterpart. Perhaps the clearest example of this hypothesis is the compressibility transformation proposed by Van Driest (1956), one of the first relations of this kind and still routinely used by present numerical tools.

If we reconsider Eq. (2.22), stating that in the log-layer turbulent stresses are in equilibrium with the total shear stress, we can now define in a more appropriate way the eddy viscosity $\mu_T = \bar{\rho} l^2 \partial \bar{u} / \partial y$, where the average density $\bar{\rho} = f(y)$ has been used instead of its value at the wall ρ_w . In this way, Eq. (2.23) becomes

$$\sqrt{\frac{\bar{\rho}}{\rho_w} \frac{\partial \bar{u}}{\partial y}} = \frac{u_\tau}{\kappa y}. \quad (2.32)$$

Equation (2.32) can not be directly integrated to obtain a log law given that density is also variable in y , but instead we aim to find a rescaled version of the mean velocity profile that would be consistent with Eq. (2.23)

$$\frac{\partial \bar{u}_{VD}}{\partial y} = \sqrt{\frac{\bar{\rho}}{\rho_w} \frac{\partial \bar{u}}{\partial y}}, \quad \bar{u}_{VD} = \int_0^u \sqrt{\frac{\bar{\rho}}{\rho_w}} d\bar{u}, \quad (2.33)$$

which is the Van Driest transformed velocity. In practice, the Van Driest (1956) transformation was found to be accurate only up to supersonic speeds $M_\infty \approx 2$ and only for adiabatic walls. This

can be explained by the physical inconsistency of physical arguments developed specifically for the log-layer which are not valid in the viscous sublayer, which is affected the most by diabatic effects (Zhang et al., 2018).

In fact, in Section 2.1.2 we showed that this region is dominated by viscous stresses, with a strong damping of turbulent fluctuations. On this note, we consider Eq. (2.20), reformulated by Carvin et al. (1988) by accounting for viscosity variations $\bar{\mu}\partial\bar{u}/\partial y = \rho_w u_\tau^2$, which upon rewriting becomes

$$\frac{\bar{\mu}}{\mu_w} \bar{\mu}_w \frac{\partial \bar{u}}{\partial y} = \rho_w u_\tau^2. \quad (2.34)$$

Once again, we recognize that Eq. (2.34) differs from Eq. (2.20) for the factor $\bar{\mu}/\mu_w$, from which a rescaled version of the velocity profile that better accounts for compressibility effects in the viscous layer can be derived

$$\frac{\partial \bar{u}_{CA}}{\partial y} = \frac{\bar{\mu}}{\mu_w} \frac{\partial \bar{u}}{\partial y}, \quad \bar{u}_{CA} = \int_0^u \frac{\bar{\mu}}{\mu_w} d\bar{u}, \quad (2.35)$$

Comparing the laws of Van Driest (1956) and Carvin et al. (1988), we have a first feeling on how different regions on the boundary layer require different physical arguments in order to obtain an accurate velocity transformation, which is one of the core issues faced by recent advancements on the field.

However, before reviewing recent studies on velocity scalings comprehensive of the whole boundary layer, Huang et al. (1995) took a step forward by pointing out that compressibility effects should be taken into account in the definition of viscous scales, such as friction velocity u_τ , Eq. (2.15), and viscous length scale δ_ν , Eq. (2.16). For this reason, they proposed a ‘semilocal’ version of these scales, namely the semilocal friction velocity $u_\tau^* = \sqrt{\tau_w/\bar{\rho}}$ and length scale $\delta_\nu^* = \bar{\mu}/(\bar{\rho}u_\tau^*)$.

Given these new definitions, a semilocal wall-normal coordinate $y^* = y/\delta_\nu^*$ can be defined, which is related to y^+ by the expression

$$y^* = \left(\frac{\mu_w}{\bar{\mu}} \right) \left(\frac{\bar{\rho}}{\rho_w} \right)^{1/2} y^+. \quad (2.36)$$

Lastly, we can also define a semilocal version of the friction Reynolds number

$$Re_\tau^* = \frac{u_\tau^* \rho_\infty \delta_{99}}{\mu_\infty} = \frac{\delta_{99}}{\delta_\nu^*}. \quad (2.37)$$

which is now describing the separation of scales using freestream values of density and viscosity (Hirai et al., 2021).

Huang et al. (1995) showed that the use of semilocal scaling was more appropriate to map the wall-normal distributions of turbulence statistics to their incompressible counterparts. This finding was later confirmed by other authors (Coleman et al., 1995), especially when diabatic walls were considered.

More recently, Trettel and Larsson (2016) and Patel et al. (2016) managed to propose a scaling that incorporates the arguments of Van Driest (1951) in the log-layer, Eq. (2.32), and the physical considerations that are relevant to the viscous layer introduced by Carvin et al. (1988), Eq. (2.34). Interestingly, the mean stress balance between these two formulations naturally suggests the use of the semilocal scaling proposed by Huang et al. (1995) when a transformed wall-normal coordinate Y is considered.

$$\frac{\partial \bar{u}_{TL}}{\partial Y} = \frac{\bar{\mu}}{\mu_w} \frac{\partial \bar{u}}{\partial y}, \quad Y = \left(\frac{\mu_w}{\bar{\mu}} \right) \sqrt{\frac{\bar{\rho}}{\rho_w}} y, \quad (2.38)$$

where the ratio Y/y is equivalent to the ratio y^*/y^+ defined on Eq. (2.36). In its final form, the Trettel and Larsson (2016) transformation reads:

$$u_{TL} = \int_0^u \left(\frac{\bar{\rho}}{\rho_w} \right)^{1/2} \left[1 + \frac{1}{2} \frac{1}{\bar{\rho}} \frac{d\bar{\rho}}{dy} y - \frac{1}{\bar{\mu}} \frac{d\bar{\mu}}{dy} y \right] d\bar{u}, \quad (2.39)$$

which can be rewritten as (Patel et al., 2016)

$$u_{TL} = \int_0^u \sqrt{\frac{\bar{\rho}}{\rho_w}} \left(1 - \frac{y}{\delta_\nu^*} \frac{d\delta_\nu^*}{dy} \right) d\bar{u}, \quad (2.40)$$

where the improvement from the Van Driest (1956) transformation is more evident looking at the bracketed term. Trettel and Larsson (2016) transformation has shown to overcome some of the shortcomings of the widely used Van Driest (1956), especially for turbulent channel flows, however still showing inaccurate results for diabatic turbulent boundary layers.

Building on this research thread, we arrive at one of the state-of-the-art scalings proposed very recently by Hasan et al. (2023). In contrast to previous studies, which predicated on the ability to incorporate compressibility effects only by accounting for the variations of the mean properties, that is, Morkovin's hypothesis, Hasan et al. (2023) showed specific cases in which this leads to considerable errors. They argued that a good parameter to account for intrinsic compressibility effects is the friction Mach number M_τ , which can be leveraged to incorporate them in an efficient scaling. The resulting expression adds a correction term to the existing Trettel and Larsson (2016) transform, maintaining the use of semilocal scaling y^* for the wall-normal coordinate

$$u_{HLPP} = \int_0^u \left(\frac{1 + \kappa y^* D^c}{1 + \kappa y^* D^i} \right) \sqrt{\frac{\bar{\rho}}{\rho_w}} \left(1 - \frac{y}{\delta_\nu^*} \frac{d\delta_\nu^*}{dy} \right) d\bar{u}. \quad (2.41)$$

Here, $D^i = [1 - \exp(-y^*/A^+)]^2$ and $D^c = [1 - \exp(-y^*/(A^+ + f(M_\tau)))]^2$ are damping functions, A^+ is a constant usually taken as 17 and $M_\tau = u_\tau / \sqrt{\gamma R T_w}$ is the friction Mach number.

Lastly, we introduce the relation proposed by Griffin et al. (2021), which builds upon the transformations of Trettel and Larsson (2016) and Zhang et al. (2012). Griffin et al. (2021) transformation is based on the total stress equation $\tau^+ = \tau_\nu^+ + \tau_R^+$, where the superscript + indicates a nondimensionalization by τ_w , without assuming that a constant-stress-layer exists ($\tau^+ \approx 1$ as in Eq. (2.14)), and invoking different physical arguments for the mean shear rate in the viscous and log layers.

In particular, in the near-wall limit, where $\tau_\nu^+ \rightarrow \tau^+$ the relation of Trettel and Larsson (2016) is used to model the mean shear rate $S_{TL}^+ = \bar{\mu}/\mu_w \partial \bar{u}^+ / \partial y^*$, arguing that its validity range is strictly in this region. In the log layer region, the relation of Zhang et al. (2012) is extended in order to take into account the semilocal scaling proposed by Huang et al. (1995) and a strictly weaker assumption of quasi-equilibrium is made concerning the turbulent production and dissipation ratio (for more details refer to the original paper), yielding the expression $S_{eq}^+ = \mu_w / \bar{\mu} \partial \bar{u}^+ / \partial y^*$ (the subscript 'eq' indicates the assumption of turbulence quasi-equilibrium).

The total stress equation is then written in terms of a generalized nondimensional mean shear

$S_t^+ = \partial \bar{u}_t^+ / \partial y^*$, which reads

$$S_t^+ = \frac{\tau^+ S_{eq}^+}{\tau^+ + S_{eq}^+ - S_{TL}^+}, \quad (2.42)$$

and the transformed velocity profile can be obtained by integrating S_t^+ with respect to the semilocal wall-normal coordinate $\bar{u}_t^+ = \int S_t^+ dy^*$.

Both Griffin et al. (2021) and Hasan et al. (2023) transformations obtained excellent results in different flows configurations, including diabatic turbulent boundary layers. However, Griffin et al. (2021) is found to be inaccurate in ideal gas cases with non-air-like viscosity laws, and supercritical fluid cases, where Hasan et al. (2023) shows good results.

2.1.5 Reynolds analogy

As discussed in previous sections, in compressible flows the momentum and energy equations are tightly coupled, and energy transfers between kinetic and thermal fields are ubiquitous. However, building from the incompressible literature, the kinetic part has been the main focus of research, given its direct implications on surface drag and its universal behaviour in wall bounded flows. In high-speed flows, the temperature profiles have a much higher variability in surface boundary condition, which can wildly vary with respect to the material properties of the solid surface and its thermal response to the different regimes encountered in the flight trajectory. In order to be able to predict the resulting heat flux transferred to the vehicle's surface without having to solve the full set of N-S equations, researchers have been interested in finding a simplified relation between average kinetic and thermal fields.

To this end, a similarity between the Reynolds-averaged momentum and energy equations was first noted by Reynolds (1874), which in the case of unit Prandtl number resulted in an algebraic temperature-velocity relation. Busemann (1931) and Crocco (1932) independently derived a similar relation for compressible laminar boundary layers, which was later extended by Van Driest (1951) to turbulent flows, resulting in the famous quadratic function

$$\frac{\bar{T}}{T_\infty} = \frac{T_w}{T_\infty} + \frac{T_{c,\infty} - T_w}{T_\infty} \frac{\bar{u}}{u_\infty} + \frac{T_\infty - T_{c,\infty}}{T_\infty} \left(\frac{\bar{u}}{u_\infty} \right)^2, \quad T_{c,\infty} = T_\infty + c \frac{u_\infty^2}{2c_p}, \quad (2.43)$$

where the parameter c equals to one in the Crocco-Busemann relation (yielding the definition of total temperature T_0), and has been later substituted by the recovery factor $r \approx Pr^{1/3}$ by Walz (1969) to account for deviation of Pr from unity. The classical relationship of Walz (1969) has showed to behave well in adiabatic turbulent boundary layers, while decreasing its performances as wall cooling increases (Duan et al., 2010). Duan and Martin (2011) tackled this problem by proposing an empirical relation accounting for finite wall flux, which was later generalized by the work of Zhang et al. (2014). In this work, a general recovery factor r_g was introduced that includes the effect of Prandtl, wall temperature and pressure gradients

$$\frac{\bar{T}}{T_\infty} = \frac{T_w}{T_\infty} + \frac{T_{rg} - T_w}{T_\infty} \frac{\bar{u}}{U_\infty} + \frac{T_\infty - T_{rg}}{T_\infty} \left(\frac{\bar{u}}{U_\infty} \right)^2, \quad (2.44)$$

where $T_{rg} = T_\infty + r_g U_\infty^2 / (2c_p)$ and $r_g = 2c_p(T_w - T_\infty)/U_\infty^2 - 2Pr q_w/(U_\infty \tau_w)$. Following the discussion of Zhang et al. (2014), the Reynolds analogy factor s comes into play to greatly simplify

the calculation of r_g , since this term can be rewritten in terms of Reynolds analogy factor s , and the diabatic parameter $\Theta = (T_w - T_\infty)/(T_r - T_\infty)$

$$r_g = r[sPr + (1 - sPr)\Theta], \quad (2.45)$$

being s defined as

$$s = \frac{2C_h}{C_f} = \frac{q_w u_\infty}{\tau_w c_p (T_w - T_r)}, \quad (2.46)$$

where $C_f = \tau_w/(1/2\rho_\infty u_\infty^2)$ is the skin friction coefficient and $C_h = q_w/(\rho_\infty u_\infty c_p(T_w - T_r))$ the Stanton number. The simplification consists of the fact that several authors (Duan et al., 2010; Zhang et al., 2014) identified the term sPr to be an empirical constant around the value of 0.8 ± 0.03 (data fitting of Zhang et al. (2014)) in several different flow cases, meaning that only T_w would be needed to be evaluated to compute r_g .

In the study of Zhang et al. (2014), the relevance of the diabatic parameter Θ is underlined for characterizing the wall temperature effects in diabatic compressible BLs, and its formulation is closely related to the definition of the Eckert number (Wenzel et al., 2022). These controlling parameters are discussed in detail in Paper II. For this work, we also highlight the fact that sPr can be considered a constant in numerous flow cases is very important for modeling purposes, as it establishes a simple relation between the expected friction and heat transfer that greatly reduce the model complexity.

A set of theoretical relations coupling the thermodynamic and kinetic fluctuating fields was firstly introduced by Morkovin (1962), which collectively goes under the name of Strong Reynolds Analogy (SRA). Originally derived for an adiabatic case, the three main relations can be expressed as

$$\begin{aligned} \frac{\left(\widetilde{T''^2}\right)^{1/2}/\tilde{T}}{(\gamma - 1)\tilde{M}^2 \left(\widetilde{u''^2}\right)^{1/2}/\tilde{u}} &\approx 1, \\ R_{u''T''} = \frac{\widetilde{u''T''}}{\sqrt{\widetilde{u''^2}}\sqrt{\widetilde{T''^2}}} &\approx 1, \\ Pr_t = \frac{\overline{\rho u'v'}(\partial \tilde{T}/\partial y)}{\overline{\rho T'v'}(\partial \tilde{u}/\partial y)} &\approx 1. \end{aligned} \quad (2.47)$$

The remaining two relations of equation (2.47) have been modified over the years to account for finite heat flux at the wall and remove wall temperature dependence (Huang et al., 1995) (HSRA). The most recent improvement has been made by Zhang et al. (2014), who proposed another definition of the turbulent Prandtl number \overline{Pr}_t which should perform better at high Mach numbers, yielding the following expression of the modified strong Reynolds analogy (modified HRSA):

$$\frac{\left(\widetilde{T''^2}\right)^{1/2}/\tilde{T}}{(\gamma - 1)\tilde{M}^2 \left(\widetilde{u''^2}\right)^{1/2}/\tilde{u}} \overline{Pr}_t \left(1 - (\partial \tilde{T}_t/\partial \tilde{T})\right) \approx 1 \quad (2.48)$$

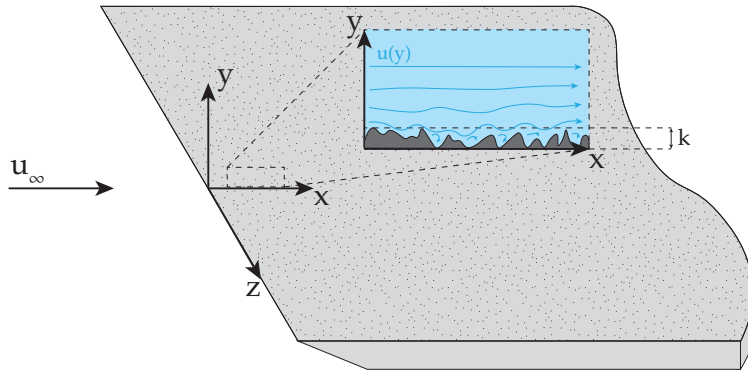


Figure 2.3: Schematic of a boundary layer over a rough surface. Here, k is the peak-to-trough roughness height.

where the proposed definition of $\overline{Pr_t}$ is

$$\overline{Pr_t} = \frac{\overline{(\rho v)'u'}\partial\tilde{T}/\partial y}{\overline{(\rho v')T'}\partial\tilde{u}/\partial y} = Pr_t \frac{1 + \bar{v}\overline{\rho'u'}/\overline{\rho v'u'}}{1 + \bar{v}\overline{\rho'T'}/\overline{\rho v'T'}}, \quad (2.49)$$

in which the difference from the classical definition is notable when both \bar{v} and ρ' are nonzero.

The validation process of the advancements in Zhang et al. (2014) is undergoing, and the present thesis represent a contribution to this end. Nevertheless, the preliminary encouraging results pave the way for a systematic prediction of mean and fluctuating temperature fields given information from the kinetic counterpart, which can in turn be rescaled to the incompressible laws of the wall thanks to compressibility transformations (see section 2.1.4). These arguments have already led to interesting modeling implications, which are discussed in chapter 3.

2.2 Roughness effects

In this section, we introduce the basic theory of wall bounded flows over rough walls, as opposed to the hydraulically smooth nature of boundary layers considered in section 2.1.2. Here, the expression 'hydraulically smooth' means that the flow is not affected by the surface imperfections, which are present in every material at some scale. This fact leads to a first important consideration, which can be counterintuitive: in fluid mechanics, whether a surface is smooth or rough does not depend only on its finishing but also on the regime of the flow occurring next to it. In practice, topographical features have to be large enough to disrupt the natural behavior of the smallest turbulent eddies, altering the transfer of momentum and heat. As discussed in section 2.1.2, in turbulent boundary layers the smallest eddies are of the order of δ_ν , which can be very different depending on the considered configuration, thus the same surface may be perceived as smooth or rough depending of the flow conditions under consideration.

When characterizing a rough surface, one of the first measures that is usually introduced is the peak-to-trough roughness height k , which gives a first feeling of the expected lenghtscale related to the topographical features (see figure 2.3). Of course, the measure of k can be quite misleading in many geometries, and it has to be complemented by several other quantities, like its mean and root-mean-square values, \bar{k} and k_{rms} , the frontal solidity λ_f , effective slope ES , etc. (Chung et al., 2021). However, for geometries composed of simple elements (cubes, bars, sinusoidal shapes),

frequently considered in fundamental research, it is a good indicator of roughness size, especially when compared to the boundary layer height δ_{99} . In fact, the ratio δ_{99}/k is a first important measure on the separation between the large turbulent scales and the roughness size. At the same time, it is also crucial to compare k with the friction lengthscale δ_ν , yielding the roughness Reynolds number $k^+ = k/\delta_\nu$, which gives a direct information on how the smallest turbulent eddies near the wall will be affected by changes in the surface elevation. In hydraulically smooth surfaces the roughness will be submerged below the viscous sublayer, $k^+ \ll 1$, while if this condition is not strictly satisfied the flow enters the transitionally rough regime. If in the opposite case the roughness size greatly exceeds the friction lengthscale, $k^+ \gg 1$, and a large separation of scales between the roughness size and the boundary layer thickness exists, $\delta_{99}/k \gg 1$, the flow is said to be fully rough. This is one of the most interesting scenarios in the study of turbulent flows over rough surfaces, since roughness effects are confined in a small sublayer, whereas the outer flow perceives its influence only by a change in the length and velocity scales. This means that the turbulence dynamics in the outer layers should be reminiscent of smooth wall-like behavior, and the presence of roughness can be viewed as a change in the boundary condition at the wall that increases shear stress τ_w . More importantly, numerous experiments find the magnitude of this added drag to be independent of the Reynolds number, since the pressure drag becomes the main contributor (Nikuradse, 1933).

This concept is referred to as the 'outer layer similarity', which greatly simplifies the characterization of different rough surfaces in the limit of the fully rough regime. Similarly to the procedure used in section 2.1.2, the physical implications of this discussion are here derived for a fluid with constant thermodynamic properties in order to be consistent with the incompressible literature (which still dominates the field). The inclusion of compressibility effects is discussed in Subsection 2.2.2.

Rewriting the log-law derived in section 2.1.2 for a smooth surface (indicated with the subscript S)

$$u_S^+ = \frac{1}{\kappa} \ln y^+ + B, \quad (2.50)$$

we can now define a similar law based on the roughness height k (Chung et al., 2021)

$$u_R^+ = \frac{1}{\kappa} \ln y/k + B_R(k^+), \quad (2.51)$$

where B_R is in general a function of both the topography and the Reynolds number. However, as discussed above, in the fully rough regime $B_R = B_{R,\infty}$ is only a function of the topography, hence a single value can be assigned once a given surface is characterized by an experiment. In the vast majority of geometries, the value of $B_{R,\infty}$ will be such that there is a negative shift between the rough and smooth velocity profiles $\Delta u^+(y^+) = u_S^+ - u_R^+$, due to the increase in drag. However, under the outer similarity hypothesis, this shift will be constant throughout the log layer, such that a single value can be extracted at a given y^+ , indicated with ΔU^+ , which is a function of the geometry under consideration

$$\Delta U^+ = \frac{1}{\kappa} \ln k^+ + B - B_{R,\infty}, \quad (2.52)$$

such that the logarithmic law for rough walls can be also expressed as

$$u_R^+ = \frac{1}{\kappa} \ln y^+ + B - \Delta U^+, \quad (2.53)$$

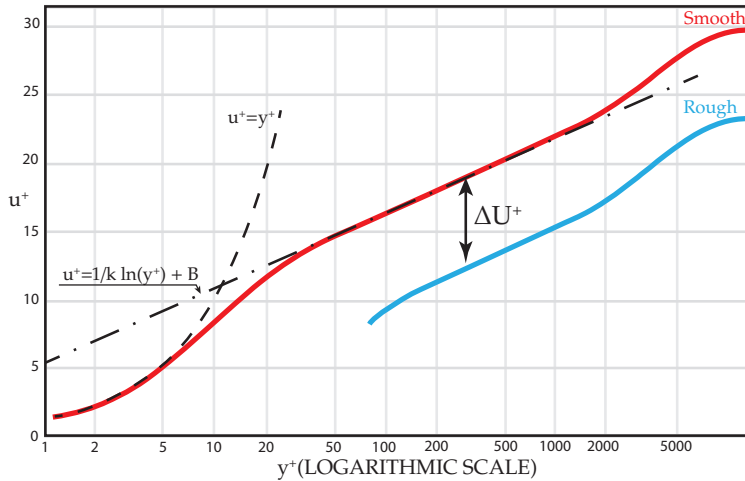


Figure 2.4: Comparison of a smooth and rough mean velocity profiles in the fully rough regime.

see figure 2.4 for reference. The velocity deficit function ΔU^+ (or Hama roughness function), introduced by Clauser (1954) and Hama (1954), allows to directly relate a given surface topography with the expected drag, given that $\Delta U^+ = f(C_{f,S}/C_{f,R})$.

The Hama roughness function ΔU^+ describes the downward shift of the viscous-scaled mean velocity profile induced by roughness compared to a smooth wall, and its soundness, as a measure of added drag, relies on the validity of the outer layer similarity (Clauser, 1954; Hama, 1954). Historically, a particular surface topography has been taken as standard given the first experiments of Nikuradse (1933), the sand-grain roughness, whose size is indicated by k_s . In this case, Eq. (2.52) can be rewritten as

$$\Delta U^+ = \frac{1}{\kappa} \ln k_s^+ + B - B_{s,\infty}, \quad (2.54)$$

where $B_{s,\infty} = 8.5$ in the fully rough regime. According to the study of Jiménez (2004), who reviewed numerous investigations on different types of roughness and flow configurations, the fully rough regime can be defined in terms of the equivalent roughness size when $k_s^+ > 80$, and other geometries can find their equivalent roughness size evaluating the ratio k/k_s , which is at the basis of the Moody diagram. Here, it is important to note that the ratio k/k_s cannot be defined by purely geometrical measures, as it also needs to consider the flow properties being a hydrodynamic measure of equivalent sand grain size that causes the same frictional drag in the fully rough regime. In this sense, knowing the equivalent k_s of a given geometry gives a direct measure of the expected fluid dynamic drag.

Nevertheless, specific topographical features (e.g. frontal solidity, or skewness) could have an influence on the resulting drag that is consistent in a variety of flows, and great effort is devoted to developing a generalized model or correlation that is robust enough to apply effectively to a wide range of rough surfaces encountered in practical applications, seeking a relation of the form

$$k_s = f(\text{topography}). \quad (2.55)$$

For example, Flack and Schultz (2010); Flack et al. (2020) proposed different correlations of this type by considering as critical measures the root mean square size k_{rms} and its skewness S_k . Some important advancements are also reviewed in Chung et al. (2021). Nevertheless, these authors

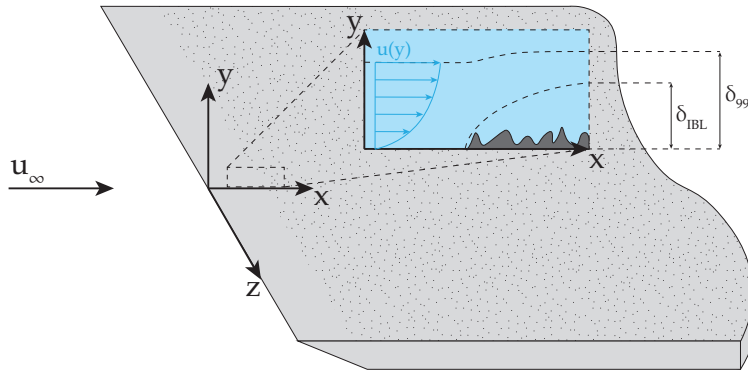


Figure 2.5: Schematic representation of a smooth-to-rough surface transition with the formation of the internal boundary layer (IBL).

underlined that further improvements of these models are inherently tied to the availability of systematic studies considering different geometries and flow configurations.

2.2.1 Variations in the surface topography

When considering the boundary layer flow case, it is important to keep in mind that the flow is constantly developing over the streamwise direction, and its dynamics may be highly influenced by abrupt changes in the surface geometry before or after the test section under consideration. In the incompressible literature, the smooth-to-rough transition (or vice versa) has been extensively investigated for atmospheric boundary layers, or biofouled patches on a ship hull (Rouhi et al., 2019), with the particular focus of addressing the question of when and how the boundary layer can be considered fully adjusted to the new surface (Li et al., 2021).

Several authors tried to measure the formation of an internal boundary layer δ_{IBL} that forms and develops within the incoming boundary layer and eventually merges with it (Rouhi et al., 2019), see figure 2.5. One of the most popular definitions is the one by Cheng and Castro (2002), who determines δ_{IBL} as the point where the velocity \tilde{u}/u_{edge} downstream the transition point is 99% of the upstream velocity. To compare velocity profiles at different streamwise locations, the wall distance is scaled by the local boundary layer thickness δ_{99} at each station. On the other hand, Elliott (1958) argues that if we consider the velocity profiles in inner units $u^+ = f(y^+)$ right after the surface transition, they will show two logarithmic layers. The upper one would be reminiscent of the upstream surface condition while the lower one is adjusted with the new one. The intersection between these two logarithmic regions is identified as the location of δ_I .

In general, multiple studies claim that a power-law dependency exists between δ_{IBL} and the streamwise coordinate x , such that

$$\delta_{IBL} \propto (x - x_r)^\alpha, \quad (2.56)$$

where α is the power law exponent and x_r is the streamwise coordinate denoting the start to the rough part in the case of a smooth-to-rough transition. The value of α is not well established in the literature, and there is not general consensus on its universality. Hence, the recovery length depends on various factors including the surface properties, the Reynolds number, and other quantities of interest.

2.2.2 Compressibility effects

In the realm of high-speed flows, the applicability of theories developed for incompressible turbulence remains uncertain, and there is a notable scarcity of literature on this topic. This issue was highlighted in the literature survey by Bowersox (2007), which detailed the high-speed experimental studies available at the time and outlined several open questions that remain relevant today.

Compressibility transformations have been evaluated as a method to scale the compressible rough velocity profile to match the incompressible counterpart, thus recovering the outer layer similarity. Various experimental studies have shown that the theory of Van Driest (1951) effectively achieves Mach number invariance when the wall is adiabatic (Ekoto et al., 2008; Kocher et al., 2022; Williams et al., 2021). Recently, Modesti et al. (2022) conducted Direct Numerical Simulation of supersonic diabatic turbulent channels, showing that more recent compressibility transformations (Volpiani et al., 2020) can account for wall temperature effects when an equivalent roughness Reynolds number is used.

Another aspect highlighted by Bowersox (2007) is the interaction between compressibility and wall roughness, which can generate shock and expansion waves as each element traverses the boundary layer and emerges into the free stream. Experimental studies at Mach numbers from 2 to 2.9 (Latin and Bowersox, 2000; Ekoto et al., 2008; Kocher et al., 2022) observed that these wave structures significantly affect first- and second-order statistics and locally vary wall shear stress. The tested geometries included 3D cubes, 2D bars, sand-grained surfaces, and a diamond-like pattern, the latter causing the most intense local flow distortions (Ekoto et al., 2008).

It remains unclear whether compressibility effects in certain configurations can be so strong as to disrupt outer layer similarity. Peltier et al. (2016) reached this conclusion by analyzing the wave structure produced by a flow over cross-hatch roughness at Mach 4.9, which consisted of a pattern of shocks and expansions perturbing the entire boundary layer. They proposed a conceptual model suggesting that compression waves dominate and enhance turbulence intensity in the lower part of the boundary layer, while expansion waves suppress it in the upper part. This observation contrasts with the experimental study by Williams et al. (2021), which, despite being conducted at hypersonic speeds (Mach number 7.3), found a general agreement with similar experiments in incompressible flows. It should be noted that the friction Reynolds number Re_τ , in their study was much lower than in Peltier et al. (2016).

Most previous experimental studies feature a smooth-to-rough transition, but few have assessed the adjustment length to the new surface condition. As discussed in section 2.2.1, in the incompressible literature, the smooth-to-rough transition (or vice versa) has been extensively studied, featuring the formation of an internal boundary layer δ_I that develops within the incoming boundary layer and eventually merges with it (Elliott, 1958; Rouhi et al., 2019). The experimental study by Kocher et al. (2022) is, to our knowledge, the only one that attempts to characterize smooth-to-rough transition in a supersonic boundary layer, although the number of streamwise locations considered was limited. They observed significant changes in turbulent statistics at least 19.5δ downstream of the transition, where δ is the thickness of the incoming boundary layer over the smooth wall.

Further studies are needed to validate these findings in turbulent boundary layers and across different surface topologies and Mach numbers.

2.3 Thermochemical effects in dissociating air

This section aims to formulate a mathematical model of a chemically-reacting mixture of ideal gases following the work of Di Renzo and Urzay (2021), accounting for dissociation processes of air below $6000K$ and with corresponding pressures typical of the post-shock environment in stratospheric flight. This study performs a statistical analysis of DNS results of a transitional hypersonic boundary layer at Mach 10 with sufficiently high enthalpy to induce air dissociation, and is chosen as reference given that the same authors performed preliminary tests of a wall modeling procedure incorporating high temperature effects (Di Renzo and Urzay, 2019), which inspired the present work (Paper V). The same mathematical model has been very recently used to create a novel DNS dataset (Williams et al., 2023), still under publication at the time we are writing, which served as validation to the present modeling efforts (see Section 3.2.3 and Paper V). Given the vastness of this topic, that requires particular attention in a multitude of physical processes that are neglected in the one-species calorically-perfect regime, this section only aims to serve as a support for the reader to be able to understand the framework of part of the present thesis. For a detailed introduction to reacting and high temperature flows, we refer to (Poinsot, 2005), (Anderson, 2006) ,(Urzay and Di Renzo, 2021). Here, we note that the selected methodology and assumptions represent a possible approach to model this particular flight regime, and the large number of controlling parameters can lead to different choices depending on the particular application. For example, the reader can find in Passiatore et al. (2022) recent efforts in the same direction targeting thermochemical non-equilibrium effects in turbulent hypersonic boundary layers.

The Navier-Stokes equation are here reported following the formulation of Di Renzo and Urzay (2021), which makes use of the vector notation (in contrast to the Einstein notation used in Eq. (2.1)), more convenient for this case

$$\frac{\partial(\rho\mathbf{u})}{\partial t} + \nabla \cdot (\rho\mathbf{u}\mathbf{u}) = -\nabla p + \nabla \cdot \bar{\sigma}, \quad (2.57a)$$

$$\frac{\partial(\rho E)}{\partial t} + \nabla \cdot (\rho E\mathbf{u}) = \nabla \cdot \left(-\mathbf{u}p + \bar{\sigma}\mathbf{u} + \lambda\nabla T - \sum_{i=1}^{N_s} \rho Y_i \mathbf{V}_i h_i \right), \quad (2.57b)$$

$$\frac{\partial(\rho Y_i)}{\partial t} + \nabla \cdot (\rho Y_i \mathbf{u}) = -\nabla \cdot (\rho Y_i \mathbf{V}_i) + \dot{w}_i \quad \text{for } i = 1, \dots, N_s. \quad (2.57c)$$

Comparing Eq. (2.57) with the single-species calorically perfect case of Eq. (2.1), the first thing that we notice is that the continuity equation has been replaced by N_s species transport equations, Eq. (2.57c), accounting for each chemical compound of mass fraction Y_i , where N_s is the number of species. Similarly to the single species case, the N-S equations are supplemented with the equation of state

$$p = \rho R^0 T / \bar{W}, \quad (2.58)$$

where R^0 is the universal gas constant and \bar{W} is the mean molecular weight computed from each component W_i

$$\bar{W} = \left(\sum_{i=1}^{N_s} Y_i / W_i \right). \quad (2.59)$$

Here, the viscous stress tensor σ retains the same expression as Eq. (2.2), however, the dynamic viscosity of the mixture μ is evaluated using Wilke's rule (Wilke, 1950).

The specific enthalpy of the mixture h is expressed by the weighted sum of each compound $h = \sum_{i=1}^{N_s} Y_i h_i$, which can be related to specific internal energy e of the mixture by the expression

$$e = h - p/\rho = \sum_{i=1}^{N_s} Y_i h_i - p/\rho. \quad (2.60)$$

In this case, each species is assumed to follow a thermally perfect behavior such that the specific heat at constant pressure is a function of the temperature (and not anymore constant). Therefore, enthalpy and temperature are related by the expression

$$h_i = h_{i,ref} + \int_{T_{ref}}^T c_{p,i}(T') dT', \quad (2.61)$$

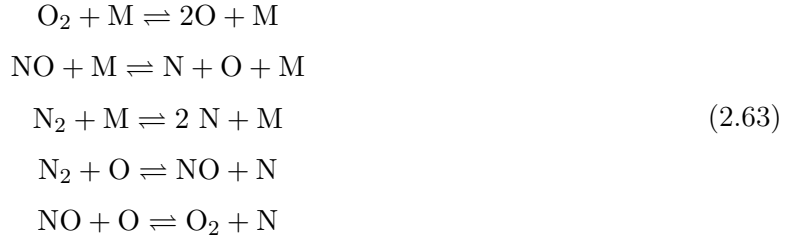
where $h_{i,ref}$ is a reference value of the specific enthalpy taken at T_{ref} . The dependency of $c_p = f(T)$ is modeled using the nine-coefficient NASA polynomials tabulated in McBride (2002), while the thermal conductivity λ is calculated by averaging the local thermal conductivities of each species in accordance with Mathur et al. (1967).

In the species conservation equation (2.57c), \mathbf{V}_i is the diffusion velocity vector defined by a two terms, a Fickian flux and a mass corrector Curtiss and Hirschfelder (1949)

$$\mathbf{V}_i = -D_i \nabla (\ln X_i) + \sum_{j=1}^{N_s} Y_j D_j \nabla (\ln X_j), \quad (2.62)$$

where $X_i = W/W_i Y_i$ is the molar fraction and D_i is mixture-averaged mass diffusivity for species i , modeled using the formulation of Bird et al. (2006).

Finally, the present model can be particularized for a compound of five species: N₂, O₂, NO, N, O, representative of dissociated air with the five reversible chemical steps (Park, 1989a,b)



where species are produced and depleted according to the rate of production $\dot{\omega}_i$ defined as

$$\dot{\omega}_i = W_i \sum_{j=R1}^{R5} (v''_{ij} - v'_i) \sum_{i=1}^{N_s} F_{ij} \left(\frac{\rho Y_i}{W_i} \right) \left[k_{f,j} \prod_{i=1}^{N_s} \left(\frac{\rho Y_i}{W_i} \right)^{v''_{ij}} - k_{b,j} \prod_{i=1}^{N_s} \left(\frac{\rho Y_i}{W_i} \right)^{v'_i} \right], \quad (2.64)$$

where v'_{ij} denotes the stoichiometric coefficient of reactant i in step j on the reactant side, and v''_{ij} represents the stoichiometric coefficient of reactant i in step j on the product side. Additionally, F_{ij} is the chaperon efficiency of species i acting as a third body in reaction j , and $k_{f,j}$ and $k_{b,j}$ are, respectively, the forward and backward rate constants of step j , both evaluated here in terms of the equilibrium temperature T .

Chapter 3

Near-wall modeling for hypersonic flows

In fluid dynamics, particularly for turbulent flows, the Large Eddy Simulation (LES) technique has become increasingly prevalent both in the academic and industrial communities due to its ability to capture the non-stationary and multiscale nature of turbulence, progressively replacing the Reynolds-averaged Navier-Stokes (RANS) approach. The need to accurately describe non-stationary phenomena cannot be adequately addressed by the RANS approach, which also suffers from a lack of universality (it requires input constants that depend on the specific flow being analyzed). The LES method is conceptually more advanced than RANS, building on the foundations of Kolmogorov's K41 theory (Pope, 2000), where the fundamental assumption is that while the larger-scale turbulent motions depend on the specific flow geometry, the smallest scales exhibit universal behavior that does not depend on the type of flow being analyzed. Thus, the underlying idea of the LES technique is to solve the Navier-Stokes equation for a filtered field representing the larger-scale turbulent motions, incorporating a model for the influence of the smaller-scale motions. These approaches are typically benchmarked using Direct Numerical Simulation (DNS), which involves directly discretizing the Navier-Stokes equations without introducing any turbulence model.

3.1 Large Eddy Simulation

The Large Eddy Simulation approach involves four main conceptual steps (see Pope (2000)):

- Define a filtering operator to decompose the velocity into the sum of a filtered and a residual (or subgrid-scale, SGS) component. The filtered velocity field represents the motion of the large eddies, while the residual component represents the small modeled scales.
- Apply the filtering operator to the Navier-Stokes equations to obtain the evolution of the filtered velocity field.
- Model the subgrid-scale (SGS) tensor σ_{ij}^{SGS} and the subgrid heat flux q_j^{SGS} to achieve closure.
- Solve numerically the filtered equations, providing an approximation to the large-scale motions in the realization of the turbulent flow.

The three-dimensional filtered compressible Navier-Stokes equations are solved for a viscous Newtonian fluid:

$$\frac{\partial \bar{\rho}}{\partial t} + \frac{\partial(\bar{\rho}\tilde{u}_j)}{\partial x_j} = 0, \quad (3.1a)$$

$$\frac{\partial(\bar{\rho}\tilde{u}_i)}{\partial t} + \frac{\partial(\bar{\rho}\tilde{u}_i\tilde{u}_j)}{\partial x_j} = -\frac{\partial \bar{p}}{\partial x_i} + \frac{\partial \bar{\sigma}_{ij}}{\partial x_j} + \frac{\partial \sigma_{ij}^{SGS}}{\partial x_j}, \quad (3.1b)$$

$$\frac{\partial(\bar{\rho}\tilde{E})}{\partial t} + \frac{\partial(\bar{\rho}\tilde{E}\tilde{u}_j)}{\partial x_j} = -\frac{\partial(\bar{\rho}\tilde{u}_j)}{\partial x_j} + \frac{\partial}{\partial x_j} \left(\lambda \frac{\partial \tilde{T}}{\partial x_j} - q_j^{SGS} \right) + \frac{\partial}{\partial x_j} [(\bar{\sigma}_{ij} + \sigma_{ij}^{SGS})\tilde{u}_i], \quad (3.1c)$$

where $\bar{\rho}$ is the filtered density, \tilde{u}_i denotes the Favre-filtered velocity component in the i th Cartesian direction ($i = 1, 2, 3$), \bar{p} is the filtered thermodynamic pressure. The working fluid is air, with thermodynamic variables related by $\bar{p} = \bar{\rho}R\tilde{T}$, where \tilde{T} is the Favre temperature and R is the gas constant. We denote with $\tilde{E} = c_v\tilde{T} + \widetilde{u_i u_i}/2$ the Favre-filtered total energy per unit mass and the dynamic viscosity $\mu(\tilde{T})$ is assumed to follow the Sutherland law; the thermal conductivity λ is related to μ via the Prandtl number with the following expression: $\lambda = c_p\mu/Pr$. The ratio between the specific heat at constant pressure c_p and the specific heat at constant volume c_v is set to 1.4 while the Prandtl number is 0.72.

The Favre-filtered viscous stress tensor $\bar{\sigma}_{ij}$ is expressed as:

$$\bar{\sigma}_{ij} = \mu \left(2\tilde{S}_{ij} - \frac{2}{3}\tilde{S}_{kk}\delta_{ij} \right), \quad (3.2)$$

\tilde{S}_{ij} is resolved strain-rate tensor with $\tilde{S}_{ij} = 1/2(\tilde{g}_{ij} + \tilde{g}_{ji})$ and $\tilde{g}_{ij} = \partial \tilde{u}_i / \partial x_j$ is the resolved velocity gradient.

The subgrid-scale (SGS) stress tensor σ_{ij}^{SGS} is modeled following Boussinesq's hypothesis as:

$$\sigma_{ij}^{SGS} = \mu_t \left(2\tilde{S}_{ij} - \frac{2}{3}\tilde{S}_{kk}\delta_{ij} \right) - \frac{2}{3}k^{SGS}\delta_{ij}, \quad (3.3)$$

and the subgrid heat flux q_j^{SGS} is modeled from Fourier's law as:

$$q_j^{SGS} = -c_p \frac{\mu_t}{Pr_t} \frac{\partial \tilde{T}}{\partial x_j}. \quad (3.4)$$

Subgrid-scale dynamic viscosity μ_t and the isotropic part k_{SGS} in the SGS stress tensor can be modeled with explicit or implicit approaches. The former leverages physical arguments to obtain a relation between the SGS and resolved quantities, e.g. the Smagorinsky (1963) model, while the latter makes use of known numerical errors related to discretization schemes that acts in a dissipative manner, mimicking the physical energy transfer to small scales, see Grinstein et al. (2007). An example of an explicit model relevant for this thesis is the Wall-Adaptive Local Eddy-viscosity (WALE) model Nicoud and Ducros (1999), which computes subgrid-scale dynamic viscosity as:

$$\mu_t = \bar{\rho}(C_w\Delta)^2 \frac{(S_{ij}^d S_{ij}^d)^{3/2}}{(S_{ij} S_{ij})^{5/2} + (S_{ij}^d S_{ij}^d)^{5/4}}, \quad (3.5)$$

where $C_w = 0.325$ and $S_{ij}^d = 1/2(\tilde{g}_{il}\tilde{g}_{lj} + \tilde{g}_{jl}\tilde{g}_{li}) - 1/3(\tilde{g}_{ml}\tilde{g}_{lm}\delta_{ij})$; Δ is the local mesh size. The Prandtl turbulent number Pr_t is assumed to be equal to 0.9 (Duan and Martin, 2011).

3.2 Near-wall turbulence modeling

The filtering of the unknowns used in LES results in a significantly lower simulation cost than DNS. However, in bounded flows, a problem arises in that the peak production of turbulence occurs in the inner part of the boundary layers, where the turbulence generated at smaller scales is transferred to the larger ones. If the grid resolution cannot accurately represent the inner-layer dynamics (such as production, dissipation, and streaks), which is often the case in high Reynolds number LES simulations to reduce computational cost, the resolved outer-layer turbulence cannot be considered a realistic representation. This issue is commonly referred to as the near-wall problem of LES and becomes more pronounced as the Reynolds number increases because the scale of the inner layer dynamics decreases. The Wall-Modeled Large Eddy simulation (WMLES) approach addresses this by modeling the energetic eddies in the near-wall inner layer, and one of the classical methods to achieve a closed-form solution is through the use of wall stress models.

3.2.1 Equilibrium wall model

We first derive the classical version of the equilibrium wall model for compressible flows (Larsson et al., 2016), which provides a closed form of the RANS equations, Eq. (2.8), approximated using the thin boundary layer assumption (Van Driest, 1951), resulting in a set of Ordinary Differential Equations (ODE).

Considering the RANS momentum equation (2.8b)

$$\frac{\partial(\bar{\rho}\tilde{u}_i)}{\partial t} + \frac{\partial}{\partial x_j}(\bar{\rho}\tilde{u}_i\tilde{u}_j) = -\frac{\partial\bar{p}}{\partial x_i} + \frac{\partial}{\partial x_j}\left(\bar{\sigma}_{ij} - \bar{\rho}\widetilde{u''_i u''_j}\right), \quad (3.6)$$

we focus on the streamwise component

$$\frac{\partial(\bar{\rho}\tilde{u})}{\partial t} + \frac{\partial}{\partial x}(\bar{\rho}\tilde{u}\tilde{u}) + \frac{\partial}{\partial y}(\bar{\rho}\tilde{u}\tilde{v}) = -\frac{\partial\bar{p}}{\partial x} + \frac{\partial}{\partial y}\left(\bar{\sigma}_{xy} - \bar{\rho}\widetilde{u'' v''}\right) + \frac{\partial}{\partial x}\left(\bar{\sigma}_{xx} - \bar{\rho}\widetilde{u'' u''}\right), \quad (3.7)$$

where in the approximation of a zero-pressure-gradient thin boundary layer (Van Driest, 1951), we obtain

$$\frac{\partial}{\partial y}\left(\bar{\mu}\frac{\partial\tilde{u}}{\partial y} - \bar{\rho}\widetilde{u'' v''}\right) = 0. \quad (3.8)$$

As done in section 2.1.2, we introduce the Boussinesq hypothesis for the turbulent stresses

$$\mu_t \frac{\partial\tilde{u}}{\partial y} = -\bar{\rho}\widetilde{u'' v''}, \quad (3.9)$$

where μ_t is the eddy viscosity. This quantity under the equilibrium assumption can be modeled in the form $\mu_t = \tau_w/(\partial\tilde{u}/\partial y)$, which combined with the Van Driest (1956) transformation, and particularly Eq. (2.32), yields in the logarithmic region the following expression

$$\mu_t = \kappa\bar{\rho}u_\tau y, \quad (3.10)$$

where $\kappa = 0.41$ is the von Kármán constant, and $\bar{\rho} = p_\infty/\tilde{T}$ denotes the density profile, obtained assuming a constant pressure distribution in the boundary layer. The expression of Eq. (3.10) has to be complemented with a damping function, D , in order to correct the near-wall behaviour, which

under the classical Van Driest formulation is given by

$$D = [1 - \exp(-y^+/A^+)]^2, \quad (3.11)$$

where $A^+ = 17$ is a model constant indicating the dimensionless height above the wall where the molecular and turbulent viscosities become of the same order of magnitude. Therefore, μ_t takes the general form

$$\mu_t = \kappa \bar{\rho} u_\tau y [1 - \exp(-y^+/A^+)]^2. \quad (3.12)$$

In this case, we have a constant stress layer (see section 2.1.2) over the near-wall region, from which the following ODE can be derived:

$$\frac{d}{dy} \left[(\tilde{\mu} + \mu_t) \frac{d\tilde{u}}{dy} \right] = 0. \quad (3.13)$$

We then consider the RANS energy equation, as in Eq. (2.8c)

$$\frac{\partial(\bar{\rho}\tilde{E})}{\partial t} + \frac{\partial}{\partial x_j} \left(\bar{\rho}\tilde{u}_j \tilde{H} \right) = \frac{\partial}{\partial x_j} (\bar{u}_i \bar{\sigma}_{ij}) - \frac{\partial \bar{q}_j}{\partial x_j} - \frac{\partial \bar{Q}_j}{\partial x_j}, \quad (3.14)$$

the term \bar{Q}_j being equal to

$$\bar{Q}_j = \bar{\rho} c_p \widetilde{u_j'' T''} + \frac{\bar{\rho} \widetilde{u_i'' u_i'' u_j''}}{2} + \bar{\rho} \widetilde{u_i u_i'' u_j''}, \quad (3.15)$$

and the term $\bar{u}_i \bar{\sigma}_{ij}$ can be decomposed as:

$$\bar{u}_i \bar{\sigma}_{ij} = \tilde{\sigma}_{ij} \tilde{u}_i + \overline{\sigma_{ij} u_i''} + \tilde{u}_i \overline{\sigma_{ij}''}. \quad (3.16)$$

In the thin boundary layer approximation, and considering $\tilde{\sigma}_{xy} \approx \mu \partial \tilde{u} / \partial y$ and $q_y = -\lambda \partial \tilde{T} / \partial y$, Eq. (3.14) reduces to

$$\frac{\partial}{\partial y} \left(\tilde{\lambda} \frac{\partial \tilde{T}}{\partial y} - \bar{\rho} c_p \widetilde{u_j'' T''} \right) = -\frac{\partial}{\partial y} \left[\tilde{u} \left(\mu \frac{\partial \tilde{u}}{\partial y} - \bar{\rho} \widetilde{u'' v''} \right) \right]. \quad (3.17)$$

Similary to the procedure used for turbulent stresses, we introduce the Boussinesq hypothesis for turbulent heat fluxes

$$\frac{\mu_t}{Pr_t} \frac{\partial \tilde{T}}{\partial y} = -\bar{\rho} \widetilde{u_j'' T''}, \quad (3.18)$$

where Pr_t is the turbulent Prandt number. Given that Eq. (3.17) is only dependent on the wall-normal direction y , we obtain the following ODE for conservation of energy

$$\frac{d}{dy} \left[c_p \left(\frac{\tilde{\mu}}{Pr} + \frac{\mu_t}{Pr_t} \right) \frac{d\tilde{T}}{dy} \right] = -\frac{d}{dy} \left[(\tilde{\mu} + \mu_t) \tilde{u} \frac{d\tilde{u}}{dy} \right]. \quad (3.19)$$

We can now write the resulting system of ODEs for the equilibrium wall model for calorically-perfect gases

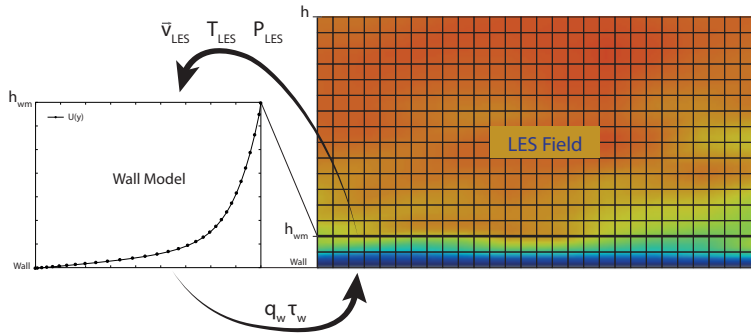


Figure 3.1: Coupling procedure between LES and wall model.

$$\frac{d}{dy} \left[(\tilde{\mu} + \mu_t) \frac{d\tilde{u}}{dy} \right] = 0, \quad (3.20a)$$

$$\frac{d}{dy} \left[c_p \left(\frac{\tilde{\mu}}{Pr} + \frac{\mu_t}{Pr_t} \right) \frac{dT}{dy} \right] = - \frac{d}{dy} \left[(\tilde{\mu} + \mu_t) \tilde{u} \frac{d\tilde{u}}{dy} \right]. \quad (3.20b)$$

where a value of $Pr_t = 0.9$ is often assumed and $\tilde{\mu} = \tilde{\mu}(\tilde{T})$ is the laminar viscosity which obeys to the Sutherland's law.

Under the equilibrium assumption, the bracketed quantities in Eqs. (3.20) are constant across the wall-modeled layer. These conserved quantities correspond to the sum of the viscous and turbulent shear stress (in Eq. (3.20a)) and to the sum of molecular heat conduction, turbulent heat transport (left hand side of Eq. (3.20b)) and aerodynamic heating (right hand side of Eq. (3.20b)). These equations need to be solved in an independent grid that goes from the wall to h_{wall} and can be stretched near the wall to increase the accuracy of the computation of τ_w and q_w , which are then fed back to the LES solver; see figure 3.1. More details on the implementation procedure and open issues on the applicability of this methodology can be found in Larsson et al. (2016).

3.2.2 Incorporating compressibility effects and strong heat transfer

The classical version of the equilibrium wall model was found by numerous studies inaccurate at high Mach numbers and particularly in strongly diabatic walls. From the discussion of Section 2.1.4, these inaccuracies are very similar to the issues connected with the Van Driest (1956) compressibility transformation, which is also present here in the definition of the eddy viscosity, Eq. (3.12).

It is natural to ask whether subsequent advances in compressibility transformations can lead to an improved version of the eddy viscosity model. To this end, Aupoix and Viala (1995) and successively Patel et al. (2017) and Yang and Lv (2018) showed that the application of the Trettel and Larsson (2016) transformation leads to a simple correction of the Van Driest damping function, Eq. (3.11), while the expression related to the logarithmic layer, Eq. (3.10), remains identical. The proposed correction consists in a change between the classical inner units y^+ and semilocal scale y^* , which lead to the the expression

$$D = [1 - \exp(-y^*/A^+)]^2, \quad (3.21)$$

where the parameter A^+ can be taken equal to the original value of 17 (calibrated in incompressible

boundary layers) by assuming that an accurate compressibility transformation should collapse into the incompressible laws of the wall.

Following this research thread, the transformation of Hasan et al. (2023) can easily be incorporated into this formulation since the building blocks of Van Driest (1956) and Trettel and Larsson (2016) are already present in its formulation. Following the same hypothesis made in section 2.1.4, an improved version of the eddy viscosity model reads

$$D = [1 - \exp(-y^*/(A^+ + f(M_\tau)))]^2, \quad (3.22)$$

where the corrective term $f(M_\tau)$ incorporates intrinsic compressibility effects (Hasan et al., 2024). According to evidence found from the evaluation of different numerical databases, they argue that the corrective term $f(M_\tau)$ should be a linear function of M_τ , fitted as $19.3M_\tau$.

The transformation of Griffin et al. (2021) was also incorporated in a wall modeling formulation, which, however, required a shift in perspective from the ones discussed so far. Griffin et al. (2023) argued that a compressibility transformation can also be employed in reverse, that is, transforming an incompressible profile into the corresponding compressible counterpart. This consideration can be leveraged by first solving the constant properties version of Eq. (3.20a), thus obtaining an incompressible version of the velocity profile, and then using the inverse velocity transformation (Griffin et al., 2021) to extrapolate the compressible velocity profile.

Following the study of Griffin et al. (2023), the inverse velocity transformation equation is first considered, which reads as

$$\frac{d\tilde{u}^+}{dy^*} = \left(\frac{1}{\bar{\mu}^+ S_t^+} - \frac{1}{\bar{\mu}^+} + \sqrt{\bar{\rho}^+} \left(1 + \frac{1}{2\bar{\rho}^+} \frac{d\bar{\rho}^+}{dy^+} y^+ - \frac{1}{\bar{\mu}^+} \frac{d\bar{\mu}^+}{dy^+} y^+ \right) \right)^{-1}. \quad (3.23)$$

In this formulation, the incompressible mean strain rate $S_t^+ = du^+/dy^+$ can be algebraically computed from the constant property version of the relation $d\tilde{u}/dy = \tau_w/(\mu_w + \mu_t)$, where μ_t is the eddy viscosity estimated with the classical mixing length model, Eq. (3.11). It is important to note that the evaluation of μ_t is needed only to compute the incompressible mean strain rate, while the compressible counterpart is evaluated without assuming any model for the eddy viscosity. In the original formulation, the velocity is coupled with the temperature using an algebraic law that assumes a quadratic relationship between the two quantities (Zhang et al., 2014). In principle, this fact considerably lowers the computational cost of solving the wall model equations by avoiding the coupling between momentum and energy equations, Eq. (3.20), a strategy also employed by Hasan et al. (2024). The relation of Zhang et al. (2014) has been reformulated by Griffin et al. (2023) to be exactly consistent with the matching data rather than the edge data (i.e., $h = h_m$ if $u = u_m$, but $h \neq h_e$ when $u = u_e$) to obtain

$$\tilde{T} = \tilde{T}_w + sPr \left(\tilde{T}_r - \tilde{T}_w \right) \frac{\tilde{u}}{\tilde{u}_e} \left(1 - \frac{\tilde{u}}{\tilde{u}_m} \right) + \left(\frac{\tilde{u}}{\tilde{u}_m} \right)^2 \left(\tilde{T}_m - \tilde{T}_w \right), \quad (3.24)$$

where subscripts $_m$ and $_e$ indicate quantities computed at the matching location and at the edge of the boundary layer, respectively. In this relation, it can be assumed that the product $sPr = 0.82$ is constant and equal to the fitted value of Zhang et al. (2014), while the recovery factor is taken as $r = 0.89$.

The proposed models of Hasan et al. (2024) and Griffin et al. (2023), formulated for calorically perfect gases, showed clear improvements from both the classical equilibrium wall model and the formulation of Yang and Lv (2018), better accounting for compressibility and wall-cooling effects, which are relevant for applications in the hypersonic regime.

3.2.3 Incorporating thermochemical effects

Notwithstanding the recent developments in high-speed boundary layer modeling, the effort to account for high-temperature effects in chemically reacting multicomponent mixtures is still in very early stages, due to the added modeling complexity and the lack of availability of reference data. Moreover, at the present stage the development of wall models that include chemical reactions is still confined to *a priori* analyses, given that key issues are still present in the formulation of accurate SGS models for these applications, which are nevertheless invaluable for enabling future advancements. To this end, one of the first extensions of the equilibrium wall model that accounts for differential diffusion and finite-rate chemistry (as described in Section 2.3) was provided by Di Renzo and Urzay (2019). This model is tailored to output not only the average wall stress and heat flux, but also the species composition of a wall-bounded flow that obeys the compressible Navier–Stokes equations subject to species transport in a chemically reacting mixture of ideal gases, Eq. (2.57).

The extended EWM for reacting flows of Di Renzo and Urzay (2019) is based on the Favre-averaged transport equations simplified with the assumption of constant stress layer. The conservation equations for momentum, enthalpy, and species partial density read

$$\begin{aligned} \frac{d}{dy} \left[(\tilde{\mu} + \mu_t) \frac{d\tilde{u}}{dy} \right] &= 0, \\ \frac{d}{dy} \left[\tilde{u} (\tilde{\mu} + \mu_t) \frac{d\tilde{u}}{dy} + \tilde{\lambda} \frac{d\tilde{T}}{dy} + \frac{\mu_t}{Pr_t} \frac{d\tilde{h}}{dy} - \sum_{i=1}^{N_s} \bar{\rho}_i \tilde{V}_{y,i} \tilde{h}_i \right] &= 0, \\ \frac{d}{dy} \left(-\bar{\rho}_i \tilde{V}_i + \frac{\mu_t}{Sc_t} \frac{d\tilde{Y}_i}{dy} \right) + \bar{w}_i &= 0, \quad \text{for } i = 1, \dots, N_s. \end{aligned} \quad (3.25)$$

The reader can find in section 2.3 the definition of mixture properties, wall-normal diffusion velocities \tilde{V}_i , partial specific enthalpies \tilde{h}_i , and the production rates \bar{w}_i . Di Renzo and Urzay (2019) invoke the laminar closure for the transport of reaction rates, $\bar{w}_i = f(\tilde{T}, \bar{\rho}, \tilde{Y}_i)$, which neglects the fluctuations of each variable and assumes statistical independence between them. The turbulent Prandtl number Pr_t and the turbulent Schmidt number Sc_t were assumed to be equal to 0.9.

The eddy viscosity μ_t is computed with a mixing length model using the semilocal formulation of Eq. (3.21). We remark that this formulation employs the semilocal-scaled wall-normal coordinate $y^* = y/(\bar{\nu}/\sqrt{\tau_w/\bar{\rho}})$ in the Van Driest damping function, which, as discussed in Section 3.2.2, improves the accuracy when strong compressibility and diabatic effects are present (Yang and Lv, 2018).

This thesis builds on this study and represents a contribution to further advancing the accuracy of wall models for chemically-reacting flows and testing them with new DNS databases.

Chapter 4

Objectives and Methodology

4.1 Research objectives

From the previous introduction, numerous subjects and physical theories in the realm of high-speed flows have been touched, some of which can lead to their own research thread. For this reason, in this section we clarify the relevance of each in the present work and the related open questions that are addressed in each attached paper.

First, in the context of high-fidelity simulations applied to compressible flows, we make a distinction between physics-oriented papers and modeling-oriented papers. Papers I to III belong to the first category, featuring Direct Numerical Simulations (DNS) of smooth and rough compressible boundary layers. In these papers, the focus is on the study of the physics of the problem and less on the methodology, since well-established numerical procedures implemented in the solver STREAmS (Bernardini et al., 2021, 2023) are used to resolve all relevant turbulent scales and geometry features, discussed in section 4.2.2. We can summarize the objectives of these works, some of which already hinted in Chapter 1, in the following points

- Contribute to the lack of systematic studies on supersonic and hypersonic turbulent boundary layers, specifically on the combined effects of Mach number, wall temperature and Reynolds number (papers I and II);
- Test the validity of recently proposed theoretical relations, such as compressibility transformations, temperature-velocity relations, and improved Reynolds analogies, while creating a publicly available dataset that can support future advancements (papers I and II);
- Propose novel physical interpretations on the individual role of compressibility and wall temperature in influencing the flow dynamics, with particular interest to the coupling between kinetic and thermal fields (papers I and II);
- Contribute to the lack of studies concerning how roughness affects compressible turbulent boundary layers, and compare the resulting dynamics to a nearly-incompressible case (paper III);

In the second category fall papers IV and V, which are dedicated to modeling aspects of hypersonic flows capable to maintain a high degree of accuracy, specifically using the LES and WMLES techniques. We can summarize the objectives of these works in the following points

- Present and validate the development of the solver URANOS, specifically tailored to LES and WMLES methodologies, showing different use cases of supersonic and hypersonic flows for calorically-perfect gases (Paper IV), some of which compared to DNS results of Paper I;
- Propose a novel wall-model formulation for chemically-reacting gases based on the velocity transformation of Griffin et al. (2023), and perform a preliminary *a priori* assessment (Paper V);

4.2 Numerical approach and discretization

Compressible flow solvers in computational fluid dynamics (CFD) come in various types, but they all share the challenge of managing the complexity of flows that consist of both smooth regions and discontinuities, such as shock waves or shocklets. These phenomena are closely linked to the discretization of convective terms in the Navier-Stokes equations, whereas the diffusion terms are generally less sensitive to such discontinuities. Among the various approaches to handle these complexities, the hybrid approach has gained significant popularity in many solvers. This approach employs energy-preserving schemes in the smooth regions of the flow, while shock-capturing schemes are used in areas where discontinuities are present. Shock-capturing schemes are numerical methods specifically designed to accurately resolve sharp gradients and discontinuities, such as shock waves, without introducing non-physical oscillations. The transition between energy-preserving and shock-capturing schemes is managed by a sensor that detects the presence of shocks and triggers the appropriate scheme accordingly. This numerical procedure is the backbone of both flow solvers used in the present thesis, namely STREAmS (see section 4.2.2), and URANOS (see section 4.2.3), the former being specifically tailored for DNS optimizing computational efficiency, while the latter being oriented to modeling applications, such as LES and WMLES.

4.2.1 CFD in the era of GPUs

Notwithstanding the particular application of each solver, recent advancements in GPU (Graphics Processing Unit) technology have revolutionized the field of CFD, which traditionally relied exclusively on CPUs (Central Processing Units). GPUs offer massive parallel processing capabilities that significantly accelerate complex computations, making simulations much faster and more efficient. This shift has made it possible to tackle larger, more detailed simulations in less time, which was previously impractical with CPUs alone. As a result, even the most accurate solvers risk becoming obsolete if they cannot leverage GPU technology, as the ability to harness this computational power has become essential for maintaining competitiveness and advancing the field.

There are multiple approaches to porting a CFD solver to run efficiently on GPUs, each with its own trade-offs between flexibility and performance. The URANOS approach (see Section 4.2.3) is to use non-vendor-specific paradigms like OpenACC, which provides a directive-based programming model for accelerator programming that is compatible with different GPU architectures. This approach allows developers to maintain a single code base that can target multiple GPU vendors, reducing long-term maintenance costs in a rapidly evolving landscape of accelerator-based computing.

On the other hand, the STREAmS solver (see Section 4.2.2) employs more vendor-specific

approaches, like CUDA, which offer highly optimized performance for NVIDIA GPUs. CUDA allows developers to fine-tune their code for NVIDIA’s architecture, often resulting in significantly higher performance compared to more general approaches. However, this optimization comes at the cost of portability, as the CUDA-optimized code is not applicable to other vendors, such as AMD. In order to overcome this problem, the most recent version of STREAmS has a modular structure that offers the possibility of implementing different back-ends depending on the specific architecture. The choice between these approaches depends on the balance between the desired performance gains and the need for flexibility across different hardware platforms.

4.2.2 STREAmS solver

The flow solver STREAmS (Bernardini et al., 2021, 2023), a Supersonic Turbulent Accelerated Navier-Stokes Solver, is an in-house, high-fidelity tool for direct numerical simulations (DNS) of canonical compressible wall-bounded flows, including turbulent plane channels, zero-pressure gradient turbulent boundary layers, and supersonic oblique shock-wave/boundary layer interactions (e.g. (Bernardini and Pirozzoli, 2011b,a; Modesti and Pirozzoli, 2016)), see figure 4.1. Additionally, the solver is capable of handling non-canonical configurations with complex geometries through the Immersed Boundary Method (IBM) (Modesti et al., 2022; Della Posta et al., 2023).

STREAmS integrates state-of-the-art numerical algorithms specifically tailored to address the challenges of solving high-speed turbulent flows and is applicable across a broad range of Mach numbers, from low subsonic to hypersonic regimes. The code is written in modern Fortran and parallelized using the MPI paradigm. Domain decomposition is performed in two directions (streamwise and spanwise) to minimize data transfer for ghost node updates. STREAmS has been designed to support multi-GPU architectures, particularly with NVIDIA cards using CUDA, and has recently been extended to support AMD and Intel GPU architectures with additional backends (Salvadore et al., 2024). An open source version is available at <https://github.com/STREAmS-CFD/STREAmS-2>.

Nonlinear terms in the Navier–Stokes equations are discretized using up to sixth-order accuracy via a hybrid energy-conservative shock-capturing scheme in a locally conservative form. The solver also includes a new family of kinetic energy and entropy preserving schemes (KEEP). Shock-capturing is implemented through Lax–Friedrichs flux vector splitting, with characteristic fluxes reconstructed at interfaces using up to fifth-order weighted essentially non-oscillatory (WENO) reconstruction (Jiang and Shu, 1996). The low-dissipative WENO-Z scheme (Borges et al., 2008) is also available. A classical shock sensor is employed to determine local smoothness and to switch between the central and shock-capturing schemes (Ducros et al., 1999). Viscous terms are expanded into a Laplacian form (De Vanna et al., 2021b) and approximated up to sixth-order central finite-difference formulas to prevent odd–even decoupling. Time integration is performed using Wray’s three-stage third-order Runge–Kutta scheme (Spalart et al., 1991).

The solver can manage complex geometries (for example rough surfaces (Modesti and Pirozzoli, 2016)) using a ghost-point-forcing immersed boundary method for arbitrarily complex shapes (Piquet et al., 2016; De Vanna et al., 2020). For three-dimensional objects, the geometry is provided in OFF format, and the computational geometry library CGAL (The CGAL Project, 2021) is utilized to execute the ray-tracing algorithm. This allows the identification of grid nodes in the fluid and solid domains and computation of distances from the interface. To maintain a consistent computational stencil near boundaries, the first three layers of interface points within the body

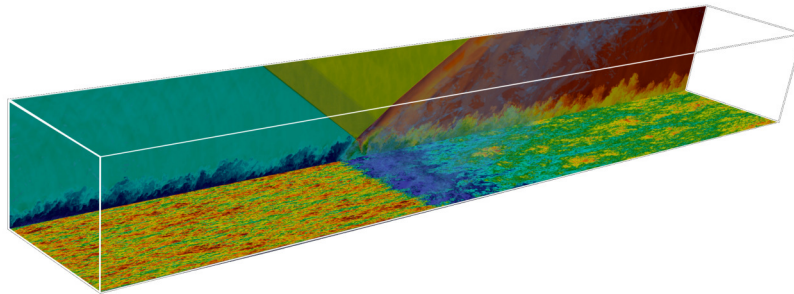


Figure 4.1: Example of a numerical simulation of a shock-wave boundary layer interaction simulated using STREAmS. Image adapted from the online GitHub repository <https://streams-cfd.github.io/STREAmS-2/>.

are marked as ghost nodes. Each ghost node has a corresponding reflected point along the wall normal, located within the fluid domain. The solution at the reflected point is interpolated using trilinear interpolation and the values are applied to the ghost nodes inside the body to enforce the desired boundary conditions. An extensive description of the algorithm is available in the work by De Vanna et al. (2020).

4.2.3 URANOS solver

The solver URANOS (De Vanna et al., 2023; De Vanna and Baldan, 2024), which stands for Unsteady Robust All-around Navier-Stokes Solver, is a compressible flow solver specifically developed for simulating wall-bounded flow configurations. It is oriented towards Large Eddy Simulation (LES) and Wall-Modeled LES techniques, while still allowing for Direct Numerical Simulation (DNS) (De Vanna et al., 2021c, 2022, 2023b). URANOS can handle various canonical wall-bounded flows and is also capable of managing complex geometries through the Immersed Boundary Method (IBM) (De Vanna et al., 2020, 2021d; De Vanna et al., 2023), see figure 4.2.

URANOS combines multiple three-dimensional MPI parallelization strategies and has recently been ported to GPU with the OpenACC standard, which enables a non-vendor-specific and open-source platform independent of the computing architecture. An open source version is available at <https://github.com/uranos-gpu/uranos-gpu>.

URANOS employs a high-order finite difference approach to discretize the Navier-Stokes equations and supports both uniform and non-uniform structured Cartesian meshes. The nonlinear convective terms use up to sixth-order central discretization, which provides semi-discrete preservation of total kinetic energy in the limit of inviscid, incompressible flows (Pirozzoli, 2010). This property ensures robust spatial discretization of the convective derivatives without introducing numerical dissipation.

In regions with strong compressibility effects and shocks, a range of shock-capturing schemes is available, including the recent Targeted Essentially Non-Oscillatory (TENO) methodology introduced by Fu et al. (2018), activated by the modified Ducros sensor (Ducros et al., 1999). The viscous fluxes are expanded using a semi-conservative formulation and discretized with up to sixth-order finite differences (De Vanna et al., 2021a). Time advancement is handled with the third-order low-storage total variation diminishing Runge-Kutta method by Gottlieb and Shu (1998).

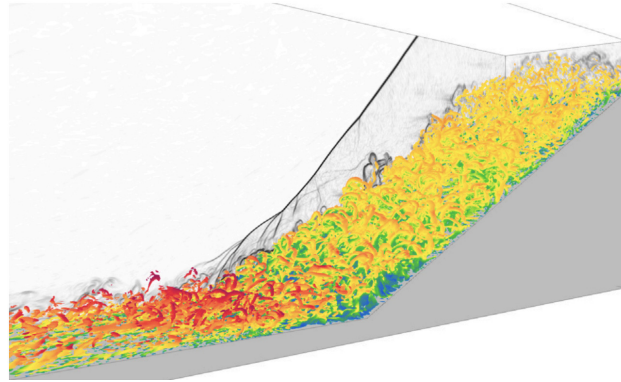


Figure 4.2: Example of a numerical simulation of a finite-angle-turning supersonic boundary layer over a compression ramp URANOS. Image adapted from (De Vanna et al., 2023a).

Complex geometries are addressed using the sharp-interface IBM as described by De Vanna et al. (2020). Specifically, URANOS processes two-dimensional representations of immersed objects in the .msh file format. Each immersed body is represented by a set of closed points and edges on a Cartesian mesh. Consequently, after obtaining the set of polygons, each Cartesian grid point is flagged as either inside or outside the polygon. This process follows a classical ray-tracing algorithm according to o'Rourke (1998) and is managed as a pre-processing step.

Concerning LES, URANOS offers the option to use various SGS models, including Smagorinsky (Smagorinsky, 1963), Mixed Time Scales (Inagaki et al., 2005), Sigma (Toda et al., 2010), and WALE (Nicoud and Ducros, 1999). Additionally, a minimally intrusive algorithm is implemented to automatically switch between wall-resolved and wall-modeled LES based on local near-wall resolution (De Vanna et al., 2021c), to which the author of the present thesis contributed in the Master thesis project. In this approach, the key to blending wall-resolved and wall-modeled methods is modifying the overall viscosity and diffusivity at the wall location, ensuring that allowable shear stress and heat flux are consistently fed back to the outer LES field while maintaining no-slip, no-penetration, isothermal, and adiabatic boundary conditions. The WMLES procedure is implemented using both classical and semi-local implementations of the eddy viscosity models, tested in turbulent boundary layers and channel configurations (De Vanna et al., 2021c, 2023), and was recently coupled with the IBM algorithm (De Vanna et al., 2023a).

Chapter 5

Summary of results

In the following sections, the main findings of Papers (I-V) are summarized briefly.

5.1 Paper I

Direct numerical simulation of supersonic and hypersonic turbulent boundary layers at moderate-high Reynolds numbers and isothermal wall condition

The study of high-speed turbulent boundary layers is crucial for understanding aerodynamic heating and drag on supersonic and hypersonic vehicles. This interest is driven by technological advancements aimed at developing vehicles for sustained hypersonic flight, sub-orbital missions, and planetary reentry.

To address these challenges, this research investigates zero-pressure-gradient turbulent boundary layers at Mach numbers 2 and 5.86, with friction Reynolds numbers in the range of 450-2000. The numerical database, composed of 4 simulations in total, was designed with the objective of investigating Mach and Reynolds number effects, while focusing on isothermal, cold walls, a common condition in aerospace applications, with a wall-to-recovery temperature ratio of 0.76.

Instantaneous visualizations of streamwise velocity revealed significant deviations from traditional adiabatic wall observations, including a lack of near-wall temperature streaks in strongly non-adiabatic cases. This divergence highlights the complex interplay between thermal and velocity fields in high-speed flows. Several flow snapshots were also scrutinized to identify uniform zones in both streamwise velocity and temperature fields, a topic marginally addressed in compressible flows. The analysis showed that while the average number of uniform temperature zones increased compared to velocity zones, both decreased in the hypersonic regime. This finding provides new insights into the structure of turbulent boundary layers under varying thermal conditions.

The mean velocity and temperature profiles were analyzed, confirming that recent relations of Volpiani et al. (2020); Griffin et al. (2021) effectively extend the validity of compressibility transformations to diabatic boundary layers. Additionally, the mean temperature profile was found to align well with recent generalized relation of Zhang et al. (2014), improving upon classical models such as the one proposed by Walz (1969).

The study also examined velocity fluctuations, revealing that high Mach numbers lead to less efficient redistribution of turbulent kinetic energy among different velocity components. This obser-

vation is consistent with previous findings by Zhang et al. (2018) and is supported by observations in the turbulent kinetic energy budget, which showed improved data collapse with semi-local scaling.

Thermodynamic fluctuations were analyzed, showing that temperature and density fluctuations increase with Mach number, while pressure fluctuations are more influenced by Reynolds number. The comparison with an adiabatic reference case (Pirozzoli and Bernardini, 2011) indicated that wall cooling reduces temperature fluctuation intensity in the near-wall region.

Lastly, the research provided a detailed length scale analysis through pre-multiplied spectra of velocity and temperature fluctuations. This analysis confirmed two peaks in the spectra for both velocity and temperature fluctuations at high Reynolds numbers, corresponding to distinct flow regions. Notably, the buffer layer peak in temperature fluctuations disappeared in the most non-adiabatic case, aligning with earlier qualitative observations.

Overall, the study enhances the understanding of turbulence in high-speed boundary layers, offering new insights into flow behavior under non-adiabatic conditions and extending the presently available DNS dataset, especially at high Reynolds numbers.

5.2 Paper II

Assessment of heat transfer and Mach number effects on high-speed turbulent boundary layers

High-speed boundary layers are subject to intense variations of thermodynamic properties, which are highly dependent on the degree of compressibility and the surface temperature. In this paper, we presented a systematic study on the effects of Mach number and wall cooling on zero-pressure-gradient turbulent boundary layers (TBLs) using direct numerical simulations. We conducted a total of 12 computations across three Mach numbers, [2,4,6], and four values of the diabatic parameter $\Theta = (T_w - T_\infty)(T_r - T_\infty)$, [0.25,0.5,0.75,1], while keeping the friction Reynolds number constant to the value of $Re_\tau = 453$. Emphasis was placed on the wall-cooling parameter Θ , first proposed by Zhang et al. (2014), which better incorporates the indirect effects of Mach number on wall cooling, yielding consistent integral behavior across different cases.

A preliminary analysis on instantaneous flow organization revealed that as the wall temperature decreases (lower Θ), temperature fluctuations near the wall are considerably damped. This was observed by comparing the turbulence streaks in the buffer layer, which in adiabatic cases are similar across velocity and temperature fields, while for extremely cold cases, the ones related to temperature become almost isotropic and lose any similarity with velocity. However, when Θ is fixed, a similar flow organization is observed across different Mach numbers, demonstrating the parameter's effectiveness in consistently representing wall-cooling effects regardless of Mach number.

The application of recent compressibility transformations by Volpiani et al. (2020) and Griffin et al. (2021) allowed us to accurately collapse all mean velocity profiles to the incompressible laws of the wall. Similarly, the mean velocity-temperature relations proposed by Zhang et al. (2014) effectively captured both non-adiabatic and compressibility effects. When this relation was approximated with the computed mean Reynolds analogy factor $s = 0.78 \pm 0.03$, which is close to the fit by Zhang et al. (2014), we achieved an excellent estimate with maximum errors of 5% from the DNS data.

As Mach number increases, we observed a greater separation between large and small scales in the outer layer, characterized by the ratio L/η . This effect is primarily due to a significant reduction in the Kolmogorov length scale η , with only a slight increase in the largest scale L . This behavior can be described effectively by the growth of the semi-local friction Reynolds number Re_τ^* .

Conversely, the enhancement of wall cooling leads to a reduction in the large-small scale separation in the outer layer, which contrasts with the effect of Mach number. This reduction is mainly due to an increase in the Kolmogorov length scale η throughout the entire boundary layer thickness. Lower wall temperatures cause the mean temperature peak to rise and induce a stratification of flow properties localized around the buffer layer. This effect manifests as an apparent promotion of compressibility, with increased streamwise velocity fluctuations and damped fluctuations in other components.

In the near-wall region, wall cooling has a dominant effect on root-mean-square (rms) temperature profiles and the turbulent kinetic energy budget, whereas the Mach number influences the buffer and log layers. When the diabatic parameter Θ is kept constant, rms temperature profiles at different Mach numbers collapse near the wall, displaying similar wall-cooling effects.

For extremely cold cases (with $\Theta = 0.25$ in our database), the impact of wall cooling is so pronounced that temperature fluctuations are significantly damped where the mean temperature gradient is zero, resulting in a secondary, minor peak in the viscous sublayer. This phenomenon decorrelates velocity and temperature fields in the near-wall region and is more pronounced at high Mach numbers. The distinct behavior of thermal production in cold cases can be explained by the persistence of a positive mean temperature gradient over a wider wall-normal region with greater intensity than in adiabatic cases.

The observed decorrelation between velocity and temperature fields due to wall cooling presents a significant challenge for developing simplified wall models, as any similarity between these fields is lost, and the present database serves as a public reference to improve current wall models for high speed flows.

5.3 Paper III

Direct numerical simulation of compressible turbulent boundary layers over smooth and rough surfaces

Turbulent boundary layers in high-speed vehicles can be altered by the presence of surface roughness. In this paper, we studied compressible turbulent boundary layers (TBLs) over smooth and rough surfaces using direct numerical simulations (DNS). Specifically, we compared the flow dynamics of subsonic ($M_\infty=0.3$) and supersonic ($M_\infty=2$) TBLs with a smooth-to-rough surface transition. The rough surface was characterized by 3D cubical elements that were equally spaced in the streamwise and spanwise directions.

Our analysis began with the examination of instantaneous flow features, where we observed clear differences in the supersonic case due to compressibility effects. In particular, the supersonic rough wall case exhibited an oblique shock wave at the onset of roughness, followed by a pattern of local waves emanating from each roughness element and extending into the freestream. This pattern significantly influenced the acoustic environment outside the boundary layer. This observation is consistent with previous experimental studies (Latin and Bowersox, 2000; Ekoto et al., 2008; Kocher

et al., 2022), which reported similar patterns resulting from the interaction between roughness and compressibility.

We were able to accurately resolve the boundary layer and found that the formation of the initial shock wave is due not only to the local compression waves generated by the first row of roughness elements but also to a local adjustment in boundary layer width, which begins before the actual surface transition. This effect was evident from the streamwise evolution of the boundary layer thickness δ_{99} for the supersonic rough wall case, which showed a smoother transition compared to the subsonic rough wall case. In the subsonic case, a sharp local bump was observed after the surface transition before the boundary layer thickness resumed its growth at a rate similar to the smooth portion. Consequently, the streamwise evolution of the friction Reynolds number Re_τ was highly influenced by these variations in boundary layer thickness.

The smooth-to-rough transition was further analyzed through a detailed study of the formation of the internal boundary layer (IBL), extending previous work (Rouhi et al., 2019) to compressible flows for the first time. We detected the edge of the IBL, δ_I , within the external boundary layer width δ_{99} using the method by Elliott (1958). This method revealed similar growth rates for the IBL in both subsonic and supersonic rough wall cases. Specifically, the IBL thickness grew as $\delta_I \propto x^{0.62}$ for the subsonic rough wall case and as $\delta_I \propto x^{0.58}$ for the supersonic rough wall case. The use of a novel definition of IBL thickness based on the wall-normal Reynolds stress component $\bar{\rho}v''^2$ proved effective in reducing noise enhanced by compressibility effects and served as a good indicator of the IBL in both conditions. The growth rates obtained with this method were $\delta_I \propto x^{0.58}$ for the subsonic rough wall case and $\delta_I \propto x^{0.57}$ for the supersonic rough wall case. Although the IBL growth in absolute terms appeared comparable between subsonic and supersonic cases, the supersonic rough wall case was found to be farther from equilibrium relative to the subsonic rough wall case when considering their relative δ_{99} growth. This is due to a sharp increase of δ_{99} in the supersonic case right after the onset of roughness. This suggests that as compressibility effects increase, the boundary layer will require longer streamwise distances to fully adjust to changes in surface roughness.

We analyzed the recovery of turbulence and thermal statistics at a streamwise station far from the surface transition ($x/\delta_{in} = 140$). Both subsonic and supersonic rough wall cases exhibited a similar velocity shift ΔU^+ compared to their smooth counterparts, which was almost identical when applying the recent compressibility transformation by Hasan et al. (2023). By shifting all velocity profiles to a virtual origin $d = 0.9k$ (Chung et al., 2021), we observed that both subsonic and supersonic cases exhibited a nearly constant velocity shift $\Delta U^+ \approx 8$, indicating outer layer similarity for this quantity. Reynolds stress profiles showed good similarity between subsonic and supersonic cases, though the supersonic case exhibited some deviations from the smooth case in the streamwise component, consistent with the slower recovery rate observed in the IBL analysis.

In terms of mean and fluctuating temperature behavior, we noted that the concept of outer layer similarity does not apply to thermodynamic quantities. This corroborates the idea proposed by Modesti et al. (2022) that the non-linear temperature-velocity relation prevents direct application of this theory to temperature. Our adiabatic database showed that the temperature profile changes from a nearly constant behavior near the roughness elements to a strong gradient farther from the wall, aligning with the freestream condition. This change is directly related to the promotion of temperature fluctuations in the outer layer, as discussed by Cogo et al. (2023).

Future work is necessary to understand the effects of various parameters controlling this flow, such as Mach number, wall temperature conditions, and different roughness geometries.

5.4 Paper IV

URANOS: A GPU accelerated Navier-Stokes solver for compressible wall-bounded flows

Computational Fluid Dynamics (CFD) has become a standard tool in both industry and research for analyzing fluid behaviour. Over the years, advancements in computational methods for simulating wall flows, coupled with the rise of GPUs to accelerate computations, have significantly transformed design processes in fields such as aerospace, energy, and process engineering. We presented URANOS, a high-fidelity, GPU-enabled compressible flow solver specifically designed for wall-bounded flow applications. The paper details the solver's structure, numerical methods, and the discretization of the Navier-Stokes equations, with a focus on variable accuracy orders, advanced shock-capturing techniques, and a specialized approach to viscous terms.

The performance of URANOS was assessed highlighting the use of OpenACC for accelerating parallel performances on GPUs. The implementation of three different MPI approaches, including GPU-aware MPI and copy-to-host communication, was documented, allowing users to choose the best MPI solutions for their architecture.

We also evaluated the accuracy of URANOS in canonical flow cases, providing results from turbulent channel and boundary layers flows using DNS, LES and WMLES over a wide range Reynolds and Mach numbers. In particular, different WMLES calculations at Mach 0.1 and 5.86 are performed using the equilibrium wall model coupled with a particular algorithm that imposes the proper wall stress and heat flux, preserving the no-slip and the isothermal and adiabatic conditions for the velocity and temperature fields, respectively (De Vanna et al., 2021c).

URANOS stands out in the CFD field due to its flexibility and multi-platform capabilities. It uses OpenACC, which ensures compatibility with both current and future GPU-based clusters in a vendor-neutral manner, making it a maintainable and adaptable open-source tool. Moreover, URANOS incorporates advanced turbulence modeling strategies like LES and WMLES, making it a valuable platform for developing complex physical models for engineering applications.

Future updates will focus on handling complex and moving geometries, and addressing more intricate engineering problems.

5.5 Paper V

Inverse-velocity transformation wall model for reacting turbulent hypersonic boundary layers

The design of supersonic and hypersonic systems relies on the ability to accurately predict the aerothermodynamic loads acting on the vehicle's surface. To achieve this goal, numerical simulations are crucial for forecasting the various flow phenomena at high speeds, including turbulence, shock waves, and the initiation of thermochemical processes (Candler, 2019). Consequently, the development of wall models is vital for reducing computational effort for canonical flows and facilitating the simulation of more complex flow configurations of scientific interest.

This study presents an *a priori* assessment of the accuracy of extending the GFM model proposed by Griffin et al. (2023) to compressible turbulent reacting wall-bounded flows, and compares it with

the accuracy of the extended Equilibrium Wall Model (EWM) proposed by Di Renzo and Urzay (2019). The assessment considers the variability in the composition of the mixture near the wall by accounting for differential diffusion and finite-rate chemistry. Both models were tested using direct numerical simulation (DNS) data from a strongly reacting turbulent boundary layer, as provided by Williams et al. (2023), which serves as a crucial reference due to the enhanced turbulence–chemistry interactions involved.

The extended GFM model demonstrates improved performance compared to the EWM in predicting the Favre-averaged wall-normal profiles of inner-scaled velocity u^+ , rescaled temperature \tilde{T}/T_w , and enthalpy \tilde{h}/h_{ref} . This improved accuracy is reflected in smaller modeling errors for wall shear stress τ_w , wall heat flux q_w , and the mass fractions of the most abundant species, namely $\tilde{Y}_{\text{N}2}$ and \tilde{Y}_{O} , all of which are below 3%.

However, both models exhibit comparable predictions of wall-normal profiles of mass fractions, with deviations from DNS data primarily in the prediction of wall-normal gradients at the matching location. These deviations are attributed to the lack of modeling for turbulence–chemistry interactions in the prediction of the chemical reaction term \bar{w} , which overshadows the differences between the models in predicting mean temperature and velocity profiles. Enforcing the DNS profiles of \bar{w} in both models clearly improves the overall composition estimates for the extended GFM, which predicated upon the development of better models accounting for the turbulence-chemistry interaction embedded in this term.

Chapter 6

Conclusions

Motivated by their pivotal role in the engineering design of high-speed flight systems, compressible turbulent boundary layers over smooth and rough surfaces represent the focus of the present thesis.

This flow configuration, indicative of the dynamics of a fluid flow next to a solid surface, embodies critical physical processes that have a direct influence on the mechanical and thermal loads applied to the vehicle, critical to the engineering design. To this end, high-fidelity simulations are an essential tool to investigate the complex interactions that characterize compressible wall-bounded turbulence, where several controlling parameters compete in regulating the resulting near-wall dynamics, such as the freestream Reynolds and Mach numbers (Zhang et al., 2018), or the absolute and relative values of freestream and wall temperature (Duan and Martin, 2011; Duan et al., 2014). Other equally important factors, such as favorable or adverse pressure gradients (Wenzel et al., 2022), or surface catalysis (Bonelli et al., 2021), are outside the scope of the present work, but important parts of a larger picture. In the realm of high-fidelity simulations, these effects can be directly studied with scale-resolved methods, like DNS, or they can be included in models that alleviate the computational cost, like wall-modeled LES, maintaining the non-stationary and multiscale features of turbulence. Both these frameworks have been considered in the present dissertation by leveraging in-house compressible flow solvers STREAmS (Bernardini et al., 2021, 2023), and URANOS (De Vanna et al., 2023; De Vanna and Baldan, 2024), respectively.

In the following, we highlight the key findings of this dissertation and offer some recommendations for future research. This discussion is organized into two parts: the first focuses on fundamental research of the physics of compressible boundary layers over smooth and rough using DNS (Papers I to III), while the second addresses the modeling aspects of the near-wall dynamics in the context of LES, including high temperature effects (Papers IV and V).

Physical aspects of turbulent compressible boundary layers through DNS

We begin by investigating zero-pressure-gradients compressible turbulent boundary layers over flat plates, considering different Reynolds numbers, Mach numbers, and wall temperature conditions (Paper I and II). The resulting datasets contribute to the lack of reference data in high-speed flows, thus offering the possibility to validate recent compressibility transformations and temperature-velocity relations.

A key point that is apparent throughout the related discussion is how each controlling parameter can influence our intuition on the behavior of other ones, especially when high compressibility effects

are present. This statement can be clarified with two examples. First, we discuss how the wall temperature condition describes the thermal state of the solid boundary T_w in relation to a reference temperature, say the recovery temperature T_r . This condition is frequently used to intuitively assess whether the expected heat flux is small, a nearly adiabatic wall, or large, a diabatic wall, which in turn affects the coupling between thermal and kinetic fields. Hence, if we force the wall to respect an isothermal condition by specifying a given wall-to-recovery temperature ratio T_w/T_r , we expect the resulting near-wall dynamics to be consistent with respect to a change in other parameters, such as the Mach number. However, we noticed a completely different degree of similarity between near-wall velocity and temperature fluctuating fields across different Mach numbers when fixing the T_w/T_r ratio, with high Mach number cases showing much higher coherence between thermal and kinetic fluctuations. Building on intuitions from previous works (Zhang et al., 2014; Wenzel et al., 2022), which proposed alternative definitions of the wall temperature condition, we show through a variety of statistics how the Mach number influence can be consistently removed using the diabatic parameter Θ , yielding a similar imprint of wall-cooling effects independently of the freestream Mach number. Thanks to this observation, the resulting dynamics of thermal and kinetic fields is systematically investigated in Paper II, and some of the proposed physical interpretations have already been leveraged in subsequent works from other research groups (Gibis et al., 2024).

The second example is related to the Reynolds number, and specifically the friction Reynolds number Re_τ , which classically denotes the separation between the outer and inner turbulent scales. In order to better account for density and viscosity variations in the outer layer, the semilocal version is often used in compressible flows $Re_\tau^* = \mu_w/\mu_\infty \sqrt{\rho_\infty/\rho_w} Re_\tau$ (Hirai et al., 2021). As the Reynolds number increases, the enhancement of outer layer motions is expected, which is a sign of the augmented scale separation of the flow. However, we show how the influence of Mach number and wall cooling can strongly increase Re_τ^* by mostly altering the smallest scales, with minor effects on the largest ones, which is in direct contrast to what we expect by transferring our intuition built in incompressible flows. For this reason, we remark that the definition of a single similarity parameter among different flow cases concerning the scale separation is prevented by the strong change of flow properties across the boundary layer.

Discerning the influence of a given controlling parameter among the others is not easy given these complex interactions, and this requires future studies. For example, the past literature frequently argued that wall cooling and compressibility effects have often a similar imprint (Duan and Martin, 2011). In our analysis, we show different physical mechanisms induced by wall-cooling and compressibility that result in apparently similar flow features, such as a higher peak in the streamwise velocity turbulence intensity, and distinct features, such as the separation of turbulent scales. New studies dedicated to the influence of controlling parameters on turbulent scales are needed to further clarify this picture.

Lastly, we discuss one of the first numerical studies on compressible turbulent boundary layers subject to a smooth-to-rough surface transition, allowing for an in-depth scrutiny of all turbulent scales and a one-to-one comparison with a subsonic case, which was impractical in previous experimental studies. For this study, we highlight two aspects. The first is the analysis on the adjustment of the boundary layer to the onset of roughness, with a specific focus on the development of the internal boundary layer. Here, we observed a similar absolute growth of subsonic and supersonic cases by using different detection algorithms. However, the supersonic case exhibits a distinct up-

ward shift in the BL thickness after the transition, which implies a slower growth of the IBL relative to the BL size. Future studies are needed to understand whether other geometries can enhance or reduce this effect.

The second point concerns the analysis of outer layer similarity in wall-normal statistics in a location far from the surface transition, where equilibrium is expected. Here, we show that outer layer similarity with a reference smooth case is reached for the velocity field quite well for both cases, especially when compressibility transformations are used, while thermodynamic quantities do not hold this feature. Future analyses are needed to study different geometries, as well as spanning different values of the controlling parameters mentioned for smooth wall cases (e.g. the Mach number).

Modeling aspects of highly compressible boundary layers including high temperature effects

Different modeling aspects of high-speed flows were considered in Papers IV and V, which discuss implementation and proposed improvements of state-of-the-art wall modeling closures for hypersonic boundary layers. Specifically, Paper IV presents the flow solver URANOS, developed for compressible flows in the calorically-perfect gas regime, and specifically tailored for LES and WMLES methodologies. From the related discussion, we underline the effort of porting the code to run efficiently on GPUs using a non-vendor-specific paradigm, OpenACC. Notwithstanding the importance of numerical algorithms, leveraging new technologies like GPUs has become an essential part of a CFD solver, which enables the possibility to tackle progressively more complex flow configurations. Then, we highlight the implementation of the classical equilibrium wall model and its coupling to the LES solver, which we test *a posteriori* in conjunction with the WALE SGS model. Future works are needed to systematically evaluate more recent wall models leveraging compressibility transformation on different configurations, for which Papers I and II stand as an invaluable reference.

Paper V presents a generalization of the wall model of Griffin et al. (2023) (GFM model), accounting for finite-rate chemistry and multicomponent diffusion in reacting hypersonic boundary layers. The novel formulation is then *a priori* against a very recent DNS database of Williams et al. (2023) that includes intense chemical activity and nonequilibrium effects. In this study, we compare the prediction of the velocity, temperature, and mass fraction profiles, as well as the wall shear stress τ_w and the heat flux q_w . A preliminary analysis demonstrates significant improvements relative to the classical equilibrium wall model when applied to compressible wall-bounded flows with strong wall-cooling, while predicates upon the research for improved modeling of the chemical reaction term, which exhibits highly nonlinear behavior. Additional studies may include the comparison of the present model with different compressibility transformations, such as the one from Hasan et al. (2023). In the realm of chemically-reacting boundary layers, future studies are needed not only for the wall modeling procedure, but even in the development of a reliable SGS model that can account for sub-grid turbulence-chemistry interaction.

Acknowledgements

The present work has been carried out at CISAS “Giuseppe Colombo” at the University of Padova from 2021 to 2024. I want to begin by thanking my supervisor, prof. Francesco Picano, who attracted me into this field first and foremost by being a very talented teacher. Thanks to his continuous support, I learned what it means to do research with curiosity, critical thinking and attention for details. I’m particularly grateful for the freedom he gave me to follow my aspirations, while continuously advising and believing in me.

I thank Francesco De Vanna for his mentorship during the master thesis and for teaching me the art of coding in Fortran, Federico Dalla Barba for being supportive in both academic and personal sides, Luca Placco for the good times we had during the PhD and at different conferences, and Xiang’en Kong for giving me a taste of the true Chinese cousin. I also want to thank the former student Jietuo Wang for being supportive at the beginning of my PhD.

I had the luck to be able to work with several people outside Padova. I want to begin with prof. Matteo Bernardini from Sapienza, whose mentorship and experience in the field of compressible flow helped me to grow a lot as a young researcher. From the same group, I also thank Giacomo Della Posta for helping me in numerous occasions and for the good times we had at international conferences.

I also learned a lot from prof. Davide Modesti, who hosted me in TU Delft, who I thank for guiding me with patience and showing me how to properly have fun in Delft’s pubs. During this visiting period, I made several friends in the Aerospace and Mechanical departments. I especially thank Haris Shahzad for his unique sense of humor and companionship, and prof. Pedro Costa for all the good times we had.

During my time at Stanford, I’m deeply grateful to prof. Parviz Moin for hosting me and making me feel included in his group. This experience was made possible by Fulbright scholarship and Ermenegildo Zegna Founder’s scholarship. I thank all PhD Students and Postdocs from Center of Turbulence Research who made me feel like I was at home, and guiding me in a environment that was very new for me.

Finally, I thank my future wife Linda for always supporting me during the ups and downs of personal and academic life.

Bibliography

- J. Anderson. *Hypersonic and High-temperature Gas Dynamics*. AIAA education series. American Institute of Aeronautics and Astronautics, 2006. ISBN 9781563477805. URL <https://books.google.it/books?id=UgWmQgAACAAJ>.
- B. Aupoix and S. Viala. Compressible turbulent boundary layer modelling. *Transitional and turbulent compressible flows*, pages 139–146, 1995.
- H. Babinsky and J. K. Harvey. *Shock wave-boundary-layer interactions*, volume 32. Cambridge University Press, 2011.
- M. Bernardini and S. Pirozzoli. Wall pressure fluctuations beneath supersonic turbulent boundary layers. *Phys. Fluids*, 23(8), 2011a. ISSN 10706631. doi: 10.1063/1.3622773.
- M. Bernardini and S. Pirozzoli. Inner/outer layer interactions in turbulent boundary layers: a refined measure for the large-scale amplitude modulation mechanism. *Phys. Fluids*, 23(6):061701, 2011b.
- M. Bernardini, D. Modesti, F. Salvadore, and S. Pirozzoli. STREAmS: a high-fidelity accelerated solver for direct numerical simulation of compressible turbulent flows. *Comp. Phys. Comm.*, 263: 107906, 2021.
- M. Bernardini, D. Modesti, F. Salvadore, S. Sathyaranayana, G. Della Posta, and S. Pirozzoli. Streams-2.0: Supersonic turbulent accelerated navier-stokes solver version 2.0. *Computer Physics Communications*, 285:108644, 2023.
- J. J. Bertin and R. M. Cummings. Fifty years of hypersonics: where we've been, where we're going. *Progress in Aerospace Sciences*, 39(6-7):511–536, 2003.
- J. J. Bertin and R. M. Cummings. Critical hypersonic aerothermodynamic phenomena. *Annu. Rev. Fluid Mech.*, 38(1):129–157, 2006.
- R. Bird, W. Stewart, and E. Lightfoot. *Transport Phenomena*. Number v. 1 in Transport Phenomena. Wiley, 2006. ISBN 9780470115398. URL <https://books.google.it/books?id=L5FnN1IaGfcC>.
- F. Bonelli, G. Pascazio, and G. Colonna. Effect of finite-rate catalysis on wall heat flux prediction in hypersonic flow. *Physical Review Fluids*, 6(3):033201, 2021.

- R. Borges, M. Carmona, B. Costa, and W. Don. An improved weighted essentially non-oscillatory scheme for hyperbolic conservation laws. *Journal of Computational Physics*, 227(6):3191–3211, 2008.
- R. Bowersox. Survey of high-speed rough wall boundary layers: invited presentation. *AIAA Paper*, pages 2007–3998, 2007.
- A. Busemann. *Gasdynamik*. Akademische Verlagsgesellschaft, 1931.
- G. V. Candler. Rate Effects in Hypersonic Flows. *Annu. Rev. Fluid Mech.*, 51(September 2018):379–402, 2019. ISSN 00664189. doi: 10.1146/annurev-fluid-010518-040258.
- C. Carvin, J. Debieve, and A. Smits. The near-wall temperature profile of turbulent boundary layers. In *26th Aerospace Sciences Meeting*, page 136, 1988.
- H. Cheng and I. P. Castro. Near-wall flow development after a step change in surface roughness. *Bound.-Lay. Meteorol.*, 105:411–432, 2002.
- D. Chung, N. Hutchins, M. P. Schultz, and K. A. Flack. Predicting the drag of rough surfaces. *Ann. Rev. Fluid Mech.*, 53:439–471, 2021.
- F. H. Clauser. Turbulent boundary layers in adverse pressure gradients. *Journal of the Aeronautical Sciences*, 21(2):91–108, 1954.
- M. Cogo, U. Baù, M. Chinappi, M. Bernardini, and F. Picano. Assessment of heat transfer and mach number effects on high-speed turbulent boundary layers. *Journal of Fluid Mechanics*, 974:A10, 2023.
- G. N. Coleman, J. Kim, and R. D. Moser. A numerical study of turbulent supersonic isothermal-wall channel flow. *Journal of Fluid Mechanics*, 305:159–183, 1995.
- L. Crocco. Sulla trasmissione del calore da una lamina piana a un fluido scorrente ad alta velocità. *L'Aerotecnica*, 12:181–197, 1932.
- C. F. Curtiss and J. O. Hirschfelder. Transport properties of multicomponent gas mixtures. *The Journal of Chemical Physics*, 17(6):550–555, 1949.
- F. De Vanna and G. Baldan. Uranos-2.0: Improved performance, enhanced portability, and model extension towards exascale computing of high-speed engineering flows. *Computer Physics Communications*, page 109285, 2024.
- F. De Vanna, F. Picano, and E. Benini. A sharp-interface immersed boundary method for moving objects in compressible viscous flows. *Computers & Fluids*, 201:104415, 2020.
- F. De Vanna, A. Benato, F. Picano, and E. Benini. High-order conservative formulation of viscous terms for variable viscosity flows. *Acta Mech.*, 232:2115–2133, 2021a.
- F. De Vanna, A. Benato, F. Picano, and E. Benini. High order conservative formulation of viscous terms for variable viscosity flows. *Acta Mechanica*, 232(6):2115–2133, 2021b.

- F. De Vanna, M. Cogo, M. Bernardini, F. Picano, and E. Benini. Unified wall-resolved and wall-modeled method for large-eddy simulations of compressible wall-bounded flows. *Physical Review Fluids*, 6(3):034614, 2021c.
- F. De Vanna, F. Picano, E. Benini, and M. K. Quinn. Large-eddy simulations of the unsteady behavior of a hypersonic intake at mach 5. *AIAA Journal*, 59(10):3859–3872, 2021d.
- F. De Vanna, M. Bernardini, F. Picano, and E. Benini. Wall-modeled les of shock-wave/boundary layer interaction. *International Journal of Heat and Fluid Flow*, 98:109071, 2022.
- F. De Vanna, F. Avanzi, M. Cogo, S. Sandrin, M. Bettencourt, F. Picano, and E. Benini. Uranos: A gpu accelerated navier-stokes solver for compressible wall-bounded flows. *Computer Physics Communications*, 287:108717, 2023.
- F. De Vanna, G. Baldan, F. Picano, and E. Benini. On the coupling between wall-modeled les and immersed boundary method towards applicative compressible flow simulations. *Computers & Fluids*, 266:106058, 2023. ISSN 0045-7930. doi: <https://doi.org/10.1016/j.compfluid.2023.106058>. URL <https://www.sciencedirect.com/science/article/pii/S0045793023002839>.
- F. De Vanna, G. Baldan, F. Picano, and E. Benini. On the coupling between wall-modeled les and immersed boundary method towards applicative compressible flow simulations. *Computers & Fluids*, 266:106058, 2023a.
- F. De Vanna, G. Baldan, F. Picano, and E. Benini. Effect of convective schemes in wall-resolved and wall-modeled les of compressible wall turbulence. *Computers & Fluids*, 250:105710, 2023b.
- G. Della Posta, E. Martelli, F. Stella, D. Barbagallo, A. Neri, F. Salvadore, and M. Bernardini. High-fidelity simulations of the aeroacoustic environment of the vega launch vehicle at lift-off. *Computers & Fluids*, 263:105945, 2023.
- M. Di Renzo and J. Urzay. An a priori study of the accuracy of an equilibrium wall model for dissociating air in supersonic channel flows. *Annual Research Briefs, Center for Turbulence Research*, pages 29–40, 2019.
- M. Di Renzo and J. Urzay. Direct numerical simulation of a hypersonic transitional boundary layer at suborbital enthalpies. *J. Fluid Mech.*, 912:A29, 2021. doi: 10.1017/jfm.2020.1144. URL <http://dx.doi.org/10.1017/jfm.2020.1144>.
- L. Duan and M. Martin. Direct numerical simulation of hypersonic turbulent boundary layers. Part 4. Effect of high enthalpy. *J. Fluid Mech.*, 684:25–59, 2011.
- L. Duan, I. Beekman, and M. Martín. Direct numerical simulation of hypersonic turbulent boundary layers. Part 2. Effect of wall temperature. *J. Fluid Mech.*, 655:419–445, 2010. ISSN 00221120. doi: 10.1017/S0022112010000959.
- L. Duan, M. M. Choudhari, and M. Wu. Numerical study of acoustic radiation due to a supersonic turbulent boundary layer. *J. Fluid Mech.*, 746:165–192, 2014.
- F. Ducros, V. Ferrand, F. Nicoud, C. Weber, D. Darracq, C. Gachet, and T. Poinsot. Large-eddy simulation of the shock/turbulence interaction. *J. of Comput. Phys.*, 152(2):517–549, 1999.

- I. W. Ekoto, R. Bowersox, T. Beutner, and L. Goss. Supersonic boundary layers with periodic surface roughness. *AIAA J.*, 46(2):486–497, 2008.
- W. P. Elliott. The growth of the atmospheric internal boundary layer. *Trans. Am. Geophys. Union*, 39(6):1048–1054, 1958.
- K. Flack, M. Schultz, and J. Barros. Skin friction measurements of systematically-varied roughness: probing the role of roughness amplitude and skewness. *Flow, Turbulence and Combustion*, 104: 317–329, 2020.
- K. A. Flack and M. Schultz. Review of hydraulic roughness scales in the fully rough regime. *J. Fluids Eng.*, 132(4):041203, 2010.
- K. A. Flack and M. P. Schultz. Roughness effects on wall-bounded turbulent flows. *Phys. Fluids*, 26(10), 2014.
- L. Fu, X. Hu, and N. Adams. A new class of adaptive high-order targeted eno schemes for hyperbolic conservation laws. *Journal of Computational Physics*, 374:724–751, 2018. doi: 10.1016/j.jcp.2018.07.043.
- D. V. Gaitonde. Progress in shock wave/boundary layer interactions. *Progress in Aerospace Sciences*, 72:80–99, 2015.
- T. B. Gatski and J. P. Bonnet. *Compressibility, turbulence and high speed flow*. Academic Press, 2013.
- T. Gibis, L. Sciacovelli, M. Kloker, and C. Wenzel. Heat-transfer effects in compressible turbulent boundary layers—a regime diagram. *Journal of Fluid Mechanics*, 995:A14, 2024.
- P. A. Gnoffo. Planetary-entry gas dynamics. *Annual Review of Fluid Mechanics*, 31(1):459–494, 1999.
- S. Gottlieb and C.-W. Shu. Total variation diminishing runge-kutta schemes. *Mathematics of computation*, 67(221):73–85, 1998.
- K. Griffin, L. Fu, and P. Moin. Velocity transformation for compressible wall-bounded turbulent flows with and without heat transfer. *P. Natl. Acad. Sci USA*, 118(34), 2021.
- K. P. Griffin, L. Fu, and P. Moin. Near-wall model for compressible turbulent boundary layers based on an inverse velocity transformation. *Journal of Fluid Mechanics*, 970:A36, 2023.
- F. F. Grinstein, L. G. Margolin, and W. J. Rider. *Implicit large eddy simulation*, volume 10. Cambridge university press Cambridge, 2007.
- F. R. Hama. Boundary layer characteristics for smooth and rough surfaces. *Trans. Soc. Nav. Arch. Marine Engrs.*, 62:333–358, 1954.
- A. M. Hasan, J. Larsson, S. Pirozzoli, and R. Pecnik. Incorporating intrinsic compressibility effects in velocity transformations for wall-bounded turbulent flows. *Phys. Rev. Fluids*, 8(11):L112601, 2023.

- A. M. Hasan, J. Larsson, S. Pirozzoli, and R. Pecnik. Estimating mean profiles and fluxes in high-speed turbulent boundary layers using inner/outer-layer scalings. *AIAA Journal*, 62(2):848–853, 2024.
- R. Hirai, R. Pecnik, and S. Kawai. Effects of the semi-local reynolds number in scaling turbulent statistics for wall heated/cooled supersonic turbulent boundary layers. *Physical Review Fluids*, 6 (12):124603, 2021.
- E. H. Hirschel and C. Weiland. *Selected aerothermodynamic design problems of hypersonic flight vehicles*, volume 229. Springer Science & Business Media, 2009.
- P. C. Huang, G. Coleman, and P. Bradshaw. Compressible turbulent channel flows: DNS results and modelling. *J. Fluid Mech.*, 305:185–218, 1995.
- M. Inagaki, T. Kondoh, and Y. Nagano. A mixed-time-scale sgs model with fixed model-parameters for practical les. *Journal of Fluids Engineering*, 127(1):1–13, 2005. doi: 10.1115/1.1852479.
- G. Jiang and C. Shu. Efficient implementation of weighted eno schemes. *Journal of Computational Physics*, 126(1):202–228, 1996.
- J. Jiménez. Turbulent flows over rough walls. *Annu. Rev. Fluid Mech.*, 36:173–196, 2004.
- B. D. Kocher, P. A. Kreth, J. D. Schmisser, E. J. LaLonde, and C. S. Combs. Characterizing streamwise development of surface roughness effects on a supersonic boundary layer. *AIAA J.*, 60(9):5136–5149, 2022.
- A. Laganelli and D. Nestler. Surface ablation patterns-a phenomenology study. *AIAA Journal*, 7 (7):1319–1325, 1969.
- J. Larsson, S. Kawai, J. Bodart, and I. Bermejo-Moreno. Large eddy simulation with modeled wall-stress: recent progress and future directions. *Mechanical Engineering Reviews*, 3(1):15–00418, 2016.
- R. M. Latin and R. Bowersox. Flow properties of a supersonic turbulent boundary layer with wall roughness. *AIAA J.*, 38(10):1804–1821, 2000.
- I. A. Leyva. The relentless pursuit of hypersonic flight. *Physics Today*, 70(11):30–36, 2017.
- M. Li, C. M. De Silva, D. Chung, D. I. Pullin, I. Marusic, and N. Hutchins. Experimental study of a turbulent boundary layer with a rough-to-smooth change in surface conditions at high reynolds numbers. *Journal of Fluid Mechanics*, 923:A18, 2021.
- S. Mathur, P. Tondon, and S. Saxena. Thermal conductivity of binary, ternary and quaternary mixtures of rare gases. *Molecular physics*, 12(6):569–579, 1967.
- B. J. McBride. *NASA Glenn coefficients for calculating thermodynamic properties of individual species*. National Aeronautics and Space Administration, John H. Glenn Research Center, 2002.
- D. Modesti and S. Pirozzoli. Reynolds and Mach number effects in compressible turbulent channel flow. *Int. J. Heat Fluid Fl.*, 59:33–49, 2016.

- D. Modesti, S. Sathyaranayana, F. Salvadore, and M. Bernardini. Direct numerical simulation of supersonic turbulent flows over rough surfaces. *J. Fluid Mech.*, 942:A44, 2022. doi: 10.1017/jfm.2022.393.
- M. Morkovin. Effects of compressibility on turbulent flows. *Mécanique de la Turbulence*, 367(380): 26, 1962.
- F. Nicoud and F. Ducros. Subgrid-scale stress modelling based on the square of the velocity gradient tensor. *Flow, turbulence and Combustion*, 62(3):183–200, 1999.
- J. Nikuradse. Strömungsgesetze in rauhen rohren. VDI-Forschungsh. Berline: Ver. Dtsch. Ing., page 363, 1933.
- D. Ninni, F. Bonelli, G. Colonna, and G. Pascazio. Unsteady behavior and thermochemical non equilibrium effects in hypersonic double-wedge flows. *Acta Astronautica*, 191:178–192, 2022.
- J. o'Rourke. *Computational geometry in C*. Cambridge university press, 1998.
- C. Park. *Nonequilibrium Hypersonic Aerothermodynamics*. Wiley, 1989a.
- C. Park. A review of reaction rates in high temperature air. In *AIAA Paper*, number 1989-1740, 1989b.
- D. Passiatore, L. Sciacovelli, P. Cinnella, and G. Pascazio. Finite-rate chemistry effects in turbulent hypersonic boundary layers: A direct numerical simulation study. *Phys. Rev. Fluids*, 6(5):054604, 2021.
- D. Passiatore, L. Sciacovelli, P. Cinnella, and G. Pascazio. Thermochemical non-equilibrium effects in turbulent hypersonic boundary layers. *J. of Fluid Mech.*, 941, 2022.
- A. Patel, B. J. Boersma, and R. Pecnik. The influence of near-wall density and viscosity gradients on turbulence in channel flows. *Journal of Fluid Mechanics*, 809:793–820, 2016.
- A. Patel, R. Pecnik, J. Peeters, B. J. Boersma, S. Hickel, and M. Moghadam. Turbulence modulation by variable density and viscosity. In *Studying Turbulence Using Numerical Simulation Databases-XVI: 2016 Summer Program*, pages 213–222. Center for Turbulence Research, Stanford University, USA, 2017.
- S. Peltier, R. Humble, and R. Bowersox. Crosshatch roughness distortions on a hypersonic turbulent boundary layer. *Physics of Fluids*, 28(4), 2016.
- A. Piquet, O. Roussel, and A. Hadjadj. A comparative study of brinkman penalization and direct-forcing immersed boundary methods for compressible viscous flows. *Computers & Fluids*, 136: 272–284, 2016.
- S. Pirozzoli. Generalized conservative approximations of split convective derivative operators. *J. Comput. Phys.*, 229(19):7180–7190, 2010.
- S. Pirozzoli and M. Bernardini. Turbulence in supersonic boundary layers at moderate reynolds number. *J. Fluid Mech.*, 688:120–168, 2011.

- T. Poinsot. Theoretical and numerical combustion. *RT Edwards*, 2005.
- S. B. Pope. *Turbulent Flows*. Cambridge University Press, 2000.
- O. Reynolds. On the extent and action of the heating surface of stream boilers. *Proc. Lit. Soc. Manchester*, 14:7–12, 1874.
- A. Rouhi, D. Chung, and N. Hutchins. Direct numerical simulation of open-channel flow over smooth-to-rough and rough-to-smooth step changes. *J. Fluid Mech.*, 866:450–486, 2019.
- F. Salvadore, G. Rossi, S. Sathyanarayana, and M. Bernardini. Openmp offload toward the ex-ascale using Intel GPU max 1550: evaluation of streams compressible solver. *The Journal of Supercomputing*, pages 1–34, 2024.
- J. Smagorinsky. General circulation experiments with the primitive equations. *Monthly Weather Review*, 91:99–164, 1963. doi: 10.1175/1520-0493(1963)0912.3.CO;2.
- P. Spalart, R. Moser, and M. Rogers. Spectral methods for the navier–stokes equations with one infinite and two periodic directions. *Journal of Computational Physics*, 96(2):297–324, 1991.
- H. W. Stock and J. J. Ginoux. Hypersonic low temperature ablation an experimental study of cross-hatched surface patterns. In *Astronautical Research 1971: Proceedings of the 22nd Congress of the International Astronautical Federation Brussels, 20–25 September 1971*, pages 105–120. Springer, 1973.
- The CGAL Project. *CGAL User and Reference Manual*, 5.2.2 edition, 2021.
- H. B. Toda, O. Cabrit, G. Balarac, S. Bose, J. Lee, H. Choi, and F. Nicoud. A subgrid-scale model based on singular values for les in complex geometries. In *Proceedings of the Summer Program*, pages 193–202, 2010.
- A. Trettel and J. Larsson. Mean velocity scaling for compressible wall turbulence with heat transfer. *Phys. Fluids*, 28(2):026102, 2016.
- J. Urzay. Supersonic combustion in air-breathing propulsion systems for hypersonic flight. *Annu. Rev. Fluid Mech.*, 50:593–627, 2018.
- J. Urzay and M. Di Renzo. Engineering aspects of hypersonic turbulent flows at suborbital enthalpies. *Annual Research Briefs, Center for Turbulence Research*, pages 7–32, 2021.
- O. Uyanna and H. Najafi. Thermal protection systems for space vehicles: A review on technology development, current challenges and future prospects. *Acta Astronautica*, 176:341–356, 2020.
- E. Van Driest. Turbulent boundary layer in compressible fluids. *J. Aeronaut. Sci.*, 18(3):145–160, 1951.
- E. Van Driest. The problem of aerodynamic heating. *Aeronaut. Engng. Rev.*, 15(10):26–41, 1956.
- P. Volpiani, P. Iyer, S. Pirozzoli, and J. Larsson. Data-driven compressibility transformation for turbulent wall layers. *Phys. Rev. Fluids*, 5(5):052602, 2020.

- A. Walz. *Boundary layers of flow and temperature*. MIT Press, 1969.
- C. Wenzel, T. Gibis, and M. Kloker. About the influences of compressibility, heat transfer and pressure gradients in compressible turbulent boundary layers. *J. Fluid Mech.*, 930, 2022.
- C. R. Wilke. A viscosity equation for gas mixtures. *The journal of chemical physics*, 18(4):517–519, 1950.
- C. T. Williams, M. Di Renzo, and P. Moin. Direct simulation of turbulence-chemistry interaction in a strongly reacting turbulent hypersonic boundary layer. *Annual Research Briefs, Center for Turbulence Research, Stanford University*, 2023.
- O. J. H. Williams, D. Sahoo, M. Papageorge, and A. J. Smits. Effects of roughness on a turbulent boundary layer in hypersonic flow. *Experiments in Fluids*, 62:1–13, 2021.
- X. I. Yang and Y. Lv. A semi-locally scaled eddy viscosity formulation for les wall models and flows at high speeds. *Theoretical and Computational Fluid Dynamics*, 32(5):617–627, 2018.
- C. Zhang, L. Duan, and M. Choudhari. Direct numerical simulation database for supersonic and hypersonic turbulent boundary layers. *AIAA J.*, 56(11):4297–4311, 2018. ISSN 00011452. doi: 10.2514/1.J057296.
- Y. Zhang, W. Bi, F. Hussain, and Z. She. A generalized Reynolds analogy for compressible wall-bounded turbulent flows. *J. Fluid Mech.*, 739:392–420, 2014.
- Y.-S. Zhang, W.-T. Bi, F. Hussain, X.-L. Li, and Z.-S. She. Mach-number-invariant mean-velocity profile of compressible turbulent boundary layers. *Physical Review Letters*, 109(5):054502, 2012.

Appendix A

Paper I

Direct numerical simulation of supersonic and hypersonic turbulent boundary layers at moderate-high Reynolds numbers and isothermal wall condition

Michele Cogo^{1,4}, Francesco Salvadore², Francesco Picano^{3,4}, Matteo Bernardini¹

1. Department of Mechanical and Aerospace Engineering, Sapienza University of Rome, via Eudossiana 18, 00184 Rome, Italy,

2. HPC Department, CINECA, Rome office, via dei Tizii 6/B, 00185 Rome, Italy,

3. Department of Industrial Engineering, University of Padova, Padova, PD 35131, Italy,

4. Centro di Ateneo di Studi e Attività Spaziali "Giuseppe Colombo" - CISAS,
University of Padova, Padova, PD 35131, Italy

Journal of Fluid Mechanics, 2022, 945, A30

Abstract: We study the structure of high-speed zero-pressure-gradient turbulent boundary layers up to friction Reynolds number $Re_\tau \approx 2000$ using direct numerical simulation (DNS) of the Navier-Stokes equations. Both supersonic and hypersonic conditions with nominal free-stream Mach numbers $M_\infty = 2$, $M_\infty = 5.86$ and heat transfer at the wall are considered. The present simulations extend the database currently available for wall-bounded flows, enabling us to explore high-Reynolds number effects even in the hypersonic regime. We first analyze the instantaneous fields to characterize the structure of both velocity and temperature fluctuations. In all cases elongated strips of uniform velocity and temperature (superstructures) are observed in the outer portion of the boundary layer, characterized by a clear association between low-/high-speed momentum and high/low temperature streaks. The results highlight important deviations from the typical organization observed in the inner region of adiabatic boundary layers, revealing that the near-wall temperature streaks disappear in strongly non adiabatic flow cases. We also focus on the structural properties of regions of uniform streamwise momentum [10] observed in turbulent boundary layers, confirming the presence of such zones in the high-speed regime at high Reynolds number and revealing the existence of similar regions for the temperature field. The accuracy of different compressibility transformations and temperature-velocity relations is assessed extending their range of validation to moderate/high Reynolds numbers. Spanwise spectral densities of the velocity and temperature fluctuations at various wall distances have been calculated revealing the energy content and the size of the turbulent eddies across the boundary layer. Finally, we propose a revised scaling for the characteristic lengthscales, that is based on the local mean shear computed according to the recent theory by Griffin et al. [19].

Keywords: compressible boundary layers, hypersonic flow, turbulence simulation

Introduction

The study of high-speed turbulent boundary layers is essential to determine the aerodynamic heating and drag on supersonic and hypersonic vehicles. The interest of the research community in this direction is fed by the technological advancements in the development of vehicles capable of sustained hypersonic flight in the atmosphere, sub-orbital flights and planetary reentry [53]. A crucial feature of these flows is their huge kinetic energy content compared to the thermal energy of the free-stream gas, which severely affects the near-wall turbulence structures. In fact, when such energetic flows are brought to rest by the presence of a wall, high thermal fluxes and intense pressure waves are generated, posing numerous technical challenges for the choice of surface materials. In the last decades, several theoretical relations have been proposed to grasp the relevant physical phenomena and understand the driving factors that are responsible for the deviations from classical laws developed for incompressible flows, on which several useful engineering models are based. However, the lack of reference data has always posed a major setback in the development of theoretical laws, in which key assumptions need to be validated.

The theory of supersonic flows relies on the so-called “compressibility transformations”, that were first presented in a broad and robust framework for both mean and fluctuating fields by Morkovin [32]. The key concept is that, when density fluctuations are small compared to the mean value, the mean velocity and Reynolds stress profiles in a compressible boundary layer can be mapped to equivalent incompressible distributions [6] by taking into account the mean density variation across the boundary layer. This assumption is the cornerstone at the base of the “Morkovin’s hypothesis”, from which several consequences can be derived, as the Van Driest velocity scaling [55], consisting in a transformation of compressible flow profiles that takes into account the density variations to collapse them onto the incompressible laws. The Van Driest transformation has been extended to account for a finite wall heat flux by Trettel and Larsson [52], who proposed an alternative formulation based on the log-layer scaling and near-wall momentum conservation. Although this transformation yields accurate results for internal flows like turbulent channels and pipes [30], some open questions remain for its application to non-adiabatic turbulent boundary layers [56]. Volpiani et al. [57] addressed this point proposing a mixed physical and data-driven transformation that shows an improved collapse with respect to the existing ones on turbulent boundary layers. Despite impressive results, the performance evaluation at higher Reynolds numbers and on different configurations (e.g. turbulent channels) is still undergoing. More recently, a total-stress-based transformation has been developed by Griffin et al. [19], yielding very promising results through the entire inner layer regardless of the wall thermal condition. As before, more reference data at high Reynolds number are needed for the assessment of the performances of the proposed velocity scaling on collapsing on the incompressible profiles.

A key aspect of the theoretical study of compressible flows is the relation between velocity and temperature fields. Despite being non-linearly coupled, a quantitative relationship between these fields was found firstly by Reynolds [44], by means of similarity arguments between momentum and energy transport in wall-bounded flows that lead to a temperature-velocity relation. This concept is generally referred to as the “Reynolds analogy”, and was extended to laminar compressible boundary layers independently by Crocco [8] and Busemann [7] in adiabatic conditions. Later, a temperature-velocity relation was developed by Walz [58] to account for the deviation of the Prandtl

number from unity. This relation was improved empirically by (Duan et al. [14], Duan and Martin [13]) and, more recently, by Zhang et al. [67], who proposed a generalization to incorporate the effects of wall heat flux, that acquire relevance as the Mach number increases. The extension of these relations to fluctuating fields, initially proposed by Morkovin [32], goes under the name of Strong Reynolds Analogy (SRA), and consists in a set of relations between the velocity and temperature fluctuations. Although the SRA relations have been extensively used to formulate turbulence models, compressibility effects can undermine their accuracy, especially when large heat fluxes are considered. Subsequent extensions of SRA accounting for non-adiabatic wall conditions have been presented by Gaviglio [18], Rubesin [45] and Huang et al. [22], and are still under validation for different flow conditions (Mach, Reynolds numbers and different wall temperatures) as computational and experimental data become available.

The advancement in the understanding of the physics involved in hypersonic turbulent boundary layers has been supported by DNS studies and experiments performed in the last two decades, although the current database is still very small compared to the subsonic and supersonic counterparts and almost exclusively limited to low Reynolds numbers. Experimental studies of high-speed flows have been historically conducted using hot-wire anemometry, that measures a combination of fluctuating mass flux and total temperature (see for example Smits et al. [48]). This technique is usually limited to the description of large-scale motions given the difficulties in resolving the near-wall flow scales and frequency response. More recently, particle image velocimetry (PIV) has been employed in hypersonic turbulent boundary layers at Mach 4.9 and 7.5 by Tichenor et al. [50] and Williams et al. [62]. Although this method allows direct measurements of spatially varying velocity fields, accurate measurements are not yet available especially on the wall-normal component of velocity or Reynolds stresses [62]. Numerical simulations provide an alternative and effective method to investigate different aspects of this type of flows overcoming some technical difficulties of experiments, but are still limited by computational resources. One of the first studies of an hypersonic turbulent boundary layer up to Mach 6 has been conducted by Martin [26], who focused on the initialization procedure to control flow conditions and reduce simulation transients. This was the first of a four part study continued by Duan et al. [14], Duan et al. [15] and [13], that extended the analysis on different features that are peculiar to highly compressible flows, namely the effect on the flow of Mach number (from 0.3 to 12), wall temperature condition (T_w/T_r ranging from 1 to 5.4) and high enthalpies. The implications of each change on the flow conditions have been assessed by looking at flow statistics, turbulent kinetic energy budget, coherent structures and their influence on the validity of the standard and modified SRA relations. An extension of the analysis on the effect of Mach number (2.5 to 20) has been provided by Lagha et al. [24], with the objective to address the variations on turbulence statistics and near-wall turbulence structures. Another relevant study at very high Mach numbers with strong wall-cooling has been recently presented by Huang et al. [20]. The effect of wall temperature has also been investigated in two separate studies by Xu et al. [63] and Xu et al. [64], who employed the Helmholtz decomposition first to characterize the variations on velocity and thermal statistics of a turbulent boundary layer at Mach 8 and then to study the implications on the kinetic energy transfer for different Mach numbers and wall temperature ratios. Zhang et al. [65] carried out an extensive study analysing boundary layers with nominal free-stream Mach number ranging from 2.5 to 14 with different wall temperature conditions, representative of the operational conditions of different hypersonic wind tunnels. A recent comprehensive study

on the effect of spatial evolution and Reynolds number has been performed by Huang et al. [21], considering a wide range of Mach numbers (from 2 to 11) with different amounts of wall cooling. At present, there is a lack of experimental and numerical studies corresponding to hypersonic diabatic turbulent boundary layers at moderate/high Reynolds number, which would be helpful to enrich our knowledge of compressible wall-bounded turbulence and to understand how the flow organization is affected by the combined variation of Mach number, Reynolds number and wall cooling. In this study, we thus present novel DNS data to investigate the behaviour and the structure of isothermal supersonic (Mach 2) and hypersonic (Mach 6) zero-pressure gradient turbulent boundary layers at moderate/high friction Reynolds numbers up to $Re_\tau \approx 2000$. First, we present instantaneous visualizations of the velocity and temperature fields, discussing the main differences between the two Mach numbers and with respect to supersonic adiabatic turbulent boundary layers reported in literature. Then we focus on the existence in the boundary layer of large regions of uniform streamwise momentum, known in literature as uniform momentum zones [29]. We discuss the influence of compressibility on the properties of such zones and, for the first time, we document the existence of similar regions for the temperature field. Then, first and second order statistics for the velocity and thermodynamic variables are presented and discussed to highlight the influence of the various parameters. The final part of the study is dedicated to the analysis of the lenghtscales of typical outer layer eddies, which are identified using power spectral densities of both the velocity and temperature fluctuations in the spanwise direction.

Computational setup and numerical database

The physical model is based on the three-dimensional compressible Navier-Stokes equations for a viscous, heat conducting gas

$$\begin{aligned} \frac{\partial \rho}{\partial t} + \frac{\partial(\rho u_j)}{\partial x_j} &= 0, \\ \frac{\partial(\rho u_i)}{\partial t} + \frac{\partial(\rho u_i u_j)}{\partial x_j} + \frac{\partial p}{\partial x_i} - \frac{\partial \sigma_{ij}}{\partial x_j} &= 0, \\ \frac{\partial(\rho E)}{\partial t} + \frac{\partial(\rho Eu_j + pu_j)}{\partial x_j} - \frac{\partial(\sigma_{ij} u_i - q_j)}{\partial x_j} &= 0, \end{aligned} \quad (1)$$

where ρ is the density, u_i denotes the velocity component in the i th Cartesian direction ($i = 1, 2, 3$), p is the thermodynamic pressure, $E = c_v T + u_i u_i / 2$ the total energy per unit mass and

$$\sigma_{ij} = \mu \left(\frac{\partial u_i}{\partial x_j} + \frac{\partial u_j}{\partial x_i} - \frac{2}{3} \frac{\partial u_k}{\partial x_k} \delta_{ij} \right), \quad q_j = -k \frac{\partial T}{\partial x_j} \quad (2)$$

represent the viscous stress tensor and the heat flux vector, respectively. The molecular viscosity μ is assumed to follow the Sutherland's law

$$\frac{\mu}{\mu_\infty} = \left(\frac{T}{T_\infty} \right)^{1/2} \frac{1 + C/T_\infty}{1 + C/T}, \quad (3)$$

where $C = 110.4$ K, $T_\infty = 100.0$ K and $\mu_\infty = 6.929 \cdot 10^{-6} kg/(m \cdot s)$. The thermal conductivity k is related to the viscosity by the expression $k = c_p \mu / Pr$, where c_p is the specific heat

at constant pressure and the Prandtl number is $Pr = 0.72$. Since the temperature field ranges between 100K to 540K for the hypersonic case, minor deviations from constant specific heat assumption are expected [2]. Therefore, we assume all cases to fall within the perfect gas regime. The investigation of high-enthalpy effects that involve the implementation of a chemically reacting model can be found in other studies, e.g. Passiatore et al. [34], [33] and Di Renzo and Urzay [12]. The equations are discretised on a Cartesian grid and solved using the in-house code STREAMS [5], a high-fidelity solver targeted to canonical wall-bounded turbulent flows, freely available at <https://github.com/matteobernardini/STREAMS>. The code has been widely employed in the past to investigate supersonic wall-bounded turbulence, considering several canonical configurations, that include zero-pressure-gradient boundary layers, shock-wave boundary layers interactions, channel and pipe flows [4, 38]. The most recent solver version has been ported to multi-GPUs architectures through the CUDA Fortran paradigm. One of the key features of the code is the availability of consolidated, high-order, energy-preserving schemes, applied in shock-free flow regions, that allow an efficient, accurate and stable discretization of the convective terms of the Navier-Stokes equations, free of numerical dissipation. A high-order shock capturing method (WENO scheme) is instead locally applied in shocked flow regions, identified by means of the Ducros shock sensor [17]. In the current version, a locally conservative formulation is also used for the viscous terms [11], expanded to Laplacian for ensuring finite molecular dissipation at all resolved wavelengths.

In this work we present results obtained from DNS of diabatic turbulent boundary layers spanning a relatively large range of Mach and Reynolds numbers. The flow conditions of the simulations conducted are reported in table 1, where relevant computational parameters are also reported. Two hypersonic cases at Mach 5.86 are considered: the first at low friction Reynolds number, matching the M6Tw076 case of Zhang et al. [65], the second increasing Re_τ up to 2000. Two additional simulations at the same friction Reynolds numbers are also carried out in the supersonic regime ($M_\infty = 2$) to enable a more comprehensive understanding of the effect of flow compressibility. Differently from our previous studies [37], focused on adiabatic wall conditions, we here consider the case of cold walls, setting the wall-to-recovery temperature ratio $T_w/T_r = 0.76$, being

$$T_r = T_\infty \left(1 + r \frac{\gamma - 1}{2} M_\infty^2 \right), \quad (4)$$

where $r = 0.89$ is the recovery factor. This value satisfies the typical choice of $r = Pr^{1/3}$, which is generally accepted for turbulent boundary layers, and is consistent with the setup of Zhang et al. [65]. Although the ratio T_w/T_r is matched for different Mach cases, it is worth highlighting that this choice corresponds to different values of the Eckert number, $Ec = (\gamma - 1)M_\infty^2 T_\infty / (T_r - T_w)$, that are reported in Table 1. The recent study by Wenzel et al. [60] has highlighted the relevance of this parameter in quantifying the combined effects of both Mach number and wall temperature on the boundary layer.

The boundary layer is simulated in a rectangular box with spanwise periodic boundary conditions, purely non-reflecting boundary conditions for the outflow and the top boundary, and unsteady characteristic boundary conditions at the bottom wall, where isothermal wall temperature is enforced. The fully developed turbulent state is reached by means of a recycling-rescaling procedure [41], and the recycling length is placed at a distance of $80 \delta_{in}$ from the inlet, δ_{in} being the boundary layer thickness (based on the 99% of the external velocity u_∞) at the inflow station. This

| Run | M_∞ | Re_τ | T_w/T_r | Ec | Δx^+ | Δy_{min}^+ | Δy_{max}^+ | Δz^+ | N_x | N_y | N_z | δ_{max}/δ_{in} |
|-----------|------------|-------------|-----------|-----|--------------|--------------------|--------------------|--------------|-------|-------|-------|----------------------------|
| M2Tw076/1 | 2.00 | 340–620 | 0.76 | 3.9 | 6.1 | 0.5 | 4.2 | 3.9 | 4096 | 320 | 512 | 2.9 |
| M2Tw076/2 | 2.00 | 1240 – 2300 | 0.76 | 3.9 | 7.9 | 0.7 | 6.5 | 4.8 | 16384 | 832 | 2048 | 2.6 |
| M6Tw076/1 | 5.86 | 290–520 | 0.76 | 8.0 | 6.1 | 0.5 | 6.2 | 3.9 | 4096 | 320 | 512 | 2.6 |
| M6Tw076/2 | 5.86 | 1080 – 1953 | 0.76 | 8.0 | 7.5 | 0.7 | 6.2 | 4.6 | 16384 | 832 | 2048 | 2.4 |

Table 1: Summary of parameters for DNS study. Grid spacings are given in wall-units according to the stations selected in table 2. The values of Δy_{min}^+ and Δy_{max}^+ refer to the wall-normal spacing at the wall and at the boundary layer edge, respectively. $Ec = (\gamma - 1)M_\infty^2 T_\infty / (T_r - T_w)$ is the Eckert number and δ_{max}/δ_{in} is the ratio between the maximum and inflow boundary layer thickness.

| Station | Run | Re_τ | Re_θ | Re_{δ_2} | Re_τ^* | $C_f \cdot 10^3$ | δ^*/δ | $\theta/\delta \cdot 10^2$ | H | $-B_q$ |
|---------|-----------|-----------|-------------|-----------------|-------------|------------------|-------------------|----------------------------|------|--------|
| M2L | M2Tw076/1 | 453 | 1423 | 1114 | 654 | 3.254 | 0.22 | 8.9 | 2.44 | 0.016 |
| M2H | M2Tw076/2 | 1947 | 7562 | 5916 | 3504 | 2.159 | 0.21 | 9.0 | 2.34 | 0.019 |
| M6L | M6Tw076/1 | 453 | 5632 | 1581 | 2815 | 1.009 | 0.43 | 3.2 | 10.9 | 0.013 |
| M6H | M6Tw076/2 | 1947 | 29349 | 8375 | 14709 | 0.6775 | 0.42 | 4.0 | 10.5 | 0.014 |

Table 2: Boundary layer properties at the selected stations. $Re_\tau = \bar{\rho}_w u_\tau \delta / \bar{\mu}_w$; $Re_\theta = \rho_\infty u_\infty \theta / \mu_\infty$; $Re_{\delta_2} = \rho_\infty u_\infty \theta / \bar{\mu}_w$; $Re_\tau^* = \sqrt{\rho_\infty \tau_w} \delta / \mu_\infty$; $H = \delta^*/\theta$ (δ^* and θ are the boundary layer displacement and momentum thickness, respectively). $B_q = q_w / (\rho_w C_p u_\tau T_w)$ is the dimensionless wall heat transfer rate.

distance is long enough to achieve a complete decorrelation of the fluctuations between the recycling station and the inflow plane [31]. The overall size of the computational domain of low Reynolds number cases is: $L_x = 100 \delta_{in}$, $L_y = 30 \delta_{in}$, $L_z = 8 \delta_{in}$, while for the high Reynolds $L_x = 120 \delta_{in}$, $L_y = 30 \delta_{in}$, $L_z = 9.2 \delta_{in}$. Table 1 summarizes the flow conditions and grid resolutions for each run, where M_∞ is the free-stream Mach number and Re_τ is the friction Reynolds number, defined as the ratio between the boundary layer thickness (δ) and the viscous length scale $\delta_\nu = \bar{\nu}_w / u_\tau$, where $u_\tau = \sqrt{\tau_w / \bar{\rho}_w}$ is the friction velocity, τ_w is the mean wall shear stress, and ν_w is the kinematic viscosity at the wall. N_x , N_y and N_z are the number of computational points employed for each spatial direction, Δx^+ and Δz^+ the uniform grid spacings in the streamwise and spanwise directions and Δy^+ represents the non-uniform wall-normal grid spacing (the minimum and maximum values are reported). For the wall-normal direction, a newly developed stretching function described in Pirozzoli and Orlandi [40] is employed, which provides a more favourable scaling of the number of grid points with the Reynolds number and has the natural property of yielding precisely constant resolution in terms of the local Kolmogorov length scale η in the outer part of the wall layer while maintaining a uniform near-wall spacing. Moreover, the effective mesh spacing $\Delta = (\Delta x \cdot \Delta y \cdot \Delta z)^{1/3}$ is always smaller than 4η , indicating that all the scales of turbulent motion are adequately resolved in the present computations. Simulations were carried out for a total period of $200\delta_{in}/u_\infty$, collecting statistics with a sampling frequency of $0.1\delta_{in}/u_\infty$, being u_∞ the freestream velocity.

In our discussion, we use the symbols u , v and w to denote the streamwise, wall-normal and spanwise velocity components and the decomposition of any variable is conducted using either the standard Reynolds decomposition ($f = \bar{f} + f'$) or the density-weighted (Favre) representation ($f = \tilde{f} + f''$), being $\tilde{f} = \bar{\rho}f/\bar{\rho}$. Actually, the Favre decomposition is generally preferred since we are dealing with highly compressible flows, but the observed Mach and Reynolds number effects are also apparent using Reynolds averages displaying only minor deviations. Table 2 summarizes the boundary-layer parameters at selected locations where the turbulence statics are gathered.

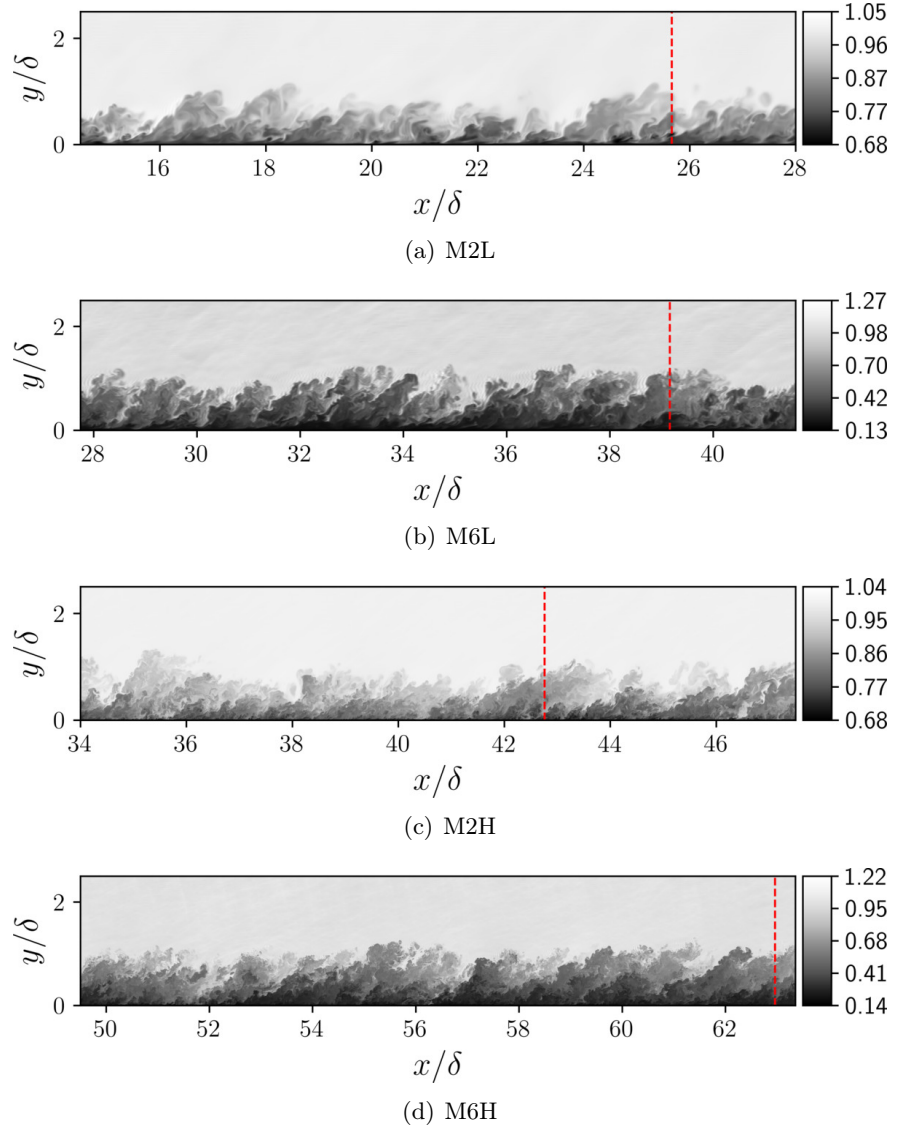


Figure 1: Contours of the instantaneous density field (ρ/ρ_∞) in a streamwise wall-normal plane for flow cases in table 1. The selected locations for this study are marked with vertical dashed lines in red.

Flow organization

Instantaneous visualization

We start providing an overview of the flow organization for the four cases here investigated by showing instantaneous density contours in a longitudinal plane in figure 1. For reference purposes, vertical lines are reported to mark the locations selected for the statistical analysis, which correspond to Reynolds numbers listed in table 2. The contours reveal the typical organization already found in low-speed and supersonic turbulent boundary layers ([47], [16]), dominated by large-scale bulges inclined at approximately 45° , separating irrotational fluid from the inner rotational motion. A greater number of fine-scale features can be observed in the high-Reynolds number cases, superimposed to a large-scale arrangement consisting of an array of rather uniform low-density bulges separated from a higher density freestream by a sharp interface. This scenario is shared by flow cases at $M = 2$ and $M = 6$, suggesting a relatively minor effect of the Mach number. Figures 2, 3 show

contours of the instantaneous velocity and temperature fluctuations for the high-Reynolds cases in wall-parallel slices taken at two different locations, representative of both the inner ($y^+ = 15$) and outer region ($y/\delta = 0.2$) at the selected stations. At this friction Reynolds number, a clear scale separation is found between the turbulent eddies of the near wall region and the outer-layer motions. In particular, consistently with previous findings for adiabatic supersonic boundary layers [3], a distinctive feature of the flow cases here analysed is the presence of large scale structures, characterized by streamwise lenghtscales of order 10δ , which are usually referred in literature as superstructures [28]. The signature of these large-scale eddies is well apparent in the outer portion of the boundary layer for both the velocity and temperature fluctuations, with an evident correlation between low-/high-speed momentum regions and high/low temperature streaks. A footprint of the outer layer structures can be observed in the near-wall region, where the small-scale velocity and temperature streaks typical of the near wall-cycle of turbulence are superposed to the large-scale organization inherited by the overlying motions. However, differently from previous observations for adiabatic walls [3], the similarity between thermal and velocity streaks in the near wall-region of the present cold flow cases is less evident, particularly at Mach 2, where the distribution of temperature fluctuations appears more isotropic than that of the velocity field. In particular, while velocity streaks are clearly visible, temperature streaks are difficult to be detected in the near wall region at $M = 2$. This observation suggests that, despite the fixed value of T_w/T_r for all flow configurations, the present supersonic flow cases are actually characterized by a greater importance of wall cooling. We note that, according to the discussion reported in Wenzel et al. [60], this behaviour is consistent with the smaller value of the Eckert number characterizing the flow cases at Mach 2. As it will be discussed in the following sections, the different organization of the near-wall temperature field between supersonic and hypersonic cases is reflected by a distinctive shape of the temperature fluctuations variance and spectra. For completeness, wall-parallel slices close to the edge of the boundary layer ($y/\delta = 0.9$ at the selected station) are also shown in figure 4. In this case, structural differences associated to the flow compressibility are not observed. Contours of both streamwise velocity and static temperature appear rather isotropic and reveal the existence of large, uniform regions of quiescent, cold free-stream fluid interspersed in the boundary layer. A clear association between high temperature turbulent regions of mushroom shape with low momentum zones is still visible at this height at both Mach numbers.

Uniform momentum zones

Recent analyses have shown that instantaneous fields exhibit a peculiar property in a confined region of a turbulent boundary layer: uniform momentum zones. This property has been examined by several authors in the context of incompressible flows (Meinhart and Adrian [29], Adrian et al. [1], De Silva et al. [10], Laskari et al. [25]), and only recently for hypersonic flows, although limited to low Reynolds numbers [62]. A uniform zone of a given quantity is defined as a region in the x-y plane with small variations along the wall normal direction, implying the presence of local peaks in the histogram that collects all the sampled values of such quantity. The minima of these histograms, the least probable values, represent the local boundary between one zone and the other and are characterized by sharp gradients of the analysed quantity, in contrast to the generally uniform distribution between them [10]. The presence of these zones have been attributed to hierarchical distribution of coherent structures within the boundary layer [10]. The existence of

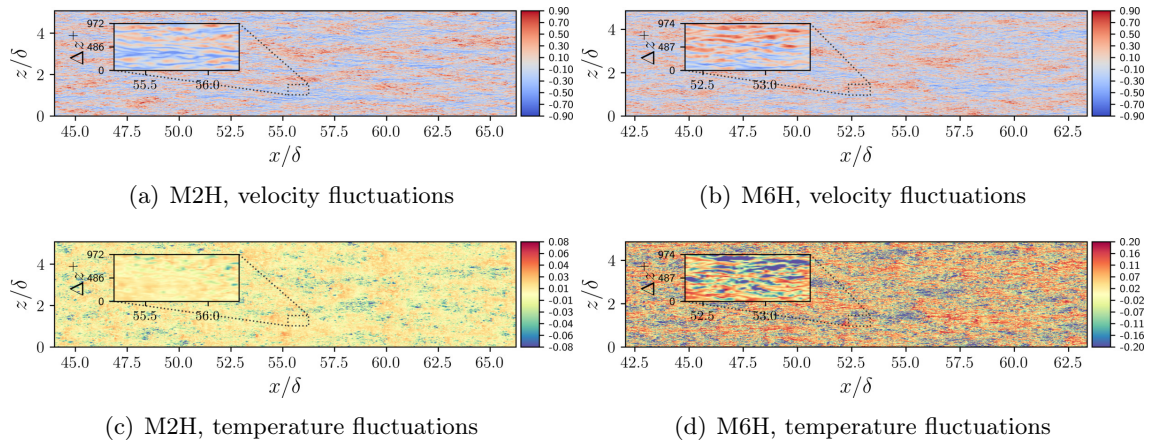


Figure 2: Visualization of velocity and temperature fluctuations in a wall-parallel slice at $y^+ = 15$. Velocity and temperature fluctuations are scaled with the mean velocity \bar{u} and mean temperature \bar{T} , respectively.

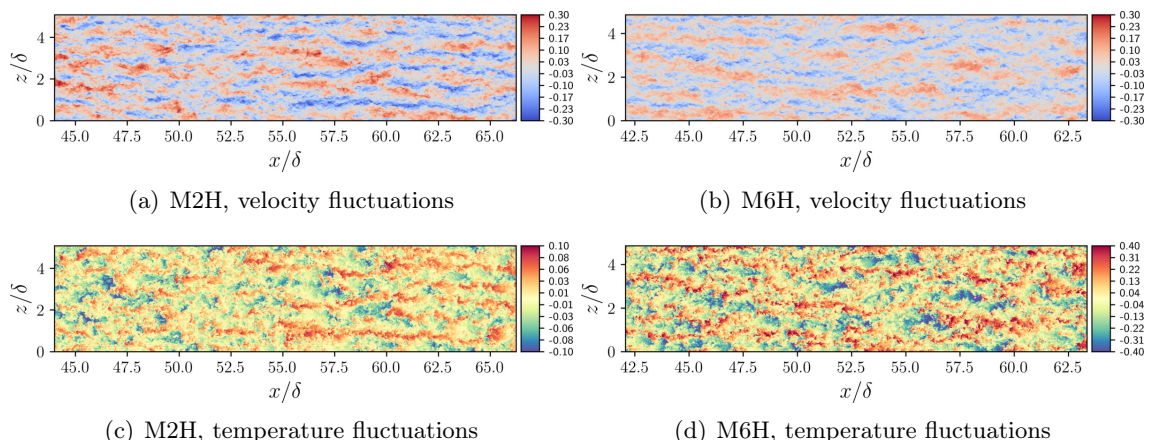


Figure 3: Visualization of velocity and temperature fluctuations in a wall-parallel slice at $y/\delta = 0.2$. Velocity and temperature fluctuations are scaled with the mean velocity \bar{u} and mean temperature \bar{T} , respectively.

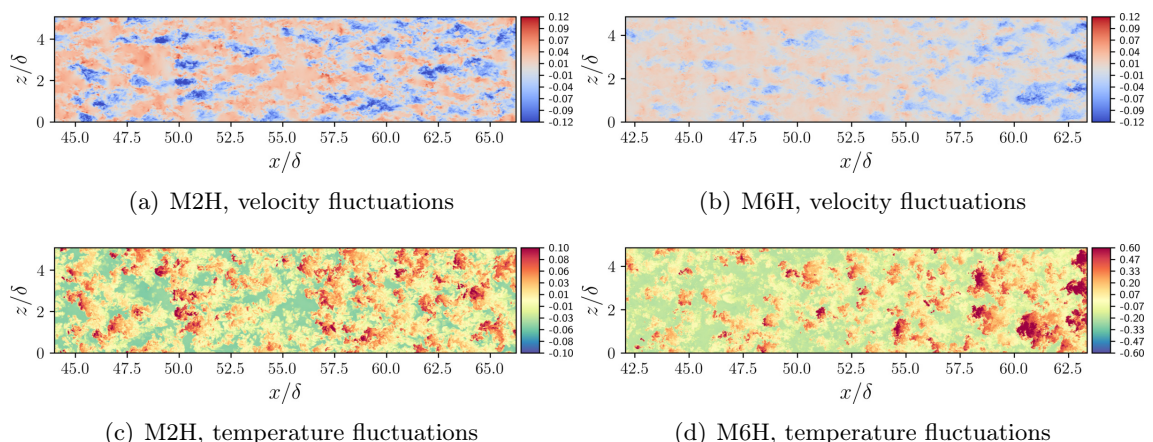


Figure 4: Visualization of velocity and temperature fluctuations in a wall-parallel slice at $y/\delta = 0.9$. Velocity and temperature fluctuations are scaled with the mean velocity \bar{u} and mean temperature \bar{T} , respectively.

these structures and their distribution along the boundary layer at different Re_τ is closely related to the fundamental hypothesis of the attached eddy model [27], which has been shown to reproduce

flow statistics for wall-bounded turbulent flows [35] and to generate synthetic instantaneous velocity fields [10]. Previous investigations focused on the analysis of the streamwise velocity, showing that uniform zones are present even at high Mach numbers [61]. Here, mining our high-Reynolds number database we confirm the presence of uniform zones of streamwise velocity and extend the analysis to the temperature field, for which a similar organization has never been documented. We also quantify the mean number of uniform zones \bar{N}_{UZ} for both velocity and temperature fields in order to gauge the effect of the Mach number. This analysis is conducted at the highest Reynolds number in the present database, given the wider range of scales of turbulent motions which can be directly associated to the presence of uniform zones, particularly in the logarithmic region. Following the set-up of De Silva et al. [10], the extracted instantaneous fields span roughly 2000 viscous units in the streamwise direction (which corresponds to a boundary layer length δ) and extends through the whole boundary layer thickness in the wall normal direction. To quantify the mean number of uniform zones for streamwise velocity and temperature, a total of 84 xy planes were sampled well-separated in the spanwise direction (more than 1 δ) and in time (more than $2\delta_{in}/u_\infty$). The selected quantity is then sampled at every point of the slice, except for the region outside the boundary layer. The latter condition requires a precise detection of the turbulent/non-turbulent interface (TNTI), that is not trivial, especially for compressible flows. Previous studies used a threshold in the kinetic energy defect [9] which produces inappropriate results in present highly compressible cases, since it does not consider the significant density fluctuations at the edge of the boundary layer. Therefore, we apply here a modified expression to detect the TNTI that involves the square of momentum defect in the streamwise and wall-normal direction, setting

$$M_{def} = \frac{(\rho U - \rho_\infty U_\infty)^2 + (\rho V - \rho_\infty V_\infty)^2}{(\rho_\infty U_\infty)^2} = 0.001. \quad (5)$$

As for previous conditions, this expression vanishes when the flow becomes non-turbulent ($\rho U \rightarrow \rho_\infty U_\infty$ and $\rho V \rightarrow \rho_\infty V_\infty = 0$) and increases its value progressively towards the wall ($M_{def} = 1$). The fundamental difference is in the inclusion of the density inside the velocity defect, which better accounts for its contribution in the boundary layer edge. Its performances can be observed in figure 5 showing the iso-level $M_{def} = 0.001$ (black line) on top of vorticity contours for both supersonic and hypersonic cases as a visual indicator of the turbulent region. A sensitivity study has been conducted on the threshold value showing minor deviations from the present contours for both flow cases. Further confirmation is given by figures 6 and 7 in which Eq. (5) correctly represents the boundary between the fluctuating field inside the boundary layer and the freestream for both U and T . Figures 6 and 7 collect histograms and contours for cases M2H and M6H of the computed uniform zones for the velocity and temperature field. Similarly to the procedure of Laskari et al. [25], each histogram has been computed with a bin width of $0.5u_\tau$ and the relative peak-finding algorithm considers a set of thresholds necessary to uniquely determine the number of uniform zones (UZ). In particular, considering the maximum height of the histogram, h_{max} , we employed a minimum height threshold for a peak detection of $0.025h_{max}$ and a limit on prominences of $0.1h_{max}$. Although the latter condition showed a non-negligible sensitivity on the predicted number of zones N_{UZ} (as noted by Laskari et al. [25]), the trends, that are discussed below, are stable since the threshold values do not affect the relative variation of the detected average uniform zones number. We therefore chose a parameter set that matches the average number of zones of De Silva

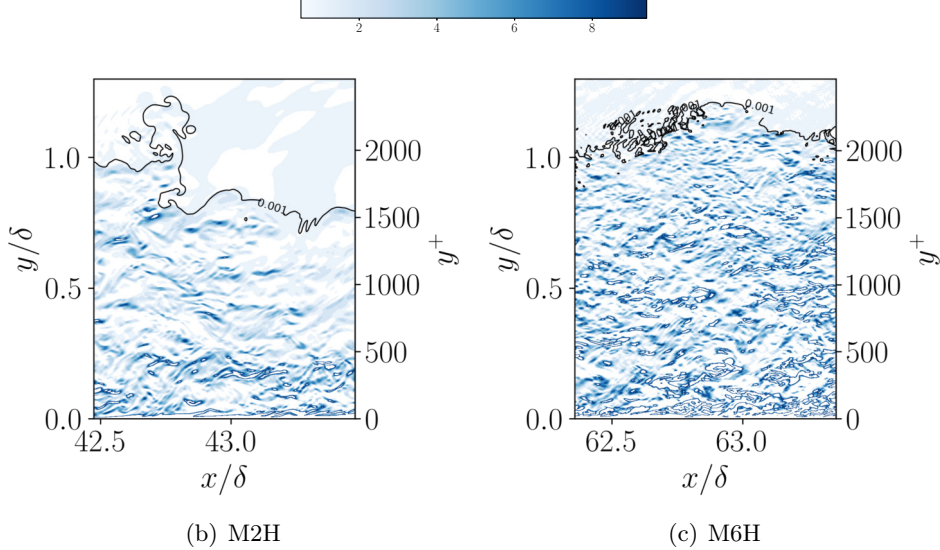


Figure 5: Contours of vorticity for case M2H (a) and M6H (b) represented with colours in the range [0-10]. The black line represents the TNTI defined with condition (5).

et al. [10] for the case M2H on streamwise velocity, and we discuss the relative changes with the Mach number. In each histogram the local maxima values, which indicate the presence of a UZ in each xy slice of the represented quantity, have been highlighted. The peak finding algorithm also automatically outputs the minima associated to the selected peaks, which are used to draw the isolines that separate one UZ from another. Figures 6 and 7 clearly reveal the existence of uniform zones for both U and T , thus suggesting that, even in the hypersonic regime, the hypothesized turbulent structures responsible for such zonal arrangement in low speed flows [1] are important in determining the flow organization of both the streamwise momentum and static temperature. After averaging multiple flow samples, we find a mean number of uniform zones for velocity of 3.6 for case M2H and 2.5 for case M6H. For the temperature, these values become 5.9 for case M2H and 4.9 for case M6H. From the computed values, we observe that the mean number of temperature zones is always greater than what found for velocity (there is a factor of roughly 1.6 for the case M2H and of 2 for the case M6H), and that the hypersonic case exhibits a lower average number of zones for both quantities. We attribute these effects to the combined influence of the non-unit Prandtl number and diabatic wall, which decreases the degree of (anti)-correlation between velocity and temperature fluctuations. The zonal-arrangement found for the temperature field supports the considerations of Pirozzoli and Bernardini [39], who concluded that this quantity can be considered an *attached variable*, similarly to the behaviour of streamwise velocity. However, higher Reynolds numbers cases spanning more than one order of magnitude are needed to confirm that the average number of zones follows a logarithmic distribution. It is also worth pointing out that we do not find a clear indication of uniform zones for the total temperature, being its fluctuations homogeneously distributed especially in the outer part of the boundary layer (not shown).

Mean flow statistics

In this section, several compressibility transformations and temperature-velocity relations are tested using the present DNS database. The scope of the former is to account for compressibility effects

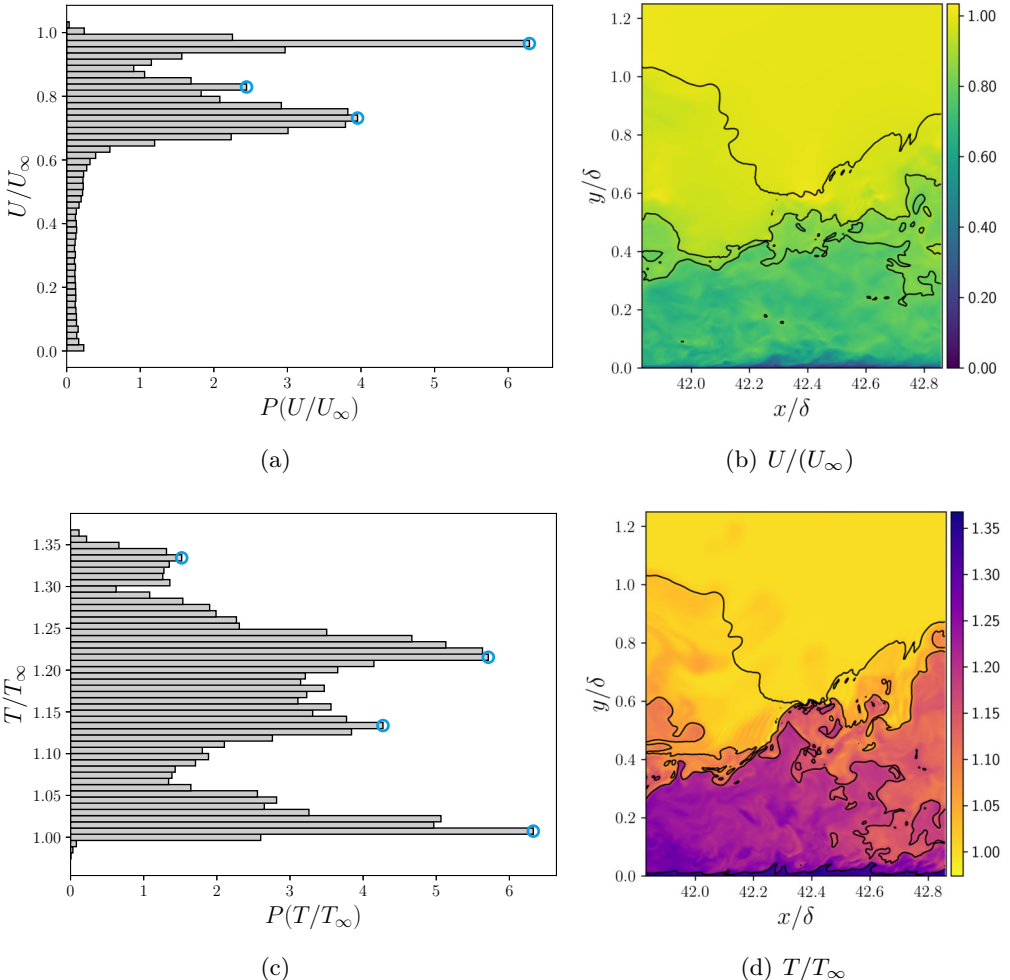


Figure 6: Uniform momentum zones of U and T in an instantaneous field for the case M2H. The left column shows the computed histograms of the quantity in the selected xy plane, with the associated maxima that indicate the presence of a UZ (blue circles). The right column shows the contours highlighting the boundary between each uniform zone and the instantaneous TNTI.

in wall-bounded flow statistics in order to recover the incompressible behaviour. The latter theoretical laws aim at predicting the relation between the mean temperature and velocity profile in compressible flows. Concerning the mean velocity, we first consider the classical velocity scaling proposed by Van Driest [54] and that recently introduced by Trettel and Larsson [52]. While the former represents a density-weighted re-scaling of the mean velocity profile, the latter is grounded on the log-layer scaling and near-wall momentum conservation to provide a transformation which is primarily tuned on turbulent channel flows with cooled walls. We further consider the recent scaling laws proposed by Volpiani et al. [57] and Griffin et al. [19], where the former takes advantage of a data-driven approach, while the latter is based on the total stress equation using different sets of hypotheses for the viscous and turbulent stress parts. According to Modesti and Pirozzoli [30], all the above transformations (except Griffin et al. [19]) can be expressed in terms of mapping functions f_I and g_I for wall distance y_I and mean velocity u_I , denoting the equivalent incompressible distributions obtained from the transformation I :

$$y_I = \int_0^y f_I dy, \quad u_I = \int_0^{\tilde{u}} g_I d\tilde{u}. \quad (6)$$

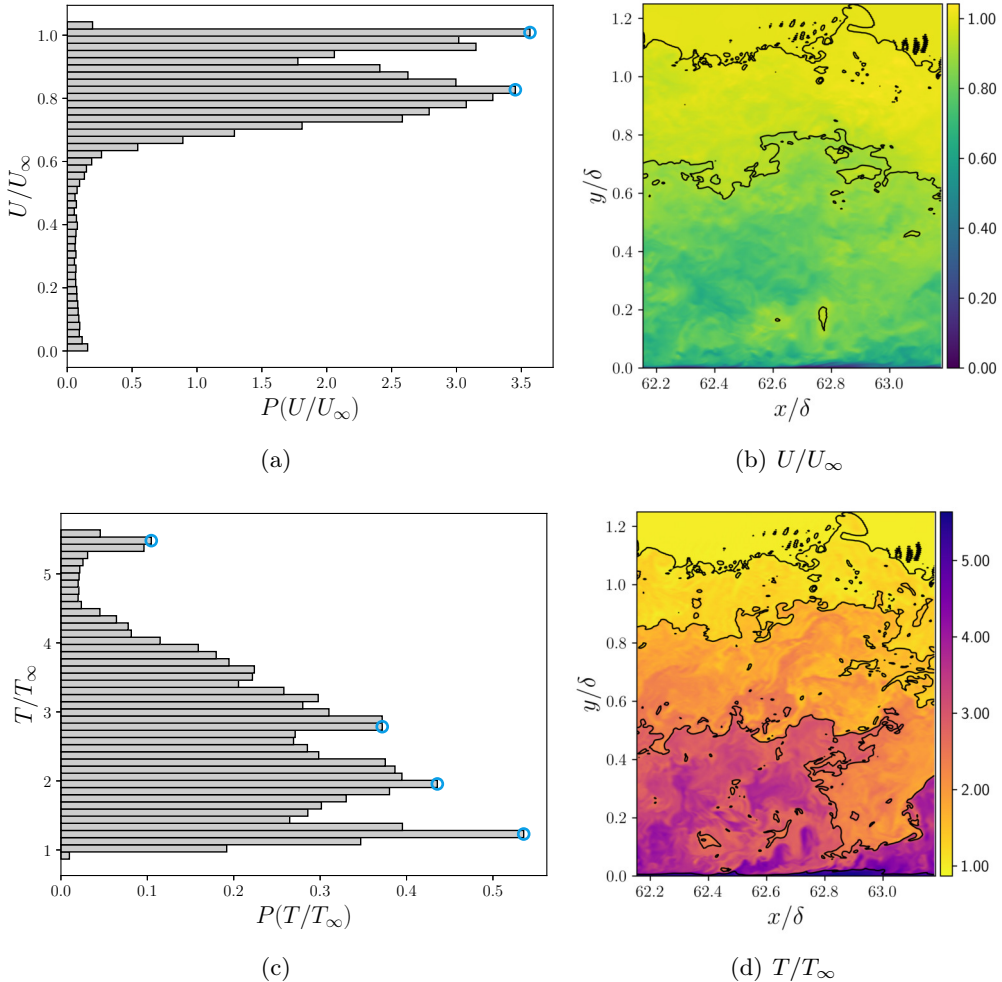


Figure 7: Uniform momentum zones of U and T in an instantaneous field for the case M6H. The left column shows the computed histograms of the quantity in the selected xy plane, with the associated maxima that indicate the presence of a UZ (blue circles). The right column shows the contours highlighting the boundary between each uniform zone and the instantaneous TNTI.

Using this convenient formulation, the aforementioned transformations are presented in table 3, where $R = \bar{\rho}/\bar{\rho}_w$ and $M = \bar{\mu}/\bar{\mu}_w$. As mentioned above, the transformation of Griffin et al. [19] is based on the total stress equation, written in terms of a generalized nondimensional mean shear $S_t^+ = \partial U_t^+ / \partial y^*$, where the subscript t means total and the superscripts + and * indicate inner and semilocal scaled variables, respectively. The latter are defined as $y^* = y/\delta_\nu^*$, where $\delta_\nu^* = \bar{\mu}/(\bar{\rho} u_\tau^*)$ and $u_\tau^* = \sqrt{\tau_w/\bar{\rho}}$. The equation reads as:

$$\tau^+ = S_t^+ \left(\frac{\tau_v^+}{S_{TL}^+} + \frac{\tau_R^+}{S_{eq}^+} \right) \quad (7)$$

where τ_v^+ and τ_R^+ are the scaled viscous and Reynolds shear stresses (whose sum is equal to τ^+), while $S_{TL}^+ = \partial U_{TL}^+ / \partial y^*$ and $S_{eq}^+ = \partial U_{eq}^+ / \partial y^*$ are the generalized nondimensional mean shear stresses derived for the viscous region (the subscript “ TL ” indicated the accordance with the Trettel and Larsson velocity transformation) and for the log layer (the subscript “ eq ” indicates the assumption of turbulence quasi-equilibrium).

Figure 8 shows the transformed mean velocity profiles u_{VD}^+ , u_{TL}^+ , u_{VI}^+ and u_{GR}^+ for each case in

| Transformation | Wall distance (f_I) | Mean velocity (g_I) |
|---------------------|---|---|
| Van Driest | $f_{VD} = 1$ | $g_{VD} = R^{1/2}$ |
| Trettel and Larsson | $f_{TL} = \frac{d}{dy} \left(\frac{yR^{1/2}}{M} \right)$ | $g_{TL} = M \frac{d}{dy} \left(\frac{yR^{1/2}}{M} \right)$ |
| Volpiani et al. | $f_{VI} = \frac{R^{1/2}}{M^{3/2}}$ | $g_{VI} = \frac{R^{1/2}}{M^{1/2}}$ |

Table 3: Compressibility transformations for wall distance and mean velocity according to Eq. (6), where $R = \bar{\rho}/\bar{\rho}_w$ and $M = \bar{\mu}/\bar{\mu}_w$.

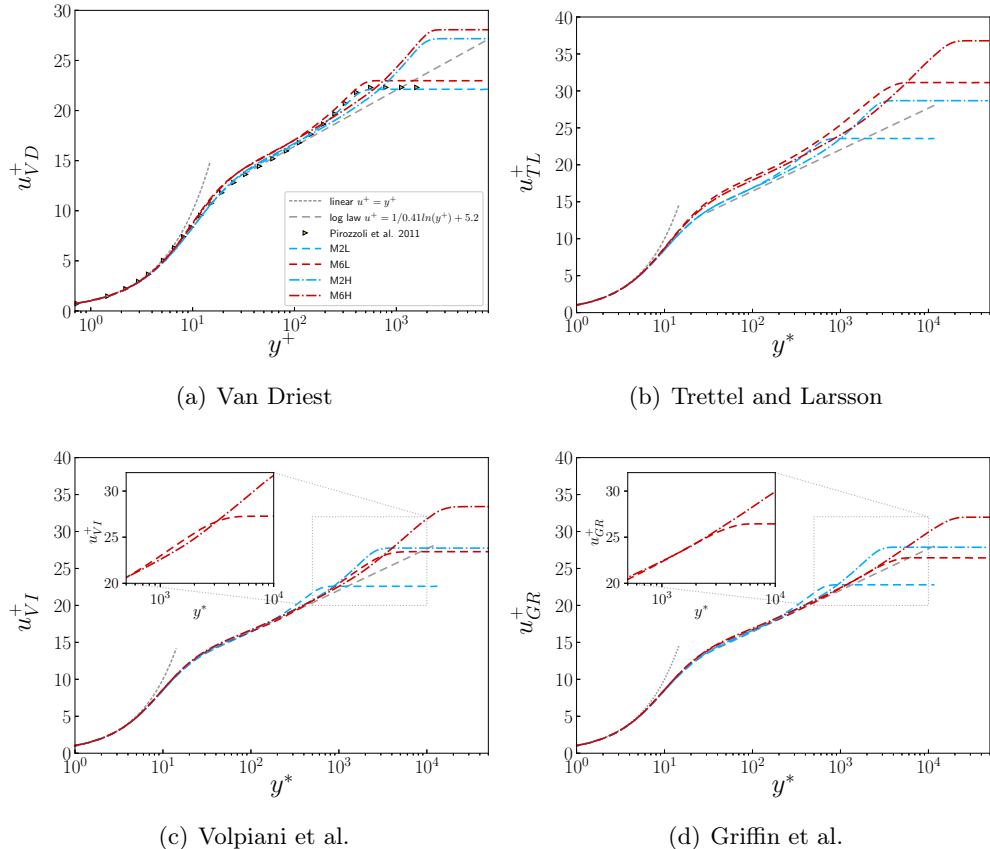


Figure 8: Mean velocity profiles at stations listed in table 2 scaled according to various compressibility transformations. The results are compared with the linear law $u^+ = y^+$ and the log law $u^+ = 1/0.41\ln(y^+) + 5.2$. Transformed velocity profiles according to Van Driest [54] are compared to the supersonic adiabatic case of Pirozzoli and Bernardini [39] at $M = 2$ and $Re_\tau = 450$.

order to assess the ability in collapsing compressible mean velocity profiles on the incompressible law-of-the-wall. The mean velocity profiles scaled using the various transformations well conform with the linear behaviour of the viscous sub-layer ($y^+ < 5$) for the chosen wall-temperature conditions. Previous studies [14] observed a decrease of the Van Driest transformed mean slope with the increase of the cooling rate, but higher values of wall heat transfer B_q were considered. Concerning the buffer and log-layer, both the Van Driest and Trettel and Larsson (TL) transformations are less accurate in collapsing the velocity profiles onto the log-law distribution, yielding to a mismatch of the additive constant that is particularly evident for hypersonic flow cases and the TL formula. Similar findings have been reported at lower Reynolds numbers by Zhang et al. [65], who suggested this discrepancy might be due to the influence of the wake component on the log region, and by [19],

who showed that the TL transformation should only be valid in the viscous layer. In this regard, the fundamental assumptions of the Van Driest transformation are strictly applicable to adiabatic walls, and even in this case some authors reported its inaccuracy in collapsing profiles in the wake region for different Mach numbers (e.g. Duan et al. [15], Wenzel et al. [59]). However, we note that the case M2L appears well agree with the adiabatic counterpart of Pirozzoli and Bernardini [39]. Looking at the performance of the two most recent transformations, an excellent collapse through the whole boundary layer can be observed for both VI and GR for all cases of present database, which demonstrates the capability of both approaches in accounting of compressibility effect in a relatively wide range of Mach and Reynolds numbers. The only difference is detected in the wake region, where the GR transformation appears more efficient at collapsing the two high Mach numbers, independently of Re_τ (see insets of figure 8). Being the accuracy of the two scaling laws comparable, the present database cannot assess which of the two proposals gives better results for the present conditions. We also remark that the proposed transformation of Griffin et al. (2021) excellently behaves even using the constant-stress-layer assumption ($\tau^+ \approx 1$), with deviations not exceeding the 0.3% from the standard one.

Figure 9 shows the profiles of mean total and static temperature as a function of y/δ . The latter is also plotted in wall units in the inset of the figure, to highlight the profile behaviour in the near-wall region ($y^+ < 25$). It can be observed the presence of a temperature peak close to the wall ($y^+ \approx 5$) due to aerodynamic heating, that is more prominent and closer to the wall at high Mach number. The flatter mean temperature profile in the near-wall region at $M = 2$ that is caused by the combination of the lower Mach number and the wall diabatic condition is consistent with the weaker temperature fluctuations observed in the discussion of figure 4 and in the following section §Thermodynamic quantities. The total temperature displays an overshoot in the outer portion of the boundary layer that is larger at Mach 6, and apparently independent of the Reynolds number. Panels (c) and (d) display the mean temperature as a function of the mean velocity for all flow cases here investigated. Since the pioneering work of Reynolds [44], several studies attempted to find a theoretical relationship between mean temperature and velocity fields, adjusting the general quadratic dependence to account for deviations of Prandtl number from unity and finite heat fluxes. The classical relationship of Walz [58] has showed to behave well in adiabatic turbulent boundary layers, while decreasing its performances as wall cooling increases [14]. Duan and Martin [13] tackled this problem by proposing an empirical relation accounting for finite wall flux, that was later generalized by the work of Zhang (2014). Here, DNS results are compared with the classical relation of Walz [58]

$$\frac{\bar{T}}{T_\infty} = \frac{T_w}{T_\infty} + \frac{T_r - T_w}{T_\infty} \frac{\bar{u}}{U_\infty} + \frac{T_\infty - T_r}{T_\infty} \left(\frac{\bar{u}}{U_\infty} \right)^2 \quad (8)$$

and the modified relation of Zhang et al. [67] which explicitly accounts for the finite wall heat flux:

$$\frac{\bar{T}}{T_\infty} = \frac{T_w}{T_\infty} + \frac{T_{rg} - T_w}{T_\infty} \frac{\bar{u}}{U_\infty} + \frac{T_\infty - T_{rg}}{T_\infty} \left(\frac{\bar{u}}{U_\infty} \right)^2 \quad (9)$$

where $T_{rg} = T_\infty + r_g U_\infty^2 / (2c_p)$ and $r_g = 2c_p(T_w - T_\infty)/U_\infty^2 - 2Pr q_w/(U_\infty \tau_w)$. Figure 9 reveals that the modified version proposed by Zhang et al. [67] yields more accurate results at both Reynolds numbers than the classical relation of Walz, being able to capture the effects of the wall heat flux

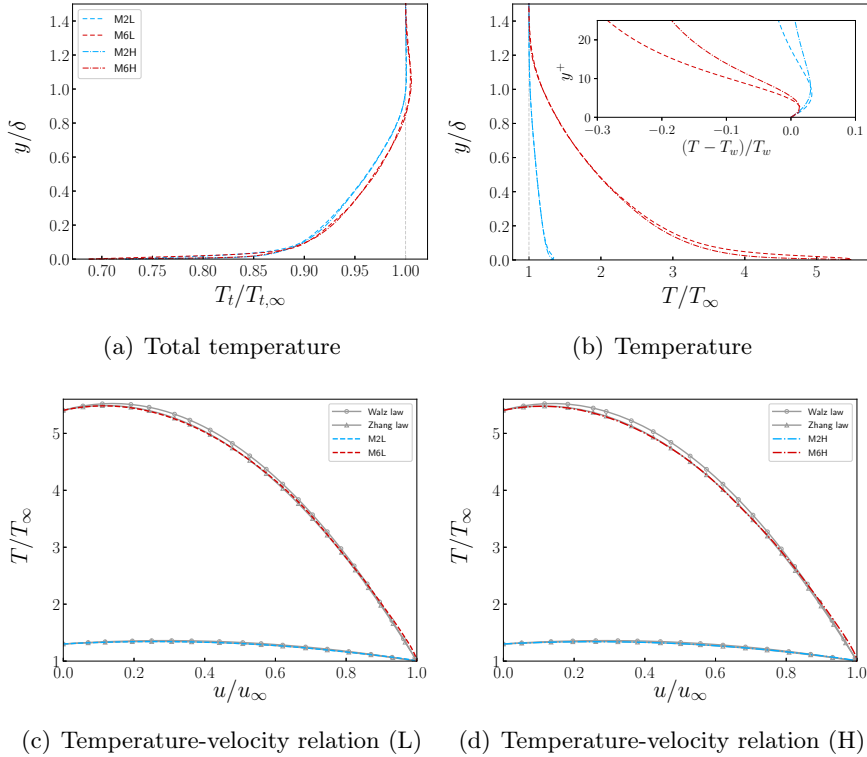


Figure 9: Temperature profiles as function of the wall-normal distance and mean velocity for all cases listed in table 2. Panel (a) and (b) show the profiles of the mean total temperature and mean temperature along the wall-normal distance y/δ . The inset shows the profiles in the near wall. Panels (c) and (d) show the mean temperature profile against mean velocity at low and high Reynolds numbers, compared with the classical law of [58] and the modified relation of Zhang et al. [67].

that exists in the present case of cooled wall. Although the mismatch showed by Walz's law is visible, it falls within 3% of the DNS values (the maximum deviations being at high Reynolds numbers). The authors attribute this behaviour to the wall cooling that is not intense enough to stress the limitations of this law. This finding is in accordance with the study of Duan et al. [15], that reports deviations up to 10% when testing more extreme diabatic cases, e.g. $T_w/T_r = 0.18$. The effect of the Reynolds number on the profiles is not significant, with the only visible difference being a slight decrease of the agreement with Walz law at high Reynolds numbers.

Fluctuation statistics

Reynolds stresses

Reynolds stresses vs wall normal distances are reported in figure 10 using the Morkovin transformation:

$$(u_i^*)^2 = \frac{\widetilde{u_i''}^2}{u_\tau^2} \frac{\bar{\rho}}{\bar{\rho}_w}, \quad (uv)^* = \frac{\widetilde{u''v''}}{u_\tau^2} \frac{\bar{\rho}}{\bar{\rho}_w} \quad (10)$$

which should collapse compressible data to the incompressible ones [32]. The profiles are shown as a function of the wall-distance rescaled in wall units y^+ and semilocal scaling y^* . For reference purposes, low Reynolds number cases are compared to the results of a low-speed turbulent boundary layer at $Re_\tau = 445$ simulated by Jiménez et al. [23], while the high Reynolds number cases are

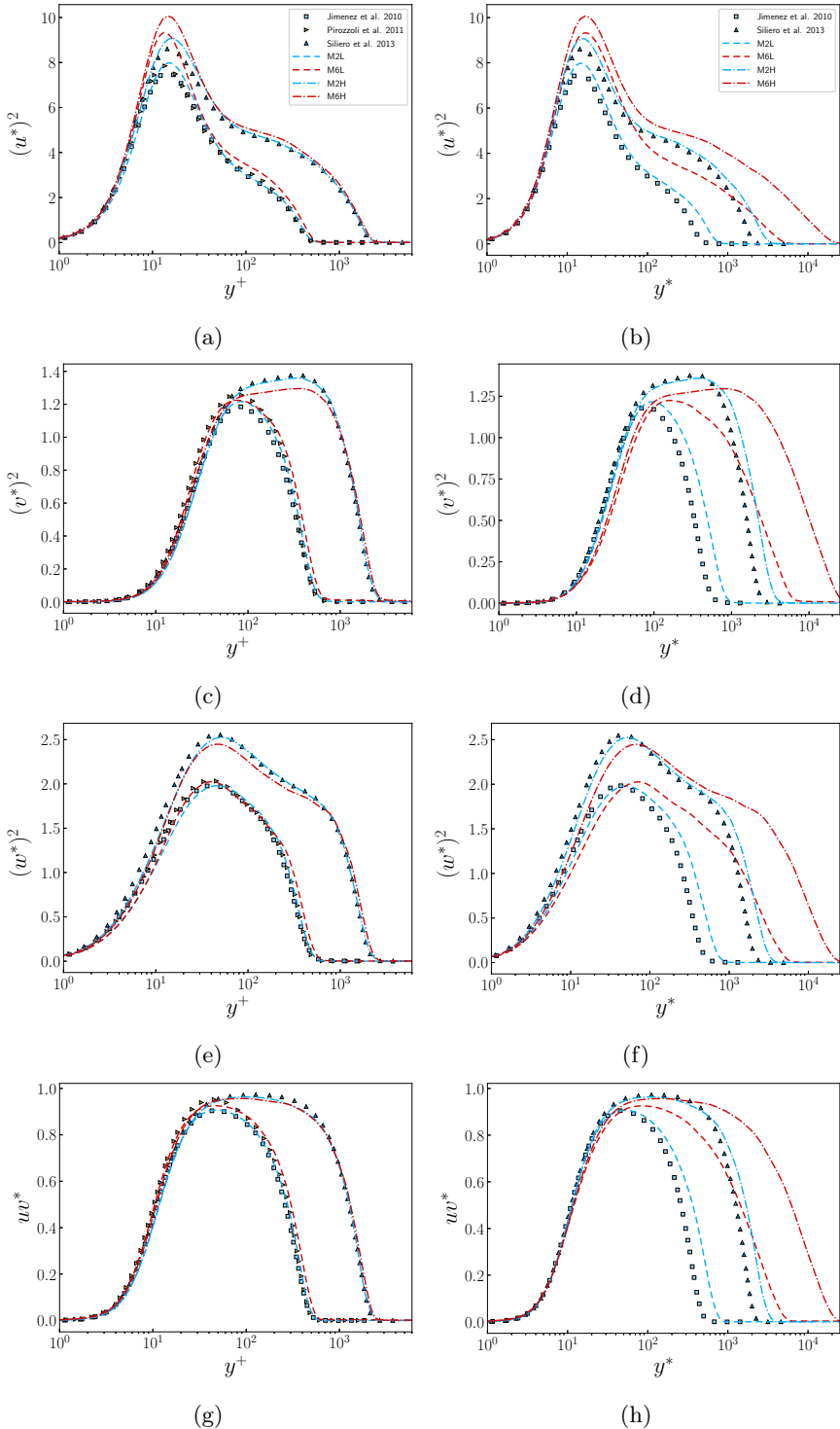


Figure 10: Inner-scaled turbulent velocity fluctuations and Reynolds shear stress scaled according to Morkovin as function of the wall-normal distance y^+ (left column) and semilocal y^* (right column). Present results are compared to the incompressible DNS of Jiménez et al. [23] at $Re_\tau = 445$, Sillero et al. [46] at $Re_\tau = 1989$ and the supersonic adiabatic case of Pirozzoli and Bernardini [39] at $M = 2$ and $Re_\tau = 450$.

compared to the incompressible counterpart at $Re_\tau = 1989$ computed by Sillero et al. [46]. The figures reveal the relevant role played by both Mach and Reynolds number, leading to distinct and well visible effects on the distribution of the various Reynolds stress components. Supersonic cases at both Reynolds numbers are in good agreement with their low-speed counterparts at matching

Re_τ , the most significant difference being an increase with the Mach number of the peak of the streamwise velocity fluctuations, already observed in previous investigations [15]. The influence of wall cooling on this regard is believed to be minor given the good accordance of case M2L with the adiabatic case of Pirozzoli and Bernardini [39]. The wide Reynolds-number range covered by the present database allows to appreciate the distinctive effect of the outer layer motions, whose relevance is known to increase with the Reynolds number, that provide large-scale contributions to the fluctuation intensities of the wall-parallel velocity components even in the near wall region. Such distant eddies, usually referred to as "inactive motions", are expected to induce a logarithmic growth with Re_τ of both u and w in the low speed regime [27], here confirmed in the supersonic regime. The Reynolds number effect on the wall-normal velocity component and Reynolds shear stress appears as a plateau that corresponds to the formation of an equilibrium layer, again without a significant influence of the Mach number in the supersonic regime. Furthermore, at high-Reynolds and Mach numbers, we also note reduced fluctuation intensities of the wall-normal and spanwise velocity in the outer layer, suggesting a less efficient redistribution of the turbulent energy from the streamwise component to the other ones in hypersonic conditions. Concerning the accuracy of the Morkovin scaling of velocity fluctuations, it offers an accurate collapse of profiles at the same Re_τ but not at different Mach numbers when plotted against the y^+ coordinate. Although the semilocal scaling y^* increases the discrepancies among different cases in the outer layer, it should be noted that the semilocal friction Reynolds number is not matched for present cases.

Turbulent kinetic energy budget

The balance equation of the turbulent kinetic energy $k = 1/2 \widetilde{u''_i u''_i}$ for a compressible boundary layer (according to the derivation of Zhang et al. [65]) is given by

$$\frac{(D\bar{\rho}k)}{Dt} = P + TT + \Pi - \phi + D + ST \quad (11)$$

with

$$P = -\bar{\rho} \widetilde{u''_i u''_j} \frac{\partial \tilde{u}_i}{\partial x_j} \quad (12)$$

$$TT = -\frac{\partial}{\partial x_j} \left[\frac{1}{2} \bar{\rho} \widetilde{u''_i u''_i u''_j} \right] \quad (13)$$

$$\Pi = -\frac{\partial}{\partial x_i} \left(\overline{p' u''_i} \right) + p' \overline{\frac{\partial u''_i}{\partial x_i}} \quad (14)$$

$$\phi = \overline{\sigma'_{ij} \frac{\partial u''_i}{\partial x_j}} \quad (15)$$

$$D = \frac{\partial}{\partial x_j} \left(\overline{\sigma'_{ij} u''_i} \right) \quad (16)$$

$$ST = -\bar{\rho} \tilde{k} \frac{\partial \tilde{u}_k}{\partial x_k} + \overline{u''_i} \left(\frac{\partial \bar{\sigma}_{ij}}{\partial x_j} - \frac{\partial \bar{p}}{\partial x_i} \right) \quad (17)$$

where P is the production term, TT represents the turbulent transport, Π includes the pressure diffusion and dilatation, $-\phi$ is the viscous dissipation, D is the viscous diffusion, and ST includes all additional terms that arise when density is not constant. In figure 11 the budget terms have been

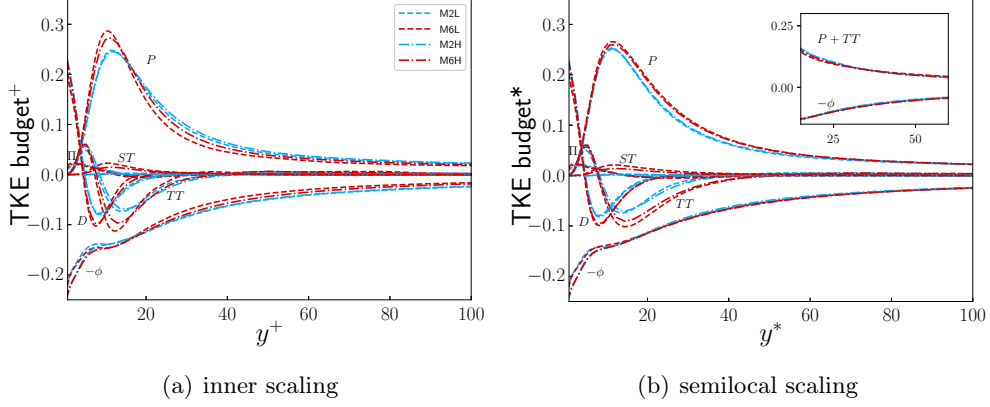


Figure 11: Turbulent kinetic energy budget in (a) inner scaling and (b) semilocal scaling.

normalized by the conventional inner and semilocal scalings. As noted by Zhang et al. [65] and Duan and Martin [13], the semilocal scaling of Huang et al. [22] has a better capability to collapse different profiles for different Reynolds and Mach numbers, although some discrepancies due to the effect of the latter are still present. In particular, while viscous dissipation appears almost independent of Re and Ma numbers in semi-local scaling, production and turbulent transport still show a Mach dependence. We highlight that dissipation and the sum of turbulent transport with production appear independent of Mach number for $y^+ > 20$, as highlighted by the inset of figure 11(b). The better scaling of the production term in the semilocal scaling is exploited to evaluate the turbulent production in the log layer region using a pre-multiplied representation as function y^* , where equal areas represent equal contribution to the total production (figure 12(a)). As noted by Smits et al. [49] and Marusic et al. [28], the contribution of the bulk production extends to the log layer as the Reynolds number increases, becoming a significant source term of turbulent energy even outside the buffer layer. It should be noted that the highest peak is exhibited by the case at the highest Reynolds and Mach numbers considered. We attribute this feature to an indirect Mach number effect on the friction Reynolds number in semi-local quantities, Re_τ^* , that for present cases is higher at $M = 6$ with respect to the corresponding $M = 2$ cases. Another important feature is the ratio between turbulent production and dissipation shown in figure 12(b), which should be close to one in the log-layer [66]. This feature is well attained in the first part of the log-layer for all present cases when the semi-local scaling is used, collapsing all the profiles in this region around one. However, data also show an excess of turbulent production farther from the wall (but still in the log-layer) for hypersonic profiles, which is balanced by an increased turbulent transport. We attribute this effect to a more intense interaction between the outer and inner region, stimulated by the relatively denser, colder and less viscous outer layer eddies, characterized by a higher momentum. Such large-scale eddies are thus able to exert a greater influence onto the inner region, which is consistent with the less efficient kinetic energy redistribution described in Section §Reynolds stresses, and with the discussion in Pirozzoli et al. [42], which argued that the excess of turbulent production in the log layer feeds inactive motions that do not contribute to the turbulent shear stress, but transfer energy to other locations of the flow.

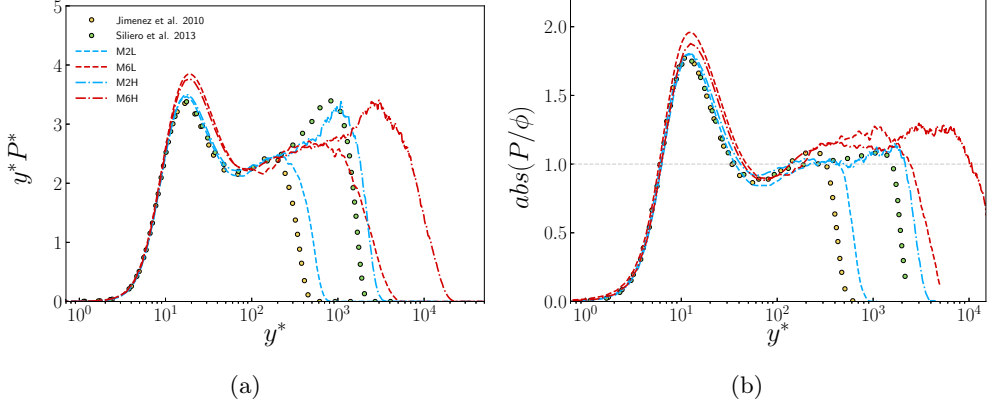


Figure 12: Turbulent kinetic energy production in premultiplied form (a) and ratio between production and dissipation (b) as function of y^* .

Thermodynamic quantities

To gain insights on the fluctuations of thermodynamic variables, the root-mean-square profiles of density, temperature and pressure are shown in figure 13 in both inner wall and semilocal scaling. In the left column the inner wall scaling is shown (together with an adiabatic case of Pirozzoli and Bernardini [39] that matches the Mach and Reynolds numbers of our case M2L). We note that at high Mach number a peak of the density fluctuation intensity establishes near the edge of the boundary layer. This peak is a consequence of the higher mean density (lower temperature) that occurs far from the wall with respect to the wall mean value ρ_w , especially at high Mach number. Actually, considering the corresponding semilocal scaling, where ρ_{rms} is normalized also with local value of the mean density $\bar{\rho}$ (panel b), we observe that the peak is smeared and the profile in the log-layer is almost flat, so the increase of the local density fluctuations is controlled by the mean local density. Similar arguments, but with the opposite behaviour, hold for the temperature fluctuations (panel c and d). Comparing the inner and semi-local scaling for density and temperature intensities, it emerges that, although the qualitative behaviour of the profiles is generally more similar in semi-local scaling, there is a clear Mach number dependency. The relative fluctuation intensities of density and temperature increase with the Mach number, while both supersonic and hypersonic cases exhibit less intense temperature fluctuations with respect to the adiabatic profile. This behaviour is consistent with the qualitative discussion of figure 4 and with the flatter mean temperature profile exhibited at $M = 2$, see figure 9. Actually, the coupling between the wall-normal velocity fluctuations and a more uniform mean temperature is less effective to produce temperature fluctuations (e.g. near wall streaks). It should be remarked that the cold wall enhances this behaviour because it produces a near-wall local maximum of the mean temperature profile, explaining the important difference of present diabatic $M = 2$ data with respect to the adiabatic case of Pirozzoli and Bernardini [39].

Conversely, the pressure fluctuations exhibit a completely different dynamics. A good collapse of the profiles emerges only using the wall scaling when cases at fixed Re_τ are considered, while the semi-local scaling is not able to provide better results. The pressure fluctuation intensity appears controlled by the Reynolds number and almost independent of Mach number, except the very near wall region and the free-stream, where the acoustic radiation increases with M_∞ .

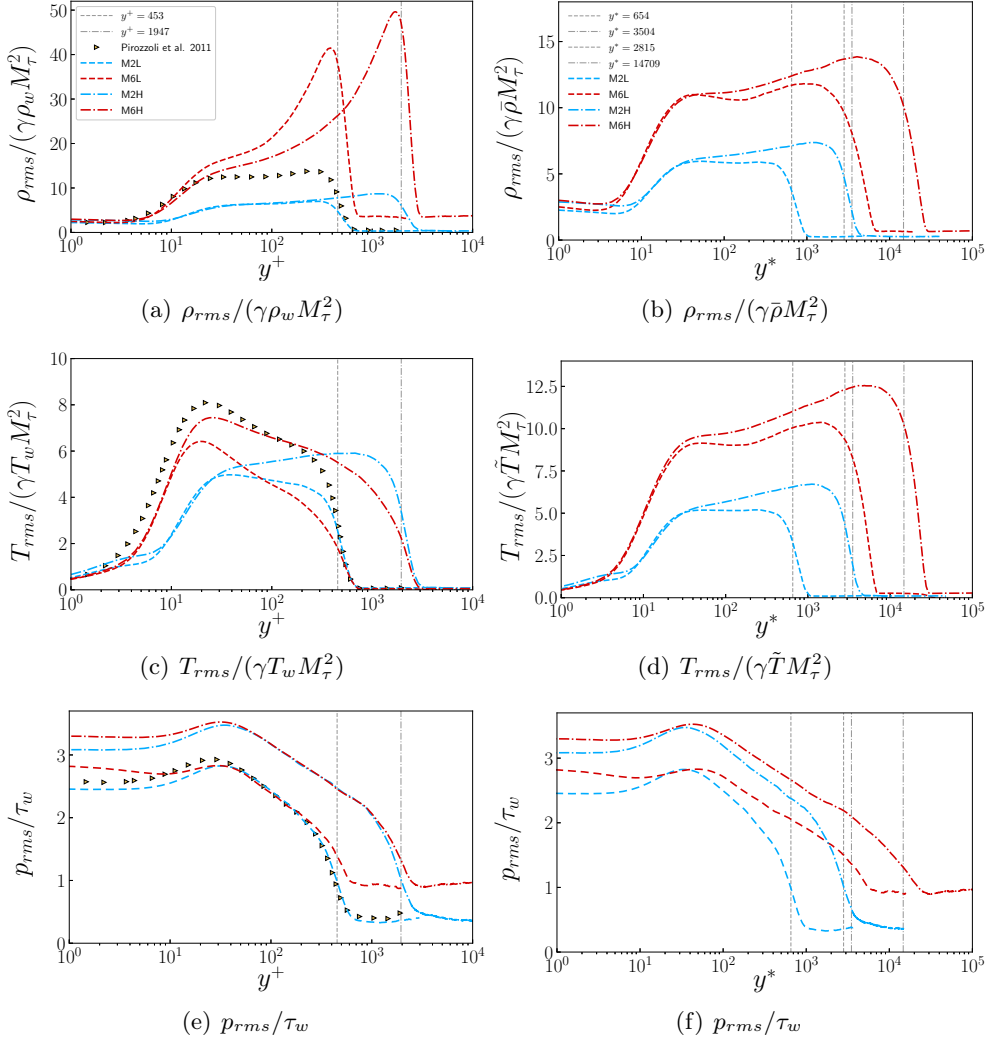


Figure 13: Profiles of RMS thermodynamic properties in inner and semilocal scalings. Grey vertical lines indicate the boundary layer edge at low Reynolds numbers (dashed line) and high Reynolds numbers (dot-dashed line), respectively. $M_\tau = u_\tau / \sqrt{\gamma R T_w}$ and $M_\tau^* = u_\tau^* / \sqrt{\gamma R \tilde{T}}$ are the friction Mach numbers in inner and semi-local scalings, respectively. Inner scaled profiles are compared with the supersonic adiabatic case of Pirozzoli and Bernardini [39] at $M = 2$ and $Re_\tau = 450$.

Summarizing, it emerges that, while the density and temperature fluctuations are strongly influenced by the Mach number as expected, the pressure fluctuations appear decoupled and *turbulence* controlled, since strongly depending only on the friction Reynolds number.

Length scales

We now address the spatial organization of the turbulent and thermal energy by looking at the pre-multiplied spectra of the streamwise velocity $k_z E_{uu}(k_z)$ and temperature fluctuations $k_z E_{tt}(k_z)$ as a function of the spanwise wavelength $\lambda_z = 2\pi/k_z$, where k_z denotes the spanwise wavenumber and E_{uu} , E_{tt} are the spectral densities computed in the spanwise direction of the velocity component u and temperature T , respectively. The maps reported in figure 14 show the variation of the spectra with the wall-normal location, in both inner and outer scaling for the high-Reynolds number cases at Mach 2 and 6. Concerning the velocity fluctuations, all cases highlight the existence of a primary

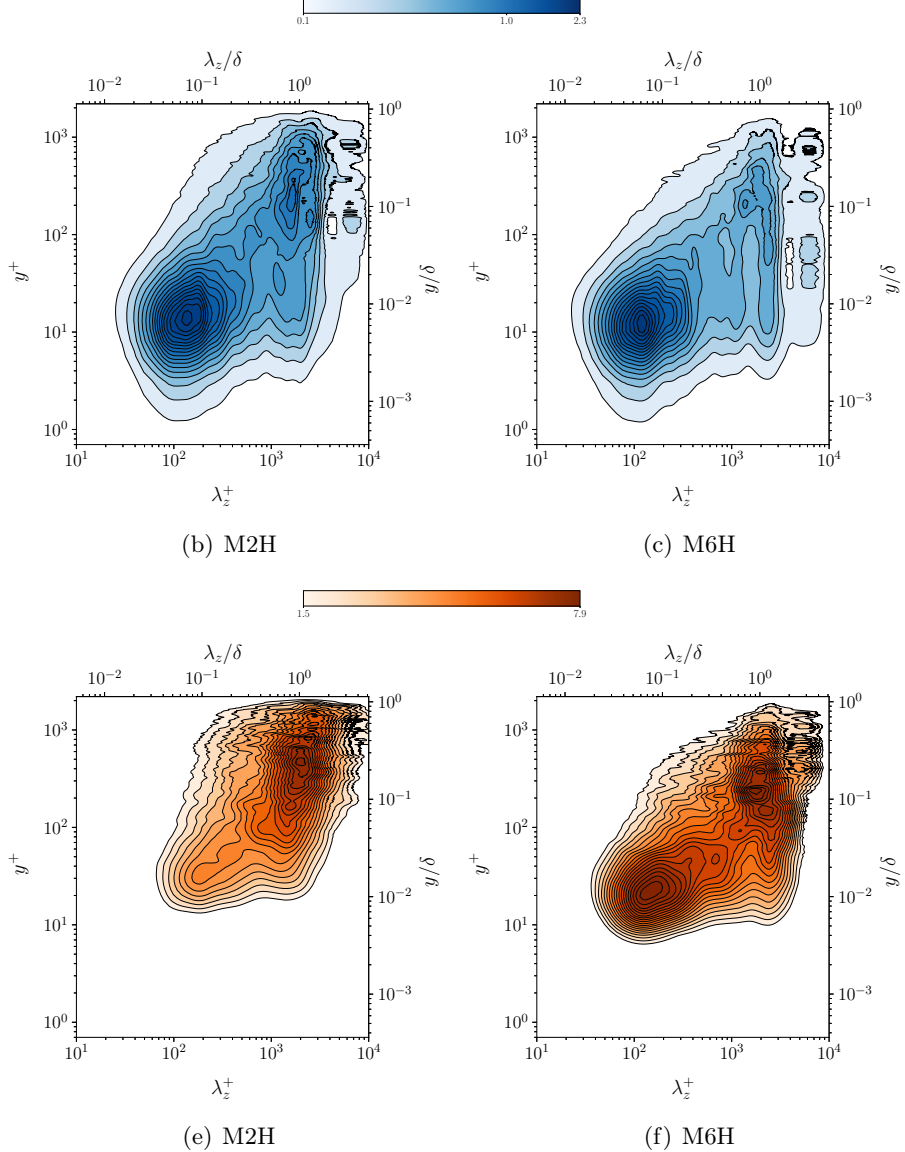


Figure 14: Pre-multiplied spanwise spectra of velocity E_{uu} and temperature E_{tt} fluctuations for cases M2H and M6H. The colormap is shown in log-scale.

energy peak in the buffer layer at $y^+ \approx 15$ with associated spanwise wavelengths of $\mathcal{O}(100)$ wall units, which is an expected feature of the near-wall cycle of turbulence self-sustainment. Far from the wall, a secondary peak is observed in the outer layer for both the supersonic and hypersonic case, corresponding to wavelengths of $\mathcal{O}(\delta)$ which is the signature of the large-scale organization of the velocity field (superstructures) in the log layer, extending its influence into the near wall region. The location of the secondary peak ($y/\delta \approx 0.1$) is in accordance with the results of Bernardini and Pirozzoli [3] and Tomkins and Adrian [51]. The spectral maps for the temperature fluctuations reveal the presence of remarkable differences between the two Mach numbers. In particular, a strong inner peak is only observed in the hypersonic case (whereas a much less intense plateau region is present at $M = 2$), located in the buffer layer ($y^+ \approx 20$) at wavelengths comparable with those of the velocity structures. Temperature streaks in the near wall region are not highlighted by the spectra of the supersonic flow case, in agreement with the qualitative observations of section §Flow organization. This behaviour is mainly attributed to the effect of wall cooling, which is

more effective in the present flow cases at Mach 2 as measured in terms of the Eckert number [60]. On the contrary, the outer peak in the temperature spectra is present for both Mach numbers in correspondence of wavelenghts comparable with that of the velocity field, although it appears to be displaced upwards in the supersonic flow case. The evaluation of velocity and temperature spectra allows to quantify the typical length scales in the outer turbulent wall layer. According to the classical theory [43] and to the predictions of the attached eddies model [35], the typical size of the energetic eddies is proportional to their distance from the wall ($l_m = ky$). Under the assumption of a constant-stress layer it directly leads to the logarithmic behaviour of the mean velocity profile. On the basis of a simple eddy-viscosity ansatz, an improved scaling has been proposed by Pirozzoli [36] and later adapted to compressible flows by Modesti and Pirozzoli [30]

$$l_{12}^*(y) \sim (u_\tau \delta) \left(\frac{\partial \tilde{u}_{VD}}{\partial y} \right)^{-1/2} \quad (18)$$

which has been demonstrated to yield accurate results for compressible channel flows. Here we propose a further improvement of this scaling, by using the local mean shear computed on the velocity profile transformed according to Griffin et al. [19]

$$l_{12,GR}^*(y) \sim (u_\tau \delta) \left(\frac{\partial \tilde{u}_{GR}}{\partial y} \right)^{-1/2}. \quad (19)$$

Equations (18) and (19) are used for the normalization of the spanwise wavelength λ_z and the results compared to the conventional normalization based on the boundary layer thickness δ . Regarding the latter choice, other suitable outer scales have been tested, such as the enthalpy thickness and the Rotta thickness, showing essentially the same behaviour. Figure 15 shows the pre-multiplied spectra of the streamwise velocity $k_z E_{uu}(k_z)$ for all flow cases and compares the capability of the aforementioned scalings for the spanwise wavelength λ_z to collapse profiles at different wall-normal distances y/δ . Figure 16 reports the pre-multiplied spectra of the temperature fluctuations $k_z E_{tt}(k_z)$ using the previously introduced scalings for the wavelength. To account for the variation of turbulence intensity across the wall-layer, spectra are normalized by $\widetilde{u''^2}$ and $\widetilde{T''^2}$, respectively, yielding \hat{E}_{uu} and \hat{E}_{tt} . Looking at panels (a,d,g,j) of figure 15, it can be seen that all cases show a distinct peak at $\lambda_z \approx \delta$, which suggests that the turbulent eddies have a characteristic spanwise length similar to the boundary layer thickness. Panels (b,e,h,k), show an improved collapse of the spectra at all off-wall locations thanks to the normalization of λ_z with l_{12}^* (Eq. 18), supporting the validity of the theory developed by Pirozzoli [36] and the arguments made by Modesti and Pirozzoli [30] for the extension to the compressible regime. Panels (c,f,i,l) show a slight improvement in collapsing the spectral curves, especially for the velocity and temperature fluctuations of the high-Reynolds number at Mach 6, that is attributed to the more accurate theory of Griffin et al. [19] for highly compressible flows, as also shown in section §Mean flow statistics.

Conclusions

This study presents an analysis of the relevant statistics of DNS of zero-pressure-gradient turbulent boundary layers at Mach numbers 2 and 5.86 with friction Reynolds numbers up to 2000. The wall is assumed to be isothermal and cold with respect to the free-stream recovery temperature, which is

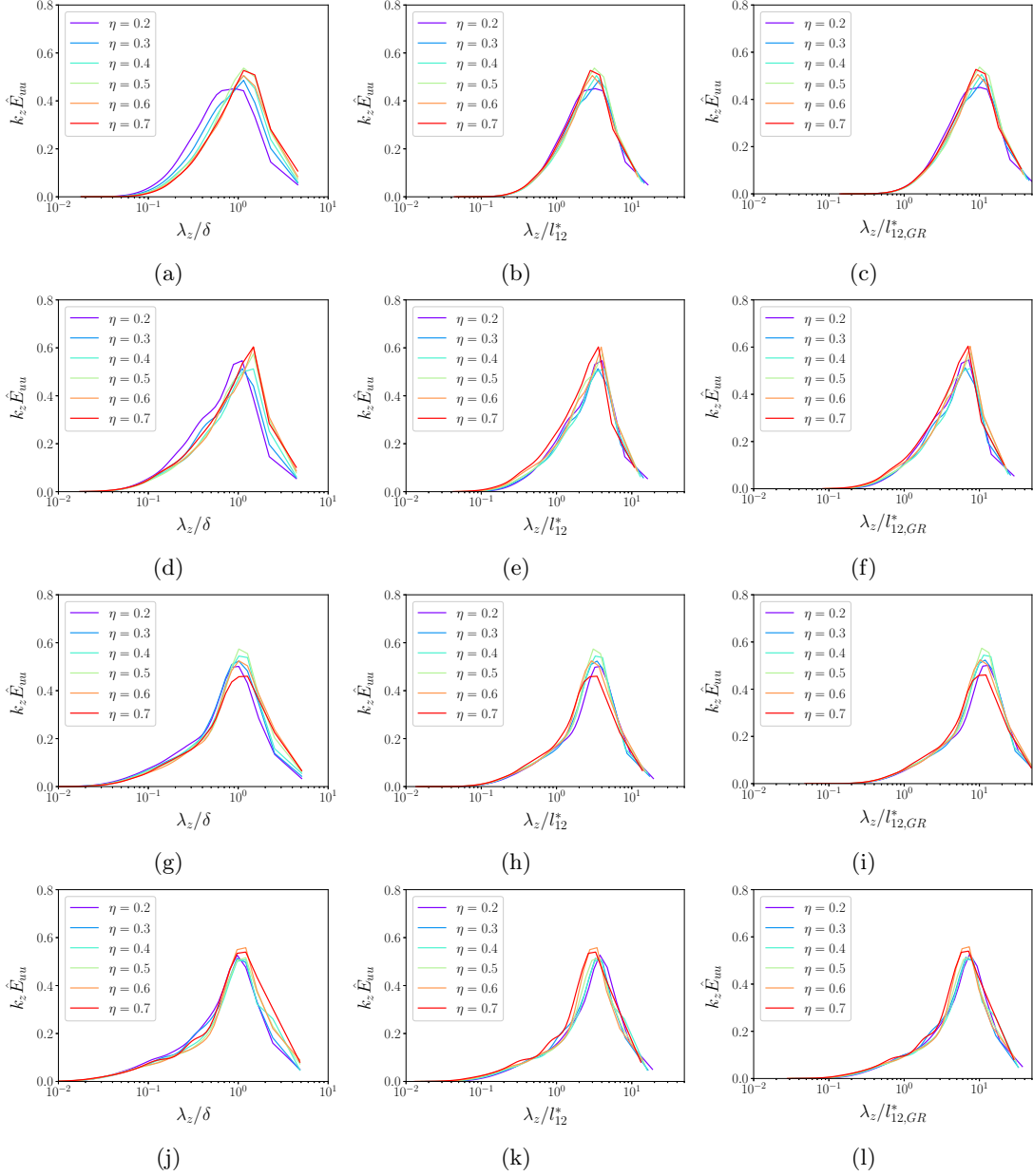


Figure 15: Pre-multiplied spanwise spectra of streamwise velocity fluctuations as function of λ_z/δ (a-d-g-j), λ_z/l_{12}^* (b-e-h-k) and $\lambda_z/l_{12,GR}^*$ (c-f-i-l) for flow cases M2L (a->c), M6L (d->f), M2H (g->i), M6H (j->l). Different colours correspond to different wall-normal distances in the range $\eta = y/\delta = 0.2 - 0.8$.

the most frequent condition for aerospace applications. In particular, to discern the various effects we compare four cases that are representative of supersonic and hypersonic regimes at low and moderately high-friction Reynolds numbers. All cases share the same value of the wall-to-recovery-temperature ratio (equal to 0.76), but are characterized by different values of the Eckert number. A qualitative analysis of the turbulent flow organization is performed by means of instantaneous visualizations of streamwise velocity on x-y and x-z slices. We note important deviations from usual observations in adiabatic walls, resulting in a less evident similarity between thermal and velocity fields. In particular, the near-wall streaks of the temperature fluctuations disappear in strongly non-adiabatic cases. The instantaneous fields have also been scrutinized in a more quantitative way to determine the existence of uniform zones [10] for the streamwise velocity and temperature,

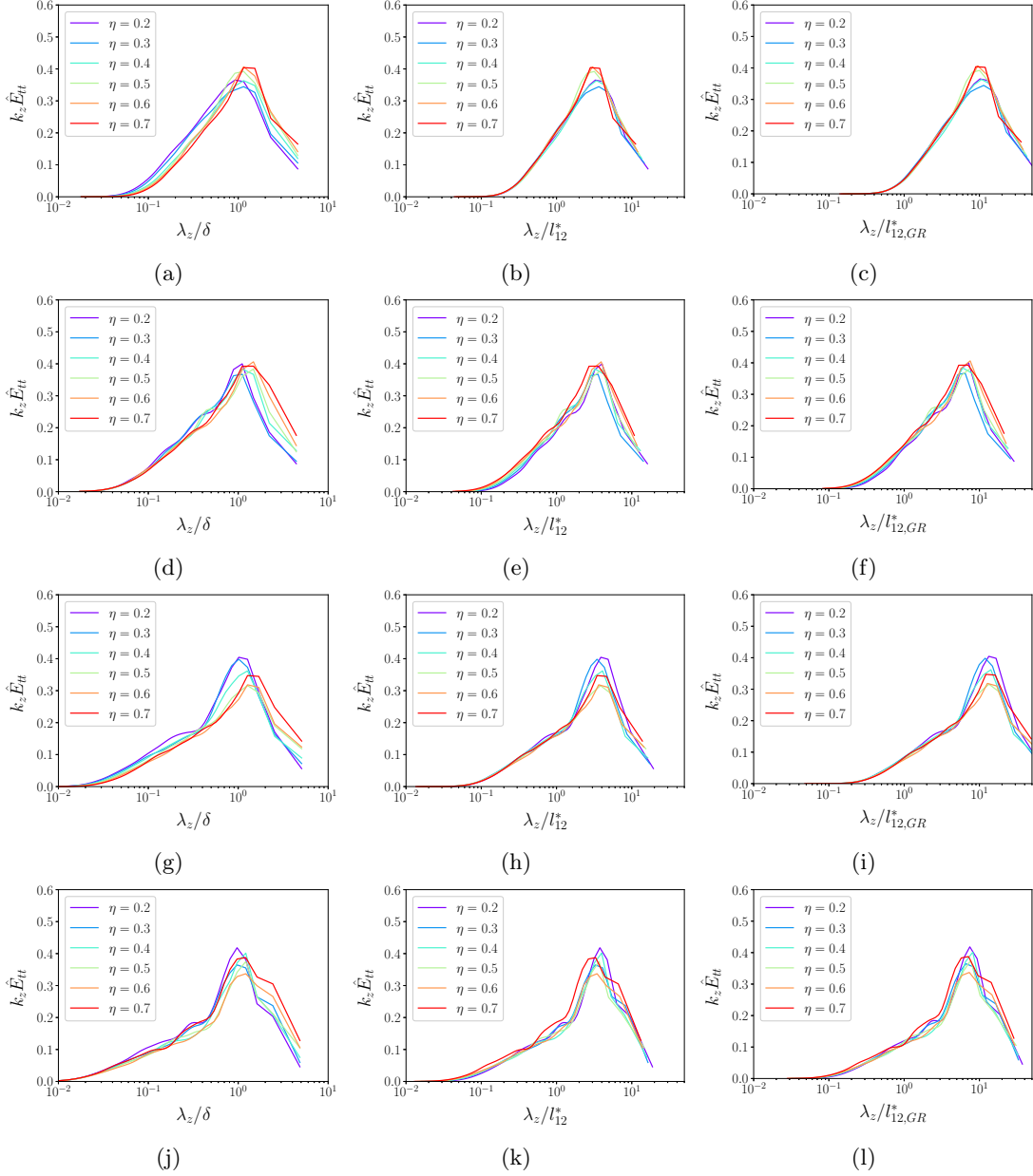


Figure 16: Pre-multiplied spanwise spectra of temperature fluctuations as function of λ_z/δ (a-d-g-j), λ_z/l_{12}^* (b-e-h-k) and $\lambda_z/l_{12,GR}^*$ (c-f-i-l) for flow cases M2L (a->c), M6L (d->f), M2H (g->i), M6H (j->l). Different colours correspond to different wall-normal distances in the range $\eta = y/\delta = 0.2 - 0.8$.

never addressed before. To detect the turbulent/non-turbulent interface, a modified expression of the kinetic energy defect is introduced to take into account the strong density variations associated to the hypersonic regime. We find that uniform zones of both U and T do exist in both supersonic and hypersonic turbulent boundary layers and we compute their average number for the high Reynolds numbers cases of the present database. We find a clear increase of the average number of uniform temperature zones with respect to that of the streamwise velocity, while both numbers decrease in the hypersonic case. The analysis of mean velocity profiles reveals that an impressive collapse of compressible data into the incompressible counterpart is obtained with the recent transformations of Volpiani et al. [57] and Griffin et al. [19], thus extending the validation of these relations to moderate/high Reynolds numbers. An excellent agreement with the relation

proposed by Zhang et al. [67] is also found for the mean temperature profiles as a function of the streamwise velocity, improving the classical law of Walz [58]. By analysing the velocity fluctuations, we observe that at high Mach numbers there is a less efficient redistribution of turbulent energy from the streamwise component to the other ones, in accordance with Zhang et al. [65]. Further evidence of this phenomenon is found by analysing the turbulent kinetic energy budget, where we note that the semi-local scaling provides a better collapse of the curves both for M_∞ and Re_τ , with the main exception of production and transport terms showing a dependence on Mach number, especially in the log-layer. We attribute this discrepancy to an increase of interaction between the inner and outer region of the boundary layer caused by the larger density differences occurring in the hypersonic flow cases. Concerning the fluctuations of the thermodynamics variables, we find that while temperature and density RMS show a clear increase with the Mach number, the pressure appears dominated by the friction Reynolds number with a weak dependence on M_∞ even in the hypersonic regime. The comparison with a reference adiabatic case of Pirozzoli and Bernardini [39] indicates that wall cooling induces a decrease of the intensity of temperature fluctuations in terms of wall units. The length scale analysis has been performed calculating the pre-multiplied spectra of velocity and temperature fluctuations in the spanwise direction. Consistently with findings in the incompressible regime, we observe two peaks for the velocity field, in the buffer and in the outer layer, respectively. Similarly, two peaks are present in the premultiplied spectra of the temperature fluctuations for the hypersonic flow cases, still associated to distinct motions in the near wall region and in the outer layer. We find that the buffer layer peak disappears in the most non-adiabatic case at $M_\infty = 2$, in agreement with the qualitative observations on the absence of temperature streaks close to the wall. Finally, we present a quite accurate scaling of the streamwise velocity and temperature spectra in the spanwise direction at different wall distances considering the characteristic length scale provided by eq. (19). This scaling uses the local velocity gradient based on the recent theory of Griffin et al. [19] in the length scale definition introduced by Modesti and Pirozzoli [30].

Acknowledgements

We acknowledge that the results reported in this paper have been achieved using the PRACE Research Infrastructure resource MARCONI 100 based at CINECA, Casalecchio di Reno, Italy, under project PRACE n. 2020225442.

Declaration of interests

The authors report no conflict of interest.

Bibliography

- [1] R.J. Adrian, C.D. Meinhart, and C.D. Tomkins. Vortex organization in the outer region of the turbulent boundary layer. *J. Fluid Mech.*, 422:1–54, 2000.
- [2] J.D. Anderson. *Hypersonic and High-temperature Gas Dynamics*. AIAA education series. American Institute of Aeronautics and Astronautics, 2006. ISBN 9781563477805. URL <https://books.google.it/books?id=UgWmQgAACAAJ>.

- [3] M. Bernardini and S. Pirozzoli. Inner/outer layer interactions in turbulent boundary layers: a refined measure for the large-scale amplitude modulation mechanism. *Phys. Fluids*, 23(6):061701, 2011.
- [4] M. Bernardini and S. Pirozzoli. Wall pressure fluctuations beneath supersonic turbulent boundary layers. *Phys. Fluids*, 23(8):085102, 2011.
- [5] M. Bernardini, D. Modesti, F. Salvadore, and S. Pirozzoli. STREAmS: a high-fidelity accelerated solver for direct numerical simulation of compressible turbulent flows. *Comp. Phys. Comm.*, 263:107906, 2021.
- [6] P. Bradshaw. Compressible turbulent shear layers. *Annu. Rev. Fluid Mech.*, 9(1):33–52, 1977.
- [7] A. Busemann. *Gasdynamik*. Akademische Verlagsgesellschaft, 1931.
- [8] L. Crocco. Sulla trasmissione del calore da una lamina piana a un fluido scorrente ad alta velocità. *L'Aerotecnica*, 12:181–197, 1932.
- [9] C. M. De Silva, J. Philip, K. Chauhan, C. Meneveau, and I. Marusic. Multiscale geometry and scaling of the turbulent-nonturbulent interface in high reynolds number boundary layers. *Phys. Rev. Lett.*, 111(4):044501, 2013.
- [10] C.M. De Silva, N. Hutchins, and I. Marusic. Uniform momentum zones in turbulent boundary layers. *J. Fluid Mech.*, 786:309–331, 2016.
- [11] F. De Vanna, A. Benato, F. Picano, and E. Benini. High-order conservative formulation of viscous terms for variable viscosity flows. *Acta Mech.*, 232:2115–2133, 2021.
- [12] Mario Di Renzo and Javier Urzay. Direct numerical simulation of a hypersonic transitional boundary layer at suborbital enthalpies. *J. Fluid Mech.*, 912:A29, 2021. doi: 10.1017/jfm.2020.1144. URL <http://dx.doi.org/10.1017/jfm.2020.1144>.
- [13] L. Duan and M.P. Martin. Direct numerical simulation of hypersonic turbulent boundary layers. Part 4. Effect of high enthalpy. *J. Fluid Mech.*, 684:25–59, 2011.
- [14] L. Duan, I. Beekman, and M.P. Martín. Direct numerical simulation of hypersonic turbulent boundary layers. Part 2. Effect of wall temperature. *J. Fluid Mech.*, 655:419–445, 2010. ISSN 00221120. doi: 10.1017/S0022112010000959.
- [15] L. Duan, I. Beekman, and M.P. Martín. Direct numerical simulation of hypersonic turbulent boundary layers. Part 3. Effect of Mach number. *J. Fluid Mech.*, 672:245–267, 2011. ISSN 14697645. doi: 10.1017/S0022112010005902.
- [16] L. Duan, M. M. Choudhari, and M. Wu. Numerical study of acoustic radiation due to a supersonic turbulent boundary layer. *J. Fluid Mech.*, 746:165–192, 2014.
- [17] F. Ducros, V. Ferrand, F. Nicoud, C. Weber, D. Darracq, C. Gachet, and T. Poinsot. Large-eddy simulation of the shock/turbulence interaction. *J. of Comput. Phys.*, 152(2):517–549, 1999.

- [18] J. Gaviglio. Reynolds analogies and experimental study of heat transfer in the supersonic boundary layer. *Int. J. Heat Mass Tran.*, 30(5):911–926, 1987.
- [19] K.P. Griffin, L. Fu, and P. Moin. Velocity transformation for compressible wall-bounded turbulent flows with and without heat transfer. *P. Natl. Acad. Sci USA*, 118(34), 2021.
- [20] Junji Huang, Gary L Nicholson, Lian Duan, Meelan M Choudhari, and Rodney D Bowersox. Simulation and modeling of cold-wall hypersonic turbulent boundary layers on flat plate. In *AIAA Scitech 2020 Forum*, page 0571, 2020.
- [21] Junji Huang, Lian Duan, and Meelan M Choudhari. Direct numerical simulation of hypersonic turbulent boundary layers: effect of spatial evolution and reynolds number. *J. Fluid Mech.*, 937, 2022.
- [22] P. C. Huang, G.N. Coleman, and P. Bradshaw. Compressible turbulent channel flows: DNS results and modelling. *J. Fluid Mech.*, 305:185–218, 1995.
- [23] J. Jiménez, S. Hoyas, M.P. Simens, and Y. Mizuno. Turbulent boundary layers and channels at moderate Reynolds numbers. *J. Fluid Mech.*, 657:335, 2010.
- [24] M. Lagha, J. Kim, J.D. Eldredge, and X. Zhong. A numerical study of compressible turbulent boundary layers. *Phys. Fluids*, 23(1):015106, 2011.
- [25] A. Laskari, R. de Kat, R. J. Hearst, and B Ganapathisubramani. Time evolution of uniform momentum zones in a turbulent boundary layer. *J. Fluid Mech.*, 842:554–590, 2018.
- [26] M.P. Martin. Direct numerical simulation of hypersonic turbulent boundary layers. Part 1. Initialization and comparison with experiments. *J. Fluid Mech.*, 570:347–364, 2007. ISSN 00221120. doi: 10.1017/S0022112006003107.
- [27] I. Marusic and J.P. Monty. Attached eddy model of wall turbulence. *Annu. Rev. Fluid Mech.*, 51:49–74, 2019.
- [28] I. Marusic, B.J. McKeon, P. A Monkewitz, H.M. Nagib, A.J. Smits, and K.R. Sreenivasan. Wall-bounded turbulent flows at high Reynolds numbers: recent advances and key issues. *Phys. Fluids*, 22(6):065103, 2010.
- [29] C. D. Meinhart and R. J. Adrian. On the existence of uniform momentum zones in a turbulent boundary layer. *Phys. Fluids*, 7(4):694–696, 1995.
- [30] D. Modesti and S. Pirozzoli. Reynolds and Mach number effects in compressible turbulent channel flow. *Int. J. Heat Fluid Fl.*, 59:33–49, 2016.
- [31] B. Morgan, J. Larsson, S. Kawai, and S. K. Lele. Improving low-frequency characteristics of recycling/rescaling inflow turbulence generation. *AIAA J.*, 49(3):582–597, 2011.
- [32] M.V. Morkovin. Effects of compressibility on turbulent flows. *Mécanique de la Turbulence*, 367 (380):26, 1962.
- [33] D. Passiatore, L. Sciacovelli, P. Cinnella, and G. Pascazio. Thermochemical non-equilibrium effects in turbulent hypersonic boundary layers. *J. of Fluid Mech.*, 941, 2022.

- [34] Donatella Passiatore, Luca Sciacovelli, Paola Cinnella, and Giuseppe Pascazio. Finite-rate chemistry effects in turbulent hypersonic boundary layers: A direct numerical simulation study. *Phys. Rev. Fluids*, 6(5):054604, 2021.
- [35] A..E Perry and I. Marušić. A wall-wake model for the turbulence structure of boundary layers. Part 1. Extension of the attached eddy hypothesis. *J. Fluid Mech.*, 298:361–388, 1995.
- [36] S. Pirozzoli. On the size of the energy-containing eddies in the outer turbulent wall layer. *J. Fluid Mech.*, 702:521–532, 2012.
- [37] S. Pirozzoli and M. Bernardini. Turbulence in supersonic boundary layers at moderate Reynolds number. *J. Fluid Mech.*, 688:120–168, 2011. ISSN 00221120. doi: 10.1017/jfm.2011.368.
- [38] S. Pirozzoli and M. Bernardini. Direct numerical simulation database for impinging shock wave/turbulent boundary-layer interaction. *AIAA J.*, 49(6):1307–1312, 2011.
- [39] S. Pirozzoli and M. Bernardini. Turbulence in supersonic boundary layers at moderate reynolds number. *J. Fluid Mech.*, 688:120–168, 2011.
- [40] S. Pirozzoli and P. Orlandi. Natural grid stretching for DNS of wall-bounded flows. *J. Comput. Phys.*, 439:110408, 2021. doi: <https://doi.org/10.1016/j.jcp.2021.110408>.
- [41] S. Pirozzoli, M. Bernardini, and F. Grasso. Direct numerical simulation of transonic shock-boundary layer interaction under conditions of incipient separation. *J. Fluid Mech.*, 657:361, 2010.
- [42] S. Pirozzoli, J. Romero, M. Fatica, R. Verzicco, and P. Orlandi. One-point statistics for turbulent pipe flow up to $re_\tau \approx 6000$. *J. Fluid Mech.*, 926, 2021.
- [43] L. Prandtl. Bericht über untersuchungen zur ausgebildeten turbulenz. *ZAMM-Journal of Applied Mathematics and Mechanics/Zeitschrift für Angewandte Mathematik und Mechanik*, 5(2):136–139, 1925.
- [44] O. Reynolds. On the extent and action of the heating surface of stream boilers. *Proc. Lit. Soc. Manchester*, 14:7–12, 1874.
- [45] M.W. Rubesin. *Extra compressibility terms for Favre-averaged two-equation models of inhomogeneous turbulent flows*. National Aeronautics and Space Administration, Ames Research Center, 1990.
- [46] J. A Sillero, J. Jiménez, and Robert D. Moser. One-point statistics for turbulent wall-bounded flows at Reynolds numbers up to $\delta+ \approx 2000$. *Phys. Fluids*, 25(10):105102, 2013.
- [47] M.W. Smith and A.J. Smits. Visualization of the structure of supersonic turbulent boundary layers. *Exp. Fluids*, 18(4):288–302, 1995.
- [48] A.J. Smits, K. Hayakawa, and K.C. Muck. Constant temperature hot-wire anemometer practice in supersonic flows. *Exp. Fluids*, 1(2):83–92, 1983.
- [49] A.J. Smits, B.J. McKeon, and I. Marusic. High-Reynolds number wall turbulence. *Annu. Rev. Fluid Mech.*, 43:353–375, 2011.

- [50] N.R. Tichenor, R.A. Humble, and R.D.W. Bowersox. Response of a hypersonic turbulent boundary layer to favourable pressure gradients. *J. Fluid Mech.*, 722:187–213, 2013.
- [51] C.D. Tomkins and R.J. Adrian. Energetic spanwise modes in the logarithmic layer of a turbulent boundary layer. *J. Fluid Mech.*, 545:141–162, 2005.
- [52] A. Trettel and J. Larsson. Mean velocity scaling for compressible wall turbulence with heat transfer. *Phys. Fluids*, 28(2):026102, 2016.
- [53] J. Urzay. Supersonic combustion in air-breathing propulsion systems for hypersonic flight. *Annu. Rev. Fluid Mech.*, 50:593–627, 2018.
- [54] E.R. Van Driest. Turbulent boundary layer in compressible fluids. *J. Aeronaut. Sci.*, 18(3):145–160, 1951.
- [55] E.R. Van Driest. The problem of aerodynamic heating. *Aeronaut. Engng. Rev.*, 15(10):26–41, 1956.
- [56] P.S. Volpiani, M. Bernardini, and J. Larsson. Effects of a nonadiabatic wall on hypersonic shock/boundary-layer interactions. *Phys. Rev. Fluids*, 5(1):1–30, 2020. ISSN 2469990X. doi: 10.1103/PhysRevFluids.5.014602.
- [57] P.S. Volpiani, P.S. Iyer, S. Pirozzoli, and J. Larsson. Data-driven compressibility transformation for turbulent wall layers. *Phys. Rev. Fluids*, 5(5):052602, 2020.
- [58] A. Walz. *Boundary layers of flow and temperature*. MIT Press, 1969.
- [59] C. Wenzel, B. Selent, M. Kloker, and U. Rist. Dns of compressible turbulent boundary layers and assessment of data/scaling-law quality. *J. of Fluid Mech.*, 842:428–468, 2018.
- [60] Christoph Wenzel, Tobias Gibis, and Markus Kloker. About the influences of compressibility, heat transfer and pressure gradients in compressible turbulent boundary layers. *J. Fluid Mech.*, 930, 2022.
- [61] O. Williams, D. Sahoo, M. Baumgartner, and Alexander A. Smits. Experiments on the structure and scaling of hypersonic turbulent boundary layers. *J. Fluid Mech.*, 834:237–270, 2018. ISSN 14697645. doi: 10.1017/jfm.2017.712.
- [62] O. Williams, D. Sahoo, M.L. Baumgartner, and A.J. Smits. Experiments on the structure and scaling of hypersonic turbulent boundary layers. *J. Fluid Mech.*, 834:237–270, 2018.
- [63] D. Xu, J. Wang, M. Wan, C. Yu, X. Li, and S. Chen. Compressibility effect in hypersonic boundary layer with isothermal wall condition. *Phys. Rev. Fluids*, 6(5):054609, 2021.
- [64] D. Xu, J. Wang, M. Wan, C. Yu, X. Li, and S. Chen. Effect of wall temperature on the kinetic energy transfer in a hypersonic turbulent boundary layer. *J. Fluid Mech.*, 929:A33, 2021.
- [65] C. Zhang, L. Duan, and M.M. Choudhari. Direct numerical simulation database for supersonic and hypersonic turbulent boundary layers. *AIAA J.*, 56(11):4297–4311, 2018. ISSN 00011452. doi: 10.2514/1.J057296.

- [66] Y.S. Zhang, W.T. Bi, F. Hussain, X.L. Li, and Z.S. She. Mach-number-invariant mean-velocity profile of compressible turbulent boundary layers. *Phys. Rev. Lett.*, 109(5):054502, 2012.
- [67] Y.S. Zhang, W.T. Bi, F. Hussain, and Z.S. She. A generalized Reynolds analogy for compressible wall-bounded turbulent flows. *J. Fluid Mech.*, 739:392–420, 2014.

Appendix B

Paper II

Assessment of heat transfer and Mach number effects on high-speed turbulent boundary layers

Michele Cogo¹, Umberto Baù², Mauro Chinappi³, Matteo Bernardini⁴, and Francesco Picano^{1,5}

1. Centro di Ateneo di Studi e Attività Spaziali "Giuseppe Colombo" - CISAS,
University of Padova, Padova, PD 35131, Italy
2. Institute of Fluid Mechanics and Heat Transfer, TU Wien, 1060 Vienna, Austria,
3. Department of Industrial Engineering, University of Rome Tor Vergata, via del Politecnico 1,
00133 Rome, Italy,
4. Department of Mechanical and Aerospace Engineering, Sapienza University of Rome, via
Eudossiana 18, 00184 Rome, Italy,
5. Department of Industrial Engineering, University of Padova, Padova, PD 35131, Italy.

Journal of Fluid Mechanics, 2022, 974, A10

Abstract: High-speed vehicles experience a highly challenging environment in which the free-stream Mach number and surface temperature greatly influence aerodynamic drag and heat transfer. The interplay of these two parameters strongly affects the near-wall dynamics of high-speed turbulent boundary layers in a non-trivial way, breaking similarity arguments on velocity and temperature fields, typically derived for adiabatic cases. In this work, we present direct numerical simulations of flat-plate zero-pressure-gradient turbulent boundary layers spanning three free-stream Mach numbers [2,4,6] and four wall temperature conditions (from adiabatic to very cold walls), emphasising the choice of the diabatic parameter Θ [44] to recover a similar flow organisation at different Mach numbers. We link qualitative observations on flow patterns to first- and second-order statistics to explain the strong decoupling of temperature-velocity fluctuations that occurs at reduced wall temperatures and high Mach numbers. For these cases, we find that the mean temperature gradient in the near-wall region can reach such a strong intensity that it promotes the formation of a secondary peak of thermal production in the viscous sublayer, which is in direct contrast with the monotonic behaviour of adiabatic profiles. We propose different physical mechanisms induced by wall-cooling and compressibility that result in apparently similar flow features, such as a higher peak in the streamwise velocity turbulence intensity, and distinct ones, such as the separation of turbulent scales.

Keywords: compressible boundary layers, turbulent boundary layers

Introduction

The study of highly compressible turbulent boundary layers is of major importance for high-speed turbulence research. Compressibility acts upon the flow by influencing the mean and fluctuating fields of thermodynamic quantities, which are in turn coupled to the momentum, promoting the energy exchange between kinetic and thermal fields. This poses several difficulties in the prediction of drag and wall heat transfer, which makes engineering design more and more difficult as higher speeds are attained.

In recent decades, supersonic turbulent boundary layers have been extensively studied and compared to their incompressible counterparts, mainly focusing on the prediction of drag assuming adiabatic walls, e.g. Bernardini and Pirozzoli [2], Duan et al. [13], Wenzel et al. [39]. In fact, at supersonic speeds the wall temperature can be considered for practical purposes very close to the recovery temperature of the flow, implying a very low heat exchange at the wall. The recovery temperature indicates the temperature that is attained by the flow when it is brought to rest in a non-isentropic manner, defined as

$$T_r = T_\infty \left(1 + r \frac{\gamma - 1}{2} M_\infty^2 \right), \quad (1)$$

being $r = Pr^{1/3}$ the recovery factor [42], where Pr is the Prandtl number. However, in hypersonic boundary layers, the recovery temperatures are so high that the wall temperature is usually lower [16, 34], generating large heat fluxes to the wall. This affects the flow dynamics in concurrency with the Mach number, enriching the physical effects that have to be accounted for when developing theoretical relations and reduced order models.

A renewed interest in hypersonic flight, along with the computational advancements that render Direct Numerical Simulations more feasible, sparked the attention on these problems, e.g. Wenzel et al. [40], Zhang et al. [42], but there is still a lack of understanding of the individual effect of different flow parameters.

The framework of theoretical relations applied to compressible flow for mean velocity and fluctuating fields aims at mapping compressible profiles onto incompressible reference by taking into account variations of mean properties such as density and viscosity. When applied to the mean velocity field, these relations are called compressibility transformations, first introduced by Van Driest [36] by accounting for mean density variations in the wall-normal velocity profile. Among the plethora of relations proposed in recent years, Volpiani et al. [37] and Griffin et al. [20] stand out as capable of efficiently collapsing velocity profiles even at high Mach numbers. While Volpiani et al. [37] uses a mixed physical and data-driven approach to determine the optimal parameters that define the weight of density and viscosity, Griffin et al. [20] base their arguments on the total-stress equation, allowing for separate assumptions for the viscous sublayer and the log layer.

Theoretical relations have also been derived to describe the interaction between kinetic and thermal fields, classically referred to as Strong Reynolds Analogy (SRA). First proposed by Morkovin [26], SRA establishes a framework based on the similarity between the momentum and total enthalpy equations, from which a direct proportionality between velocity and total enthalpy can be inferred. Under the more restrictive condition of wall adiabaticity, a set of relations coupling velocity and temperature can be derived for both mean and fluctuating fields, in which the temperature resembles a passive scalar field.

These relations have been extensively validated for adiabatic TBLs at different Mach numbers, e.g. Bernardini and Pirozzoli [2], Guarini et al. [21], Wenzel et al. [39], although at hypersonic speeds ($M_\infty > 5$) discrepancies start to arise [42]. Subsequent extensions of the SRA accounting for diabatic walls have been recently proposed (e.g. Zhang et al. [44]), which obtained promising results for different flow conditions, even when thermochemical effects are present [10, 27, 28].

A cold wall imposes a change in the sign of the mean temperature gradient near the wall, affecting the production of temperature fluctuations, which may result in a severe loss of similarity

between velocity and temperature fields, a building block of SRA, clearly visible in instantaneous snapshots of turbulent structures [8, 43]. However, these studies also noted that comparing cases with different Mach numbers at a fixed wall-to-recovery temperature ratio $T_w/T_r (< 1)$ resulted in vastly different near-wall dynamics for temperature fluctuations, in a way that cold cases at high M_∞ seemed “more adiabatic” than their low M_∞ counterparts. Recently, other definitions of the wall temperature condition have been proposed, such as the diabatic parameter $\Theta = (T_w - T_\infty)/(T_r - T_\infty)$ [44] or the Eckert number $Ec = (\gamma - 1)M_\infty^2 T_\infty/(T_r - T_w)$ [40], which are capable to account for the indirect effect of Mach number on the wall temperature condition. Although progress has been made to incorporate the effects of compressibility and heat transfer on these relations, their individual influence is still not well understood. While compressibility effects induced by the increase in Mach number can be similar to a change in wall temperature condition (and vice versa) for certain mechanisms, such as redistribution of turbulent kinetic energy [11], their relative role is still unclear in other aspects, such as separations of turbulent scales [23]. In this regard, wall-cooling has been shown to reduce the separation between the large and small turbulence scales in hypersonic flows [15, 23], but the specific role of the Mach number is still debated. Furthermore, while wall-cooling has been shown to be dominant in regulating energy exchanges in the near-wall region [15], the effect of the Mach number is still not clear. These and other authors called upon the need for additional computations to determine their individual effects.

The aim of this study is to unveil the physical mechanisms that yield similarities and differences between the effect of compressibility and wall-cooling. To pursue this objective, an extensive DNS database consisting of 12 simulations of zero-pressure-gradient TBLs has been computed fixing the friction Reynolds number ($Re_\tau \approx 450$), while spanning three Mach numbers $M_\infty = [2, 4, 6]$ and four diabatic parameters $\Theta = [0.25, 0.5, 0.75, 1.0]$, going from extremely cold walls, $\Theta = 0.25$, to adiabatic cases, $\Theta = 1$. The database is discussed in the present paper and made available to the scientific community to be used for the development of simplified models for high-speed wall-bounded flows with strong heat flux.

The remainder of the paper is organised as follows. The numerical method and details on the simulation setup are outlined in section §Simulation parameters and computational setup. In section §Instantaneous visualisation, a general visualisation of instantaneous velocity and temperature fields is given, describing the individual effect of Mach and wall temperature conditions on the flow dynamics and turbulent structures. Then, first-order statistics for mean velocity and temperature are presented in section §Mean flow statistics, which also compares different SRA formulations. Finally, second-order statistics are presented in section §Fluctuation statistics, focusing on the effect of wall-cooling on thermal production, and its implications on velocity-temperature correlations.

Simulation parameters and computational setup

The three-dimensional compressible Navier-Stokes equations are numerically solved for a viscous, heat-conducting gas

$$\begin{aligned} \frac{\partial \rho}{\partial t} + \frac{\partial(\rho u_j)}{\partial x_j} &= 0, \\ \frac{\partial(\rho u_i)}{\partial t} + \frac{\partial(\rho u_i u_j)}{\partial x_j} + \frac{\partial p}{\partial x_i} - \frac{\partial \sigma_{ij}}{\partial x_j} &= 0, \\ \frac{\partial(\rho E)}{\partial t} + \frac{\partial(\rho Eu_j + pu_j)}{\partial x_j} - \frac{\partial(\sigma_{ij} u_i - q_j)}{\partial x_j} &= 0, \end{aligned} \quad (2)$$

where ρ is the density, u_i denotes the velocity component in the i th Cartesian direction ($i = 1, 2, 3$), p is the thermodynamic pressure, $E = c_v T + u_i u_i / 2$ the total energy per unit mass and

$$\sigma_{ij} = \mu \left(\frac{\partial u_i}{\partial x_j} + \frac{\partial u_j}{\partial x_i} - \frac{2}{3} \frac{\partial u_k}{\partial x_k} \delta_{ij} \right), \quad q_j = -k \frac{\partial T}{\partial x_j} \quad (3)$$

represents the viscous stress tensor and the heat flux vector, respectively. The molecular viscosity μ is assumed to follow Sutherland's law

$$\frac{\mu}{\mu_\infty} = \left(\frac{T}{T_\infty} \right)^{1/2} \frac{1 + C/T_\infty}{1 + C/T}, \quad (4)$$

where $C = 110.4$ K and $T_\infty = 220.0$ K, representing the typical conditions that are met in the stratosphere. The thermal conductivity k is related to the viscosity by the expression $k = c_p \mu / Pr$, where c_p is the specific heat at constant pressure and the Prandtl number is $Pr = 0.72$. The thermodynamic variables are correlated to each other by means of the equation of state for a calorically perfect gas. This choice was also assumed for cases at $M_\infty = 6$, after having verified that by introducing a dependence of specific heat with temperature $c_p = f(T)$ differences in all statistics were negligible. Moreover, gas dissociation effects are also not expected in the present database, according to the observations of Passiatore et al. [28] who observed negligible effects with $T_w = 1800K$ (our highest imposed value is $T_w = 1640K$ for $M_\infty = 6$). The system of equations is solved on a Cartesian grid using the in-house code STREAmS [5, 6], which has been extensively validated in numerous canonical configurations [3, 4, 8]. Convective terms are discretised using high-order, energy-preserving schemes applied in shock-free regions, while a fifth-order shock capturing scheme (WENO) is applied when strong compressions are identified by the Ducros sensor [14]. Diffusive terms are discretised using a locally conservative formulation [9], expanded to Laplacian form to ensure finite molecular dissipation at all resolved wavelengths. The solver takes advantage of a multi-GPU architecture by means of the CUDA Fortran paradigm. The domain is a rectangular box of length $L_x = 100 \delta_{in}$, $L_y = 15 \delta_{in}$, $L_z = 9 \delta_{in}$, where δ_{in} is the boundary layer thickness at the inflow station, based on the 99% of the freestream velocity u_∞ (which is referred for other stations as δ_{99}). For all cases, the domain size in terms of the boundary-layer thickness measured in the proximity of the outflow is larger than $L_x/\delta_{99} = 39$, $L_y/\delta_{99} = 5.8$, $L_z/\delta_{99} = 3.5$, respectively. For each spatial direction, the number of computational points employed for all cases is $N_x = 5120$, $N_y = 320$, and $N_z = 512$. We verified that selected the grid satisfies the resolution requirement of $\Delta x_i/\eta < 5$ throughout the entirety of the BL thickness for all cases, being η the Kolmogorov

length scale. Periodic boundary conditions are enforced in the spanwise direction, purely non-reflecting boundary conditions are employed for the outflow and the top boundary, and unsteady characteristic boundary conditions are used at the bottom wall [31], where an isothermal wall temperature condition is enforced. The recycling-rescaling procedure [30] is applied at the inflow to reach a fully developed state, the recycling length being placed at a distance of $80 \delta_{in}$ from the inlet, ensuring a complete decorrelation of the fluctuations between the recycling station and the inflow plane [25].

Table 1 summarises the flow conditions and grid resolutions for each run, where M_∞ is the free-stream Mach number and Re_τ is the friction Reynolds number, defined as the ratio between the boundary layer thickness δ_{99} and the viscous length scale $\delta_\nu = \nu_w/u_\tau$, where $u_\tau = \sqrt{\tau_w/\rho_w}$ is the friction velocity, τ_w is the mean wall shear stress, and ν_w is the kinematic viscosity at the wall. $\Delta x^+ = \Delta x/\delta_\nu$ and $\Delta z^+ = \Delta z/\delta_\nu$ are the uniform grid spacings in the streamwise and spanwise directions and $\Delta y^+ = \Delta y/\delta_\nu$ represents the non-uniform wall-normal grid spacing (the wall and edge values are reported). In the wall-normal direction, the stretching function of Pirozzoli and Orlandi [29] is employed, which provides a more favourable scaling of the number of grid points with the Reynolds number. Furthermore, this function has the natural property of yielding precisely constant resolution in terms of the local Kolmogorov length scale η in the outer part of the wall layer while maintaining a uniform near-wall spacing.

The present database is composed of a total of 12 simulations, spanning three Mach numbers $M_\infty = [2, 4, 6]$ and four diabatic parameters $\Theta = [0.25, 0.5, 0.75, 1.0]$ (see Table 1). We stress that the choice of using the diabatic parameter throughout this study is made in order to recover a similar degree of wall-cooling across different Mach numbers. In fact, the goal of a suitable parameter is not to be independent of M_∞ , but to incorporate it in order to have “the same integral behaviour between different cases, regardless of whether its variation is caused by the change of the Mach number or of the wall temperature” [40]. This is the rationale with which Wenzel et al. [40] argued that the Eckert number $Ec = (\gamma - 1)M_\infty^2 T_\infty/(T_r - T_w)$ represents a more suitable option than the conventional T_w/T_r ratio. The Eckert number happens to be directly related to the diabatic parameter $\Theta = (T_w - T_\infty)/(T_r - T_\infty)$ proposed by Zhang et al. [44], since it can be shown that $Ec = 2/[r(1 - \Theta)]$. This parameter shows more clearly the improvement over the conventional ratio T_w/T_r , showing that T_∞ needs to be subtracted from both T_w and T_r to compare only the ΔT that is recovered when the flow is brought at rest, being the only one responsible for kinetic-internal energy exchange. In this study, we choose to use the diabatic parameter Θ over Ec given its simplicity, but we also report the latter in Table 1. Table 2 summarises the boundary layer parameters at selected locations where turbulence statistics are gathered. All the simulations were initially run for about $600 \delta_{in}/u_\infty$, a time sufficient to achieve a fully developed turbulent condition before starting to collect statistics. The time averaging period for all cases exceeds $1000 \delta_{in}/u_\infty$ ($28 \delta_{99}/u_\tau$) and approximately 1000 flow samples, equally spaced in time, were considered.

Throughout this study, we use the symbols u , v , and w to denote the streamwise, wall-normal and spanwise velocity components and the decomposition of any variable is conducted using either the standard Reynolds decomposition ($f = \bar{f} + f'$) or the density-weighted (Favre) representation ($f = \tilde{f} + f''$), being $\tilde{f} = \bar{\rho}f/\bar{\rho}$. Here, the averaging is conducted using multiple samples and along the periodic direction z .

| Run | M_∞ | Re_τ | Θ | T_w/T_r | Ec | Δx^+ | $\Delta y_{w,edge}^+$ | Δz^+ |
|--------|------------|-----------|----------|-----------|----------|--------------|-----------------------|--------------|
| M2T025 | 2.00 | 436 – 579 | 0.25 | 0.69 | 2.975 | 4.51 | 0.71-4.64 | 4.07 |
| M2T050 | 2.00 | 427 – 564 | 0.5 | 0.79 | 4.463 | 4.52 | 0.71-4.64 | 4.07 |
| M2T075 | 2.00 | 424 – 561 | 0.75 | 0.9 | 8.926 | 4.53 | 0.71-4.65 | 4.08 |
| M2T100 | 2.00 | 415 – 548 | 1.0 | 1.0 | ∞ | 4.52 | 0.71-4.64 | 4.07 |
| M4T025 | 4.00 | 404 – 535 | 0.25 | 0.44 | 2.975 | 4.36 | 0.68-4.52 | 3.93 |
| M4T050 | 4.00 | 391 – 521 | 0.5 | 0.63 | 4.463 | 4.38 | 0.68-4.53 | 3.94 |
| M4T075 | 4.00 | 379 – 507 | 0.75 | 0.81 | 8.926 | 4.37 | 0.68-4.53 | 3.94 |
| M4T100 | 4.00 | 371 – 494 | 1.0 | 1.0. | ∞ | 4.38 | 0.68-4.53 | 3.95 |
| M6T025 | 6.00 | 376 – 500 | 0.25 | 0.35 | 2.975 | 4.24 | 0.66-4.42 | 3.82 |
| M6T050 | 6.00 | 351 – 470 | 0.5 | 0.57 | 4.463 | 4.21 | 0.66-4.40 | 3.80 |
| M6T075 | 6.00 | 343 – 462 | 0.75 | 0.78 | 8.926 | 4.24 | 0.66-4.43 | 3.83 |
| M6T100 | 6.00 | 337 – 451 | 1.0 | 1.0 | ∞ | 4.26 | 0.67-4.44 | 3.84 |

Table 1: Summary of parameters for DNS study. Grid spacings are given in wall-units according to the stations selected in table 2. The values of Δy_w^+ and Δy_{edge}^+ refer to the wall-normal spacing at the wall and at the boundary layer edge, respectively. The range of Re_τ is representative of the statistical growth of the boundary layer’s thickness along x . Ranges reported for Re_τ refer to the second half of the domain, while all cases share the same inflow friction Reynolds number of $Re_\tau = 250$.

| Station | Re_τ | Re_θ | Re_{δ_2} | Re_τ^* | δ^*/δ | θ/δ | H | $-B_q(\cdot 10^{-2})$ | $C_f(\cdot 10^{-3})$ |
|---------|-----------|-------------|-----------------|-------------|-------------------|-----------------|--------|-----------------------|----------------------|
| M2T025 | 443 | 1226 | 1071 | 551 | 0.210 | 0.092 | 2.291 | 2.29 | 3.40 |
| M2T050 | 443 | 1470 | 1150 | 661 | 0.224 | 0.088 | 2.528 | 1.34 | 3.16 |
| M2T075 | 443 | 1698 | 1209 | 772 | 0.234 | 0.085 | 2.756 | 0.57 | 2.99 |
| M2T100 | 443 | 1961 | 1288 | 886 | 0.246 | 0.083 | 2.979 | -0.08 | 2.79 |
| M4T025 | 443 | 1795 | 1178 | 886 | 0.314 | 0.067 | 4.669 | 6.10 | 2.19 |
| M4T050 | 443 | 2680 | 1379 | 1346 | 0.331 | 0.061 | 5.460 | 3.07 | 1.85 |
| M4T075 | 443 | 3601 | 1565 | 1815 | 0.355 | 0.056 | 6.297 | 1.17 | 1.61 |
| M4T100 | 443 | 4453 | 1703 | 2285 | 0.367 | 0.052 | 7.030 | -0.17 | 1.43 |
| M6T025 | 443 | 2675 | 1313 | 1466 | 0.399 | 0.048 | 8.279 | 8.89 | 1.39 |
| M6T050 | 443 | 4702 | 1704 | 2529 | 0.426 | 0.043 | 9.813 | 4.05 | 1.09 |
| M6T075 | 443 | 6460 | 1932 | 3603 | 0.443 | 0.039 | 11.485 | 1.49 | 0.93 |
| M6T100 | 443 | 8254 | 2146 | 4675 | 0.454 | 0.036 | 12.800 | -0.16 | 0.81 |

Table 2: Boundary layer properties averaged at the selected station. $Re_\tau = \rho_w u_\tau \delta / \mu_w$; $Re_\theta = \rho_\infty u_\infty \theta / \mu_\infty$; $Re_{\delta_2} = \rho_\infty u_\infty \theta / \mu_w$; $Re_\tau^* = \sqrt{\rho_\infty \tau_w \delta} / \mu_\infty$; $H = \delta^*/\theta$ (δ^* and θ are the boundary layer displacement and momentum thickness, respectively). $B_q = q_w / (\rho_w C_p u_\tau T_w)$ and $C_f = \tau_w / (1/2 \rho_\infty u_\infty^2)$ are the nondimensional wall heat transfer $q_w = -\bar{k} \partial \tilde{T} / \partial y$ and skin friction coefficient $\tau_w = \bar{\mu} \partial \tilde{u} / \partial y$, respectively.

Instantaneous visualisation

To highlight the emerging features of the flow in a qualitative way, we selected the two extreme cases with regard to the wall-cooling condition, $\Theta = 0.25$ and $\Theta = 1.0$, for each Mach number in our database. Figure 1 shows a portion of wall-normal x - y planes coloured with the instantaneous density, whose variability is a clear sign of the degree of compressibility. The effect of Mach number is clearly apparent for all cases moving from top to bottom with a decrease of the minimum value of density and an increase of the general level of acoustic disturbances, generated in the boundary layer and emanated towards the far field. However, a stronger wall-cooling (lower Θ , left column of figure 1) attenuates this effect, since lower wall temperatures generate higher density fields in the near wall region.

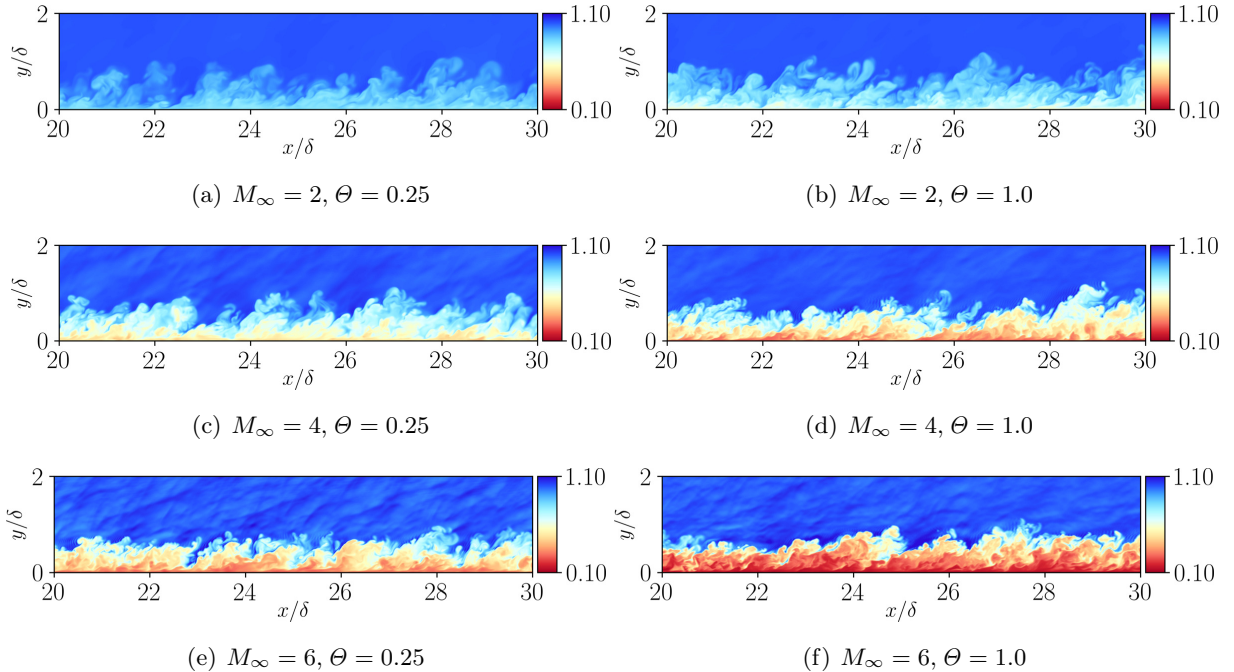


Figure 1: Instantaneous density in wall-normal slices (x - y plane), with a window size of $\Delta x = 20\delta - 30\delta$ and $\Delta y = 0\delta - 2\delta$. Here, all Mach numbers are shown while the two extremes are chosen with regard to wall-cooling ($\Theta = 0.25$ and $\Theta = 1.0$).

The intensity of wall-cooling strongly affects the coupling between velocity and temperature fluctuations, especially in the near-wall region. This is apparent in figure 2, which compares these quantities in wall-parallel slices located at approximately $y^* \approx 10$, representing the onset turbulence activity after the viscous sub-layer. Here, $y^* = y/\delta_{\nu,SL}$ is the semilocal scaled wall-normal coordinate, with $\delta_{\nu,SL} = \bar{\nu}/\sqrt{\tau_w/\bar{\rho}}$. The chosen x - z planes are centred at the selected stations of table 1 spanning a window of $\Delta x^* = 4000$ and $\Delta z^* = 600$. Velocity fluctuations $\sqrt{\bar{\rho}u'}/\sqrt{\tau_w}$ are scaled according to the Morkovin's transformation [26] (also used in section §Velocity fluctuations and length scales), which enables comparison across different Mach numbers and wall temperature values by accounting for the variation of the mean properties of the flow. In other words, velocity fluctuations are scaled by the semilocal friction velocity $u_{\tau,SL} = \sqrt{\tau_w/\bar{\rho}}$, which differs from the conventional one by employing the mean density $\bar{\rho}$ instead of the wall density ρ_w . Temperature fluctuations $\bar{\rho}T'/(R\tau_w)$ are scaled in a similar fashion, assuming τ_w as proper parameter to scale pressure fluctuations, then $\tau_w/(R\bar{\rho})$ can be used to scale temperature (for further details refer to

section §Thermodynamic quantities). A general look at the velocity fluctuations shows the presence of near-wall streaks for all cases, representative of the near-wall self-sustaining cycle of turbulence. Similar values of intensities appear across all cases. This result is not observed for temperature fluctuations, where cold cases ($\Theta < 1$) show reduced intensity and a clear breakdown of elongated streaks, appearing more isotropic when compared to their adiabatic counterpart. Adiabatic cases maintain a streaky pattern, which shows a clear coupling with the velocity field. It is worth noting that the similarity between cold cases across different Mach numbers (left column of figure 2) is attained using the same value of Θ , while effectively the wall-to-recovery temperature ratio T_w/T_r varies. Clearly different patterns emerge matching the latter, as visible in Cogo et al. [8]. Although this behaviour will be further discussed in the following sections by analysing temperature fluctuations and thermal production profiles, these qualitative results are consistent with the discussion of Wenzel et al. [40], which states that the same general behaviour due to the effect of wall-cooling is expected when comparing flows with the same Eckert number (or diabatic parameter Θ).

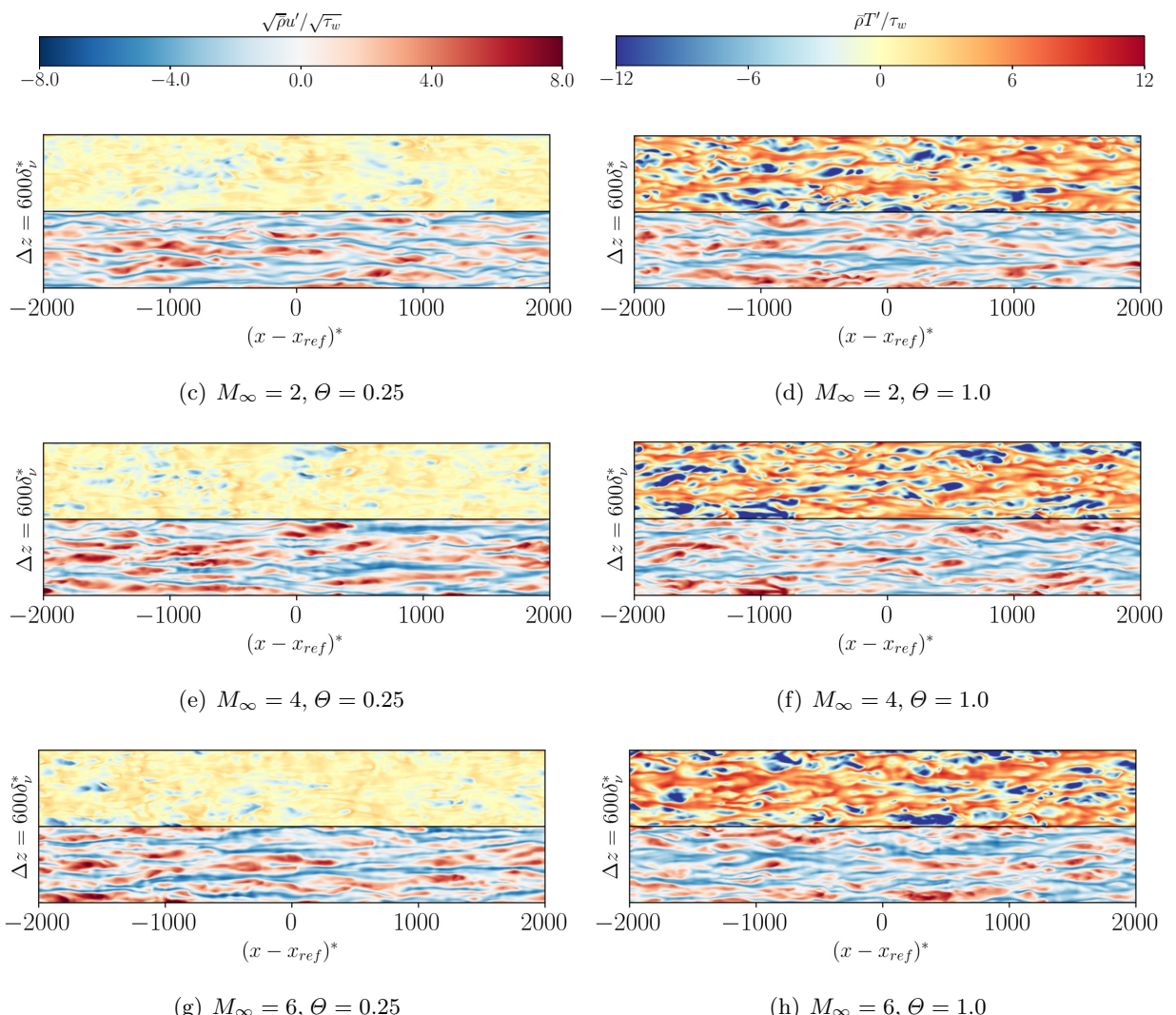


Figure 2: Temperature fluctuations $\bar{\rho}T'/\tau_w$ (top) and streamwise velocity fluctuations $\sqrt{\bar{\rho}u'}/\sqrt{\tau_w}$ (bottom) in wall-parallel slices (x - z plane) selected at $y^* \approx 10$. Here, all Mach numbers are shown while the two extremes are chosen with regard to wall-cooling ($\Theta = 0.25$ and $\Theta = 1.0$). Here, x_{ref} is the streamwise location of the selected station.

Mean flow statistics

In this section, we present the wall-normal profiles of averaged quantities such as velocity and temperature, selected at stations listed in table 2. In the framework of compressibility transformations, we consider the classical relation of Van Driest [35] (which has been the standard for several decades and widely employed in wall modelling) and the recent transformations of Volpiani et al. [37] and Griffin et al. [20]. In general, we find that the latter developments have a wide range of applicability over our database, while Van Driest [35] transformation shows poor accuracy as Mach number and wall-cooling increase. The results confirm the overall behaviour noted by Cogo et al. [8], and the interested reader can find them in Appendix .

Figures 3(a) to 3(e) show the mean temperature profiles throughout the height of the boundary layer and in the near-wall region, respectively. In particular, all profiles are scaled considering their incremental variation and their relative intensity with respect to T_w . This is done in order to highlight the effects of wall-cooling on the peak intensity and location. As expected, the adiabatic wall temperature greatly increases with the Mach number, while enhanced wall-cooling (lower Θ) forces the mean temperature profiles to slant towards lower wall temperatures ($T_w < T_r$). The combination of these two conditions imposes a change in the sign of temperature gradient near the wall, which is necessary to adjust to a wall temperature lower than the recovery value. Thus, a local peak arises, whose prominence and location are directly connected to the phenomenon of aerodynamic heating, generating a net heat flux from the flow to the solid boundary. Local temperature peaks are marked in figures 3(b) to 3(e) with dots. An increase in the Mach number generates more intense gradients and higher peak temperatures for non-adiabatic cases, enhancing aerodynamic heating. However, the wall-normal position of the peaks seems to be mainly affected by the change Θ , and weakly dependent on the Mach number. This is apparent in Figure 3(f), which shows a progressive departure from the wall of the peak location as the wall-cooling increases, with a mild downward shift at high Mach numbers. As anticipated in section §Instantaneous visualisation, the position of the local maximum of the temperature profile has major implications in the generation of temperature fluctuations, which affect both their overall intensity and their spatial organisation (breakdown of near-wall streaks). Actually, the departure from a monotonic adiabatic profile to increasingly prominent local peaks of mean temperature profiles prevents the formation of organised temperature streaks that are generated by thermal production (see section §Thermodynamic quantities).

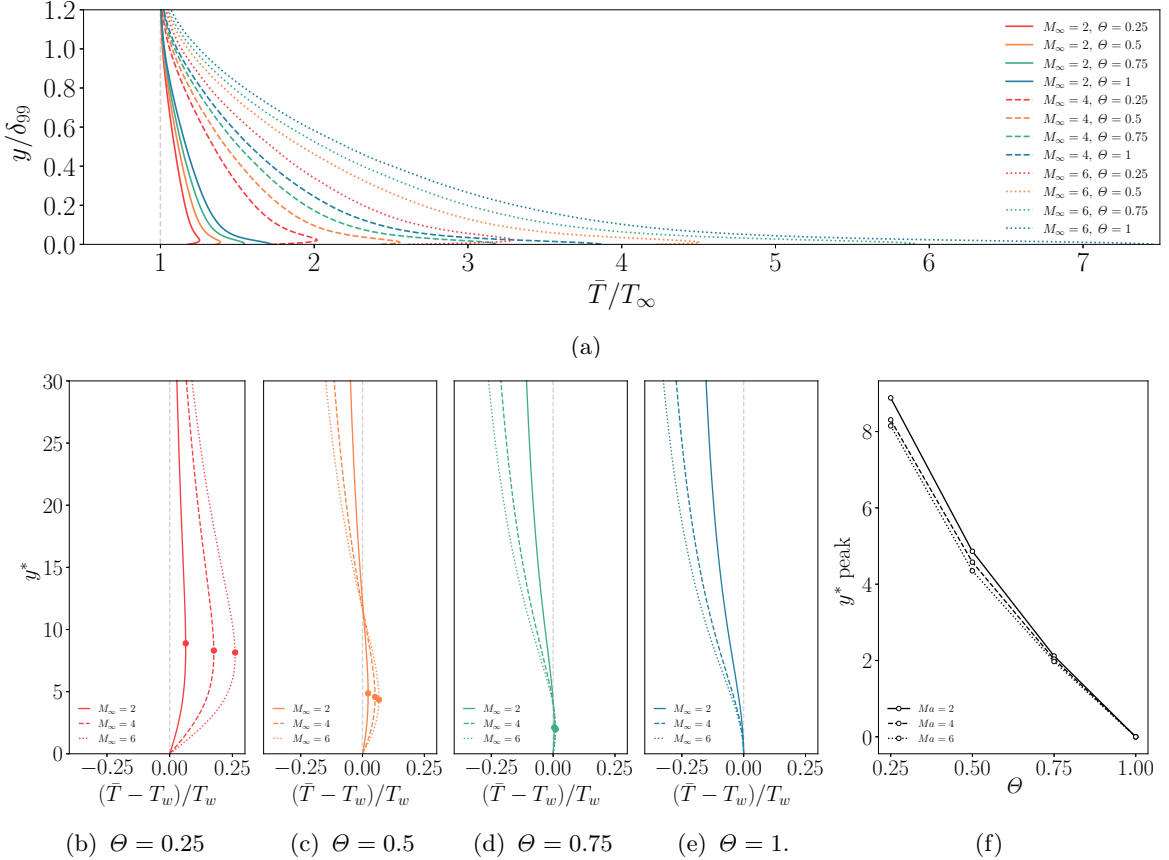


Figure 3: Panel (a): Mean temperature profiles for all cases of table 1 as a function of the wall-normal coordinate y/δ_{99} . Panels (b-c-d-e): Mean temperature profiles and relative peaks as a function of the wall-normal coordinate y^* scaled with T_w . Panel (f): Wall-normal position of mean temperature peaks as a function of the wall-cooling Θ parameter.

Reynolds analogy

In the framework of the Reynolds analogy, we discuss the coupling between velocity and temperature with a particular focus on the validity of theoretical relations across the present database. The relation between mean temperature and velocity can be approximated by a quadratic law, as apparent by the classical relation of Walz [38]

$$\frac{\bar{T}}{T_\infty} = \frac{T_w}{T_\infty} + \frac{T_r - T_w}{T_\infty} \frac{\bar{u}}{U_\infty} + \frac{T_\infty - T_r}{T_\infty} \left(\frac{\bar{u}}{U_\infty} \right)^2 \quad (5)$$

More recently, Zhang et al. [44] improved this relation in order to account for high Mach number and large heat fluxes:

$$\frac{\bar{T}}{T_\infty} = \frac{T_w}{T_\infty} + \frac{T_{rg} - T_w}{T_\infty} \frac{\bar{u}}{U_\infty} + \frac{T_\infty - T_{rg}}{T_\infty} \left(\frac{\bar{u}}{U_\infty} \right)^2 \quad (6)$$

where $T_{rg} = T_\infty + r_g U_\infty^2 / (2c_p)$ and $r_g = 2c_p(T_w - T_\infty)/U_\infty^2 - 2Pr q_w/(U_\infty \tau_w)$. As reported in the Appendix, our database confirms the aptness of the latter expression, with minor deviations for the most challenging case (M6T025). For engineering design purposes, the value of r_g can be difficult to evaluate given its dependence on the wall temperature T_w and the ratio of the wall heat flux q_w and the wall shear stress τ_w . Following the discussion of Zhang et al. [44], the Reynolds analogy

factor s comes into play to greatly simplify the calculation, since r_g can be rewritten in terms of s

$$r_g = r[sPr + (1 - sPr)\Theta] \quad (7)$$

being s defined as

$$s = \frac{2C_h}{C_f} = \frac{q_w u_\infty}{\tau_w c_p (T_w - T_r)} \quad (8)$$

where $C_f = \tau_w / (1/2 \rho_\infty u_\infty^2)$ is the skin friction coefficient and $C_h = q_w / (\rho_\infty u_\infty c_p (T_w - T_r))$ the Stanton number. The simplification consists in the fact that several authors [12, 41, 44] identified the term sPr to be an empirical constant around the value of 0.8 ± 0.03 (data fitting of Zhang et al. [44]) over several different flow cases, meaning that only T_w would be needed to be evaluated to compute r_g .

Figure 4 reports the computed values of sPr in our database showing a good agreement to Zhang et al. [44] fit. A slight decreasing trend with Θ can be observed, and it is interesting to note that at a given Θ the values appear to be independent of M_∞ .

The data reported in figure 4 have a mean value and standard deviation of 0.78 ± 0.03 , which is close to the value reported by [44]. By approximating r_g in Eq. (7) with the mean value of sPr and comparing it with DNS data, we obtain a maximum error of 5% (for the case M6T025), which can be considered acceptable for engineering purposes.

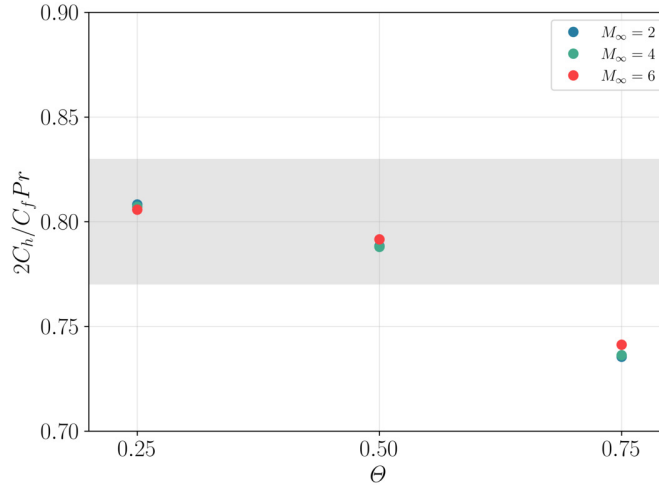


Figure 4: Reynolds analogy factor $s = 2C_h/C_fPr$ as a function of the diabatic parameter Θ for different Mach numbers. The grey band refers to the data fitting of 0.8 ± 0.03 of Zhang et al. [44].

Another important set of theoretical relations that couple the thermodynamic and kinetic fluctuating fields is given by the Strong Reynolds Analogy (SRA) [26]. This set of relations has been modified over the years to account for finite heat flux at the wall and remove wall temperature dependence [19, 24, 44] (HSRA). Our database shows that the most recent developments clearly improve its accuracy and the insensitivity to the freestream Mach number and wall temperature condition, with only slight deviations at the edge of the boundary layer (see Appendix). Moreover, results also highlight the ability of the diabatic parameter Θ in recovering the same behaviour in terms of wall-cooling across different Mach numbers.

Fluctuation statistics

Velocity fluctuations and length scales

The distribution of velocity fluctuation intensities and Reynolds shear stress is reported in the left panels of figures 5 and 6, using the classical transformation of Morkovin [26]:

$$(u_i^*)^2 = \frac{\widetilde{u_i''}^2}{u_\tau^2} \frac{\bar{\rho}}{\bar{\rho}_w}, \quad (uv)^* = \frac{\widetilde{u''v''}}{u_\tau^2} \frac{\bar{\rho}}{\bar{\rho}_w}. \quad (9)$$

The profiles are shown as a function of the wall-normal distance in semilocal scaling y^* [24], considering its ability to collapse compressible profiles of different Mach numbers and wall temperature conditions, in particular with respect to the peak positions [42, 43]. This choice facilitates the comparison across different cases of our database in terms of wall-normal location, even though differences in their intensity are preserved. Right panels of figures 5 and 6 show the corresponding turbulent kinetic energy budget terms, (being $k = \widetilde{u_i''}^2/2$ the turbulent kinetic energy, TKE) according to the derivation of Zhang et al. [42], where P is the production term, TT represents the turbulent transport, Π includes the pressure diffusion and dilatation, $-\phi$ is the viscous dissipation and D is the viscous diffusion. For these results, semilocal scaling is also employed in the normalisation of budget terms (refer to Zhang et al. [42]) and for the wall-normal distance y^* , enabling a good collapse between different profiles [8, 42].

The effect of wall-cooling on velocity fluctuations, shown in the left panels of figure 5, is apparent as an increase in the peak of the streamwise component located at $y^* \approx 15$ that is more prominent at high Mach numbers. In contrast, the spanwise component of highly cooled cases shows the opposite behaviour, being reduced in intensity compared to the adiabatic reference. This implies an increase in the anisotropy of normal components of Reynolds stresses in the near-wall region, which is discussed in more detail at the end of this section. The semilocal scaling provides an excellent collapse of the peak positions for all cases, preventing the outward shift that is present for cold cases when plotted in wall units (not shown). This is also true for the position of the turbulent production peak (right panels of figure 5), which would move farther from the wall if displayed in wall units. In general, the effect of wall-cooling on the turbulent kinetic energy budget is marked in the very near-wall region, especially at high Mach numbers, while all profiles progressively collapse in the outer layer.

The effect of the Mach number on velocity fluctuations is reported in the left panels of figure 6, where an increase of the streamwise component peak with the Mach number is apparent, while the other normal components intensities are observed to weakly decrease until $y^* < 40$. Unlike the wall-cooling effect, all normal components increase in the log layer as M_∞ increases. We note that this effect could be reduced at the BL edge by matching the semilocal friction Reynolds number Re_τ^* in place of the conventional definition (see table 1), which would allow all profiles to collapse when $y^* \approx Re_\tau^*$. In fact, Re_τ^* has been shown by several authors to better incorporate compressibility and wall-cooling effects on the separation of scales in highly-compressible flows (e.g. Griffin et al. [20], Hirai et al. [22]). However, in the present study we preferred to match wall-related quantities (i.e. Re_τ) and discuss the influence of M_∞ and Θ on the separation of turbulent scales through the boundary layer thickness.

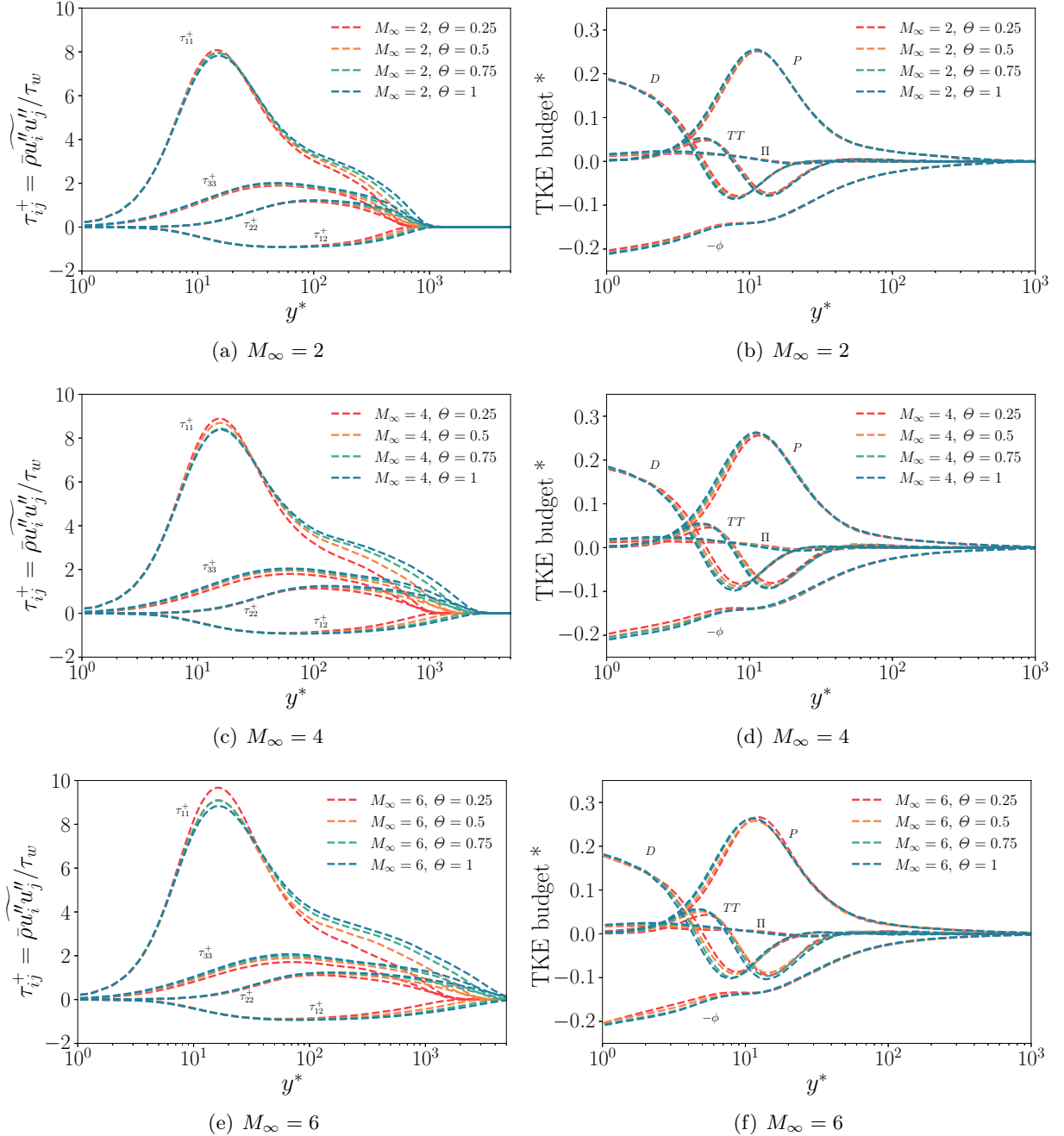


Figure 5: Semilocal-scaled turbulent velocity fluctuations (a,c,e) and turbulent kinetic energy budget (b,d,f) as function of the wall-normal distance y^* . Here, different diabatic parameters Θ are compared at a given Mach number M_∞ .

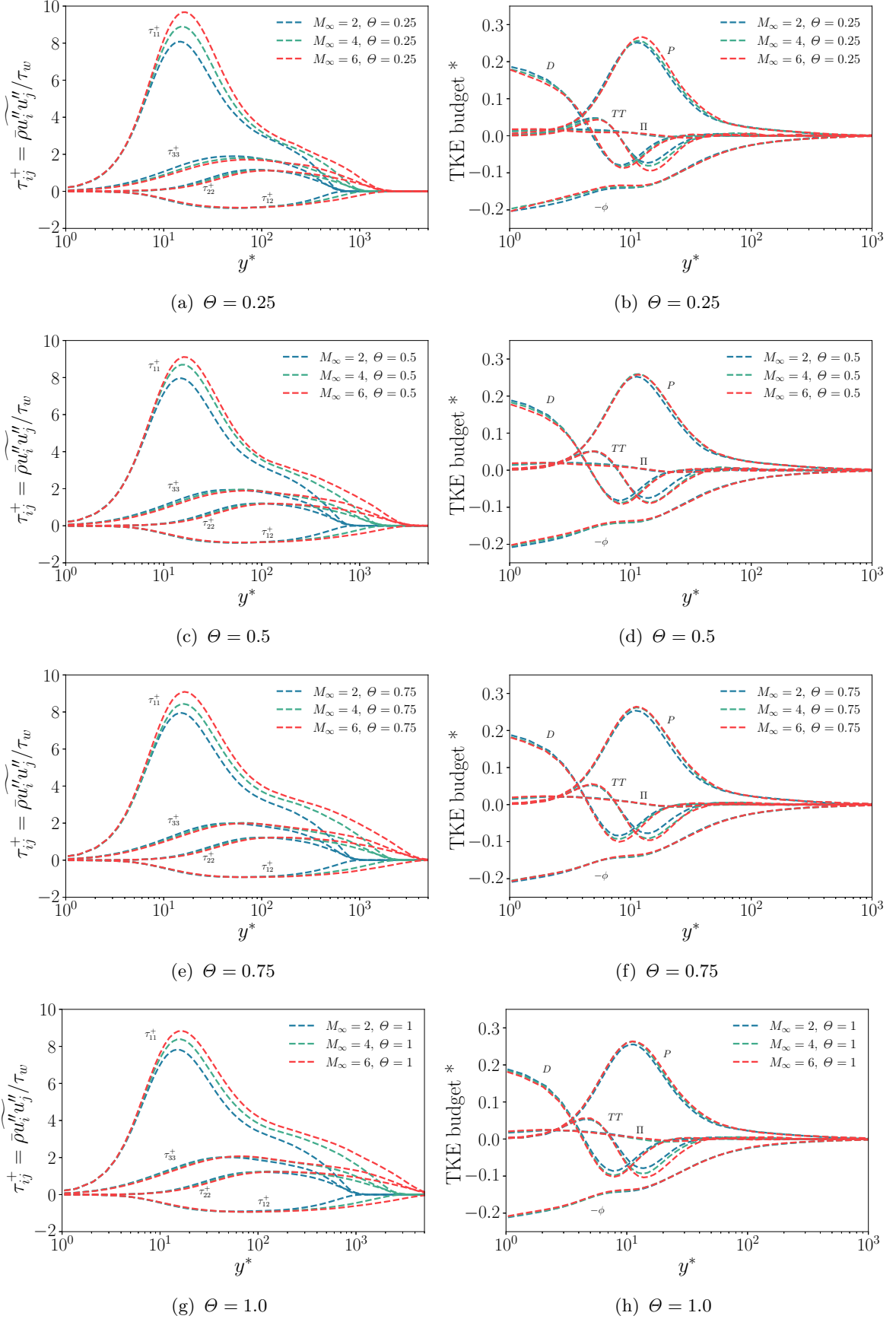


Figure 6: Semilocal-scaled turbulent velocity fluctuations (a,c,e,g) and turbulent kinetic budget (b,d,f,h) as function of the wall-normal distance y^* . Here, different Mach number M_∞ are compared at a given diabatic parameter Θ .

This suggests that compressibility acts in the direction of increasing the scale separation in the outer layer, while wall-cooling has the opposite effect [15]. For all values of Θ , the turbulent kinetic energy budget (right panels of figure 6), shows an increase of the production term P in the buffer and log layers as the Mach number increases and a corresponding decrease of diffusion D and turbulent transport TT in the same regions, consistently with Cogo et al. [8], who noted the presence of this effect also in the outer region at higher Re_τ . While the effect of wall-cooling on the TKE budget seems confined in the near-wall region, the influence of Mach number is more prominent after the peak of production and throughout the log layer. Further insights on the mechanism of redistribution of turbulent kinetic energy in the near-wall region can be gained by looking at the ratio between the streamwise component of the pressure-strain term and the streamwise component of turbulent production [12]:

$$\mathcal{R} = \left(\overline{p' \frac{\partial u''}{\partial x}} \right) / \left(\overline{\rho u'' v''} \frac{\partial \tilde{u}}{\partial y} \right) \quad (10)$$

which is a measure of the energy transfer from the streamwise velocity fluctuations to the others.

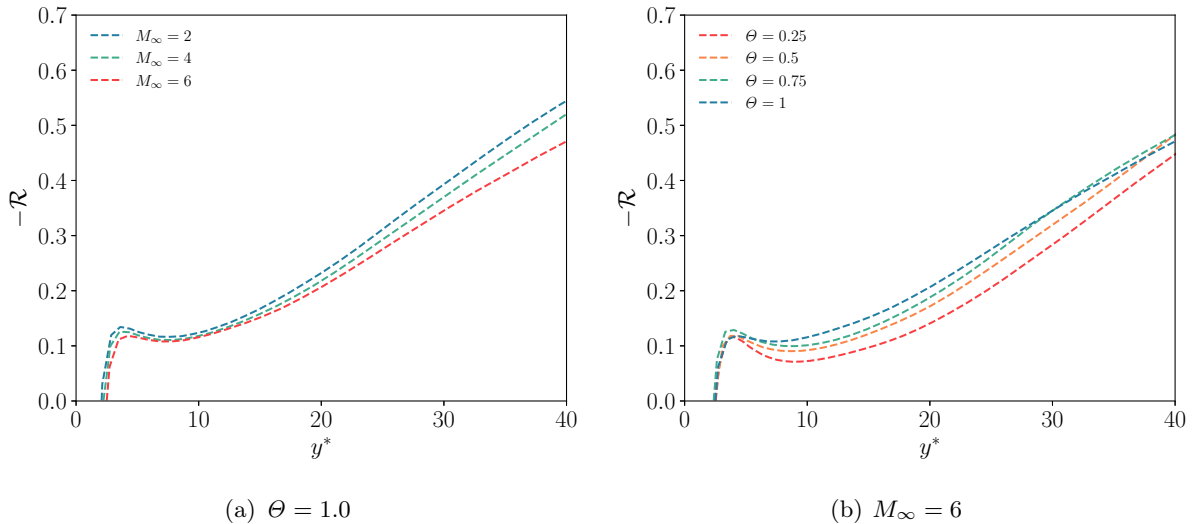


Figure 7: Ratio of streamwise components of pressure-strain and turbulent production terms for cases at (a) $\Theta = 1.0$ and (b) $M_\infty = 6$, as function of the wall-normal distance in semilocal units.

The role of the pressure-strain term in increasing turbulence anisotropy was also noted for other flows (e.g. Foysi et al. [17]). To gauge the respective effects of the Mach number and the wall temperature condition, figure 7 compares $-\mathcal{R}$ for cases at $\Theta = 1.0$ (figure 7(a)) and at $M_\infty = 6$ (figure 7(b)). In panel 7(a), profiles of $-\mathcal{R}$ are reduced in magnitude as compressibility increases, with greater intensity farther from the wall.

This is consistent with the less efficient redistribution of turbulent kinetic energy discussed before, and is attributed to the absence of a solenoidal condition for the velocity field for highly-compressible cases preventing an efficient energy transfer between velocity components. Looking at panel 7(b), we observe that wall-cooling acts similarly to an increase of compressibility, strongly decreasing the profiles of $-\mathcal{R}$, but its effect is localised in the near-wall region and strongly reduced after the buffer layer.

We attribute this effect to a localised stratification of flow properties in the near-wall region. As wall-cooling is increased and the location of the mean temperature peak approaches the buffer

layer, the flow above and below the peak location is relatively colder and denser. This is true for all Mach numbers in our database (although with different intensities), since the temperature peak location remains unaffected (see figure 3(f)). However, the effect is marked when the peak intensity is higher (i.e. $M_\infty = 6$). This is visible in figure 8, where case M6T025 of panel (a) exhibits a high temperature substrate in the near-wall region surrounded by a colder flow above and below, which is in direct contrast with the adiabatic case shown in panel (b).

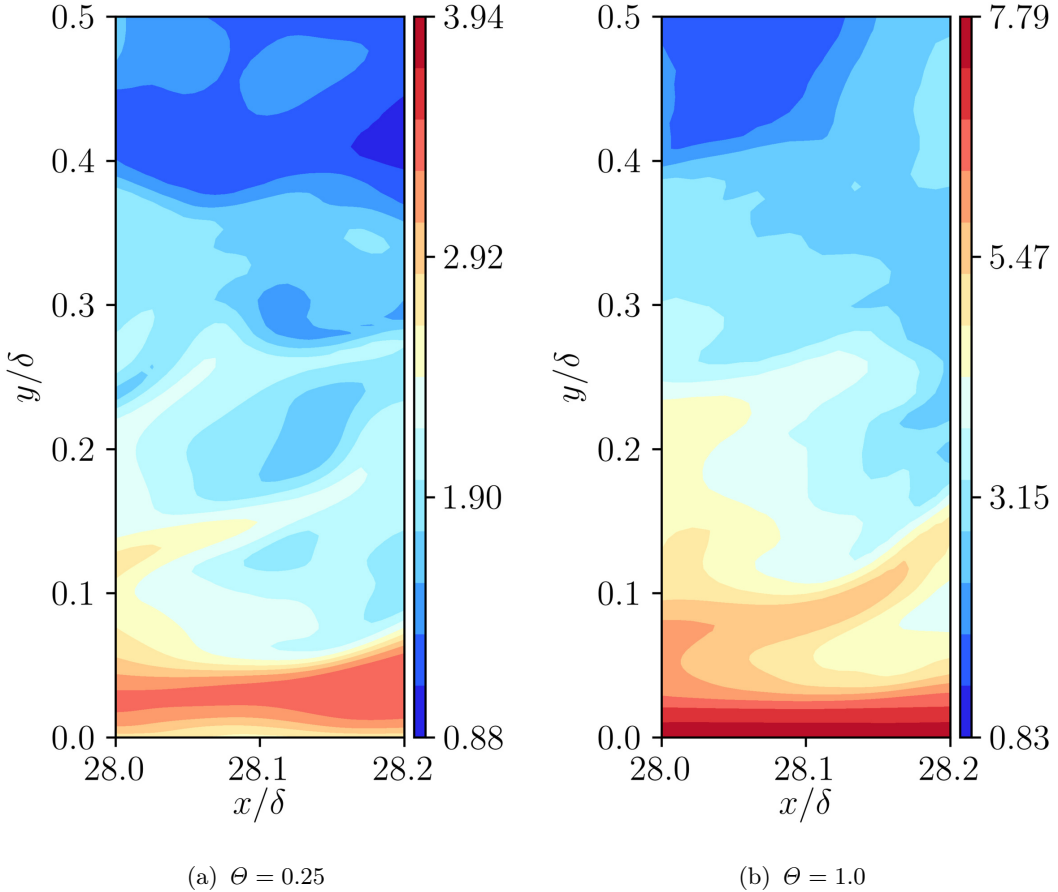


Figure 8: Instantaneous temperature contours in wall-normal slices (x - y plane) at $M_\infty = 6$. Panel (a): case M6T025 (cold wall), panel (b): case M6T100 (adiabatic).

This localised stratification forces turbulent fluctuations to be active almost only in the streamwise direction, while the other components tend to be suppressed.

This effect is quantified in figure 9 by showing the barycentric map of Banerjee et al. [1], which shows principal components of turbulence anisotropy. The invariant map is composed of three limiting states: one-component (x_{1c}), axisymmetric two-component (x_{2c}) and isotropic (x_{3c}); which are representative of the relative strengths of the fluctuating velocity components. Looking at figure 9(a), we note that the cusp point, which coincides approximately with the peak of velocity fluctuations in the buffer layer, shifts towards a one-component behaviour (x_{1c}) as M_∞ increases. This effect is strongly enhanced by wall cooling, figure 9(b), which further promotes the one-dimensional state of the flow.

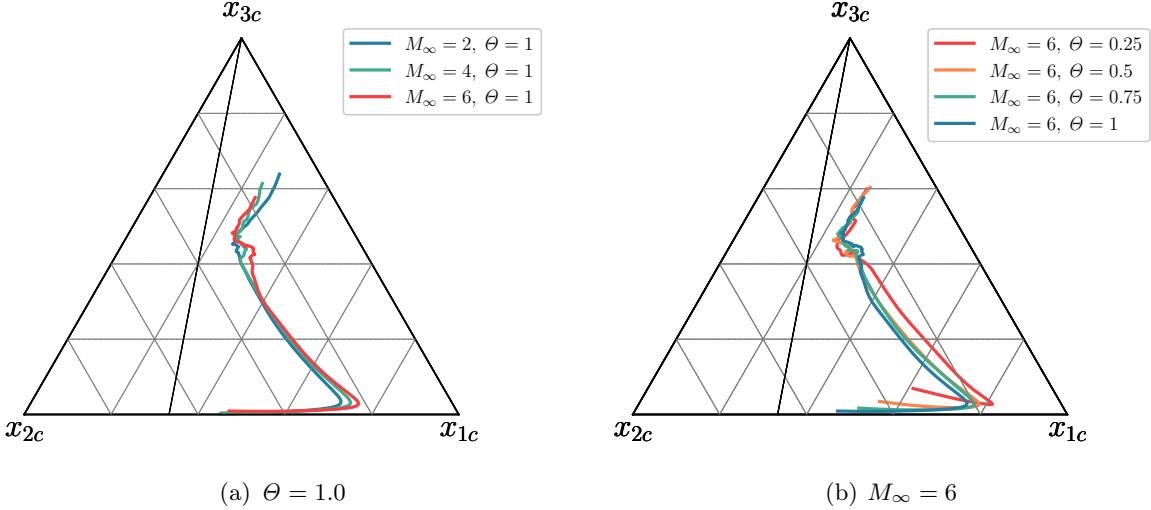


Figure 9: Barycentric map of Banerjee et al. [1] for cases at (a) $\Theta = 1.0$ and (b) $M_\infty = 6$. Each point in the trajectories represents a different wall-normal location within the boundary layer up to the edge.

We note that although this effect resembles a promotion of compressibility, as noted by several authors [7, 11], the underlying mechanism is strongly different and relevant only when M_∞ is high. In fact, different wall-cooling and compressibility signatures are clearly noted for other effects, such as their effect on scale separation and their region of influence through the BL.

To provide further insights on these differences, we analyse the characteristic turbulent lengths. We consider the length scale characterising large eddies as $L = \bar{\rho}k^{3/2}/\phi$ [32], and the Kolmogorov length scale $\eta = [(\bar{\mu}/\bar{\rho})^3/(\phi/\bar{\rho})]^{0.25}$ for the smallest ones, with ϕ being the local dissipation rate of TKE. The ratio of these two scales, reported in figure 10, measures the separation between large and small scales, which in our discussion can be ascribed to the effect of M_∞ and Θ numbers (since Re_τ is fixed). In agreement with previous observations, figure 10(a) shows that the separation of scales in the outer layer increases with the Mach number, while the opposite behaviour is found reducing the diabatic parameter Θ , see figure 10(b). The insets in figures 10(a) and 10(b) show the individual change of $L^+ = L/\delta_\nu$ and $\eta^+ = \eta/\delta_\nu$, revealing that M_∞ and Θ strongly affect the Kolmogorov length η^+ , with a minor impact on large scales L^+ , influencing the separation of large to small scales L/η in the outer layer.

On this aspect, we remark that while an increase in compressibility, i.e. M_∞ , reduces the Kolmogorov length, the opposite holds decreasing the wall temperature, i.e. Θ .

The variation of L/η in the outer layer is effectively captured by the change of $Re_\tau^* = \mu_w/\mu_\infty \sqrt{\rho_\infty/\rho_w} Re_\tau$ (see table 2), which better account for density and viscosity variations in the outer layer. It should be noted, however, that the definition of a single similarity parameter among different flow cases concerning the scale separation is prevented by the strong change of flow properties across the BL. In particular, while Re_τ essentially regulates the outer-inner scale separation, i.e. L^+ , Re_τ^* controls the large-small scale separation in the outer layer, i.e. L/η . These two variables are strongly related in incompressible flows and both growing functions of y^+ in the log-layer [32], while they appear to be decoupled for highly compressible flows due to the influence of M_∞ and Θ numbers. For this reason, specific flow features associated with the outer-inner scales separation, such as the enhancement of outer layer motions at high Re_τ [8], are not visible here, even though L/η actually increases in the outer layer.

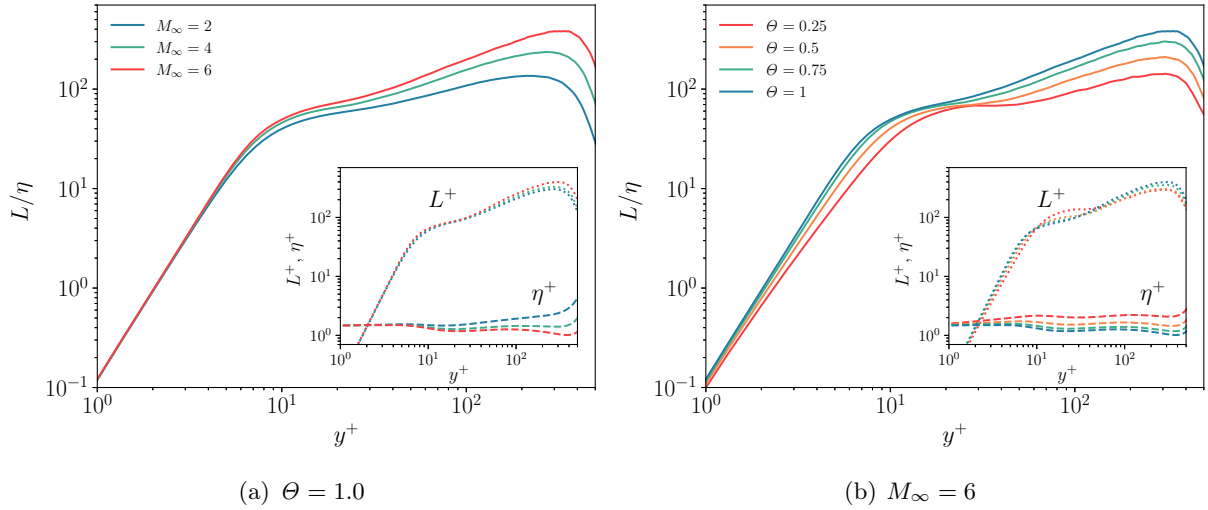


Figure 10: Ratio of integral length scale L and Kolmogorov scale η for cases at (a) $\Theta = 1.0$ and (b) $M_\infty = 6$, as function of the wall-normal distance y^+ . The inset shows separately L^+ and η^+ , normalized with the viscous length δ_ν .

Thermodynamic quantities

Important insights into the respective roles of Mach number and wall-cooling can also be attained by looking at root-mean-square profiles of temperature and pressure fluctuations shown in figures 11 and 12. The semilocal scaling is used to better account for fluid property variations across the boundary layer and rms quantities are scaled accordingly. In particular, rms profiles of pressure are scaled with the wall shear stress τ_w , while the resulting scaling for temperature is obtained using the ideal gas law $P = R\rho T$:

$$\frac{\tau_w}{R\bar{\rho}} = \frac{\bar{\rho}u_{\tau,SL}^2}{R\bar{\rho}} = \frac{u_{\tau,SL}^2}{R} = \gamma\bar{T}\frac{u_{\tau,SL}^2}{R\gamma\bar{T}} = \gamma\bar{T}M_{\tau,SL}^2 \quad (11)$$

being $u_{\tau,SL} = \sqrt{\tau_w/\bar{\rho}}$ the semilocal friction velocity and $M_{\tau,SL} = u_{\tau,SL}/\sqrt{\gamma R \bar{T}}$ the semilocal friction Mach number. First, the effect of Θ at a given Mach number is presented in figure 11. Considering the region starting from $y^* > 10$, both temperature and pressure fluctuations show a reduction in intensity as Θ decreases, although more intense for the temperature. In particular, the suppression of temperature fluctuations by wall-cooling forms a plateau for the coldest case that is due to the great attenuation of the turbulent heat flux in the log-layer, consistently with Fan et al. [15]. Around $y^* \approx 10$, the aforementioned attenuation of temperature fluctuations reaches its maximum for highly cooled cases ($\Theta = 0.25$), which is the point where mean temperature gradients are close to zero. In the near-wall region ($y^* < 10$), strongly cooled cases exhibit a peculiar behaviour, which goes in direct contrast to the monotonic attenuation of adiabatic profiles. In fact, in this region, there is an increase in the intensity of the temperature fluctuations that forms a local peak. We attribute this phenomenon to the large increase of conductive heat flux close to the wall, which is able to overcome the expected attenuation of turbulent heat flux that concurs with the generation of thermal production (see figure 13(d)). This is due to the large increase of near-wall temperature gradients that generate steeper mean profiles and for a wider region of y^* values (before reaching the temperature peak), as visible in figure 3(a) of section §Mean flow statistics.

The increase in pressure fluctuations in this region is shared only by the high-Mach number case, showing that additional physical interpretations are needed on the distinct role of vorticity and acoustic modes, for which we remind to the recent study of Zhang et al. [43]. Figure 12 shows the effect of Mach number at a given Θ . Here, temperature fluctuation profiles are very similar up to roughly $y^* < 15$, while the main differences are present in the outer layer, where at higher Mach numbers a peak is formed. This result indicates that Θ is an adequate parameter to recover the same general behaviour with respect to wall-cooling at different Mach numbers, as noted by Wenzel et al. [40] (we remark the similarity between Θ and Eckert number). Building on the choice of the diabatic parameter Θ , we can clearly see how the Mach number exerts its influence mainly beyond the buffer layer, while wall-cooling dominates the near-wall region. This is in agreement with the trends of TKE budget previously reported in §Velocity fluctuations and length scales. Moreover, as discussed for velocity fluctuations in section §Velocity fluctuations and length scales, we note the tendency of compressibility to increase the separation of scales (figure 11), while the opposite is true for enhanced wall-cooling (figure 12). This effect would be greatly reduced if profiles were compared at the same Re_τ^* , which incorporates these effects (not shown). Pressure fluctuations exhibit a good collapse at the peak location around $y^* \approx 30$, in accordance with Zhang et al. [43], but do not share the collapse between profiles in the near-wall region noted for temperatures.

Further insights on the sources of production of temperature fluctuations, which are highly influenced by wall-cooling, can be gained by considering the temperature variance budget $K_T = \widetilde{T''^2}$, which can be written as (ref. Gatski and Bonnet [18]):

$$\begin{aligned} \bar{\rho} \frac{DK_T}{Dt} = & -\widetilde{\rho u_k'' T''} \frac{\partial \widetilde{T}}{\partial x_k} - \frac{\partial}{\partial x_k} \left(\frac{\widetilde{\rho u_k'' T''^2}}{2} \right) + \gamma \overline{T''} \frac{\partial}{\partial x_k} \left(\frac{\bar{k}_T}{c_p} \frac{\partial \bar{T}}{\partial x_k} \right) \\ & + \bar{\rho} D_T - \bar{\rho} \varepsilon_T + \bar{\rho} C_T, \end{aligned} \quad (12)$$

where the terms on the right-hand side are in order of appearance: thermal production, turbulent velocity transport, mean thermal conduction, thermal diffusion, thermal dissipation rate, and contributions due to pressure-dilatation and viscous dissipation, respectively. Details on the composition of each term can be found on Gatski and Bonnet [18]. Here, we analyse the thermal production term, which acts in a similar way to turbulent production, transferring internal energy from the mean field to the fluctuating one Fan et al. [15]. For turbulent boundary layers, its wall-normal component is the main contributor, especially as we approach the wall, which we refer to as \mathcal{P}_T :

$$\mathcal{P}_T = -\widetilde{\bar{\rho} v'' T''} \frac{\partial \widetilde{T}}{\partial y} \quad (13)$$

Here, two terms concur to the heat exchange between different flow regions by two distinct processes: the first part $\widetilde{\bar{\rho} v'' T''}$ is dominated by turbulence with the velocity-temperature fluctuations correlation, while $\partial \widetilde{T} / \partial y$ represent the conductive part and is related to the mean temperature gradient. Profiles of \mathcal{P}_T are reported in figures 13, showing the effect of wall-cooling at different Mach numbers. Similarly to temperature fluctuations, cold profiles behave differently before and after $y^* \approx 10$, where mean temperature gradients change after the peaks. While adiabatic profiles monotonically rise from zero to a clear peak at around $y^* \approx 15$, proving their coupling with velocity fluctuations, cold cases progressively exhibit a reduction and outward shift of the main peak, with

the creation of another peak in the viscous sub-layer. An insight to understand this process, which is more apparent at $M_\infty = 6$, can be gained by analysing the individual behaviour of turbulent and convective heat exchange terms in thermal production [15], which are shown in figure 13(d).

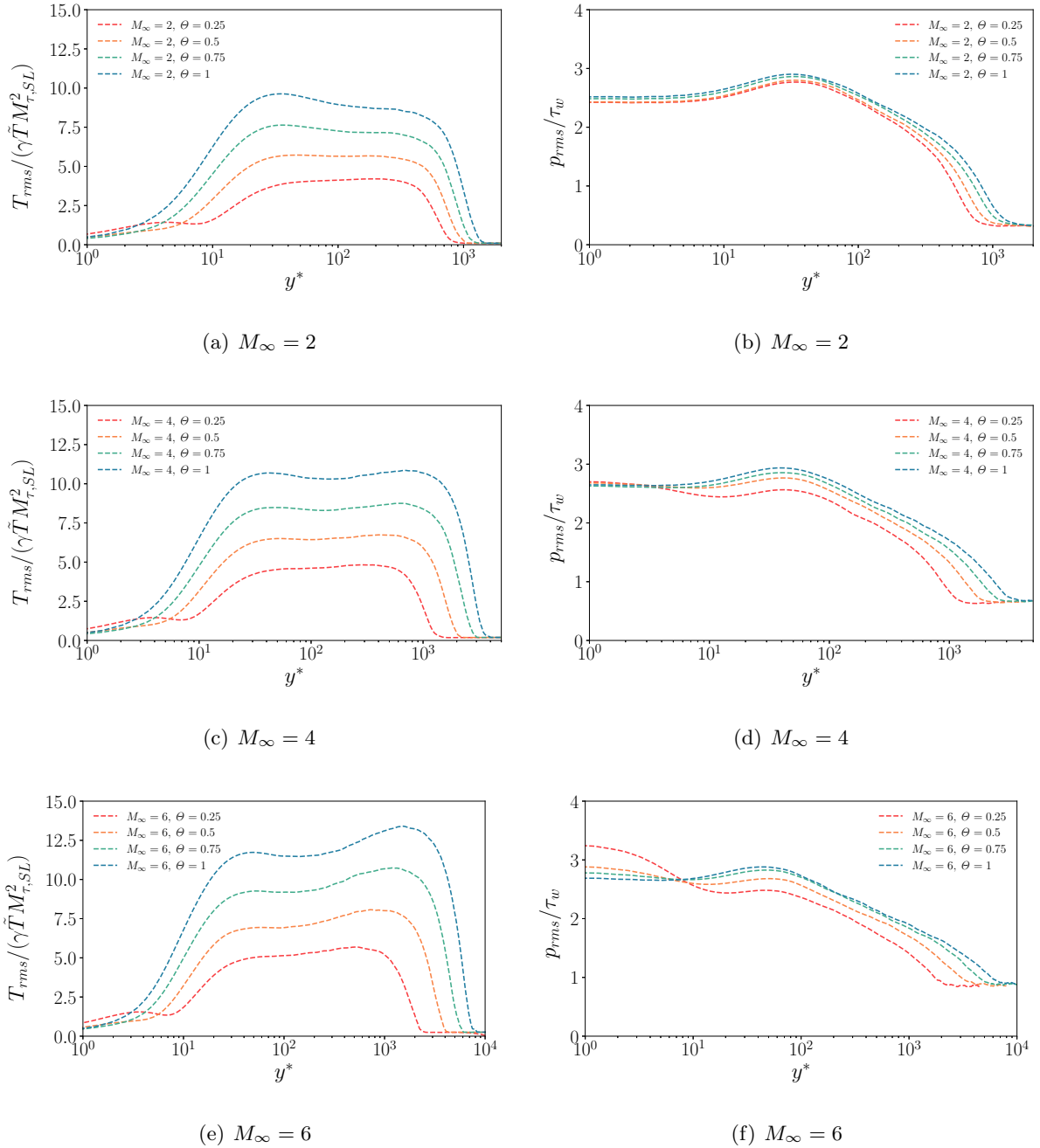


Figure 11: Profiles of RMS temperature (left) and pressure (right) in semilocal scaling. Here, different diabatic parameters Θ are compared at a given Mach number M_∞ .

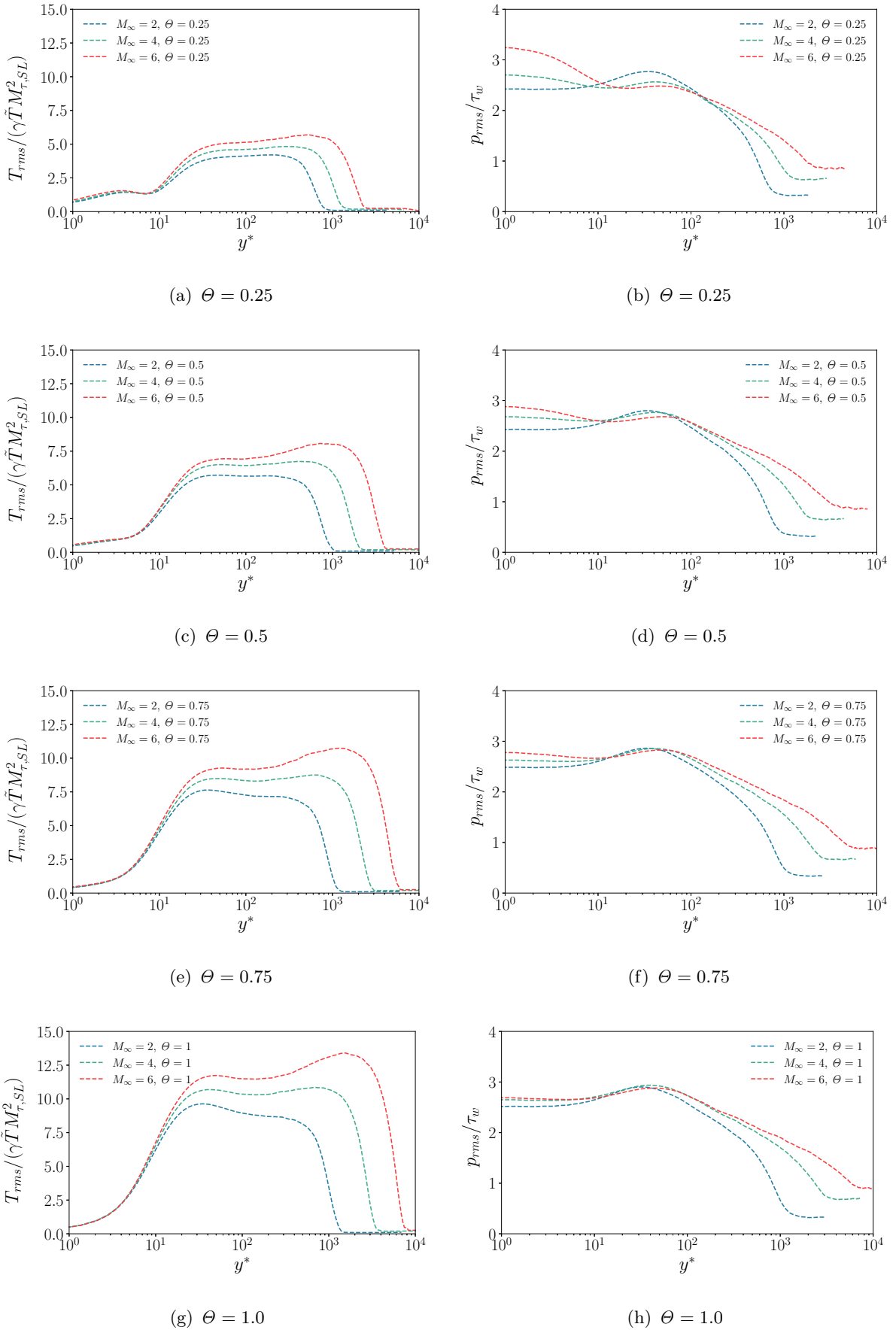


Figure 12: Profiles of RMS temperature (left) and pressure (right) in semilocal scaling. Here, different Mach number M_∞ are compared at a given diabatic parameter Θ .

Here, it can be seen that while the turbulent term is significantly far from the wall with reduced intensity for cold cases, convective heat exchange dominates the near-wall region as wall-cooling increases. In this region, even though $\bar{\rho}v''\widetilde{T''}$ is close to zero for all cases, the temperature gradient raises considerably for $\Theta = 0.25$ which result in a non-zero product that is visible in plots of thermal production. Thus, the formation of a peak of thermal fluctuation production in the viscous sublayer is promoted. The vanishing mean temperature gradient in the buffer layer reduces the production of temperature fluctuations and promotes a decorrelation with velocity fluctuations, as discussed in the previous sections. This mechanism is clearly visible for all Mach numbers in our database, although with progressively lower intensities. This fact corroborates the importance of the role of Θ in isolating the effect of wall-cooling from compressibility, which greatly helps in the identification of individual trends.

At this point, it is possible to reconsider the qualitative results presented in figure 2 in a more quantitative way. Wall parallel slices of velocity and temperature fluctuations were taken approximately at $y^* = 10$, where $\partial\tilde{T}/\partial y \approx 0$ for extremely cold cases. It is now apparent that the decorrelation between $\bar{\rho}T''/\tau_w$ and $\sqrt{\bar{\rho}u''}/\sqrt{\tau_w}$ can be explained with the interplay of the mean temperature gradient and $\bar{\rho}v''\widetilde{T''}$, which entirely damps the production of temperature fluctuations. This is also visible in figure 14, which shows the joint probability density function between velocity and temperature fluctuations only for extreme cases at $M_\infty = 6$ (other cases are similar). Here, a direct contrast is present between figures 14(a) and 14(b)). While the latter (M6T100) shows a good correlation between the two fields, supporting their similarity, the former (M6T025) shows a strong decorrelation, especially when velocity fluctuations are negative, which is due to the influence of wall-cooling.

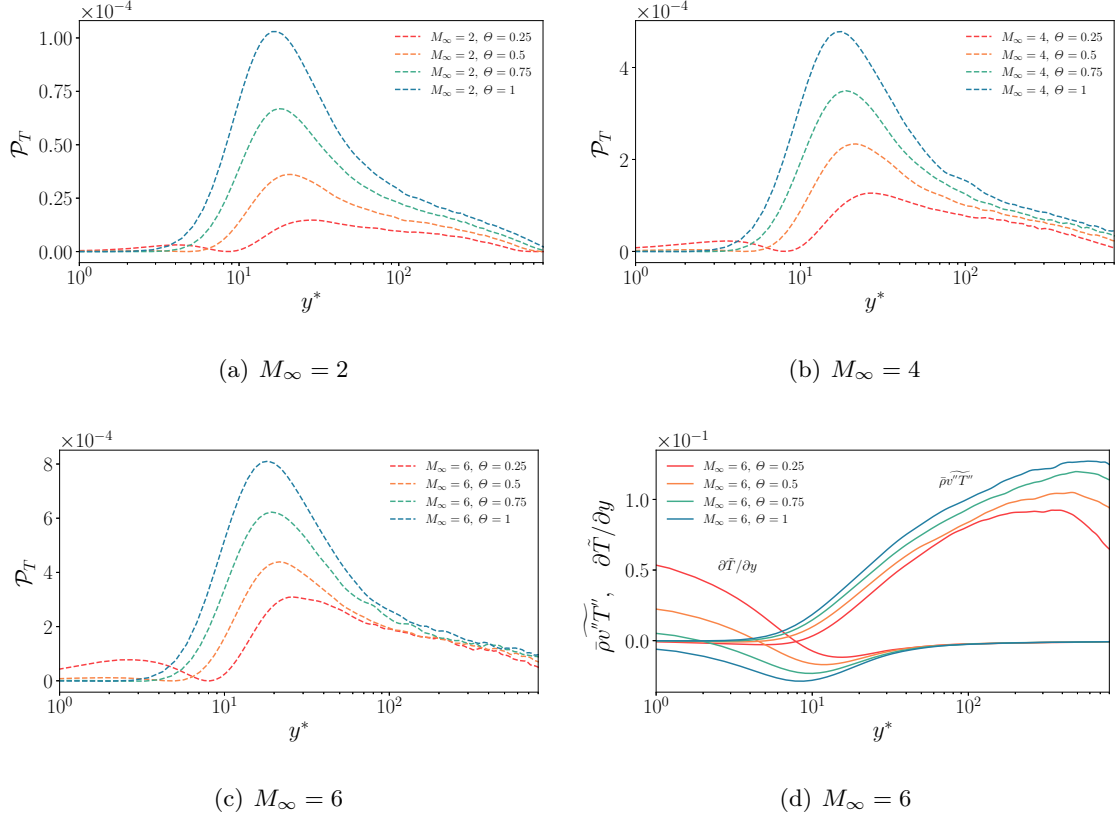


Figure 13: Panels (a → c): Production of temperature variance \mathcal{P}_T as function of y^* and scaled by $\bar{\rho}u_{\tau,SL}\tilde{T}^2/\delta_{\nu,SL}$. Here, different wall-cooling conditions are compared for each Mach number. Panel (d): Turbulent $\widetilde{\bar{\rho}v''T''}$ and conductive $\partial\tilde{T}/\partial y$ heat transfer terms in the thermal production. Here, different wall-cooling conditions are compared for case $M_\infty = 6$.

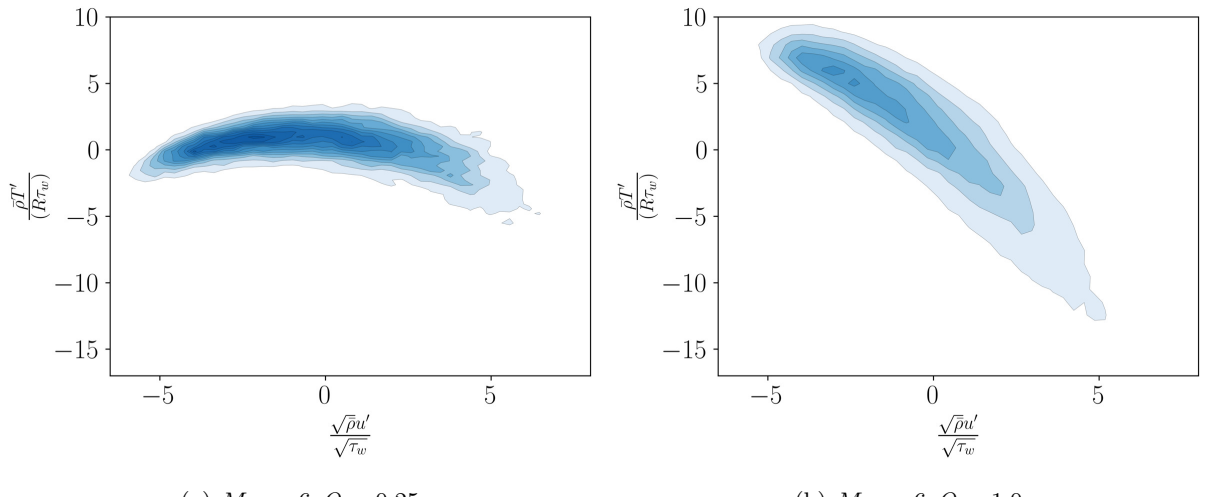


Figure 14: Scatter plot of $\bar{\rho}T''/\tau_w$ vs $\sqrt{\bar{\rho}u''}/\sqrt{\tau_w}$. Here, only the cases M6T025 and M6T100 are shown. Data were collected in the same plane shown in figure 2 ($y^* \approx 10$).

Conclusions

In this paper, we have presented a systematic study on the effect of the Mach number and wall-cooling on zero-pressure-gradient TBLs using direct numerical simulations. A total of 12 computations have been carried out spanning three Mach numbers and four values of the diabatic parameter Θ , while the friction Reynolds number has been kept constant. In this parameter space, we put emphasis on the choice of the wall-cooling parameter Θ , first proposed by Zhang et al. [44], which can better incorporate the indirect effects of the Mach number on wall-cooling, yielding the same integral behaviour between different cases. It is worth noting that Θ can be directly related to the Eckert number Ec , whose relevance has recently been discussed by Wenzel et al. [40]. These parameters show an improved ability to account for the wall-cooling effect at different Mach numbers with respect to the more classically used wall-to-recovery temperature ratio T_w/T_r , which has been shown to produce vastly different effects of wall temperature on the flow dynamics in the near-wall region across different Mach numbers (e.g. Cogo et al. [8], Zhang et al. [43]).

A summary of the most important remarks is presented below.

1. The instantaneous flow organisation of temperature fluctuations near the wall, which for adiabatic cases is clearly discernible with the presence of near-wall elongated streaks highly correlated to streamwise velocity, breaks down as the wall temperature is progressively lowered, showing an isotropic behaviour for extremely cold cases without organised patterns. Nevertheless, a similar flow organisation is attained at different Mach numbers when Θ is fixed, a first sign of the aptness of this parameter to yield the same wall-cooling effects across different M_∞ .
2. The recent compressibility transformations of Volpiani et al. [37] and Griffin et al. [20] correctly collapse all mean velocity profiles of our database to the incompressible laws of the wall. Similarly, Zhang et al. [44] mean velocity-temperature relations are able to capture non-adiabatic and compressibility effects in an excellent manner. When this relation is approximated with the computed mean value of the Reynolds analogy factor $s = 0.78 \pm 0.03$ (which is close to the fit of Zhang et al. [44]), an excellent estimate is recovered, with maximum errors of 5% from the DNS data.
3. As the Mach number increases, we observe an increased separation between large and small scales in the outer layer measured by the ratio L/η , which is mainly regulated by the strong reduction of the Kolmogorov length η , and only weakly by a growth of the largest scale L . This effect can be effectively described by the growth of the semilocal friction Reynolds number Re_τ^* , even though the resulting flow dynamics is different from a pure increase of the friction Reynolds number Re_τ , the latter also leading to an increase of the inner-outer scale separation L^+ , feeding outer layer motions. In the near-wall region, compressibility enables a less efficient redistribution of turbulent kinetic energy, which results in a promotion of the peak of the streamwise velocity component and a decrease of the others.

-
- 4. The enhancement of wall-cooling appears as a reduction of the large-small scale separation in the outer layer (as opposed to the effect of Mach number), which is mainly due to an increase of the Kolmogorov length scale η that occurs throughout the whole BL thickness. Lower wall temperatures force the rise of the mean temperature peak, inducing a stratification of flow properties localised around the buffer layer. This effect is visible as an apparent promotion of compressibility, since velocity fluctuations are enhanced in the streamwise direction, while the other components are damped.
 - 5. In the near-wall region, a dominant effect of wall-cooling is present in the RMS temperature profiles and TKE budget, while the Mach number exerts its influence mainly through the buffer and log layers. When the diabatic parameter Θ is kept constant, the RMS temperature profiles at different M_∞ collapse into each other near the wall, displaying a similar wall-cooling effect.
 - 6. For extremely cold cases (in our database $\Theta = 0.25$), the effect of wall-cooling is so marked that temperature fluctuations are massively damped at the point where the mean temperature gradient is zero (thus thermal production is also zero), and a second (minor) peak arises in the viscous sublayer. This phenomenon completely decorrelates velocity and temperature fields in the near-wall region, and is more pronounced at high Mach numbers. The different behaviour of thermal production for cold cases can be explained by looking at the mean temperature gradient, which persists with a positive value for a wider wall-normal region (before reaching the mean temperature peak at y_{peak}^*), and with a much stronger intensity than for adiabatic cases.

Acknowledgements

We acknowledge that the results reported in this paper have been achieved using the PRACE Research Infrastructure resource MARCONI 100 based at CINECA, Casalecchio di Reno, Italy, under project PRACE call 23 n. 0058. M. Bernardini, U. Baù and M. Chinappi have also been supported by the grant agreement No A0375-2020-36614, project GREEN H2 CFD, POR FESR LAZIO 2014-2020.

Declaration of interests

The authors report no conflict of interest.

Data availability statement

The data that support the findings of this study are openly available at <http://newton.dma.uniroma1.it/highspeedbl/>.

| Transformation | Wall distance (f_I) | Mean velocity (g_I) |
|----------------------|------------------------------------|------------------------------------|
| Van Driest [35] | $f_{VD} = 1$ | $g_{VD} = R^{1/2}$ |
| Volpiani et al. [37] | $f_{VI} = \frac{R^{1/2}}{M^{3/2}}$ | $g_{VI} = \frac{R^{1/2}}{M^{1/2}}$ |

Table 3: Compressibility transformations for the wall distance and the mean velocity according to Eq. (14), where $R = \bar{\rho}/\bar{\rho}_w$ and $M = \bar{\mu}/\bar{\mu}_w$.

Appendix

In this section, we consider mean velocity profiles in the framework of compressibility transformations, which aim at incorporating compressibility effects in wall-bounded flow statistics in order to recover the incompressible behaviour. Since the pioneering work of Van Driest [35], several relations have been proposed to account for the variations of mean fluid properties, such as density and viscosity. These relations can be cast in terms of mapping functions f_I and g_I for wall distance y_I and mean velocity u_I , which denote the equivalent incompressible distributions obtained from the transformation I :

$$y_I = \int_0^y f_I dy, \quad u_I = \int_0^{\tilde{u}} g_I d\tilde{u}. \quad (14)$$

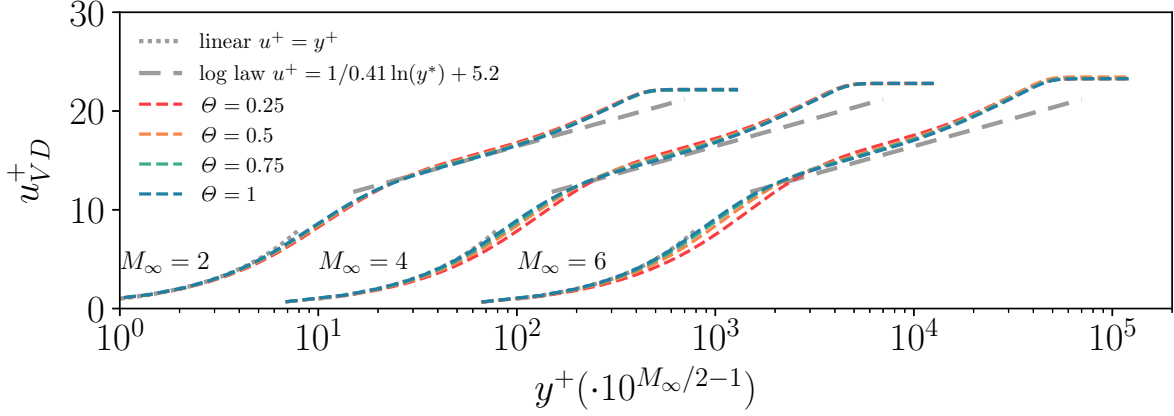
Table 3 shows the relative values of f_I and g_I for Van Driest [35] and the recent transformation of Volpiani et al. [37], which employs a partially data-driven approach to derive the mapping exponents.

Griffin et al. [20] transformation, instead, is based on the total stress equation, which reads:

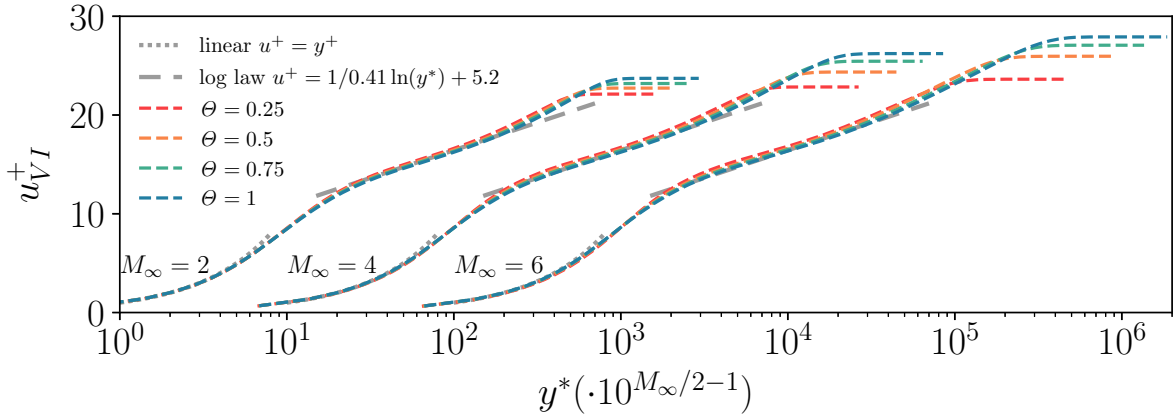
$$\tau^+ = S_t^+ \left(\frac{\tau_v^+}{S_{TL}^+} + \frac{\tau_R^+}{S_{eq}^+} \right) \quad (15)$$

where τ_v^+ and τ_R^+ are the scaled viscous and Reynolds shear stresses (whose sum is equal to τ^+), while $S_{TL}^+ = \partial U_{TL}^+ / \partial y^*$ and $S_{eq}^+ = \partial U_{eq}^+ / \partial y^*$ are the generalised nondimensional mean shear stresses derived for the viscous region (the subscript TL indicated the accordance with the Trettel and Larsson [33] velocity transformation) and for the log layer (the subscript eq indicates the assumption of turbulence quasi-equilibrium). The generalised nondimensional mean shear $S_t^+ = \partial U_t^+ / \partial y^*$ is the unknown and once computed it can be integrated with respect to the semilocal wall-normal coordinate y^* , leading to the transformed velocity $u_{GR}^+ = \int S_t^+ dy^*$.

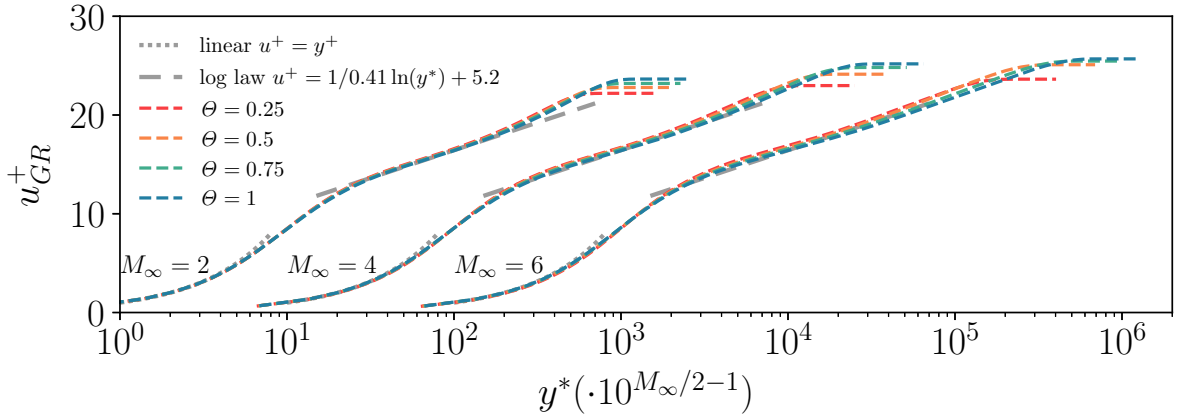
We report in figure 15 the scaled profiles according to the classical law of Van Driest [35] and the latest transformations of Volpiani et al. [37] and Griffin et al. [20]. Panel 15(a) reveals the main weaknesses of the Van Driest [35] scaling, whose accuracy is affected both by the increase of the Mach number and wall-cooling. In particular, non-adiabatic cases at $M_\infty = 4, 6$ show a clear departure from the linear law of the wall, while even adiabatic cases show a positive shift from the log-law as compressibility increases. Panels 15(b) and 15(c) show a great improvement in collapsing all profiles to the laws of the wall, the only minor discrepancy being present in the log layer for extremely cold cases at high Mach numbers. Overall, our database supports Volpiani et al. [37] and Griffin et al. [20] transformations, proving their wide range of applicability.



(a) Van Driest et al.



(b) Volpiani et al.



(c) Griffin et al.

Figure 15: Mean velocity profiles at stations listed in table 2 scaled according to (a) Van Driest [35], (b) Volpiani et al. [37] and (c) Griffin et al. [20] compressibility transformations. Profiles have been translated along the x axis according to the law $10^{M_{\infty}/2-1}$ to enable better comparison.

In this section, we report DNS results regarding theoretical relations developed to predict the coupling between velocity and temperature for both mean and fluctuating fields. First, we consider

the classical relations of Walz [38] and the modified relation of Zhang et al. [44], as described in section §Reynolds analogy. Figure 16 compares the relations (5) and (6) with the present database. As expected, Walz [38] relation greatly degrades its accuracy when the wall-cooling is increased, while Zhang et al. [44] is able to better perform under these conditions, the only minor deviations being present for the case M6T025. However, we note that Walz [38] law still excellently holds for adiabatic cases at high Mach numbers, while being incapable of correctly capturing wall-cooling effects.

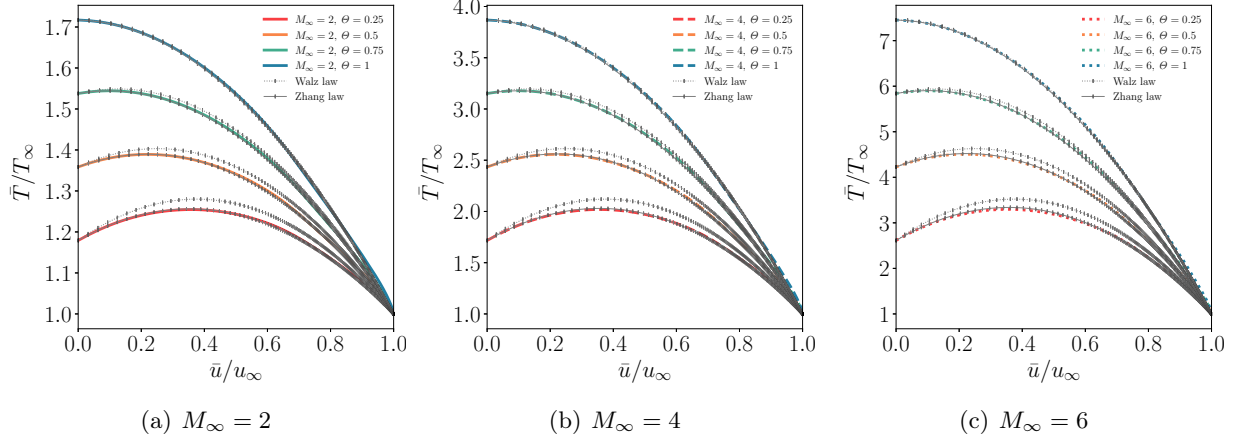


Figure 16: Mean temperature profiles against the mean velocity compared with the classical law of Walz [38] (Eq. (5)) and the modified relation of Zhang et al. [44] (Eq. (6)).

We then consider the Strong Reynolds Analogy (SRA) [26], which consists of a set of theoretical relations that couple the thermodynamic and kinetic fluctuating fields. Originally derived for an adiabatic case, the three main relations can be expressed as

$$\begin{aligned} \frac{\left(\widetilde{T''^2}\right)^{1/2}/\tilde{T}}{(\gamma-1)\tilde{M}^2\left(\widetilde{u''^2}\right)^{1/2}/\tilde{u}} &\approx 1, \\ R_{u''T''} = \frac{\widetilde{u''T''}}{\sqrt{\widetilde{u''^2}}\sqrt{\widetilde{T''^2}}} &\approx 1, \\ Pr_t = \frac{\rho u'v'(\partial\tilde{T}/\partial y)}{\rho T'v'(\partial\tilde{u}/\partial y)} &\approx 1. \end{aligned} \quad (16)$$

where we remind the Favre average definition $\tilde{f} = \overline{\rho f}/\bar{\rho}$ and that $f'' = f - \tilde{f}$.

Figure 17 shows the profiles of $R_{u''T''}$ that clearly deviate from unity, which is expected since it was derived assuming zero total temperature fluctuation [26]. All profiles collapse around the value $-R_{u''T''} = 0.6$, except in the near-wall region, which is marked with an inset [12]. The inset of Figure 17 shows that the crossover location, where $R_{u''T''} = 0$, corresponds approximately to the location of the maximum mean temperature. Here, we observe that as the wall gets progressively cold, the crossover location moves at higher y^* values, indicating a temperature-velocity decorrelation that is progressively moved farther from the wall. Our database also shows that this location is almost independent of the Mach number when Θ is fixed, whereas distinct Mach and wall-cooling effects are visible on the near-wall peak intensity and position of $R_{u''T''}$.

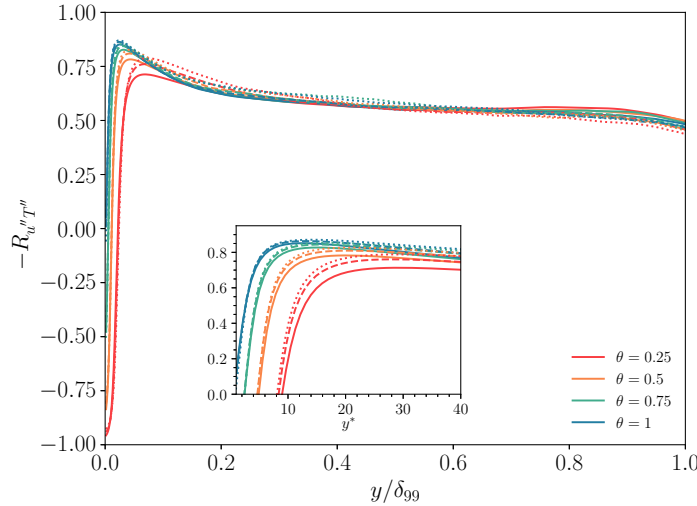


Figure 17: Velocity and temperature correlation $R_{u''T''}$ as function of y/δ_{99} . Solid lines indicate $M_\infty = 2$, dashed lines $M_\infty = 4$ and dotted lines $M_\infty = 6$.

The remaining two relations of equation (16) have been modified over the years to account for finite heat flux at the wall and remove wall temperature dependence [24] (HSRA). The most recent improvement has been made by Zhang et al. [44], who proposed another definition of the turbulent Prandtl number \overline{Pr}_t which should perform better at high Mach numbers, yielding the following expression of the modified strong Reynolds analogy (modified HRSA):

$$\frac{\left(\widetilde{T''^2}\right)^{1/2}/\tilde{T}}{(\gamma-1)\tilde{M}^2\left(\widetilde{u''^2}\right)^{1/2}/\tilde{u}}\overline{Pr}_t\left(1-(\partial\tilde{T}_t/\partial\tilde{T})\right)\approx 1 \quad (17)$$

where the proposed definition of \overline{Pr}_t is

$$\overline{Pr}_t=\frac{(\rho v')u'\partial\tilde{T}/\partial y}{(\rho v')T'\partial\tilde{u}/\partial y}=Pr_t\frac{1+\bar{v}\overline{\rho'u'}/\overline{\rho v'u'}}{1+\bar{v}\overline{\rho'T'}/\overline{\rho v'T'}} \quad (18)$$

in which the difference from the classical definition is notable when both \bar{v} and ρ' are nonzero.

Figure 18 compares the wall-normal profiles obtained with the original SRA and the modified version of Eq. (17), as well as the profiles of Pr_t and the modified \overline{Pr}_t of Eq. (18). Figure 18(c) shows that the modified version of Zhang et al. [44] clearly improves the insensitivity to the freestream Mach number and wall temperature condition, with only slight deviations at the edge of the boundary layer. It is also interesting to note the excellent collapse that the original SRA of panel 18(a) exhibits for profiles at fixed Θ , independently of the Mach number, highlighting the relevance of the diabatic parameter Θ in accounting for the effects of different wall temperatures independently of the Mach number.

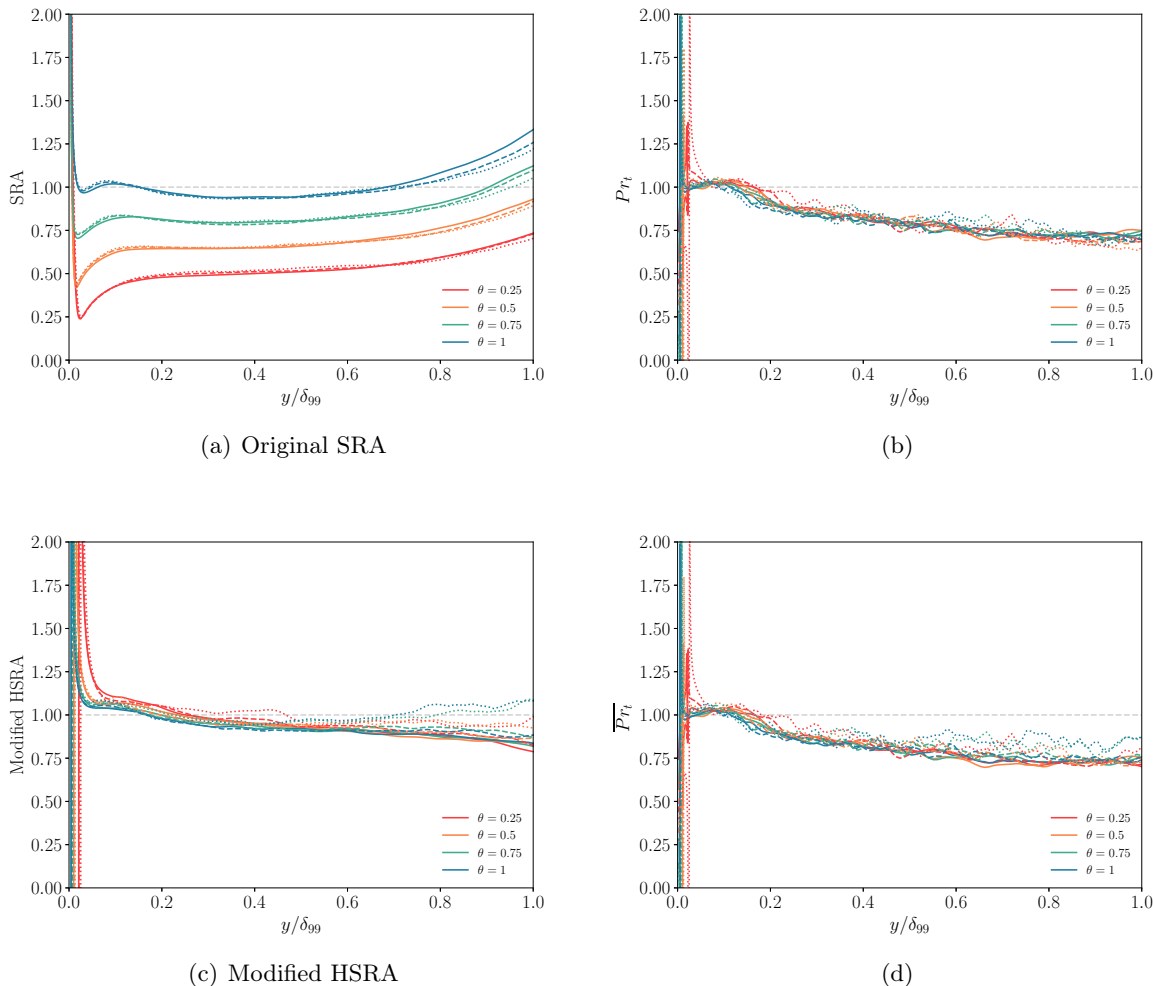


Figure 18: Comparison of the Strong Reynolds Analogies in the (a,b) original form (Eq. (16)), (c,d) Modified HSRA [44]) (Eqs. (17), (18)). Solid lines indicate $M_\infty = 2$, dashed lines $M_\infty = 4$ and dotted lines $M_\infty = 6$.

Bibliography

- [1] S. Banerjee, R. Krahl, F. Durst, and C. Zenger. Presentation of anisotropy properties of turbulence, invariants versus eigenvalue approaches. *J. of Turbul.*, (8):N32, 2007.
- [2] M. Bernardini and S. Pirozzoli. Inner/outer layer interactions in turbulent boundary layers: a refined measure for the large-scale amplitude modulation mechanism. *Phys. Fluids*, 23(6):061701, 2011.
- [3] M. Bernardini and S. Pirozzoli. Wall pressure fluctuations beneath supersonic turbulent boundary layers. *Phys. Fluids*, 23(8):085102, 2011.
- [4] M. Bernardini, S. Pirozzoli, and F. Grasso. The wall pressure signature of transonic shock/boundary layer interaction. *J. Fluid Mech.*, 671:288–312, 2011.
- [5] M. Bernardini, D. Modesti, F. Salvadore, and S. Pirozzoli. STREAmS: a high-fidelity accel-

- erated solver for direct numerical simulation of compressible turbulent flows. *Comp. Phys. Comm.*, 263:107906, 2021.
- [6] M. Bernardini, D. Modesti, F. Salvadore, S. Sathyamarayana, G. Della Posta, and S. Pirozzoli. Streams-2.0: Supersonic turbulent accelerated navier-stokes solver version 2.0. *Comput. Phys. Commun.*, 285:108644, 2023.
- [7] Y. B. Chu, Y. Q. Zhuang, and X. Y. Lu. Effect of wall temperature on hypersonic turbulent boundary layer. *Journal of Turbulence*, 14(12):37–57, 2013.
- [8] M. Cogo, F. Salvadore, F. Picano, and M. Bernardini. Direct numerical simulation of supersonic and hypersonic turbulent boundary layers at moderate-high reynolds numbers and isothermal wall condition. *J. Fluid Mech.*, 945:A30, 2022.
- [9] F. De Vanna, A. Benato, F. Picano, and E. Benini. High-order conservative formulation of viscous terms for variable viscosity flows. *Acta Mech.*, 232:2115–2133, 2021.
- [10] M. Di Renzo and J. Urzay. Direct numerical simulation of a hypersonic transitional boundary layer at suborbital enthalpies. *J. Fluid Mech.*, 912:A29, 2021. doi: 10.1017/jfm.2020.1144. URL <http://dx.doi.org/10.1017/jfm.2020.1144>.
- [11] L. Duan and M.P. Martin. Direct numerical simulation of hypersonic turbulent boundary layers. Part 4. Effect of high enthalpy. *J. Fluid Mech.*, 684:25–59, 2011.
- [12] L. Duan, I. Beekman, and M.P. Martín. Direct numerical simulation of hypersonic turbulent boundary layers. Part 2. Effect of wall temperature. *J. Fluid Mech.*, 655:419–445, 2010. ISSN 00221120. doi: 10.1017/S0022112010000959.
- [13] L. Duan, I. Beekman, and M.P. Martín. Direct numerical simulation of hypersonic turbulent boundary layers. Part 3. Effect of Mach number. *J. Fluid Mech.*, 672:245–267, 2011. ISSN 14697645. doi: 10.1017/S0022112010005902.
- [14] F. Ducros, V. Ferrand, F. Nicoud, C. Weber, D. Darracq, C. Gacherieu, and T. Poinsot. Large-eddy simulation of the shock/turbulence interaction. *J. of Comput. Phys.*, 152(2):517–549, 1999.
- [15] Y. Fan, W. Li, and S. Pirozzoli. Energy exchanges in hypersonic flows. *Phys. Rev. Fluids*, 7(9):L092601, 2022.
- [16] H. H. Fernholz and P. J. Finley. *A critical commentary on mean flow data for two-dimensional compressible turbulent boundary layers*. North Atlantic Treaty Organization, Advisory Group for Aerospace Research, 1980.
- [17] H. Foysi, S. Sarkar, and R. Friedrich. Compressibility effects and turbulence scalings in supersonic channel flow. *J. Fluid Mech.*, 509:207–216, 2004.
- [18] T. B. Gatski and J. P. Bonnet. *Compressibility, turbulence and high speed flow*. Academic Press, 2013.

- [19] J. Gaviglio. Reynolds analogies and experimental study of heat transfer in the supersonic boundary layer. *Int. J. Heat Mass Tran.*, 30(5):911–926, 1987.
- [20] K. P. Griffin, L. Fu, and P. Moin. Velocity transformation for compressible wall-bounded turbulent flows with and without heat transfer. *P. Natl. Acad. Sci USA*, 118(34), 2021.
- [21] S. E. Guarini, R. D. Moser, K. Shariff, and A. Wray. Direct numerical simulation of a supersonic turbulent boundary layer at mach 2.5. *J. Fluid Mech.*, 414:1–33, 2000.
- [22] R. Hirai, R. Pecnik, and S. Kawai. Effects of the semi-local reynolds number in scaling turbulent statistics for wall heated/cooled supersonic turbulent boundary layers. *Phys. Rev. Fluids*, 6(12):124603, 2021.
- [23] J. Huang, L. Duan, and M. M. Choudhari. Direct numerical simulation of hypersonic turbulent boundary layers: effect of spatial evolution and reynolds number. *J. Fluid Mech.*, 937, 2022.
- [24] P. C. Huang, G. N. Coleman, and P. Bradshaw. Compressible turbulent channel flows: DNS results and modelling. *J. Fluid Mech.*, 305:185–218, 1995.
- [25] B. Morgan, J. Larsson, S. Kawai, and S. K. Lele. Improving low-frequency characteristics of recycling/rescaling inflow turbulence generation. *AIAA J.*, 49(3):582–597, 2011.
- [26] M. V. Morkovin. Effects of compressibility on turbulent flows. *Mécanique de la Turbulence*, 367(380):26, 1962.
- [27] D. Passiatore, L. Sciacovelli, P. Cinnella, and G. Pascazio. Finite-rate chemistry effects in turbulent hypersonic boundary layers: A direct numerical simulation study. *Phys. Rev. Fluids*, 6:054604, May 2021. doi: 10.1103/PhysRevFluids.6.054604. URL <https://link.aps.org/doi/10.1103/PhysRevFluids.6.054604>.
- [28] D. Passiatore, L. Sciacovelli, P. Cinnella, and G. Pascazio. Thermochemical non-equilibrium effects in turbulent hypersonic boundary layers. *J. Fluid Mech.*, 941, 2022.
- [29] S. Pirozzoli and P. Orlandi. Natural grid stretching for DNS of wall-bounded flows. *J. Comput. Phys.*, 439:110408, 2021. doi: <https://doi.org/10.1016/j.jcp.2021.110408>.
- [30] S. Pirozzoli, M. Bernardini, and F. Grasso. Direct numerical simulation of transonic shock-boundary layer interaction under conditions of incipient separation. *J. Fluid Mech.*, 657:361, 2010.
- [31] T. J. Poinsot and S. K. Lele. Boundary conditions for direct simulations of compressible viscous flows. *J. Comput. Phys.*, 101(1):104–129, 1992.
- [32] S. B. Pope. *Turbulent Flows*. Cambridge University Press, 2000.
- [33] A. Trettel and J. Larsson. Mean velocity scaling for compressible wall turbulence with heat transfer. *Phys. Fluids*, 28(2):026102, 2016.
- [34] J. Urzay and M. Di Renzo. Engineering aspects of hypersonic turbulent flows at suborbital enthalpies. *CTR Annu. Res. Briefs*, pages 7–32, 2021.

- [35] E. R. Van Driest. Turbulent boundary layer in compressible fluids. *J. Aeronaut. Sci.*, 18(3):145–160, 1951.
- [36] E. R. Van Driest. The problem of aerodynamic heating. *Aeronaut. Engng. Rev.*, 15(10):26–41, 1956.
- [37] P. S. Volpiani, P. S. Iyer, S. Pirozzoli, and J. Larsson. Data-driven compressibility transformation for turbulent wall layers. *Phys. Rev. Fluids*, 5(5):052602, 2020.
- [38] A. Walz. *Boundary layers of flow and temperature*. MIT Press, 1969.
- [39] C. Wenzel, B. Selent, M. Kloker, and U. Rist. DNS of compressible turbulent boundary layers and assessment of data/scaling-law quality. *J. Fluid Mech.*, 842:428–468, 2018.
- [40] C. Wenzel, T. Gibis, and M. Kloker. About the influences of compressibility, heat transfer and pressure gradients in compressible turbulent boundary layers. *J. Fluid Mech.*, 930:A1, 2022.
- [41] Christoph Wenzel, Tobias Gibis, Markus Kloker, and Ulrich Rist. Reynolds analogy factor in self-similar compressible turbulent boundary layers with pressure gradients. *J. Fluid Mech.*, 907:R4, 2021.
- [42] C. Zhang, L. Duan, and M.M. Choudhari. Direct numerical simulation database for supersonic and hypersonic turbulent boundary layers. *AIAA J.*, 56(11):4297–4311, 2018. ISSN 00011452. doi: 10.2514/1.J057296.
- [43] P. Zhang, Z. Wan, N. Liu, D. Sun, and X. Lu. Wall-cooling effects on pressure fluctuations in compressible turbulent boundary layers from subsonic to hypersonic regimes. *J. Fluid Mech.*, 946:A14, 2022.
- [44] Y. S. Zhang, W. T. Bi, F. Hussain, and Z. S. She. A generalized Reynolds analogy for compressible wall-bounded turbulent flows. *J. Fluid Mech.*, 739:392–420, 2014.

Appendix C

Paper III

Surface roughness effects on supersonic turbulent boundary layers

Michele Cogo¹, Davide Modesti², Matteo Bernardini³, and Francesco Picano^{1,4}

1. Centro di Ateneo di Studi e Attività Spaziali "Giuseppe Colombo" - CISAS,
University of Padova, Padova, PD 35131, Italy

2. Faculty of Aerospace Engineering, Delft University of Technology, Kluyverweg 2, 2629 HS
Delft, The Netherlands,

3. Department of Mechanical and Aerospace Engineering, Sapienza University of Rome, via
Eudossiana 18, 00184 Rome, Italy,

4. Department of Industrial Engineering, University of Padova, Padova, PD 35131, Italy.

Journal of Fluid Mechanics, under review

Abstract: We present direct numerical simulations of a supersonic zero-pressure-gradient adiabatic turbulent boundary layer at freestream Mach number $M_\infty = 2$ over cubical roughness elements. This simulation is complemented by a subsonic rough-wall boundary layer on the same geometry and reference smooth-wall data, allowing us to elucidate compressibility effects. Simulations feature a turbulent flow that transitions from a smooth to a rough surface with a long computational domain to allow for recovery. At the smooth-to-rough transition, we compare the development of an internal boundary layer between subsonic and supersonic cases, introducing a novel definition of its height that is less sensitive to local compressibility effects. We show that despite the internal boundary layer growth is similar to the subsonic case, a delayed equilibrium is expected for the supersonic case due to a sudden growth of the external boundary layer thickness at the onset of roughness. Turbulence statistics are then evaluated far from the surface transition, where different compressibility transformations show outer-layer similarity for the mean velocity. We find that the classical van Driest II transformation can also be used on rough walls, at least in the adiabatic case. Analysis of thermal statistics for the supersonic case confirmed the strong influence that roughness has on mean and fluctuating temperature fields, which, unlike the velocity, do not show outer layer similarity.

Keywords: compressible boundary layers, roughness

Introduction

Turbulent boundary layers in high-speed vehicles can be altered by the presence of surface roughness. Although the majority of flight systems are usually designed to have a relatively smooth surface, roughness can be present or arise for several reasons. For example, the surface topology can be affected by localized variations due to pitting, corrosion, spallation or contamination deposits [24]. Roughness can also be distributed in larger portions of the surface where thermal protection systems (TPSs) are in place. Tiled TPSs often show seams at the interface between each tile, which interact with the incoming turbulent boundary layer deeply affecting drag and heat transfer [16]. On the other hand, ablative TPSs undergo the removal of sacrificial material that can produce reg-

ular or irregular patterns [32, 43]. Because of the complexities of supersonic and hypersonic flows in comparison to the incompressible counterpart, the added effect of surface roughness has been rarely studied. Although important insights on the topic have been provided by experimental campaigns [5], high-fidelity simulations on this topic are scarce, and they could provide useful insights on critical aspects of flow dynamics.

In the incompressible regime, roughness effects in wall-bounded turbulent flows have been extensively investigated both with experimental and numerical studies, recently reviewed by [8, 23]. These researches advanced our knowledge of turbulent flows over rough surfaces and pointed out that predictive tools for the total drag τ_w and heat flux q_w per plane are available, primarily in the form of empirical correlations [19, 27, 45], and, to some extent, as more robust physics models [28, 46, 48]. Roughness characterization relies on the relevant importance of the different length scales involved, namely the boundary layer thickness δ , the roughness height k , and the viscous length scale $\delta_\nu = \nu_w/u_\tau$, where $u_\tau = \sqrt{\tau_w/\rho_w}$ is the friction velocity, ν_w and ρ_w are the kinematic viscosity and density at the wall, respectively. At sufficiently high friction Reynolds numbers $Re_\tau = \delta/\delta_\nu$ and roughness Reynolds numbers $k^+ = k/\delta_\nu$ the flow can be considered fully rough, namely, the drag per plane area is independent from the Reynolds number, as pressure drag becomes the main contributor [31]. However, a quantity of engineering interest is often the relative drag increase compared to a smooth wall, which remains a function of the Reynolds number. For this reason, the Hama roughness function is preferred to quantify the added drag, as it is fairly independent of the Reynolds number. The Hama roughness function ΔU^+ describes the downward shift of the viscous-scaled mean velocity profile induced by the roughness compared to a smooth wall, and its soundness, as a measure of added drag, relies on the validity of outer layer similarity.

The similarity of the outer flow implies that roughness only affects a small region in the vicinity of the wall, whereas turbulence in the outer layer is independent of the wall condition [23], perceiving the different surface only as a change in the mean drag [20]. The vast majority of surface patterns exhibit outer layer similarity; therefore, the estimate of the added drag translates into finding a relation between the geometrical features of the roughness (e.g. k) and ΔU^+ , which is in general different for every surface pattern. In an attempt to have a semblance of universality, the equivalent sand grain roughness k_s is introduced, defined as the height that sand grain roughness should have to produce the same ΔU^+ as the surface examined [18, 31].

In the context of high-speed flows, it is not clear whether the theories developed for incompressible turbulence apply and the literature on the subject is scarce. This was clearly underlined in the literature survey of Bowersox [5], who described the high-speed database available at the time, composed exclusively of experimental studies, and outlined some of the open questions that are still relevant at the present time. First, compressibility transformations are assessed as a way to scale the compressible rough velocity profile into the incompressible counterpart, thus recovering the outer layer similarity described above. It has been shown by different experimental studies that the theory of Van Driest [40] is effective in obtaining Mach number invariance when the wall is adiabatic [15, 24, 44]. Recently, Modesti et al. [30] performed Direct Numerical Simulation (DNS) of supersonic diabatic turbulent channels, showing that more recent compressibility transformations [42] can account for wall temperature effects if an equivalent roughness Reynolds number is used. Future studies are needed to confirm this finding in turbulent boundary layers and with different surface

topologies and Mach numbers.

Another aspect noted in the survey of Bowersox [5] is that the interaction between compressibility and wall roughness can produce shock and expansion waves generated by each element traversing the boundary layer and emerging into the free stream. This was noted by several experimental studies at Mach numbers from 2 to 2.9, [15, 24, 25], where the wave structure was found to significantly affect first and second-order statistics, as well as locally varying the wall shear stress. Tested geometries consisted of 3D cubes, 2D bars, sand-grained surfaces, and a diamond-like pattern; the latter being the one that produced the most intense local distortions of the flow [15].

In this respect, it is still unclear if for certain configurations compressibility effects can be so strong to break outer layer similarity. Peltier et al. [32] came to this conclusion analysing the wave structure produced by a flow over crosshatch roughness at Mach 4.9, constituted of a pattern of shocks and expansions that perturbed the entirety of the boundary layer. They provided a conceptual model in which they hypothesize that the lower part of the boundary layer exhibits the dominance of compression waves that enhance turbulence intensity, while expansion waves suppress it in the second half. This observation is in contrast with the experimental study of Williams et al. [44], which performed experiments at hypersonic speeds (Mach number 7.3), but noted a general agreement with similar experiments in incompressible flows. We note that the friction Reynolds number, Re_τ , for this study was much lower compared to the experiments by [32].

All previous experimental studies, feature a smooth-to-rough transition but almost none of them assessed the adjustment length to the new surface condition. In the incompressible literature smooth-to-rough transition (or vice versa) has been extensively investigated and it features the formation of an internal boundary layer δ_I which forms and develops within the incoming boundary layer and eventually merges with it [17, 36]. The experimental study of Kocher et al. [24] is, to our knowledge, the only one that attempts to characterize smooth-to-rough transition in a supersonic boundary layer, although the number of streamwise locations considered is limited. They observed a significant change in turbulent statistics at least after 19.5δ downstream of the transition, where δ is the BL thickness of the incoming smooth-wall boundary layer.

In this work, we perform DNS of zero-pressure-gradient turbulent boundary layer at free-stream Mach numbers of $M_\infty = [0.3, 2]$ and friction Reynolds number up to $Re_\tau \approx 1700$ over both smooth and rough walls in order to gain valuable insights in the flow physics. We limit ourselves to one roughness geometry constituted by cubical roughness elements, preceded by an incoming smooth-wall boundary layer. This configuration allows us to study, for the first time, the streamwise development of a supersonic boundary layer that adjusts to a rough surface with the goal of assessing similarities and differences compared to the subsonic case. Turbulence and thermal statistics are then analysed downstream of the surface transition to understand if any outer layer similarity can be observed with reference smooth wall cases.

| Run | M_∞ | Re_τ | L_x | L_y | L_z | N_x | N_y | N_z |
|--------|------------|------------|-------|-------|-------|-------|-------|-------|
| RH_M2 | 2 | 600 – 1700 | 150 | 25 | 8.28 | 20240 | 556 | 1408 |
| RH_M03 | 0.3 | 650 – 1650 | 150 | 25 | 8.28 | 20240 | 556 | 1408 |
| SM_M2 | 2 | 600 – 1520 | 300 | 25 | 9 | 15360 | 556 | 740 |

Table 1: Summary of parameters for DNS study. Domain lengths L_x, L_y, L_z are given in terms of the inflow BL thickness δ_{in} .

Methodology

We solve the compressible Navier–Stokes equations for a viscous, heat-conducting gas

$$\begin{aligned} \frac{\partial \rho}{\partial t} + \frac{\partial(\rho u_j)}{\partial x_j} &= 0, \\ \frac{\partial(\rho u_i)}{\partial t} + \frac{\partial(\rho u_i u_j)}{\partial x_j} + \frac{\partial p}{\partial x_i} - \frac{\partial \sigma_{ij}}{\partial x_j} &= 0, \\ \frac{\partial(\rho E)}{\partial t} + \frac{\partial(\rho Eu_j + pu_j)}{\partial x_j} - \frac{\partial(\sigma_{ij} u_i - q_j)}{\partial x_j} &= 0, \end{aligned} \quad (1)$$

where ρ is the density, u_i denotes the velocity component in the i th Cartesian direction ($i = 1, 2, 3$), p is the thermodynamic pressure, $E = c_v T + u_i u_i / 2$ the total energy per unit mass and

$$\sigma_{ij} = \mu \left(\frac{\partial u_i}{\partial x_j} + \frac{\partial u_j}{\partial x_i} - \frac{2}{3} \frac{\partial u_k}{\partial x_k} \delta_{ij} \right), \quad q_j = -k \frac{\partial T}{\partial x_j} \quad (2)$$

are the viscous stress tensor and the heat flux vector, respectively. The molecular viscosity μ is assumed to follow Sutherland’s law, with a reference free-stream temperature $T_\infty = 220.0$ K. The thermal conductivity k is related to the viscosity through the Prandtl number $Pr = 0.72$, $k = c_p \mu / Pr$, where c_p is the specific heat at constant pressure. This model is complemented by the equation of state for a calorically perfect gas. The system of equations is solved on a Cartesian grid using the in-house code STREAmS [3, 4], which has been extensively validated in numerous canonical flow configurations [1, 2, 9, 10, 29]. Convective terms are discretised using sixth-order, energy-preserving schemes applied in shock-free regions, while a high-order shock capturing scheme (WENO) is applied when shock waves are identified by the Ducros sensor [14]. Viscous terms are discretised using a locally conservative formulation [13] with second-order accuracy.

The present database is composed of two simulations featuring compressible turbulent boundary layers over rough surfaces at $M_\infty = 0.3$ (RH_M03) and $M_\infty = 2$ (RH_M2), alongside a supersonic smooth wall case for comparison (SM_M2), (see table 1).

The rough wall simulations consist of three regions: an initial smooth wall part dedicated to the development of a turbulent boundary layer, obtained through a recycling/rescaling procedure, where the recycling plane is placed at $x = 40\delta_{in}$. The second part starts at $x = 55\delta_{in}$, ends at $x = 147\delta_{in}$ and consists of cubic elements of side k , which are representative of the structured roughness patterns forming over ablative surfaces [30]. Finally, a small smooth wall part is placed at the end of the domain until $x = 150\delta_{in}$ as a buffer region before the outflow. The roughness elements are spaced by a distance $2k$ in the wall-parallel directions, as shown in figure 1. The complexity of the geometry is handled using a ghost-point-forcing immersed boundary method [12, 33], which is used to enforce

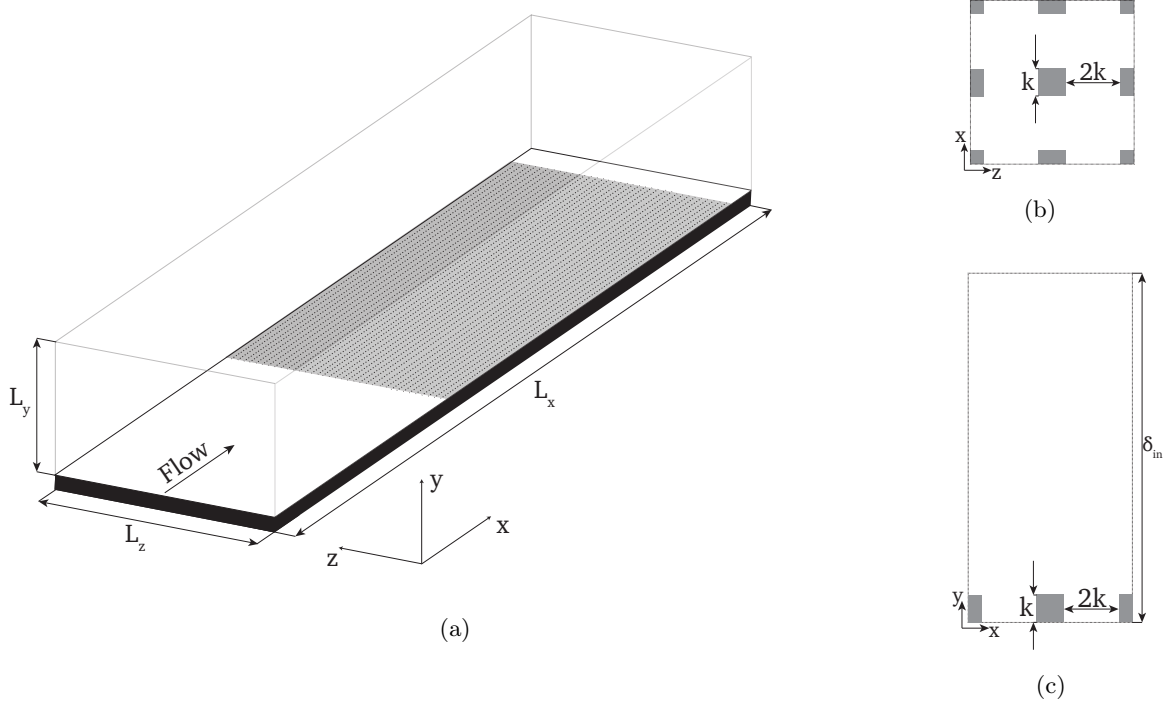


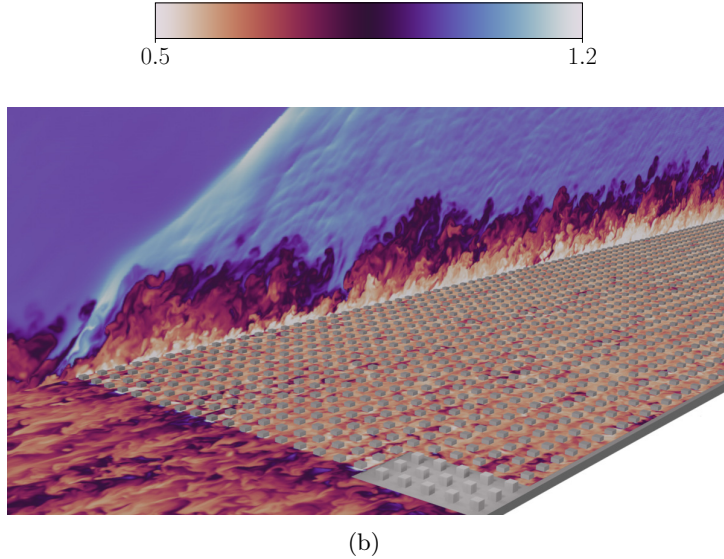
Figure 1: Schematic of the computational set-up for a turbulent boundary layer flow over cubical roughness. The elements have size k and spacing $2k$ in the wall-parallel directions. Here δ_{in} is the inflow boundary layer thickness (not to scale).

| Label | Station x/δ_{in} | Re_τ | Δx^+ | $\Delta y_{min/max}^+$ | Δz^+ | k^+ | k_s^+ | δ_{99}/k |
|--------|-------------------------|-----------|--------------|------------------------|--------------|-------|---------|-----------------|
| RH_M03 | 140 | 1549 | 2.9 | 0.48–7 | 2.9 | 56 | 103 | 28 |
| RH_M2 | 140 | 1635 | 2.8 | 0.47–7 | 2.8 | 57 | 105 | 29 |
| SM_M2 | 278 | 1484 | 6.5 | 0.33–8 | 4 | — | — | — |

Table 2: Boundary layer properties at the selected stations. Grid spacings are given in wall units according to the selected station. The values of Δy_{min}^+ and Δy_{max}^+ refer to the wall-normal spacing at the wall and at the boundary layer edge, respectively.

no-slip adiabatic boundary conditions on the solid wall. Following the mesh convergence study of [30], which simulated the same roughness geometry in turbulent channel flows, the number of computational nodes per element is 20, 40, 20 in the three directions x, y, z , respectively. Throughout this study, mean flow statistics are collected at selected streamwise locations, reported in table 2. For rough wall cases, we selected a station x/δ_{in} far from the surface transition to avoid non-equilibrium effects, whereas smooth wall statistics are collected at a similar Re_τ number. Table 2 also reports the computed roughness Reynolds number k^+ and the ratio δ_{99}/k at the selected stations for rough cases, where we note that at these stations we expect a fully rough regime as $k_s^+ > 80$. Here, the ratio $k_s/k = 1.84$ is computed as discussed in section §Velocity statistics.

Throughout this study, we use the symbols u , v , and w to denote the streamwise, wall-normal and spanwise velocity components and the decomposition of any variable is conducted using either the standard Reynolds decomposition ($f = \bar{f} + f'$) or the density-weighted (Favre) representation ($f = \tilde{f} + f''$), being $\tilde{f} = \bar{\rho}\bar{f}/\bar{\rho}$. Here, mean quantities are computed using different samples in time, exceeding $500\delta_{in}/u_\infty$ for all cases, and space, considering the periodic spanwise direction z .



(b)

Figure 2: Instantaneous density field ρ/ρ_∞ for flow case case RH_M2. The flow domain is excluded in a portion around the transition region to highlight the roughness elements.

and a moving average over a small window λ_x in the streamwise direction x . The latter corresponds to four roughness periods, or equivalently, $\lambda_x = 1.44\delta_{in}$, which is approximately half of the mean boundary layer thickness after the onset of roughness. The presence of computational nodes inside the solid domain is taken into account by considering the intrinsic average of mean flow statistics only in the fluid plane area S_f , such that $\bar{f} = 1/S_f \int_{fluid} f dS$.

Instantaneous flow

We start by providing an overview of the instantaneous flow organization to build a qualitative understanding of the main flow features, particularly at the smooth-to-rough surface transition. First, we inspect the instantaneous density field of the supersonic case in figure 2 in a longitudinal and wall-parallel plane. Before the roughness, we find a canonical smooth-wall organization which is abruptly disrupted by the occurrence of a shock wave caused by the first row of roughness elements. In the longitudinal plane, behind the shock wave, we also note a series of expansion and compression waves possibly caused by the roughness pattern below. On the roughness, we note that low density fluid is preferentially located in the troughs, where velocity is higher, due to the cubes alignment.

Figure 3 shows the instantaneous contours of streamwise velocity for both subsonic, RH_M03, and supersonic, RH_M2, cases, indicating the development of the turbulent boundary layer and its influence into the freestream. In contrast to the streamwise evolution of case RH_M03, which seems to be weakly affected by the onset of surface roughness, supersonic case RH_M2 shows emerging features that are clearly related to the interaction between compressibility and the roughness. A strong compression is observed around $x/\delta_{in} = 55$, where roughness starts. The first compression wave is not directly emanated by the first row of cubical elements, but by a sudden adjustment of the boundary layer thickness due to an upward shift forced by the new surface condition.

After the first compression, we observe a series of smaller compression/expansion waves that protrude into the freestream. The level of acoustic disturbances emanated from the boundary layer

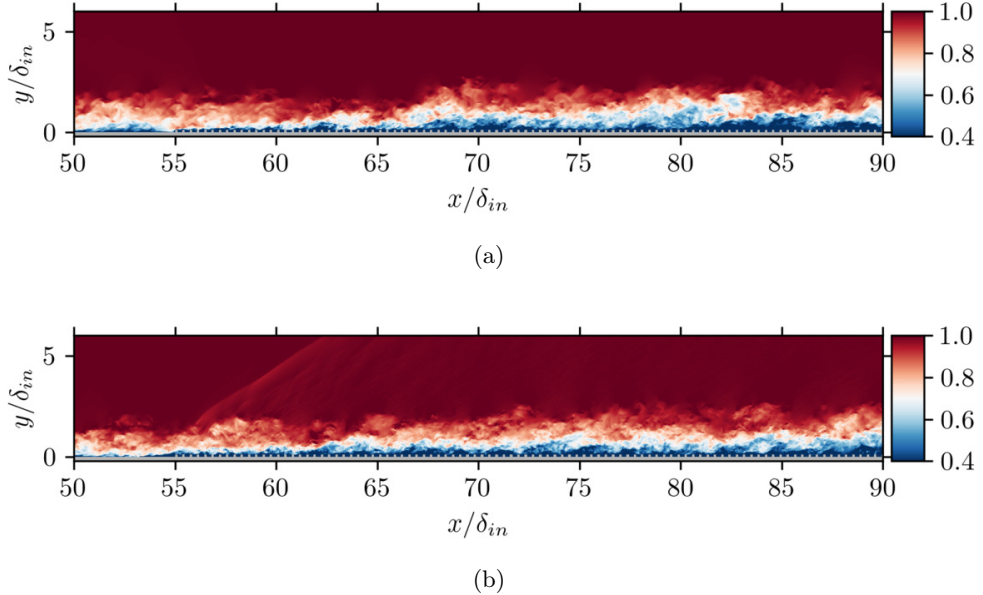


Figure 3: Instantaneous contours of the streamwise velocity u/u_∞ on a wall-normal plane. Panel (a): RH_M03 case, Panel (b): RH_M2 case.

tends to be lower downstream, but still present until the end of the domain (not shown).

Similar patterns can be observed in the instantaneous contours of the density gradient, visualized as a numerical Schlieren in figure 4(a). Here, we also report the time-averaged version of the same quantity over a short period of $75\delta_{in}/u_\infty$ in figure 4(b). This averaged flow better highlights the formation of the first strong compression, primarily caused by the vertical shift of the boundary layer, although a subsequent distortion is emanated from the first cubical element. We classify this first compression as a shock wave given that the propagation angle is estimated as 31.8° , while Mach waves have a theoretical angle of 30° at $M_\infty = 2$. Figure 4(b) also shows the sequence of compression waves emanated from each element and propagating into the freestream, which is visible throughout the domain and is in agreement with experimental studies that reported similar wave patterns [15, 24]. Finally, from the time-averaged numerical Schlieren we have a first glimpse of the formation of an internal boundary layer, visible as a dark blue region progressively growing as we move downstream.

Additional insights can be gained from the streamwise velocity fluctuations in a wall-parallel plane close to the roughness crest, at $y/k = 0.97$, figure 5. In both flow cases, the smooth wall region features the presence of small-scale velocity streaks typical of near-wall turbulence. After the onset of roughness, both the subsonic and supersonic flow cases exhibit a breakdown of the near-wall streaks, although a roughness-induced coherence is apparent as high-speed velocity streaks are preferentially aligned in the troughs between cubes. An important difference between the subsonic and supersonic cases is that the breakdown of the near-wall cycle occurs earlier in the latter, as evident from the small separated region preceding the first row of cubes. This is attributed to the adverse pressure gradient imposed by the shock wave at this location.

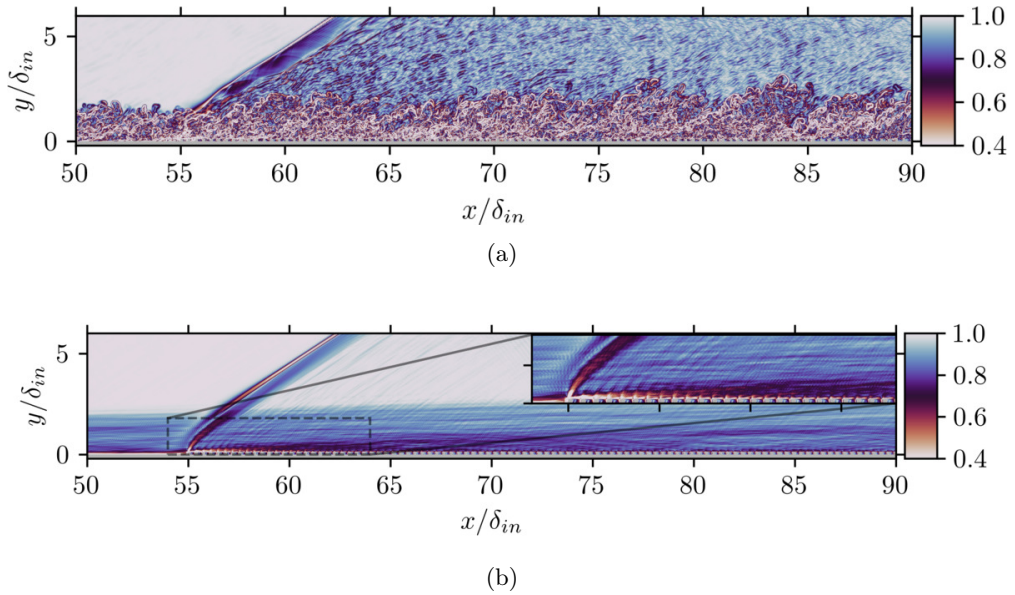


Figure 4: Instantaneous (a) and time-averaged (b) contours of the numerical Schlieren $\exp(-|\nabla \rho|)$ on a wall-normal plane for the case RH_M2. In panel (b) the flow has been time averaged for a short time interval $75\delta_{in}/u_\infty$ to filter out incoherent fluctuations.

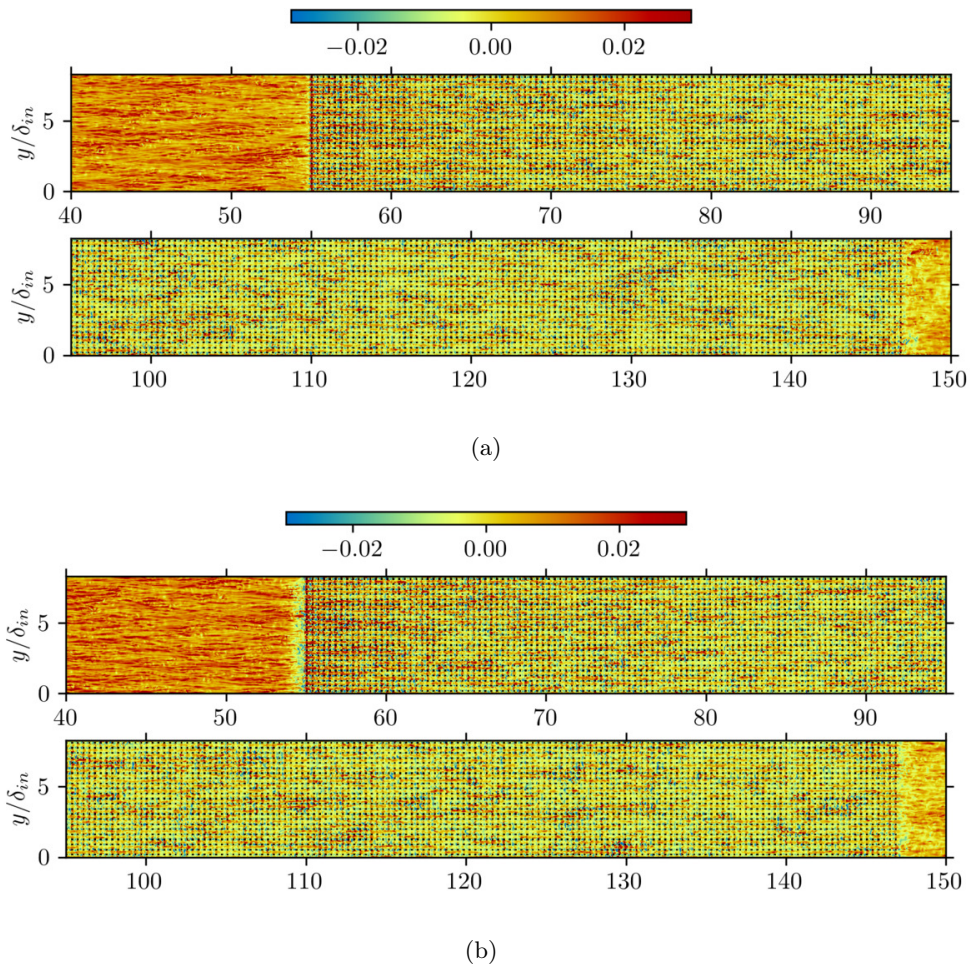


Figure 5: Instantaneous contours of the streamwise velocity fluctuations normalized by the freestream velocity u'/u_∞ on a wall-parallel plane at $y/k = 0.97$ (close to the roughness crest). Panel (a): RH_M03 case, Panel (b): RH_M2 case.

Results

Added drag and boundary layer development

We report a first assessment of the mean flow statistics, analysing their streamwise evolution of the boundary layer in figure 6. Figure 6(a) shows the mean streamwise evolution of the friction coefficient $C_f = \tau_w/(1/2\rho_\infty u_\infty^2)$, where the smooth-to-rough transition is clearly visible for both RH_M03 and RH_M2 cases downstream of $x/\delta_{in} \approx 55$, resulting in an increase of the local drag induced by the roughness. After an initial overshoot, the friction coefficient C_f decreases following a similar trend in subsonic and supersonic conditions, although with different intensities, and in the last part of the domain it drops as a result of the rough-to-smooth transition right before the outflow.

Figure 6(b) shows the streamwise growth of the boundary layer thickness δ_{99} . The supersonic and subsonic cases exhibit similar growth rates, but the relative intensity is affected by the surface change. The supersonic case RH_M2 exhibits a sharp upward bump in the boundary layer thickness after the onset of roughness, from which the boundary layer continues to grow. This effect is milder in subsonic case RH_M03, which in turn is only marginally affected by the surface change.

The increased boundary layer growth for supersonic case RH_M2 is visible when compared to the smooth-wall counterpart SM_M2, and amounts to approximately 1.4 times the reference boundary layer thickness $\delta_{99,ref}$ computed before the transition at $x/\delta_{in} = 45$. This effect was already visible in the instantaneous flow visualizations in section §Instantaneous flow, and we argue that it is directly related to the formation of an initial shock wave, representing a distinct feature of the smooth-to-rough supersonic transition, playing an important role in the development of the internal boundary layer (discussed in section §Internal boundary layer).

The differences in the streamwise development of typical lengths of the boundary layer are clearly noted in the profiles of the friction Reynolds number Re_τ , figure 6(c). On the initial smooth wall, subsonic and supersonic rough wall cases follow similar trends in the Re_τ number. However, on its rough region, the supersonic case RH_M2 attains slightly higher values of Re_τ than the subsonic counterpart RH_M03, as a result of the sharp growth of δ_{99} . We highlight that in order to compare rough and smooth wall at approximately matched Re_τ number, the domain of the latter is twice as long, see figure 6(e).

To complete the picture, profiles of the wall density are shown in figure 6(d). Subsonic case, RH_M03, shows a 2% variation compared to its freestream value, while supersonic case, RH_M2, shows variations of more than 40%, which is expected given the higher Mach number. In addition, we note that the wall density is slightly influenced by the smooth-to-rough transition, increasing by approximately 3% at the onset of the roughness, and then slowly decreasing as the post-shock effects attenuate.

A topic of practical interest is the validity of classical compressibility transformations for predicting the friction coefficient of high-speed flows over rough walls. One of the most employed transformations is van Driest II [41], which allows one to map the compressible friction coefficient into the incompressible one, and it is known to be accurate for adiabatic walls [34],

$$C_{f,i} = F_c C_f, \quad Re_{\theta,i} = \frac{\mu}{\bar{\mu}_w} Re_\theta = Re_{\delta_2}, \quad (3)$$

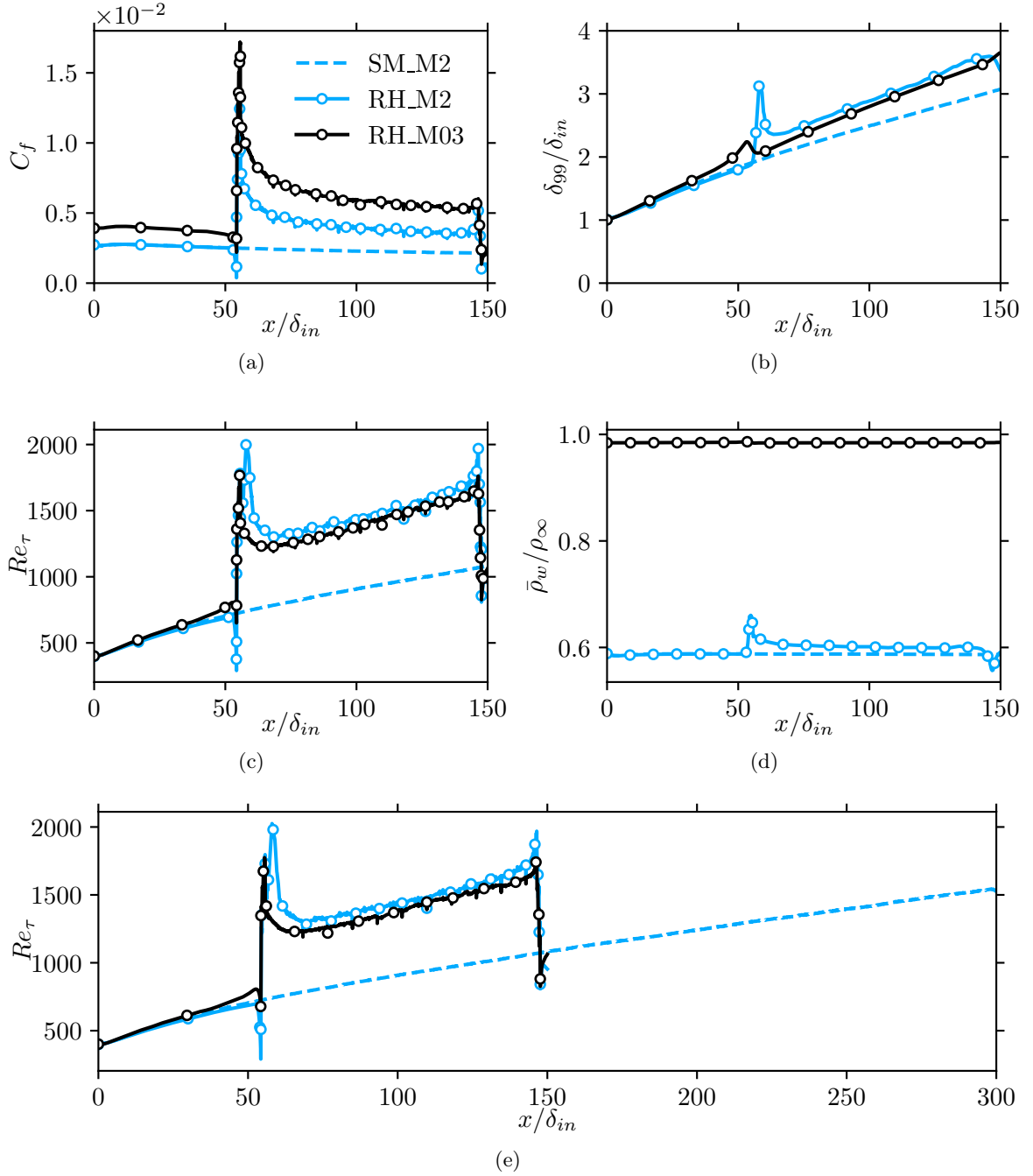


Figure 6: Mean streamwise profiles of (a) skin friction coefficient $C_f = \tau_w/(1/2\rho_\infty u_\infty^2)$, (b) boundary layer thickness δ_{99} , (c) friction Reynolds number Re_τ and (d) wall density ρ_w as a function of the streamwise coordinate x/δ_{in} . Panel (e) shows the friction Reynolds number Re_τ over the whole domain of case SM_M2.

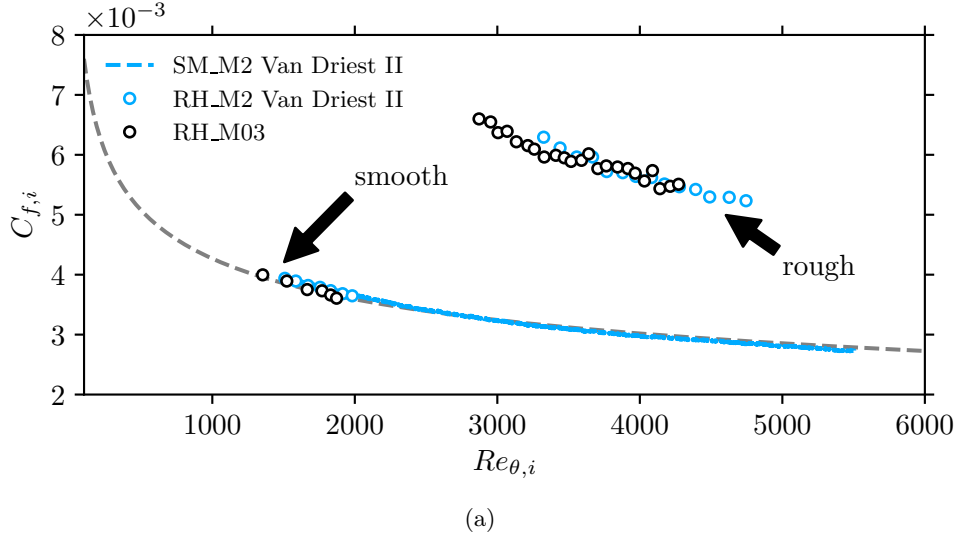


Figure 7: Transformed skin friction coefficient $C_{f,i}$ (equation (3)) as a function of the Reynolds number based on the incompressible momentum thickness $Re_{\theta,i}$. The dashed gray line represents the friction formulas $C_{f,i} = 0.024Re_{\theta,i}^{1/4}$.

where $Re_{\theta} = \rho_{\infty}u_{\infty}\theta/\mu_w$ is the Reynolds number based on the momentum thickness θ and F_c takes the expression

$$F_c = \frac{\bar{T}_w/T_{\infty} - 1}{\arcsin^2 \alpha}, \quad \alpha = \frac{\bar{T}_w/T_{\infty} - 1}{\sqrt{\bar{T}_w/T_{\infty}(\bar{T}_w/T_{\infty} - 1)}}. \quad (4)$$

The transformed distribution is compared with the friction formula $C_{f,i} = 0.024Re_{\theta,i}^{-1/4}$ by [38]. Figure 7 shows the performance of the aforementioned scaling for all cases in the present database. Here, only specific portions of the domain are considered in order to be far enough from the inlet/outlet and the smooth-to-rough transition, which for the smooth cases results in the range $20 < x/\delta_{in} < 50$ and for the rough cases $80 < x/\delta_{in} < 130$. In general, a very good collapse is observed when using the van Driest II transformation for the smooth supersonic case SM_M2 and both in the smooth and rough portions of cases RH_M2 and RH_M03.

Internal boundary layer

This section aims to discuss the growth of the Internal Boundary Layer (IBL), forming at the smooth-to-rough transition because the boundary layer progressively adjusts to the new surface condition. We focus on comparing the theory developed for incompressible boundary layers [36] to supersonic flows and proposing improvements for predicting the growth of the internal boundary layer thickness δ_I when compressibility effects are present.

Several definitions of internal boundary layer thickness are available for incompressible flows. One of the most popular is the one by [7] who determines δ_I as the point where the velocity \tilde{u}/u_{edge} downstream the transition point is 99% of the upstream velocity. To compare velocity profiles at different streamwise locations, the wall distance is scaled by the local boundary layer thickness δ_{99} at each station.

In our database, we found that this method has some degrees of arbitrariness, which makes it very sensitive, especially in supersonic cases. On the other hand, we look for a definition for the

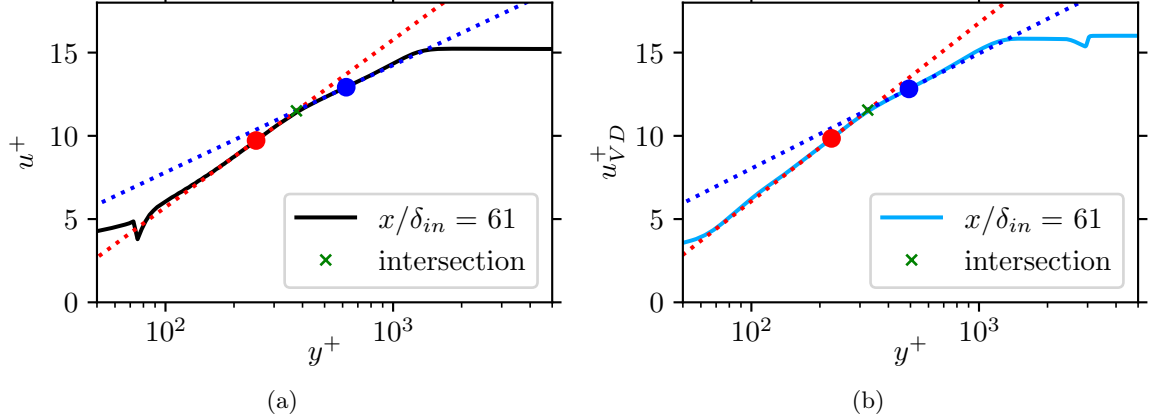


Figure 8: Visualization of the procedure for determining the internal boundary layer thickness δ_I using the method by Elliott [17] for flow case RH_M03 (a) and RH_M2 (b). The internal boundary layer thickness is the intersection (green cross) between two logarithmic regions (dotted lines).

IBL height that should not directly rely on the local boundary thickness value (both δ_{99} or integral values) to scale profiles at different streamwise locations, and not be based on the difference between different streamwise locations (e.g. smooth reference).

Among the different definitions developed for incompressible flows, the one from Elliott [17] is in line with requirements, and has been regarded by Rouhi et al. [36] as one of the most consistent with turbulence statistics, while being not dependent on specific thresholds. Elliott [17] argues that if we consider the velocity profiles in inner units $u^+ = f(y^+)$ right after the surface transition, they will show two logarithmic layers. The upper one would be reminiscent of the upstream surface condition while the lower one is adjusted with the new one. The intersection between these two logarithmic regions is identified as the location of δ_I . Looking at figure 8, which shows inner-scaled velocity profiles at approximately $x/\delta_{in} = 60$ and the corresponding logarithmic fits, we preliminary observe good evidence of this theory in both subsonic and supersonic regimes. This observation is confirmed by looking at figure 9, which shows the contours of $\partial u_V^+ / \partial \ln y^+$. Here, we used the Van Driest [40] transformation to scale velocities profiles in order to have comparable ranges in the contours. This relation has been tested successfully by several authors in supersonic adiabatic boundary layers over rough walls [15, 25]. A detailed comparison with more advanced compressibility transformations is given in section §Velocity statistics, considering a station $x/\delta_{in} = 140$, where the BL is expected to have reached a good equilibrium with the rough wall. A drawback of the definition by Elliott [17] is that the IBL growth (black dashed line in figure 9) is detectable only for a small streamwise extension after the roughness onset ($x/\delta_{in} < 75$), for both the subsonic and supersonic cases. This occurs because the sharp interface demarcating the internal boundary layer only exists for a small extent, before becoming more blurred and difficult to identify with precision.

Most definitions of IBL thickness proposed for incompressible flows [36] that we tested revealed to be very sensitive, inaccurate, or inconsistent at supersonic Mach numbers. In particular, we find important effects of the acoustic disturbances and the shock wave emanated at the surface transition, which substantially hamper the reliability of canonical definitions used at lower speeds. From the discussion above, we look for a quantity of interest that is weakly affected by strong compressibility effects. We thus consider the Favre-averaged wall-normal momentum equation,

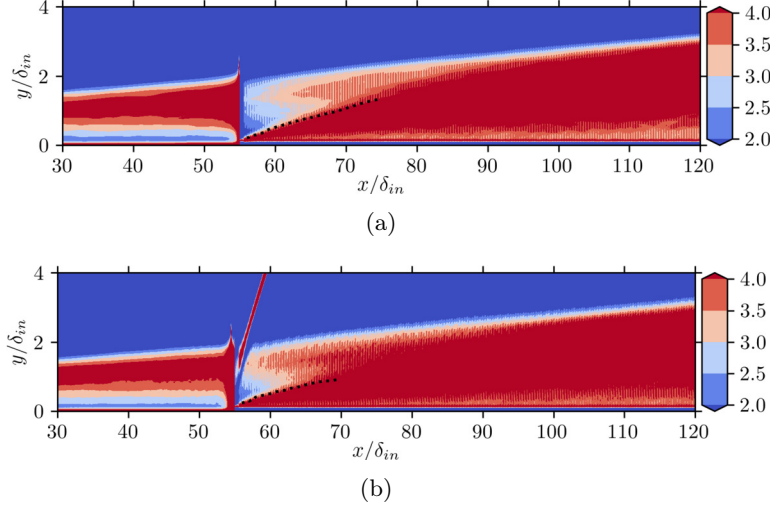


Figure 9: Contour plots of $\partial u_{VD}^+ / \partial \ln y^+$ for flow case RH_M03 (a) and RH_M2 (b). The dotted black lines indicate the IBL height δ_I predicted using the method by [17].

which in the boundary layer approximation reads [35]

$$\frac{\partial \bar{p}}{\partial y} + \frac{\partial(\bar{\rho}v''^2)}{\partial y} = 0. \quad (5)$$

In its integral form, equation (5) indicates that the freestream pressure is equal to the sum of the static pressure and the wall-normal turbulent stress. From a preliminary analysis of the flow structure of the supersonic case, we argue that since the local distortion emanated from each element tends to be almost normal to the flow right above the roughness crest (see figure 4(b)) the wall-normal component of velocity fluctuations should be the least affected by compression waves in this region, while still being tightly related to the vertical displacement of turbulence caused by the roughness. Additionally, the wall-normal velocity is less affected by compressibility effects, since it is much smaller than the speed of sound, even at supersonic speed. Figure 10 shows the contours of $\partial(\bar{\rho}v''^2)/\partial y$ in a longitudinal plane for both RH_M03 and RH_M2 cases. Comparing figures 10(a) and 10(b), the behaviour of $\partial(\bar{\rho}v''^2)/\partial y$ seems to consistently indicate the presence of the IBL for both Mach numbers without spurious effects due to local pressure gradients or shock waves. Figure 11 shows the wall-normal profiles of $\bar{\rho}v''^2$ at a given streamwise location, where we observe an inflection point clearly separating two (approximately) linear regions, whose intersection defines δ_I . To be more precise, we determine the slope and intersection point of these lines by selecting the relative height and location of minima and maxima of the function $\partial(\bar{\rho}v''^2)/\partial y$. We argue that this procedure can be considered similar to finding the point of maximum concavity, although more reliable from a numerical standpoint.

Figure 12 shows the predicted height of the IBL scaled by a reference boundary layer thickness at $x/\delta_{in} = 45$ as function of the streamwise distance from the surface transition using the algorithm of [17] and the present method. Note that points have been logarithmically spaced in the streamwise direction to enhance the accuracy of the power law fitting near the surface transition. We observe that the size of the IBL evaluated with the two methods is comparable, but the proposed definition leads to smoother results compared to the one by [17]. Moreover, both methods exhibit two distinct regions with different power law exponents $\delta_I \propto x^\alpha$, approximately before and after $2.5\delta_{99,ref}$, the

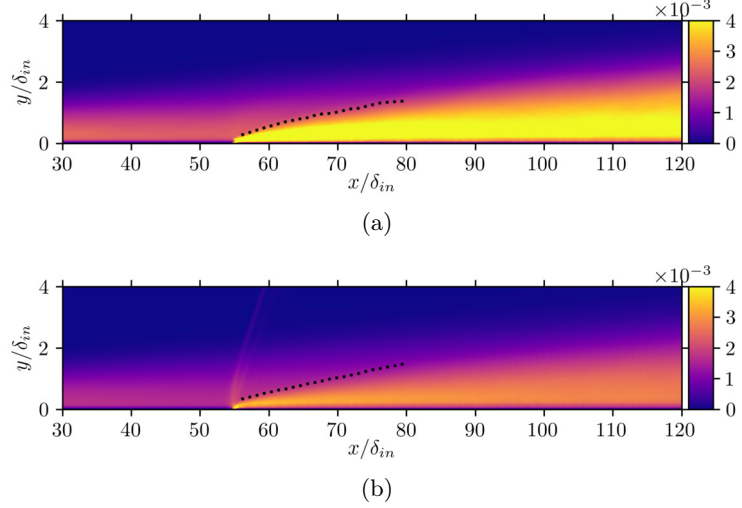


Figure 10: Contours of $\partial(\widetilde{\rho v''^2})/(\rho_\infty u_\infty)^2$ in a wall-normal plane for cases RH_M03 (a) and RH_M2 (b). The dotted black lines indicate the predicted IBL height δ_I using the present method.

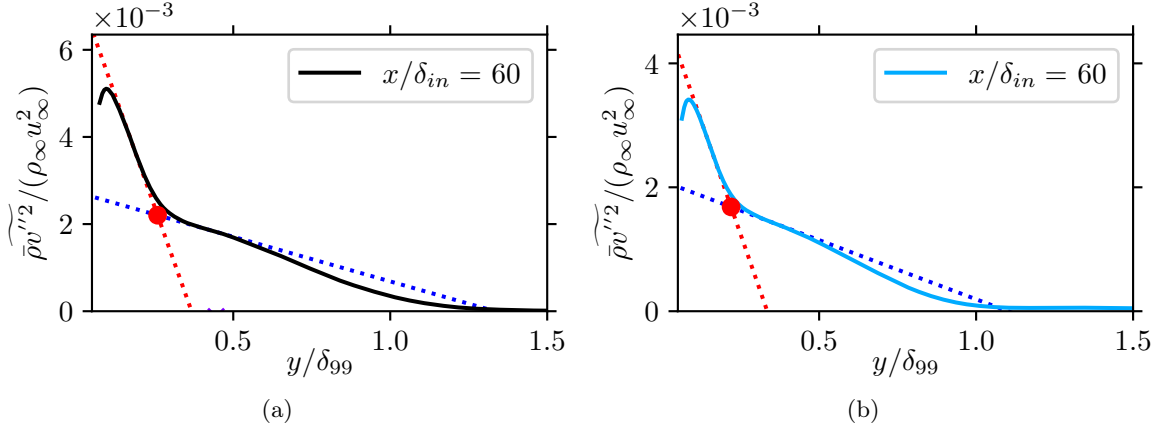


Figure 11: Visualization of the procedure for determining the internal boundary layer thickness δ_I using the present method for flow case RH_M03 (a) and RH_M2 (b). The internal boundary layer thickness is the intersection (red bullet) between two linear regions (dotted lines) to identify the slope change in the wall-normal Reynolds stress component $\widetilde{\rho v''^2}$.

first being clearly lower for both cases and methods.

We argue that the first region might be affected by an adverse pressure gradient imposed by the roughness right at the transition point, which could influence the boundary layer statistics further downstream. Focusing on the second region, we find that the aforementioned methods are consistent with each other and estimate a similar exponent α for supersonic, RH_M2, and subsonic, RH_M03, cases. In particular, the method of [17] yields $\alpha = 0.62$ for subsonic case RH_M03 and $\alpha = 0.58$ for supersonic case RH_M2. Similarly, the present method yields $\alpha = 0.58$ for subsonic case RH_M03 and $\alpha = 0.57$ for supersonic case RH_M2.

It is important to relate these results to the growth of the external boundary layer, which is significant especially for case RH_M2 (as discussed in section §Added drag and boundary layer development). Figure 13 shows the internal boundary layer growth estimated with the power-law fit and extended throughout the whole domain, and compares it with the growth of the external boundary layer. In particular, figures 13(a) and 13(b) show that the IBL growth predicted by the

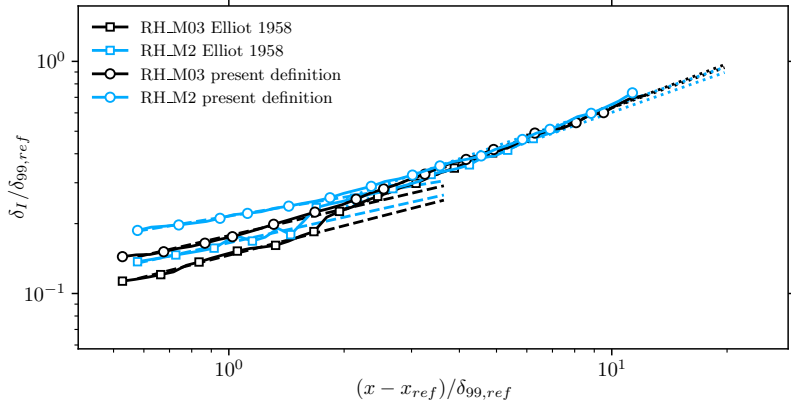


Figure 12: Predicted IBL height $\delta_I/\delta_{99,ref}$ as a function of the streamwise distance from the surface transition, calculated using the method by Elliott [17] and the present approach. Symbols represent DNS data at $M_\infty = 0.3$ (black) and $M_\infty = 2$ (blue). Dotted lines represent power law extrapolations. Both axes are normalized with a reference boundary layer thickness $\delta_{99,ref}$ at $x/\delta_{in} = 45$.

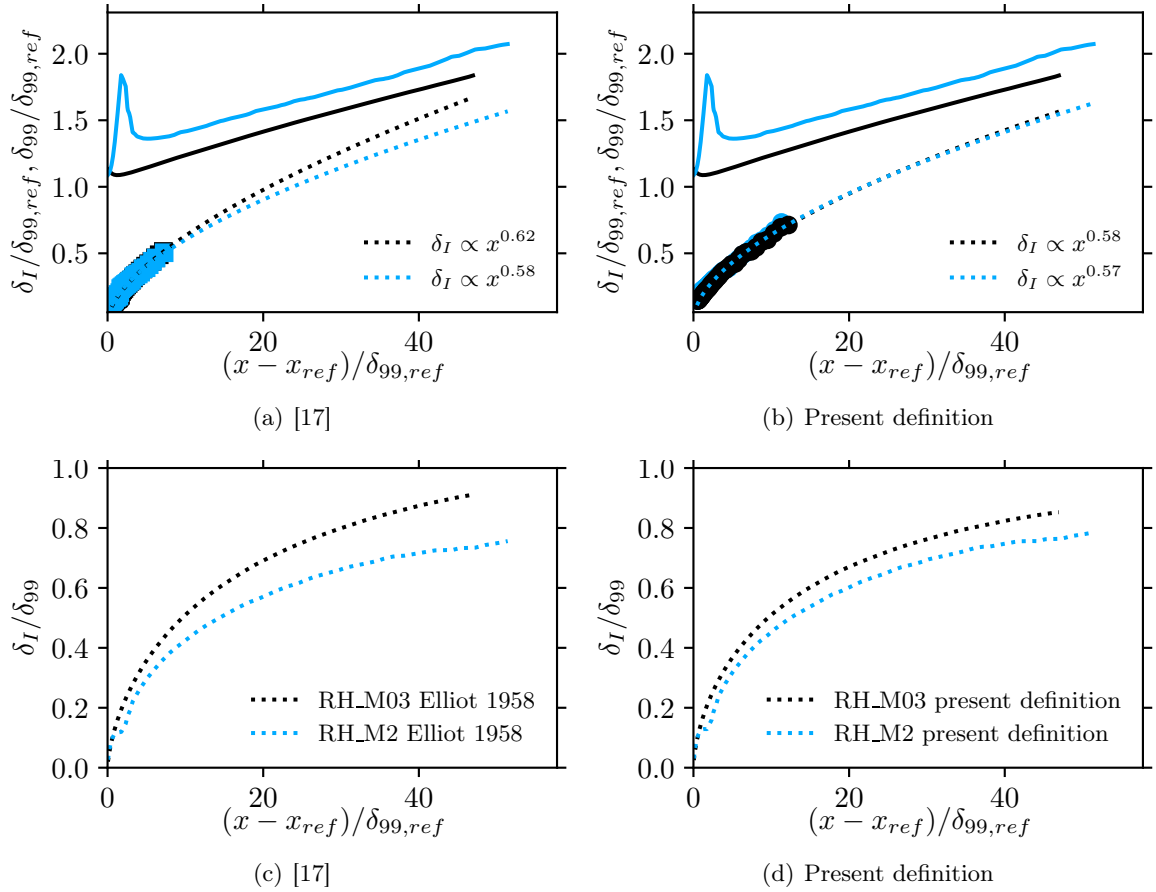


Figure 13: Height of the internal boundary layer $\delta_I/\delta_{99,ref}$ as a function of the streamwise distance from the surface transition: (a,c) using the method by Elliott [17] and (b,d) using the present method. Different normalizations are considered, namely using a reference boundary layer thickness $\delta_{99,ref}$ at $x/\delta_{in} = 45$ (just ahead of the smooth-to-rough transition) (a,b), and using the local boundary layer thickness (c,d). DNS data (symbols) are compared to the power law fittings $\delta_I \propto x^\alpha$ (dotted lines). Solid lines in (a,b) represent the boundary layer thickness $\delta_{99}/\delta_{99,ref}$.

fitted power laws is much more similar across subsonic and supersonic cases if compared to the respective behaviour of δ_{99} . Figures 13(c) and 13(d) show the relative growth of IBL on the BL, revealing a much slower pace for establishing an equilibrium for the rough-wall dynamics in the supersonic condition. This behaviour is attributed to the upward shift of the external boundary layer after the surface transition. Actually, while the IBL for the subsonic case, RH_M03, reaches 90% of the boundary layer height at the end of the domain, the supersonic case still lies below the 80%. These estimates provide a measure of the degree of equilibrium reached by the boundary layer in its adjustment to the different surface condition. We consequently expect the supersonic case RH_M2 to retain mild effects of the smooth-to-rough transition in streamwise stations located downstream, discussed in section §Velocity statistics.

We conclude that the formation and development of the IBL are similar across subsonic and supersonic cases, but when compared to the growth of the external boundary layer we observe a worse situation for the supersonic case RH_M2, which is attributed to the upward shift of the external boundary layer induced by the shock-wave located downstream of the onset of roughness.

Velocity statistics

In this section, we consider average velocity profiles at stations listed in table 2. In particular, rough wall cases are all located at the station $x/\delta_{in} = 140$ in order to minimize the out-of-equilibrium effects induced by the surface transition and the development of the internal boundary layer (section §Internal boundary layer). We use compressibility transformations to incorporate the effect of Mach number, comparing roughness-induced velocity deficit to the incompressible counterpart. It is worth mentioning that rough-wall velocity profiles have been shifted by an effective virtual origin of the flow [8], which has been chosen as $d = 0.9k$. This parameter was found to reduce the uncertainty of the velocity shift and it is in agreement with the value used by [30] for the same roughness geometry. Among the plethora of compressibility transformations, we select to first report the classical velocity scaling proposed by Van Driest [40], subscript ‘VD’, together with the two most recent and successful transformations proposed, namely the ones by [21], subscript ‘GFM’, and [22], subscript ‘HLPP’, which show improved accuracy in the case of strong density variations. All the above transformations (except the one by Griffin et al. [21]) can be expressed in terms of convolution integrals mapping the compressible velocity and wall distance into the incompressible ones (denoted with the subscript I),

$$y_I = \int_0^y f_I dy, \quad u_I = \int_0^{\tilde{u}} g_I d\tilde{u}. \quad (6)$$

the kernels functions f_I and g_I are reported in table 3. The transformation of Trettel and Larsson [39] is also reported here for clarity. For details on the approach of Griffin et al. [21] the reader can refer to the original paper.

Figure 14 shows the transformed mean velocity profiles for smooth and rough wall cases. For the smooth wall, the untransformed mean velocity profile of supersonic case SM_M2 in figure 14(a) shows some compressibility effects, which are accounted for by the compressibility transformations. We find only minor differences between the various transformations, which is expected on an adiabatic wall at this Mach number. Rough wall cases show the typical downward shift compared to the smooth wall, indicative of higher drag, with a small variance due to the application of different compressibility transformations, although visible.

| Transformation | Wall distance (f_I) | Mean velocity (g_I) |
|--------------------------|---|--|
| Van Driest [40] | $f_{VD} = 1$ | $g_{VD} = R^{1/2}$ |
| Trettel and Larsson [39] | $f_{TL} = \frac{d}{dy} \left(\frac{yR^{1/2}}{M} \right)$ | $g_{TL} = M \frac{d}{dy} \left(\frac{yR^{1/2}}{M} \right)$ |
| Hasan et al. [22] | $f_{HLPP} = f_{TL}$ | $g_{HLPP} = \left(\frac{1 + \kappa y_{TL} D^c}{1 + \kappa y_{TL} D^i} \right) g_{TL}$ |

Table 3: Compressibility transformations for wall distance and mean velocity according to Eq. (6), where $R = \bar{\rho}/\bar{\rho}_w$ and $M = \bar{\mu}/\bar{\mu}_w$. In the transformation by Hasan et al. [22], $D^i = [1 - \exp(-y^*/A^+)]^2$ and $D^c = [1 - \exp(-y^*/(A^+ + f(M_\tau)))]^2$ are damping functions, A^+ and κ are constants and $M_\tau = u_\tau/\sqrt{\gamma RT_w}$ is the friction Mach number.

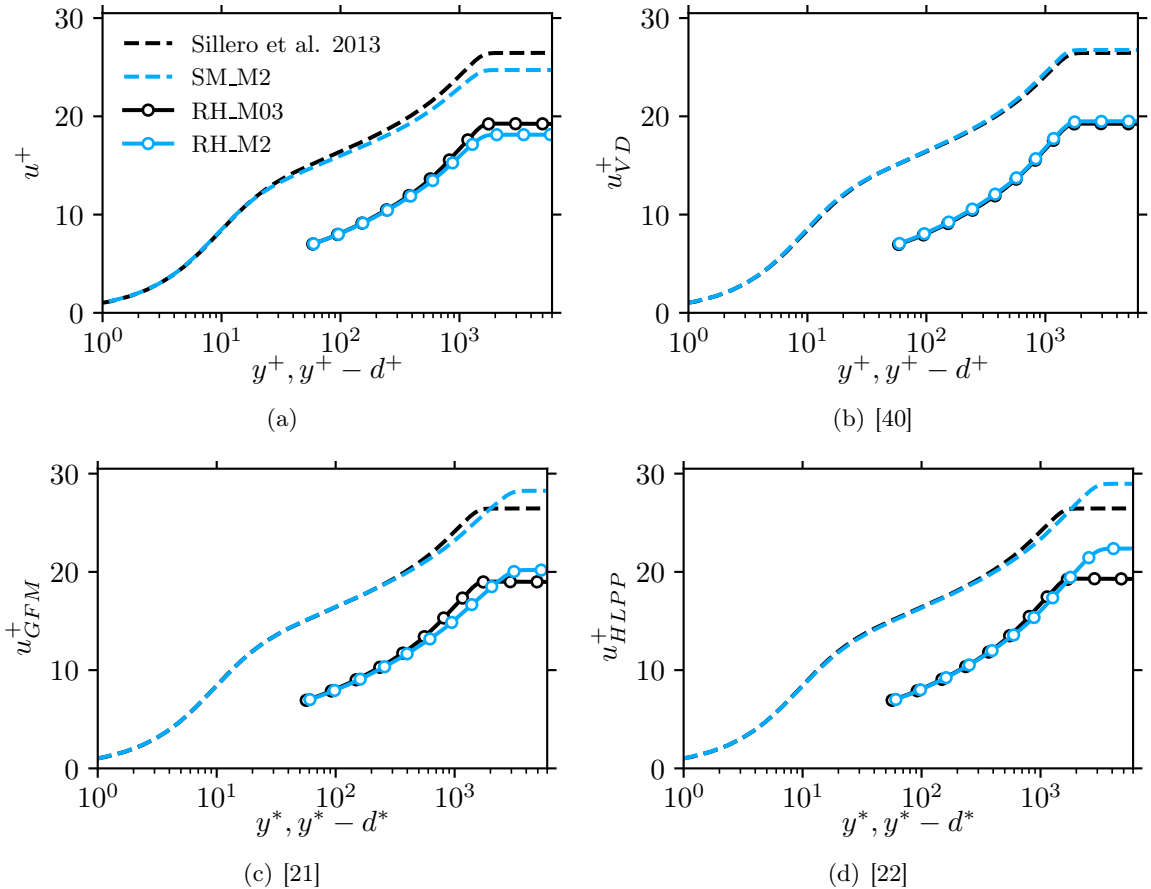


Figure 14: Mean velocity profiles for smooth and rough wall cases obtained at stations listed in table 2, for different compressibility transformations: (a) untransformed, (b) [40, VD], (c) Griffin et al. [21, GFT], (d) Hasan et al. [22, HLPP]. The smooth wall incompressible case of [37] at $Re_\tau = 1571$ is used as a reference.

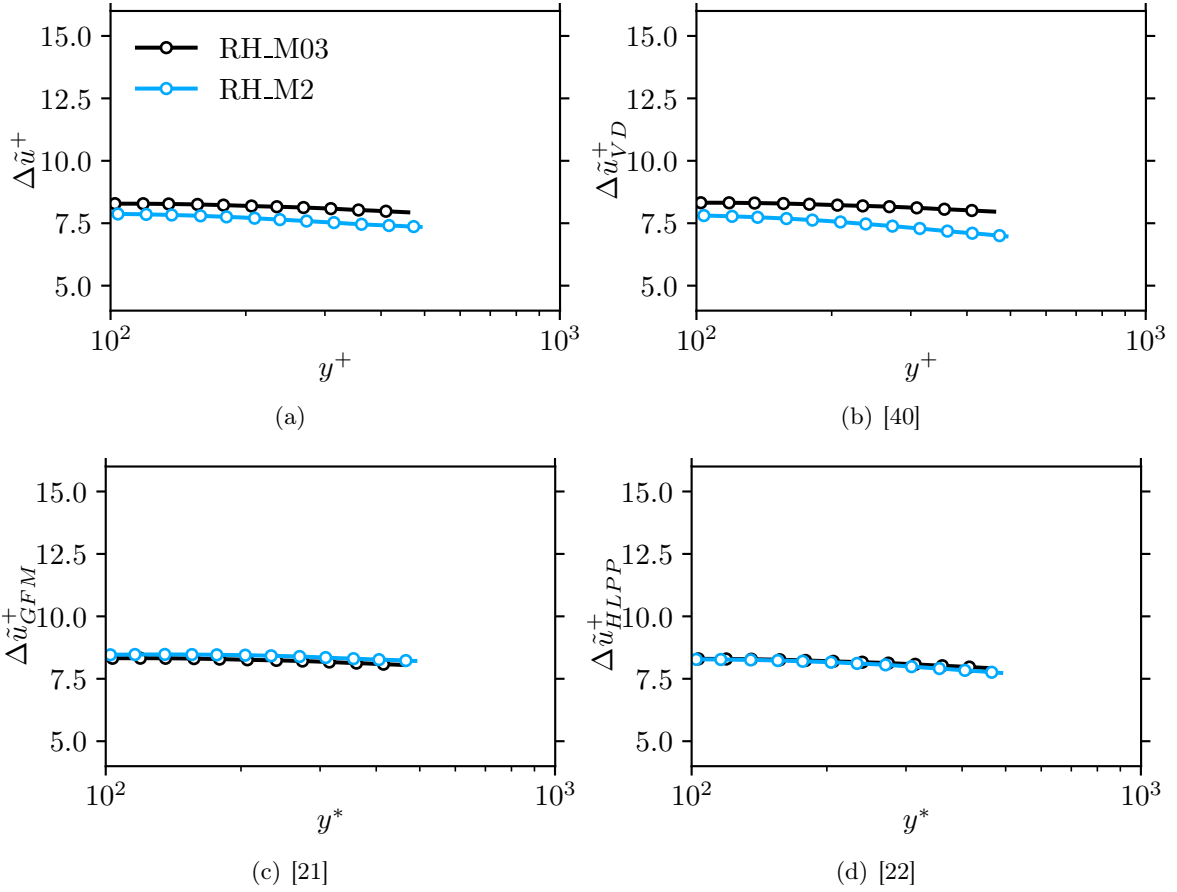


Figure 15: Mean velocity deficit between smooth and rough cases $\Delta\tilde{u}^+$.

In order to assess the performance of each transformation in collapsing both smooth and rough velocity profiles, we consider the velocity deficit function

$$\Delta\tilde{u}^+ = \tilde{u}_S^+(y^+) - \tilde{u}_R^+(y^+) \quad (7)$$

with $\tilde{u}_S^+(y^+)$ and $\tilde{u}_R^+(y^+)$ the average velocity of the smooth and rough wall cases, respectively. If outer layer similarity holds, $\Delta\tilde{u}^+$ is nearly constant in the log-layer (i.e. $100 < y^+ < 0.3Re_\tau$), although this is only a necessary condition as second-order quantities may still be out of equilibrium [26]. Figure 15 shows $\Delta\tilde{u}^+$ of the untransformed and transformed velocity profiles. In general, we observe a nearly constant behaviour across the different compressibility transformations, but the most recent transformations of [21] and [22] show a superior agreement with the subsonic reference. Even though in the incompressible regime the drag variation is directly related to ΔU^+ , it is important to note that in compressible cases the density ratio $R = \rho_\infty/\rho_w$ plays a role and the ratio between smooth and rough skin frictions C_{fs}/C_f can be written as $C_{fs}/C_f = R/R_s(1 - \Delta U^+/\tilde{u}_s^+)^2$ [30].

As customary for rough walls, introducing the equivalent sand-grain roughness k_s helps the standardization of the present roughness geometry, therefore, we evaluate its relation to the geometric roughness height k . The relation between k and k_s is at the basis of the Moody diagram, where the drag of a given rough geometry can be estimated by relating it to the drag produced by an equivalent sand-grain level. As discussed in [8], if the roughness Reynolds number is based on the

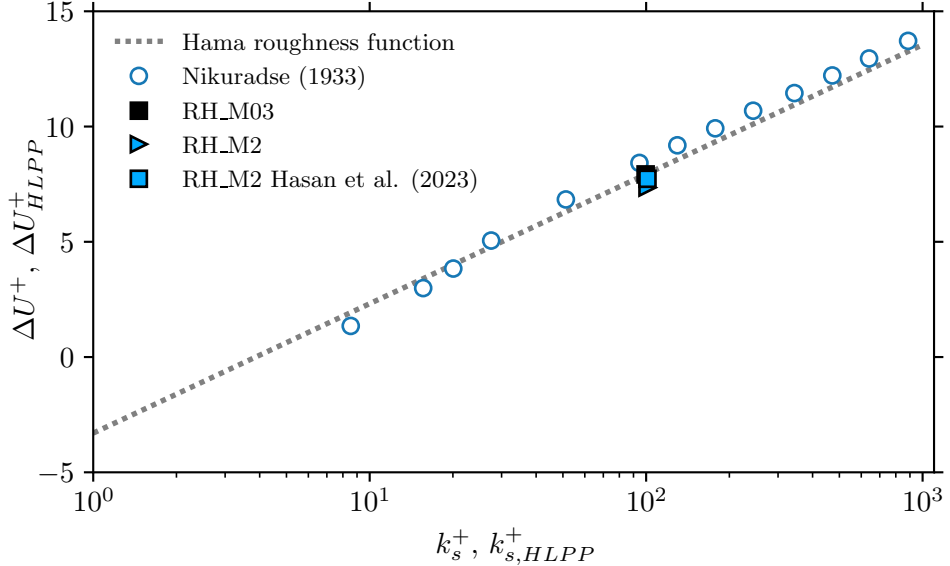


Figure 16: Shift of the mean streamwise velocity $\Delta\tilde{u}^+$ as a function of the inner-scaled equivalent sand-grain roughness height k_s^+ . The case RH_M2 is also reported using velocity profiles transformed with the relation of [22]. The dotted grey line indicates the Hama roughness function $\Delta U^+ = 1/k \ln k_s^+ + 8.5 - 5.2$, while open circles are data from Nikuradse [31].

equivalent sand-grain roughness height, $k_s^+ = k_s/\delta_\nu$, and the separation of scales is large enough to yield the fully-rough regime, the velocity deficit function ΔU^+ takes the form

$$\Delta U^+ = 1/\kappa \ln k_s^+ + A - B_s \quad (8)$$

Here, $\kappa = 0.41$ is the von Karman constant, $A = 5.2$ and $B_s = 8.5$.

We first find the ratio between k_s and k by matching the incompressible case RH_M03 with the fully rough asymptote, equation (8), which yields $k_s/k = 1.84$. This is in agreement with Modesti et al. [30], who reported a value of 1.9 for the same roughness geometry in a turbulent channel flow. The same ratio is used for the supersonic case RH_M2 to relate the resulting k_s^+ with the corresponding velocity deficit ΔU^+ , computed at the nominal edge of the logarithmic region $0.3Re_\tau$. Figure 16 shows ΔU^+ as a function of k_s^+ for the RH_M2 case using both the untransformed and transformed values according to [22], used for both ΔU_{HLPP}^+ and $k_{s,HLPP}^+$, computed using the relation $k_I = y_I(k)$ [30].

We observe that using a suitable compressibility transformation, which in our case is mainly acting on the velocity deficit ΔU_{HLPP}^+ , yields a slightly better agreement with the incompressible asymptote.

Figure 17 reports the Reynolds stress components as a function of y^+ , figure 17(a), and y/δ_{99} , figure 17(b). Here, the wall-normal coordinates for rough wall cases are again shifted by the virtual origin in order to assess the outer layer similarity. In general, we note that both cases follow quite well the behaviour of the smooth-wall counterpart in the outer layer, with few discrepancies in the streamwise component τ_{11} . Among the two rough cases, the subsonic RH_M03 seems to better agree with the reference case of [37] up to $y^+ > 300$, while both profiles exhibit a plateau approaching the roughness crest, located at approximately $y^+ \approx k^+ \approx 60$. For the same component, supersonic case RH_M2 shows a more intense level of fluctuations when compared to the corresponding smooth case SM_M2 at a similar Re_τ number. For this case, the influence of the smooth-to-rough transition

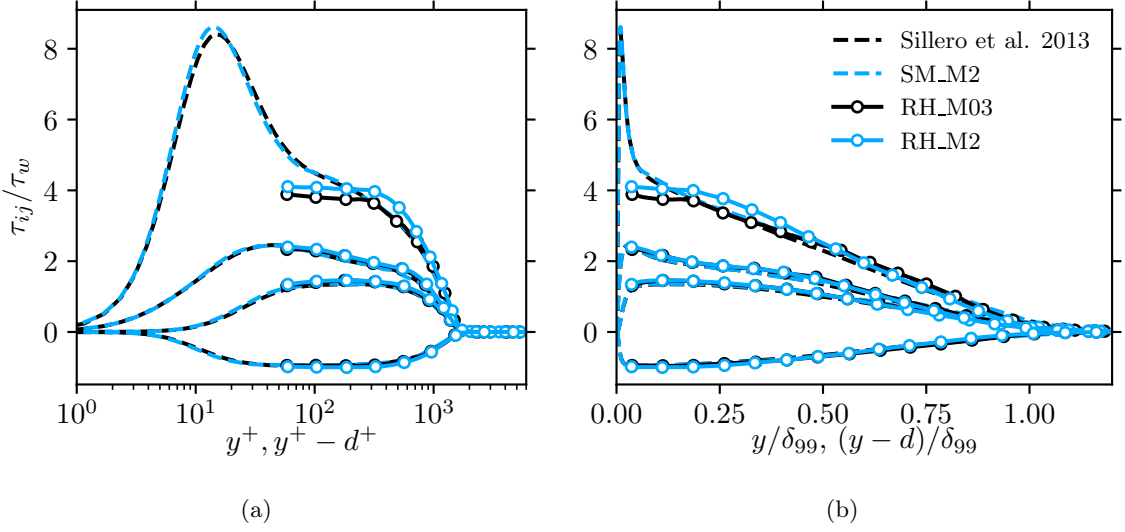


Figure 17: Turbulent velocity fluctuations $\tau_{ij} = \widetilde{u_i u_j}$ scaled with the wall shear stress τ_w as function of the wall-normal distance in wall units (a) $y^+, y^+ - d^+$ and outer units (b) $y/\delta_{99}, (y - d)/\delta_{99}$. Rough wall cases are adjusted using a virtual origin shift $d = 0.9k$.

extends further downstream, as discussed in section §Internal boundary layer, and this is especially true for the second-order statistics. We attribute this effect to the modulation of the turbulent structures on the outer layer induced by the initial shock-wave, that is expected to mainly affect the streamwise velocity fluctuations.

The Reynolds shear stress τ_{12} of the rough wall cases shows an excellent collapse even with the respective smooth wall reference case. A clear plateau close to a value of $\tau_{12}/\tau_w \approx 1$ in the log-layer is established, meaning that a constant stress layer exists in all cases.

Thermal statistics

We consider thermodynamic statistics at stations listed in Table 2 for smooth and rough supersonic cases, SM_M2 and RH_M2, respectively. This aspect is particularly interesting in order to assess if the outer layer similarity, extensively studied for velocity statistics, can be also observed in the temperature field. Figure 18 shows the mean, \tilde{T} , and root-mean-square, \tilde{T}_{rms} , temperature profiles as a function of y^+ . Profiles are not shifted with a virtual origin in order to show their behavior even below the roughness crest. Both \tilde{T} and \tilde{T}_{rms} of flow cases RH_M2 and SM_M2 are fundamentally different. In particular, the mean temperature profile \tilde{T} , figure 18(a), is consistently higher for the rough case, excluding the region very close to the wall where it settles to slightly lower values. Looking at the temperature fluctuations rms, \tilde{T}_{rms} , figure 18(b), we note even more significant differences between the smooth and rough cases. In particular, temperature fluctuations are mostly damped in the roughness layer, while an intense peak appears in the outer layer, right below the edge of the boundary layer. These findings are consistent with the results of [30] for turbulent channel flows over rough walls with isothermal wall condition. They concluded that there is no evidence of outer layer similarity for the temperature field, and roughness is able to influence the temperature fluctuations throughout up to the edge of the boundary layer. Similar conclusions are evident for the present cases despite the fact that adiabaticity is enforced at the wall, which for smooth cases is a condition that yields a strong similarity between velocity and temperature fields

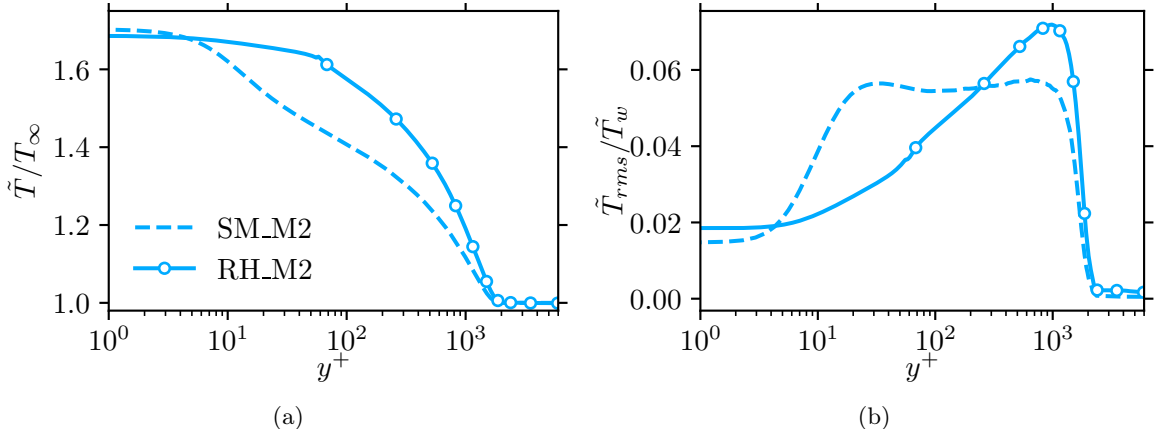


Figure 18: Panel (a): Normalised temperature profiles \tilde{T}/T_∞ for cases RH_M2 and SM_M2 as a function of the wall-normal distance y^+ . Panel (b): Temperature fluctuations scaled with the wall temperature $\tilde{T}_{rms}/\tilde{T}_w$ as a function of y^+ .

even at higher Mach numbers [10]. This aspect suggests that the interaction between compressibility and roughness fundamentally alters the thermal field and this process dominates over the influence of the wall temperature condition.

From a physical point of view, we can explain the influence of roughness in altering the temperature fluctuations profile by considering the definition of the thermal production term $\mathcal{P}_T = -\bar{\rho}\bar{v}''\bar{T}''\partial\tilde{T}/\partial y$, see for example [10]. In particular, it should be noted the behaviour of the wall-normal component of Reynolds stresses $\bar{\rho}\bar{v}''^2$, figure 17, which influences the velocity-temperature fluctuations correlation $\bar{\rho}\bar{v}''\bar{T}''$, and the mean temperature profile \tilde{T} , figure 18(a), whose gradient appears in the expression of \mathcal{P}_T . The temperature profile appears to stagnate around a nearly constant value, roughly \tilde{T}_w , up to the roughness crest, while the smooth profile is already at much lower and decreasing temperatures. Hence, the vanishing mean temperature gradient in the buffer layer damps the near-wall thermal fluctuations production \mathcal{P}_T . Far from the wall, the rough wall profile is forced to have a higher wall-normal temperature gradient $\partial\tilde{T}/\partial y$ in order to reach the edge temperature, while wall-normal velocity fluctuations $\bar{\rho}\bar{v}''^2$ are similar to those of the smooth wall profile in the same region (see figure 17). Hence, we attribute the outer layer peak of temperature fluctuations \tilde{T}_{rms} , figure 18(b), to the steeper mean temperature gradient $\partial\tilde{T}/\partial y$, which increases the thermal fluctuations production \mathcal{P}_T .

We finally assess the coupling between average thermal and kinetic fields through the well-known temperature-velocity quadratic relation [6, 11], which has been improved over the years to account for finite heat transfers and high Mach numbers [47]

$$\frac{\tilde{T}}{T_\infty} = \frac{T_w}{T_\infty} + \frac{T_{rg} - T_w}{T_\infty} \frac{\tilde{u}}{U_\infty} + \frac{T_\infty - T_{rg}}{T_\infty} \left(\frac{\tilde{u}}{U_\infty} \right)^2 \quad (9)$$

where $T_{rg} = T_\infty + r_g U_\infty^2 / (2c_p)$ and $r_g = 2c_p(T_w - T_\infty)/U_\infty^2 - 2Pr q_w/(U_\infty \tau_w)$. Figure 19 compares smooth and rough wall profiles of the mean temperature as a function of the mean velocity with their respective estimate given by the Zhang et al. [47] relation. As expected, the smooth DNS profile is well approximated by the temperature-velocity relation, Eq. (9). The supersonic rough wall case RH_M2 closely follows its smooth counterpart in the region denoted by $\tilde{u}/u_\infty > 0.5$, showing a slight mismatch below this threshold. Despite this small difference, we conclude that

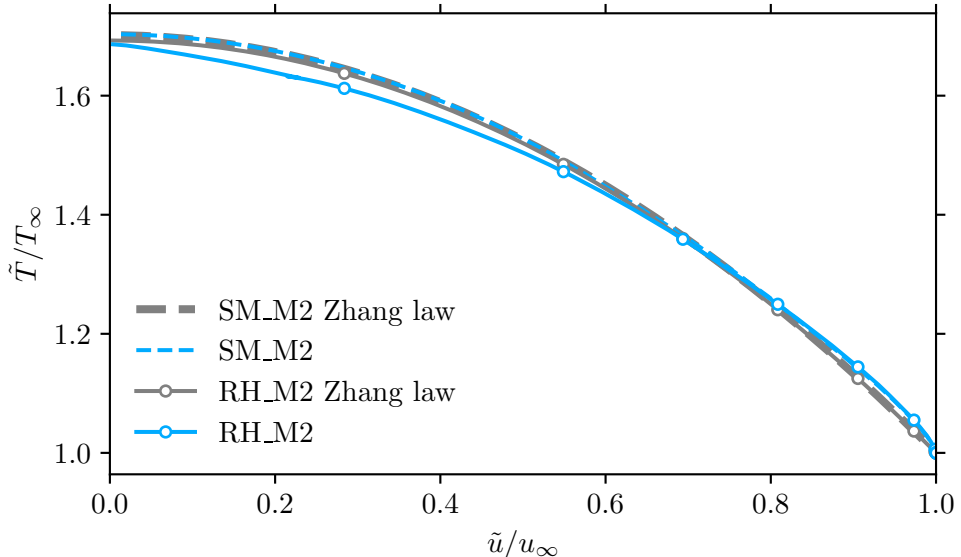


Figure 19: Temperature-velocity relation for cases RH_M2 (solid) and SM_M2 (dashed). DNS data (blue) is compared to equation (9), in grey.

the temperature-velocity relation of Zhang et al. [47] appears to be a robust tool even in rough wall supersonic boundary layers. As pointed out by [30], the fact that a quadratic relation exists between temperature and velocity invalidates the outer layer similarity for the mean temperature by construction.

Conclusions

We have studied compressible turbulent boundary layers over smooth and rough surfaces using DNS. In particular, we compared the flow dynamics of subsonic ($M_\infty=0.3$) and supersonic ($M_\infty=2$) turbulent boundary layers with a smooth-to-rough surface transition, the rough part being composed of 3D cubical elements equally spaced in the streamwise and spanwise directions.

First, we analyzed the instantaneous flow features of each case, noting clear differences in the supersonic case due to compressibility effects. In particular, the supersonic case RH_M2 features an oblique shock wave at the onset of roughness, followed by a pattern of subsequent local waves emanated from each element and extending into the freestream, considerably influencing the acoustic environment outside the boundary layer. This observation is in line with several experimental studies [15, 24, 25], which reported similar patterns as a result of the interaction between roughness and compressibility.

Being able to accurately resolve the boundary layer, we observed that the formation of the initial shock wave is due not only to the multitude of local compression waves generated by the first row of elements, but also to the local adjustment of the boundary layer width, which appears to begin before the actual location of the surface transition. This fact is clearly apparent looking at the streamwise evolution of the boundary layer thickness δ_{99} for supersonic case RH_M2, if compared with the subsonic case RH_M03 exhibiting a sharp local bump after the surface transition, before continuing to grow at a similar rate to what observed in the smooth portion. As a result, the streamwise evolution of the friction Reynolds number Re_τ is highly influenced by the different development of the boundary layer thickness.

The smooth-to-rough transition is then analysed with a detailed study on the formation of the internal boundary layer [36], extended here for the first time to compressible flows. In order to detect its edge δ_I within the external boundary layer width δ_{99} , we first consider the widely adopted method by [17], which reveals a similar growth rate between subsonic, RH_M03, $\delta_I \propto x^{0.62}$ and supersonic case, RH_M2, $\delta_I \propto x^{0.58}$. This finding is supported by the use of a novel definition of the IBL thickness based on the wall-normal Reynolds stress component $\bar{\rho}v''^2$. This appears to be an effective quantity to reduce undesired noise enhanced by compressibility effects, demonstrating to be a good indicator of the IBL in both subsonic and supersonic conditions. Using the proposed method, we find a similar growth rate with respect to the classical definition of [17] and among the two cases, namely $\delta_I \propto x^{0.58}$ for RH_M03 and $\delta_I \propto x^{0.57}$ for RH_M2. Although we conclude that the growth of the IBL appears comparable between subsonic and supersonic cases in our database, we underline that when it is related to their respective external thickness δ_{99} , the case RH_M2 appears farther from equilibrium compared to RH_M03. In this sense, we expect that as compressibility effects grow, the boundary layer will fully adjust in longer streamwise distances to a change in the surface roughness.

The degree of recovery of turbulence and thermal statistics is analysed considering rough wall cases at a streamwise station far from the surface transition, $x/\delta_{in} = 140$. Here, subsonic and supersonic cases exhibit a very similar velocity shift ΔU^+ when compared to their smooth counterpart, which turns out to be almost identical when using the recent compressibility transformation of [22]. By shifting all velocity profiles to an amount corresponding to the virtual origin $d = 0.9k$, [8], we are able to observe that both subsonic and supersonic cases exhibit a nearly constant velocity shift $\Delta U^+ \approx 8$, a sign that the outer layer similarity is present for this quantity. A good degree of similarity is also noted in the profiles of the Reynolds stress in both subsonic, RH_M03, and supersonic, RH_M2, cases, although the latter shows some small deviations from the smooth case for the streamwise component, in agreement with the slower recovery rate suggested by the IBL analysis.

Considering the behaviour of mean and fluctuating temperature, we clearly note that the concept of outer layer similarity cannot be applied, corroborating the idea of [30] that the non-linear temperature-velocity relation prevents a direct application of this theory for thermodynamic quantities. This is even more true when considering that our database is adiabatic, hence the similarity between temperature and velocity should be promoted. In this context, we observe the temperature profile to change from a nearly constant behaviour near the roughness elements to a strong gradient far from the wall in order to match the freestream condition. This effect can be directly related to the promotion of temperature fluctuations in the outer layer by considering the mechanism behind thermal fluctuations production [10].

Future works on this topic are needed to understand the effects of the large number of parameters controlling this flow, such as the Mach number, wall temperature condition and different roughness geometries.

Acknowledgements

We acknowledge that the results reported in this paper have been achieved using the EuroHPC JU Extreme Scale Access Infrastructure resource Leonardo Booster based at CINECA, Casalecchio di

Reno, Italy, under project EUHPC_E02_044. We also acknowledge the CINECA award under the ISCRA initiative, for the availability of high-performance computing resources and support.

Funding

This research received financial support from ICSC – Centro Nazionale di Ricerca in "High Performance Computing, Big Data and Quantum Computing", funded by European Union – NextGenerationEU.

Declaration of interests

The authors report no conflict of interest.

Data availability statement

The data that support the findings of this study are available upon reasonable request.

Bibliography

- [1] M. Bernardini and S. Pirozzoli. Wall pressure fluctuations beneath supersonic turbulent boundary layers. *Phys. Fluids*, 23(8):085102, 2011.
- [2] M. Bernardini, S. Pirozzoli, and F. Grasso. The wall pressure signature of transonic shock/boundary layer interaction. *J. Fluid Mech.*, 671:288–312, 2011.
- [3] M. Bernardini, D. Modesti, F. Salvadore, and S. Pirozzoli. STREAmS: a high-fidelity accelerated solver for direct numerical simulation of compressible turbulent flows. *Comp. Phys. Comm.*, 263:107906, 2021.
- [4] M. Bernardini, D. Modesti, F. Salvadore, S. Sathyaranayana, G. Della Posta, and S. Pirozzoli. Streams-2.0: Supersonic turbulent accelerated navier-stokes solver version 2.0. *Comput. Phys. Commun.*, 285:108644, 2023.
- [5] R. Bowersox. Survey of high-speed rough wall boundary layers: invited presentation. *AIAA Paper*, pages 2007–3998, 2007.
- [6] A. Busemann. *Gasdynamik*. Akademische Verlagsgesellschaft, 1931.
- [7] H. Cheng and I. P. Castro. Near-wall flow development after a step change in surface roughness. *Bound.-Lay. Meteorol.*, 105:411–432, 2002.
- [8] D. Chung, N. Hutchins, M. P. Schultz, and K. A. Flack. Predicting the drag of rough surfaces. *Ann. Rev. Fluid Mech.*, 53:439–471, 2021.
- [9] M. Cogo, F. Salvadore, F. Picano, and M. Bernardini. Direct numerical simulation of supersonic and hypersonic turbulent boundary layers at moderate-high reynolds numbers and isothermal wall condition. *J. Fluid Mech.*, 945:A30, 2022.

- [10] M. Cogo, U. Baù, M. Chinappi, M. Bernardini, and F. Picano. Assessment of heat transfer and mach number effects on high-speed turbulent boundary layers. *J. Fluid Mech.*, 974:A10, 2023.
- [11] L. Crocco. Sulla trasmissione del calore da una lamina piana a un fluido scorrente ad alta velocità. *L'Aerotecnica*, 12:181–197, 1932.
- [12] F. De Vanna, F. Picano, and E. Benini. A sharp-interface immersed boundary method for moving objects in compressible viscous flows. *Computers & Fluids*, 201:104415, 2020.
- [13] F. De Vanna, A. Benato, F. Picano, and E. Benini. High-order conservative formulation of viscous terms for variable viscosity flows. *Acta Mech.*, 232:2115–2133, 2021.
- [14] F. Ducros, V. Ferrand, F. Nicoud, C. Weber, D. Darracq, C. Gachet, and T. Poinsot. Large-eddy simulation of the shock/turbulence interaction. *J. Comput. Phys.*, 152(2):517–549, 1999.
- [15] I. W. Ekoto, R. Bowersox, T. Beutner, and L. Goss. Supersonic boundary layers with periodic surface roughness. *AIAA J.*, 46(2):486–497, 2008.
- [16] I. W. Ekoto, R. Bowersox, T. Beutner, and L. Goss. Response of supersonic turbulent boundary layers to local and global mechanical distortions. *J. Fluid Mech.*, 630:225–265, 2009.
- [17] W. P. Elliott. The growth of the atmospheric internal boundary layer. *Trans. Am. Geophys. Union*, 39(6):1048–1054, 1958.
- [18] K. A. Flack and M. P. Schultz. Roughness effects on wall-bounded turbulent flows. *Phys. Fluids*, 26(10), 2014.
- [19] K. A. Flack and M.P. Schultz. Review of hydraulic roughness scales in the fully rough regime. *J. Fluids Eng.*, 132(4):041203, 2010.
- [20] K. A. Flack, M. P. Schultz, and J. S. Connally. Examination of a critical roughness height for outer layer similarity. *Phys. Fluids*, 19(9), 2007.
- [21] K. P. Griffin, L. Fu, and P. Moin. Velocity transformation for compressible wall-bounded turbulent flows with and without heat transfer. *P. Natl. Acad. Sci USA*, 118(34), 2021.
- [22] A. M. Hasan, J. Larsson, S. Pirozzoli, and R. Pecnik. Incorporating intrinsic compressibility effects in velocity transformations for wall-bounded turbulent flows. *Phys. Rev. Fluids*, 8(11): L112601, 2023.
- [23] J. Jiménez. Turbulent flows over rough walls. *Annu. Rev. Fluid Mech.*, 36:173–196, 2004.
- [24] B. D. Kocher, P. A. Kreth, J. D. Schmisser, E. J. LaLonde, and C. S. Combs. Characterizing streamwise development of surface roughness effects on a supersonic boundary layer. *AIAA J.*, 60(9):5136–5149, 2022.
- [25] R. M. Latin and R. Bowersox. Flow properties of a supersonic turbulent boundary layer with wall roughness. *AIAA J.*, 38(10):1804–1821, 2000.

- [26] M. Li, C. M. De Silva, A. Rouhi, R. Baidya, D. Chung, I. Marusic, and N. Hutchins. Recovery of wall-shear stress to equilibrium flow conditions after a rough-to-smooth step change in turbulent boundary layers. *J. Fluid Mech.*, 872:472–491, 2019.
- [27] R.W. Macdonald, R.F. Griffiths, and D.J. Hall. An improved method for the estimation of surface roughness of obstacle arrays. *Atmos. Environ.*, 32(11):1857–1864, 1998.
- [28] C. Meneveau, N. Hutchins, and D. Chung. The wind-shade roughness model for turbulent wall-bounded flows. *arXiv preprint arXiv:2406.05062*, 2024.
- [29] D. Modesti and S. Pirozzoli. Reynolds and Mach number effects in compressible turbulent channel flow. *Int. J. Heat Fluid Fl.*, 59:33–49, 2016.
- [30] D. Modesti, S. Sathyaranayana, F. Salvadore, and M. Bernardini. Direct numerical simulation of supersonic turbulent flows over rough surfaces. *J. Fluid Mech.*, 942:A44, 2022. doi: 10.1017/jfm.2022.393.
- [31] J. Nikuradse. Strömungsgesetze in rauhen rohren. VDI-Forschungsh. Berline: Ver. Dtsch. Ing., page 363, 1933.
- [32] S.J. Peltier, R.A. Humble, and R. Bowersox. Crosshatch roughness distortions on a hypersonic turbulent boundary layer. *Physics of Fluids*, 28(4), 2016.
- [33] A. Piquet, O. Roussel, and A. Hadjadj. A comparative study of brinkman penalization and direct-forcing immersed boundary methods for compressible viscous flows. *Computers & Fluids*, 136:272–284, 2016.
- [34] S. Pirozzoli and M. Bernardini. Turbulence in supersonic boundary layers at moderate reynolds number. *J. Fluid Mech.*, 688:120–168, 2011.
- [35] S. B. Pope. *Turbulent Flows*. Cambridge University Press, 2000.
- [36] A. Rouhi, D. Chung, and N. Hutchins. Direct numerical simulation of open-channel flow over smooth-to-rough and rough-to-smooth step changes. *J. Fluid Mech.*, 866:450–486, 2019.
- [37] J. A Sillero, J. Jiménez, and Robert D. Moser. One-point statistics for turbulent wall-bounded flows at Reynolds numbers up to $\delta+ \approx 2000$. *Phys. Fluids*, 25(10):105102, 2013.
- [38] A.J. Smits, N. Matheson, and P. N. Joubert. Low-reynolds-number turbulent boundary layers in zero and favorable pressure gradients. *J. Ship Res.*, 27(03):147–157, 1983.
- [39] A. Trettel and J. Larsson. Mean velocity scaling for compressible wall turbulence with heat transfer. *Phys. Fluids*, 28(2):026102, 2016.
- [40] E. R. Van Driest. Turbulent boundary layer in compressible fluids. *J. Aeronaut. Sci.*, 18(3): 145–160, 1951.
- [41] E. R. Van Driest. The problem of aerodynamic heating. *Aeronaut. Engng. Rev.*, 15(10):26–41, 1956.

-
- [42] P. S. Volpiani, P. S. Iyer, S. Pirozzoli, and J. Larsson. Data-driven compressibility transformation for turbulent wall layers. *Phys. Rev. Fluids*, 5(5):052602, 2020.
 - [43] Michael C Wilder and Dinesh K Prabhu. Rough-wall turbulent heat transfer experiments in hypersonic free flight. In *AIAA Aviation 2019 Forum*, page 3009, 2019.
 - [44] O. J. H. Williams, D. Sahoo, M. Papageorge, and A. J. Smits. Effects of roughness on a turbulent boundary layer in hypersonic flow. *Experiments in Fluids*, 62:1–13, 2021.
 - [45] J. Yang, A. Stroh, S. Lee, S. Bagheri, B. Frohnapfel, and P. Forooghi. Prediction of equivalent sand-grain size and identification of drag-relevant scales of roughness—a data-driven approach. *J. Fluid Mech.*, 975:A34, 2023.
 - [46] X.I.A. Yang, J. Sadique, R. Mittal, and C. Meneveau. Exponential roughness layer and analytical model for turbulent boundary layer flow over rectangular-prism roughness elements. *J. Fluid Mech.*, 789:127–165, 2016.
 - [47] Y. S. Zhang, W. T. Bi, F. Hussain, and Z. S. She. A generalized Reynolds analogy for compressible wall-bounded turbulent flows. *J. Fluid Mech.*, 739:392–420, 2014.
 - [48] K. Zhong, N. Hutchins, and D. Chung. Heat-transfer scaling at moderate Prandtl numbers in the fully rough regime. *J. Fluid Mech.*, 959:A8, 2023.

Appendix D

Paper IV

URANOS: a GPU accelerated Navier-Stokes solver for compressible wall-bounded flows

Francesco De Vanna¹, Filippo Avanzi¹, Michele Cogo², Simone Sandrin¹, Matt Bettencourt³, Francesco Picano^{1,2}, Ernesto Benini¹

1. Department of Industrial Engineering, University of Padova, Padova, PD 35131, Italy,

2. Centro di Ateneo di Studi e Attività Spaziali "Giuseppe Colombo" - CISAS,
University of Padova, Padova, PD 35131, Italy,

3. NVIDIA corporation, Via Melchiorre Gioia, 8, Milano 20124, Italy

Computer Physics Communications, 287, 2023, 108717

Abstract: URANOS, a massively parallel GPU-accelerated compressible flow solver for high-fidelity modeling of compressible wall flows, is presented. URANOS is based on modern high-fidelity and high-resolution discretization strategies for time-accurate compressible flow predictions. The solver provides six different convective scheme implementations, a cutting-edge method for viscous terms treatment, and three different frameworks for turbulence modeling (DNS, LES, and innovative WMLES), while utilizing a high-order finite-difference approach, ranging from second to sixth order spatial accuracy. This paper details all of these numerical models and implementation issues. Computationally, URANOS combines multiple three-dimensional MPI parallelization strategies with the open standard, OpenACC, for machine wide, on node, and on GPU parallelism, tailoring the software to match the state-of-the-art HPC computing facilities. Special attention is given to the GPU porting and data management, detailing the solver scaling properties and performance for multi-node/-GPU systems on three distinct architectures. In these experiments the different MPI strategies are compared for both GPU-aware MPI/GPU (Host-based MPI) and results are provided proving, consistently, that the GPU-aware MPI outperforms the GPU (Host-based MPI) approach. Furthermore, the GPU version is compared to the CPU only demonstrating over a three times speed-up for a node-to-node comparison, even at large scales, with an efficiency of about 80% while using 1024 GPUs. Finally, the manuscript presents several validation benchmarks, from simple academic comparisons to turbulent channel and boundary layer configurations. URANOS is compared with the best DNS data available in the literature across various Mach numbers, ranging from almost incompressible conditions to hypersonic regimes, illustrating the solver's capability in treating a wide range of complex wall-flows problems using DNS, wall-resolved, and wall-modeled LES approaches. Thus, using OpenACC as a paradigm, URANOS provides a straightforward and efficient platform that can efficiently exploit the most modern GPU-accelerated computing architectures in a totally open-source and non-vendor-specific way. The solver represents a framework where the CFD community can explore the limits of modeling, test new models/methods all across a broad range of Mach and Reynolds numbers flows. The solver is released under a BSD license.

Program summary

Program title: Unsteady Robust All-around Navier-Stokes Solver (URANOS)

Developer's repository link: https://gitlab.com/fralusa/uranos_gpu

Licensing provisions: BSD License 2.0

Programming language: Fortran 90, OpenACC, MPI

Nature of problem: Solving the compressible Navier-Stokes system of equations in a three-dimensional

Cartesian framework from low to high Mach and Reynolds numbers conditions.

Solution method: Convective terms are treated with several high-order high-resolution shock-capturing schemes (WENO/TENO) in hybrid and non-hybrid versions. The system dynamics is advanced in time with a three-stage, third-order total variation diminishing Runge-Kutta method. Three-dimensional MPI parallelization is implemented in several optimized arrangements and coupling OpenACC directives in a genuinely multi-GPU logic.

Keywords: GPU, OpenACC, Compressible flows, DNS, LES , WMLES , Open-source

Introduction

Computational Fluid Dynamics (CFD) is now widely used in industry and research for problems involving the evolution of fluids. Computational methods for the simulation of wall flows have progressed rapidly over the decades and fundamentally changed the design processes in sectors such as aerospace, energy, and process engineering. CFD has reduced testing requirements, becoming increasingly popular over the years, delivering a superior understanding of critical physical phenomena which can limit components' performance. However, these improvements require a deep knowledge of flow physics and accurate predictive methods are still an active area for research. In contemporary CFD, two strategies can be considered the most trustworthy in studying complex unsteady flows: Direct Numerical Simulations (DNS) and Large-Eddy Simulations (LES). DNS is the most straightforward approach since it discretizes space and time with very dense grids, resolving all the flow features. Because computational costs are directly linked to the grid resolution, DNS are still prohibitively expensive for high-Reynolds flows occurring in industrial applications, and today only academic configurations are affordable. LES, on the other hand, lays on Kolmogorov's theory by modeling the universal smallest turbulent scales, while directly solving the largest ones that are problem-dependent. However, LES approaches in wall flows require direct solutions for the near-wall boundary layer with resolutions comparable to DNS. From investigations of Chapman [6] and Choi and Moin [7], it has been estimated that the number of grid points necessary to resolve the near-wall eddies for DNS and Wall-Resolved LES (WRLES), i.e., a LES strategy where the boundary layer is fully resolved, is about $N_{DNS} \sim Re^{37/14}$ and $N_{WRLES} \sim Re^{13/7}$, respectively, where Re is the Reynolds number based on a characteristic length. Even though WRLES is less expensive than DNS, the roughly quadratic relationship with the Reynolds number is still excessively demanding. This is why Reynolds-Averaged Navier-Stokes (RANS) approaches, which involve modeling the entire turbulent spectrum, are still the most popular approach for many applications. This is true even though turbulence modeling errors directly impact its predictive capability, especially for flows with complex behaviors.

Nevertheless, the need to overcome the RANS limitations is an increasingly pressing aspect of the current modeling landscape. That is why several strategies have appeared in the CFD panorama to reduce the computational cost associated with LES. One of the most promising strategies is the Wall-Modeled LES (WMLES) approach. This method aims at directly solving the isotropic/turbulence-homogenous flow away from the wall as in a classical LES framework, taking all the valuable characteristics of standard LES (i.e., time-dependency of the solution and accurate representation

of complex flow features) while modeling the close-to-wall regions with a greatly simplified method to reduce computational costs compared to a WRLES. Choi and Moin [7] estimate that the number of grid points for a WMLES is approximately a linear function of Re , making this a promising strategy in industrial-based applications. However, any scale-resolved approach is still much more computationally expensive than the RANS methods, requiring simulation of three-dimensional flows in a time-accurate framework.

Fortunately, today the High-Performance Computing (HPC) market is rapidly evolving, and high-fidelity CFD methods, once only theoretical, are becoming tractable thanks to the emergence of modern, accelerator based, computing. General Purpose GPUs (GPGPUs) have increasingly caught on in recent years and today represent the state-of-the-art to increase the execution speed of computational applications. Such architectures, in fact, are orders of magnitude more efficient than standard CPU-only architectures, both at the computational and energy-consumption levels. However, the contemporary CFD community struggles with the development of an accurate and general-purpose solver suitable for wall-flows applications in a wide range of Reynolds and Mach numbers. In particular, most contributions to open-source tools which utilize GPUs are mainly devoted to DNS methods, both for incompressible and compressible flow regimes. None of these are capable of addressing a broad spectrum in terms of flexibility and turbulence modeling. The most popular publicly available GPU-accelerated solutions for incompressible flows are AFiD [69] and CaNS [12], both structured solvers for massively parallel DNS of canonical flows. The compressible community have OpenSBLI [42], a DNS Python framework for the automated derivation of finite differences solvers both for CPUs and GPUs architectures; PyFr [68] and ZEFR [61], with the latter two being general-purpose DNS, unstructured flow solvers with high-order flux reconstruction. More recently, STREAmS [4], a DNS high-order structured finite-difference code has appeared. In addition to the lack of an efficient and accurate CFD solver for simulating flows where turbulence modelling in realistic geometries is required, the available open-source solutions implement vendor-specific GPU programming paradigms, being tuned for NVIDIA, AMD, or Intel clusters, with a marked predominance for CUDA-based solvers. While making these applications efficient when combined with their target architecture, this limits their portability and forces maintainers to continuously follow the HPC market's sudden changes.

The work described below documents the results obtained with the GPU-enabled version of the URANOS solver. URANOS (Unsteady Robust All-around Navier-Stokes Solver) is a fully compressible CFD solver specifically developed for simulations of wall-bounded flow configurations. The solver was developed exclusively at the Industrial Engineering Department of the University of Padova, Italy, and exploits the OpenACC paradigm to deal with GPU acceleration in an abstract fashion. URANOS offers considerable advantages over other general-purpose solvers. In particular, dealing with OpenACC makes URANOS a truly non-vendor-specific and open-source platform since OpenACC is configured as a standard GPU-enabling framework fully independent of the computing architecture. This allows for high flexibility and portability in a constantly evolving HPC market. Furthermore, OpenACC, being less invasive than other GPU-enabling approaches (e.g., CUDA), is decidedly easily manageable for less experienced users who want to include novel features to the present open-source solver. Finally, unlike other GPU-executable open-source platforms, URANOS already implements several state-of-the-art DNS/WRLES/WMLES algorithms combined with advanced numerical methods for convective and viscous terms discretization. Here we present code

performance in terms of accuracy and computational efficiency, providing insights regarding GPU porting and code profiling. Several benchmarks are documented, showing solver validation for a wide range of Reynolds and Mach numbers, ranging from simple numerical tests to DNS, WRLES and WMLES of wall-flows in canonical configurations. URANOS represents a clear and straightforward development platform in which one can address a broad spectrum of applications efficiently and genuinely.

The paper is organized as follows: Section §Solver structure presents the URANOS structure in terms of governing equations and turbulence modeling. Section §Numerical methods describes in detail the numerical methods and the discretization process concerning the spatial and the temporal contributions of the Navier-Stokes equations. Section §GPU porting presents the porting strategy and the GPU-acceleration performance in a fully multi-GPU framework. Section §Solver validation and results discussion provides both CPU/GPU validation listing several increasingly complex benchmarks. Finally, Section §Conclusions draws the conclusions.

Solver structure

Governing equations

URANOS represents a well-established CFD solver entirely developed at the Industrial Engineering Department of the University of Padova [13, 17, 18]. The solver deals with the filtered compressible Navier-Stokes system of equations in a conservative formulation. In particular, using the Reynolds ($\phi = \bar{\phi} + \phi'$) and the Favre ($\phi = \tilde{\phi} + \phi''$, $\tilde{\phi} = \bar{\rho\phi}/\bar{\rho}$) decompositions, the model reads as following:

$$\frac{\partial \bar{\rho}}{\partial t} + \frac{\partial \bar{\rho}\tilde{u}_j}{\partial x_j} = 0 \quad (1a)$$

$$\frac{\partial \bar{\rho}\tilde{u}_i}{\partial t} + \frac{\partial \bar{\rho}\tilde{u}_i\tilde{u}_j}{\partial x_j} = -\frac{\partial \bar{\rho}\delta_{ij}}{\partial x_j} + \frac{\partial \bar{\tau}_{ij}}{\partial x_j} - \frac{\partial T_{ij}^{SGS}}{\partial x_j} + f_i \quad (1b)$$

$$\frac{\partial \bar{\rho}\tilde{E}}{\partial t} + \frac{\partial \bar{\rho}\tilde{u}_j\tilde{E}}{\partial x_j} = -\frac{\partial \bar{\rho}\tilde{u}_j}{\partial x_j} + \frac{\tilde{u}_j\bar{\tau}_{ij}}{\partial x_j} - \frac{\partial \bar{\mathcal{J}}_j}{\partial x_j} - \frac{\partial E_j^{SGS}}{\partial x_j} + f_i\tilde{u}_i \quad (1c)$$

Here $\bar{\rho}$ is the filtered density, \tilde{u}_i is the filtered velocity component along with the i -th direction, \bar{p} is the filtered thermodynamic pressure, $\tilde{E} = \tilde{e} + \tilde{u}_i\tilde{u}_i/2$ is the filtered total energy per unit mass, \tilde{e} is the filtered internal energy per unit mass and $\bar{\mathcal{J}}_j$ is the j -th component of the filtered molecular heat flux. The above system of conservation equation is completed by the ideal gas equation of state, $\bar{p} = \bar{\rho}R\tilde{T}$, and a constitutive expression for the internal energy, $\tilde{e} = c_p\tilde{T}$. Here \tilde{T} denotes the filtered temperature, R is the specific gas constant, $c_v = R/(\gamma - 1)$ and $c_p = \gamma R/(\gamma - 1)$ are the specific heat at constant volume and pressure, respectively, while $\gamma = c_p/c_v$ is specific heat ratio. The viscous stress tensor, $\bar{\tau}_{ij}$, and heat flux components, $\bar{\mathcal{J}}_j$, are expressed as:

$$\bar{\tau}_{ij} = \mu(\tilde{T}) \left(\frac{\partial \tilde{u}_i}{\partial x_j} + \frac{\partial \tilde{u}_j}{\partial x_i} - \frac{2}{3} \frac{\partial \tilde{u}_k}{\partial x_k} \delta_{ij} \right) \quad (2)$$

$$\bar{\mathcal{J}}_j = -\lambda(\tilde{T}) \frac{\partial \tilde{T}}{\partial x_j} \quad (3)$$

where $\mu(\tilde{T})$ and $\lambda(\tilde{T}) = c_p \mu(\tilde{T}) / Pr$ denote the molecular viscosity and thermal diffusivity, respectively. Viscosity is assumed obeying to the Sutherland's two coefficient law

$$\bar{\mu}(\tilde{T}) = \tilde{T}^{3/2} \left(\frac{T_0 + S}{\tilde{T} + S} \right) \quad (4)$$

where T_0 is the flow reference temperature and $S = 110.4$ K is an empirical fitting parameter [64]. Equation (4) is one of the top-rated choices for laminar viscosity description in compressible flows. Other formulations, definitively less adopted, are reported by Keyes [37]. The model is made non-dimensional so that by setting γ , Re , Ma and Pr , the system conditions are univocally determined. These parameters can be set in the pre-processing phase according to the user's needs. Apart where different stated $\gamma = 1.4$ and $Pr = 0.71$. Finally, the forcing term, f_i , in Eq. (1b) is added in order to discretely enforce constant mass-flow-rate in time to deal with channel flow simulations. The corresponding power, $f_j \tilde{u}_j$, is also added to the right-hand-side of the total energy equation.

Subgrid scale modelling

Concerning the SubGrid Scale (SGS) contribution, $T_{ij}^{SGS} = \overline{\rho u_i u_j} - \bar{\rho} \tilde{u}_i \tilde{u}_j$, is accounted via a canonical Boussinesq's hypothesis

$$T_{ij}^{SGS} - \frac{1}{3} T_{kk}^{SGS} \delta_{ij} = -2\mu_{SGS} \left(\tilde{S}_{ij} - \frac{1}{3} \tilde{S}_{kk} \delta_{ij} \right) \quad (5)$$

where μ_{SGS} denotes the SGS viscosity and T_{kk}^{SGS} is the isotropic contribution that is neglected according to Garnier et al. [29]. μ_{SGS} is variously modelled using in particular the classical Smagorinsky model, the Wall-Adaptive Large-Eddy (WALE) model by Nicoud and Ducros [47], the Sigma model by Toda et al. [65], and the MiXed Time Scale (MXTS) model by Inagaki et al. [34]. The reader is addressed to the specific literature for a complete discussion of these models. Finally, SGS terms in the energy equation are given by

$$E_j^{SGS} = \overline{(\rho E + p) u_j} - (\bar{\rho} \tilde{E} + \bar{p}) \tilde{u}_j = \quad (6a)$$

$$= \underbrace{\left[\overline{\rho c_p T u_j} - \bar{\rho} c_p \tilde{T} \tilde{u}_j \right]}_{\mathcal{Q}_j} + \underbrace{\left[\frac{1}{2} (\overline{\rho u_i u_i u_j} - \bar{\rho} \tilde{u}_i \tilde{u}_i \tilde{u}_j) \right]}_{\psi_{iij}} - \frac{1}{2} T_{ii}^{SGS} \tilde{u}_j \quad (6b)$$

where $\mathcal{Q}_j = -\lambda_{SGS} \partial \tilde{T} / \partial x_j$ denotes the SGS heat flux, with $\lambda_{SGS} = \frac{\gamma R}{(\gamma-1)} \mu_{SGS} / Pr_{SGS}$, and ψ_{iij} is the velocity triple correlation tensor whose contribution is neglected. Pr_{SGS} , the SGS Prandtl number, is assumed equal to 0.9.

Equilibrium wall-stress model

To deal with the near-wall treatment in case of insufficient resolution, URANOS implements a wall-modelled LES framework. In particular, the present code version accounts for an equilibrium-based model that assumes the instantaneous balancing between convection terms and the pressure gradi-

ent. Thus, two unknowns arise, U_{wm} and T_{wm} , representing the mean wall parallel speed and mean wall temperature distribution, respectively. The subscript wm emphasizes that these quantities are obtained using the wall model rather than the LES solver. According to such hypotheses, the near-wall Navier-Stokes system of equations reduces to:

$$\frac{d}{dy} \left[(\mu_{wm} + \mu_{t,wm}) \frac{dU_{wm}}{dy} \right] = 0 \quad (7a)$$

$$\begin{aligned} \frac{d}{dy} \left[c_p \left(\frac{\mu_{wm}}{Pr} + \frac{\mu_{t,wm}}{Pr_{t,wm}} \right) \frac{dT_{wm}}{dy} \right] &= \\ -\frac{d}{dy} \left[(\mu_{wm} + \mu_{t,wm}) U_{wm} \frac{dU_{wm}}{dy} \right] \end{aligned} \quad (7b)$$

Here, c_p still represents the specific heat at constant pressure, $Pr_{t,wm} = 0.9$ is the turbulent Prandtl number, $\mu_{wm} = \mu_{wm}(T_{wm})$ represents the laminar viscosity, still assumed satisfying Sutherland's law, and $\mu_{t,wm} = \kappa \rho_{wm} u_\tau y D$ is the wall model eddy viscosity. Here $\kappa = 0.41$ is the von Kármán constant, $\rho_{wm} = p_{LES}/(RT_{wm})$ is the wall model density distribution, p_{LES} is the external LES pressure and $D = [1 - \exp(-y^*/A^+)]^2$ is the Van Driest dumping function with $A^+ = 17$ and $y^* = y\sqrt{\rho_{wm}\tau_{w,wm}}/\mu_{wm}$ the model parameter and the wall-normal distance in semi-local scaling, respectively. Such a system of Ordinary Differential Equations (ODEs) is solved on an independent grid embedded in the LES main mesh. The grid for the wall model begins at $y = 0$ wall location, where speed and temperature/temperature-gradient are enforced as boundary conditions, to an exchange site, $y = h_{wall}$, where the model meets the outer flow conditions, $U_{wm} = u_{/\!/LES}$, $T_{wm} = T_{LES}$ and $P_{wm} = p_{LES}$. Here $u_{/\!/LES}$, T_{LES} and p_{LES} are the wall-parallel velocity, the static temperature and static pressure obtained with the outer LES solution. Once Eqs. 7 are solved, the U_{wm} and T_{wm} distributions are used to gather the wall shear stress and the heat flux. The information is then fed to the outer LES solver as a boundary condition. The technicalities of how the process works are thoroughly described in [15, 16, 19, 20, 22, 23].

Numerical methods

URANOS uses a High-Order Finite Difference (HOFD) approach to discretize the Navier-Stokes system of equations and allows for both uniform and non-uniform structured Cartesian meshes.

Convective fluxes discretization

The user can select among six different convective schemes. In particular, URANOS implements a central, nominally zero-dissipative, 6th order fully-split convective Energy-Preserving (EP) method [58] to deal primarily with shock-free or smooth flows; three increasingly high-order Weighted Essentially Non-Oscillatory (WENO) methods [35] and two low-dissipative Targeted Essentially Non-Oscillatory (TENO) approaches [26–28].

The EP method is intended to provide semi-discrete preservation of total kinetic energy within the limit of incompressible, inviscid flows. The property works on both uniform and non-uniform Cartesian meshes [57], guaranteeing a robust treatment of convective terms without adding numerical viscosity. An extensive description of the method is reported by Pirozzoli [56] and Coppola

et al. [11]. The method is found to be robust and accurate in a wide range of applications ranging in very different purposes [11, 43, 44, 57, 62].

The EP approach, although being substantially more resilient than a normal central-FD discretization, cannot stably develop shocks/shocklets. As a consequence, to evolve the Navier-Stokes system stably under shocked flows or hypersonic conditions, the WENO/TENO strategies are used. In particular, URANOS adopts the WENO-Z strategy according to Castro et al. [5], which enhances the spectral features of the numerical discretization over the original WENO-JS method by Jiang and Shu [35]. The third, fifth, and seventh order variants are implemented. To limit dissipation, the ε parameter, which is utilized to prevent division by zero while building polynomial smoothness indicators, is adjusted to 10^{-12} . More advanced TENO approaches are also at the user's disposal. The approaches use a discrete cut-off function to exclude non-smooth upwind-biased candidate stencils from the flux reconstruction so that smooth stencils are used in the flux reconstruction to decrease numerical dissipation when compared to the WENO methods. In addition, a shock sensor is introduced to the TENO-A scheme to modify the threshold of the C_T parameter in different regions of the domain and recover more stencils from the reconstruction in smooth regions [32, 55]. The parameters used in URANOS are those provided by Fu et al. [27] for TENO 5 and Fu et al. [28] for TENO-A 5. In particular, in the TENO approach, a fixed threshold $C_T = 10^{-7}$ is defined, but in the adaptive version, it varies between 10^{-7} and 10^{-10} given $\alpha_1 = 10.5$, $\alpha_2 = 3.5$, $C_r = 0.25$, and $\xi = 10^{-3}$.

Shock detection

To limit the numerical viscosity injection and reduce the non-linear operations per time step, we restrict the shock-capturing reconstruction just around the shocks/shocklets locations, letting the EP method deal with smooth flow regions. Thus, we detect a priori the regions where the shocks are located by selectively employing the shock-capturing reconstruction in these flow portions. URANOS carries out such a task with three different implementations, the selection of which is demanded by the user.

The first approach consists of a density-gradient-based detector that reads as:

$$\theta_{i+1/2} = \max_{j=1}^3 \left| \frac{\rho_{j+1} - \rho_j}{x_{j+1} - x_j} \right| \quad (8)$$

The second approach is the density-jump formulation

$$\theta_{i+1/2} = \max_{j=1}^3 |\rho_{j+1} - \rho_j| \quad (9)$$

that generally reduces the WENO/TENO intervention compared to the density gradient. Finally, especially for wall-flows applications, the improved Ducros sensor [24]

$$\theta_{i+1/2} = \max \left(-\frac{\text{div}(\mathbf{u})}{\sqrt{\text{div}^2(\mathbf{u}) + \text{rot}^2(\mathbf{u}) + \varepsilon}}, 0 \right) \quad (10)$$

is recommended. Here $\text{div}(\mathbf{u})$ and $\text{rot}(\mathbf{u})$ are the velocity divergence and vorticity, respectively,

while $\varepsilon = (u_\infty/L)^2$ is a reference velocity gradient. Additionally, the user must specify a threshold, $\bar{\theta}$, to distinguish between shocked and smooth regions of the flow. Thus, if $\theta_{i+1/2} > \bar{\theta}$ the flow is considered shocked. The thickness related to the activated cells depends on the WENO/TENO order of accuracy. In particular, all the two, three, or four cells in the immediate circumstance of one cell detected as shocked are flagged as shocked too as the WENO/TENO order of accuracy varies from 3 to 7. The EP scheme is employed in the rest of the flow. This method, although particularly successful in dealing with shocked turbulent flows, causes the hybrid scheme to lose the reference for numerical error scaling. In reality, hybrid methods are distinguished by discontinuous error scaling due to the inherent character of the shock-detection process. This feature is determined by the grid level below which a discontinuity is perceived as a shock or an intense gradient. This is why the error scaling will be reported for schemes in pure state only. Finally, it is not worthless to be mentioned that the $\bar{\theta}$ value is strongly dependent on the flow in itself and some preliminary settings are always needed.

Viscous fluxes discretization

URANOS has a peculiar feature of managing viscous fluxes. In particular, the latter are expanded so that the incompressible and the compressible contributions are highlighted. The strategy allows treating the incompressible terms with a fully-conservative approximation using a HOFD approach according to De Vanna et al. [14], enhancing the solver stability compared to standard colocated finite-difference approaches and reducing spurious oscillation, especially in case of intense viscosity gradients or under-resolved flow portions. Thus, the following expression holds:

$$\frac{\partial}{\partial x} \left(\bar{\mu}_{tot} \frac{\partial \tilde{u}}{\partial x} \right) \simeq \frac{1}{\Delta x_i} (\hat{\tau}_{i+1/2} - \hat{\tau}_{i-1/2}) \quad (11)$$

Here $\hat{\tau}_{i+1/2}$ is a high-order numerical description of the viscous stresses at cell board

$$\hat{\tau}_{i+1/2} = \frac{1}{\Delta x_{i+1/2}} \sum_{l=m}^n \beta_l \bar{\mu}_{i+l} \cdot \gamma_l \tilde{u}_{i+l} \quad (12)$$

$\{\beta_l, \gamma_l\}_{l=m}^n$ denote the interpolation coefficients as reported by De Vanna et al. [14], while $\bar{\mu}_{tot} = \bar{\mu} + \mu_{SGS}$ is the overall viscosity. When the overall viscosity is smooth, the method reverts to standard colocated finite-difference formulations with the corresponding accuracy. Conversely, in the case of incompressible or slightly compressible flows, the present formulation conserves viscous fluxes independently of grid stretching/resolution or viscosity variations. Because of the mathematical equivalence to Equation (11), the numerical representation of the heat flux components

$$\frac{\partial}{\partial x} \left(\bar{\lambda}_{tot} \frac{\partial \tilde{T}}{\partial x} \right) = \frac{1}{\Delta x_i} (\mathcal{J}_{i+1/2} - \mathcal{J}_{i-1/2}) \quad (13)$$

is treated in the same manner, being $\bar{\lambda}_{tot} = \bar{\lambda} + \bar{\lambda}_{SGS}$ the overall diffusivity.

Numerical treatment of temporal components

Temporal integration takes advantage of a third-order Total-Variation-Diminishing (TVD) low-storage Runge-Kutta method as prescribed by Gottlieb and Shu [30], the algorithm being one of the top-rated choices for compressible flows simulations. Thus, being $\mathcal{N}(\mathbf{U})$ a numerical representation of the non-linear spatial differential operators applied to the conserved variables $\mathbf{U} = \{\bar{\rho}, \bar{\rho}\tilde{u}_i, \bar{\rho}\tilde{E}_{tot}\}^T$, the method reads as:

$$\mathbf{U}^{(1)} = \mathbf{U}^n + \Delta t \mathcal{N}(\mathbf{U}^n) \quad (14a)$$

$$\mathbf{U}^{(2)} = \frac{3}{4} \mathbf{U}^n + \frac{1}{4} \mathbf{U}^{(1)} + \frac{1}{4} \Delta t \mathcal{N}(\mathbf{U}^{(1)}) \quad (14b)$$

$$\mathbf{U}^{(n+1)} = \frac{1}{3} \mathbf{U}^n + \frac{2}{3} \mathbf{U}^{(2)} + \frac{2}{3} \Delta t \mathcal{N}(\mathbf{U}^{(2)}) \quad (14c)$$

Temporal stability is recovered by dynamically computing the time step according to the Courant-Friedrichs-Lowy and the Fourier criteria. In particular, the following expressions hold:

$$\Delta t_{CFL} = CFL \min_{i=1}^3 \left(\frac{\min(\Delta x_i)}{\max(|\tilde{u}_i| + \tilde{c})} \right) \quad (15a)$$

$$\Delta t_{Fo1} = FO \frac{\min^2(\Delta x, \Delta y, \Delta z)}{\max(\bar{\mu}_{tot})} \quad (15b)$$

$$\Delta t_{Fo2} = FO \frac{\min^2(\Delta x, \Delta y, \Delta z)}{\max(\bar{\lambda}_{tot})} \quad (15c)$$

Here $\Delta x, \Delta y$ and Δz are the grid step along the x , the y and the z coordinate, respectively, while \tilde{c} is the filtered speed of sound. CFL and FO denotes the Courant-Friedrichs-Lowy and the Fourier numbers that can be set by URANOS' user. The linear analysis applied to the method of Gottlieb and Shu [30] proved that the stability is recovered up to $CFL = 1$. Thus, a proper choice for practical applications consists in setting the $CFL = 0.5 \div 0.8$ and $FO = 0.1 \div 0.3$. During a simulation, the minimum time step according to Eqs. (15) is selected as the one to advance the solution, so that

$$\Delta t = \min(\Delta t_{CFL}, \Delta t_{Fo1}, \Delta t_{Fo2}) \quad (16)$$

GPU porting

The present section explains the details of the GPU implementation of URANOS. Different approaches exist for accelerator based computing and vary in terms of their degrees of portability, adaptability and computational performance. When migrating an existing code to a GPU based architecture one must consider, not only the initial cost of code development, but also, the long term maintenance costs in a rapidly changing landscape of accelerator based computing. For this reason, it is handy to have a single code base which targets different architectures. For this reason, the directive-based OpenACC paradigm was chosen in the present work.

OpenACC [53] is an open standard, thread parallel programming model for directive-based accelerator programming with applicability to GPUs. As a joint standardization between CAPS, Cray, PGI, and NVIDIA, OpenACC was announced at the ACM/IEEE Supercomputing Conference in 2011 as a new paradigm for parallel programming targeting hardware accelerators. Rather than

programming with vendor-specific languages, the programmer can focus on exposing available parallelism in his source code using pragmas, or directives, that can be used in conjunction with C/C++ and FORTRAN codes for acceleration in a vendor-neutral manner. A compiler transforms these directives automatically into device-specific application code [54]. In addition to parallel directives, various clauses and intrinsic functions are provided for enabling conditional execution, controlling launch parameters, specifying data scope for host and accelerator memory, and determining task asynchrony. Directives are ignored by non-OpenACC compilers, while being activated by adding the `-acc` and the `-ta=[target]` flags to the NVIDIA HPC-SDK compiler command line (formerly PGI) [49]. In such a way, the compiler recognizes the OpenACC directives and will generate code for the accelerator. The OpenACC paradigm, therefore, allows the user to maintain a single code base, compatible with various compilers which is portable across different platforms. The following section details how the OpenACC directives are utilized for the URANOS solver.

OpenACC and MPI implementations

Directives implementation strategy

The main idea of GPU acceleration using OpenACC is to take advantage of the high concurrency of the GPU by offloading the calculation process from the CPU to the GPU. The first step is to identify the most computationally demanding section of the code to accelerate. This section must be computationally intensive enough to amortize the expense of the data transfer to the GPU. In URANOS this is represented by the time loop. This portion of the code computes the Navier-Stokes solution over the whole computational grid at each time step. After problem initialization, solver data must be migrated to the device. One utilizes *data regions*, specifically the `!$acc data copy(list)` directive to achieve the data movement. The `data` directive allows for managing Host-to-Device (H2D) and Device-to-Host (D2H) data transfers: a process which can represent a significant cost. To achieve good performance, H2D/D2H data movements must be avoided as much as possible since memory copy operations can often be orders of magnitude more expensive than computing kernels. Data transfers are minimized by having a single data region outside the main time loop that manages all the H2D and D2H operations. The code structure is reported in Algorithm 1. Such an implementation produces a time-consuming data transfer at the beginning and end of the time loop, but never as much as the sum of the smaller data movements inside the iterations.

Listing 1: Sequence of operations from the *main* module of URANOS

```
program uranos
...
!$acc data copy (variables list)
!---- Time loop begins ----!
do while ( time .le. tmax .and. it < itmax )
...
!---- Runge - Kutta substeps ----!
do ik = 1, n_step
    call rhs_navier_stokes
    call runge_kutta
    call mpi_bc_communications
```

```

    call set_bc_conditions
    call update_all
enddo
it = it + 1
enddo
...
 !$acc end data
...
end program uranos

```

After moving data from the host to the device, it is necessary to accelerate all the routines inside the Runge-Kutta substeps regardless of their computational cost. For this purpose, the `parallel` and the `kernels` constructs can be used. In particular, a region enclosed by the `kernels` construct treats each of the subsequent loops as accelerator kernels automatically. Nevertheless, such a strategy is not used in URANOS as it leaves all the parallelization management to the compiler. Conversely, the `parallel` construct is adopted. Such an approach enables controlling the loop granularity within the parallel region through its `loop` clause, the latter allowing various controls of computation, including coarse-grained parallelism (i.e., *gang*), fine-grained parallelism (called *worker*), and Single Instruction Multiple Data (SIMD) level parallelism (addressed as *vector*). These multi-level parallelization approaches represent the natural forms of parallelism found in modern GPU architectures. Furthermore, the `collapse` clause allows unifying all the iterations of nested loops in a single iteration space to increase the parallelization speedup. In conclusion, the difference between the `kernels` and the `parallel` constructs is that the former gives the compiler more freedom to find and map parallelism according to the requirements of the target accelerator, while the latter is fully explicit but requires more-in-depth knowledge of the kernel operations by the programmer. Here an example of how a parallel construct appears in URANOS is presented.

Listing 2: Example of accelerated kernel computation, depicting the enforcing of RHS term.

```

subroutine forcing_terms
...
!---- Definition of forcing term ----!
f = 2._rp*mu_inf*Mach*sqrt(gamma0)

!---- Updating RHS with forcing term ----!
 !$acc parallel default(present)
 !$acc loop gang, vector collapse(3)
do      k = sz,ez
    do      j = sy,ey
        do i = sx,ex
            RHS(i,j,k,2) = RHS(i,j,k,2) + f
        enddo
    enddo
enddo
 !$acc end parallel loop

```

```
...
end subroutine forcing_terms
```

OpenACC and MPI for multiple GPUs

Efficiently exploiting the distributed-memory environment of HPC infrastructures has been indispensable over the last few decades to let the computational research community access the solution to more complex and larger-size problems. In this regard, Message Passing Interface (MPI) has become the standard for inter-node data transfers, with high-fidelity and validated implementations available for the majority of the programming languages. Many previous studies already gave proof of the remarkable parallel efficiency of URANOS in scaling massive computations [14, 15, 19, 66].

Anyhow, the transition to a multi-GPU logic is by no means straightforward and hardware-unrelated. In fact, depending on the available machine, the architecture may provide several ways of a direct connection between GPU cards. Traditional MPI communications take advantage of InfiniBand (IB) networks, linking nodes' system memories, often utilizing Peripheral Component Interconnect Express (PCI-e) standard. As aforementioned, graphical devices are provided with their own memory, where data must be present in order for the calculation to be performed by the accelerator. Such a scenario would require an uninterrupted sequence of D2H and H2D copies of the data pointers to allow communications through the RAM-based MPI. Conversely, GPU-aware MPI interfaces avoid the need to rely on the host memory, thus providing faster transfers through a straight linking between devices' memories. In this respect, GPU-aware MPI handles different technologies made available by the Unified Virtual Addressing (UVA), which combines into a single virtual space the memories of the system and of all its GPUs. Thus, direct connection may occur as either intra-node, the so-called Peer-to-Peer (P2P), or inter-node architecture, the latter even supporting the lately introduced Remote Direct Memory Access (RDMA) [39]. With versatility being a fundamental requirement for URANOS, the MPI module is implemented in such a way that any machine-specific multi-GPU configuration could be exploited.

Through initialization of the MPI environment, ranks are allocated to GPUs in the same fashion as they are assigned to processors in non-accelerated applications. A common practice for improving timing performance is to force the process instead of letting the device be initialized by default on the first call. This task is accessed thanks to the dedicated function (`acc_init`) available from the OpenACC runtime library, which performs the association of each MPI rank (`rank`) with a device identification number (`dev_id`). A portion of the MPI initialization module of the code is reported in Algorithm 3.

Listing 3: Fragment of code from the MPI initialization module.

```
...
call MPI_Init( mpi_err )
call MPI_Comm_rank(MPI_COMM_WORLD, rank , mpi_err )
call MPI_Comm_size(MPI_COMM_WORLD, nprocs , mpi_err )

#ifndef _OPENACC
call MPI_Comm_split_type(MPI_COMM_WORLD, MPI_COMM_TYPE_SHARED, 0, MPI_INFO_NULL,
call MPI_Comm_rank(local_comm , local_rank , mpi_err )
```

```

call acc_init(acc_device_nvidia)
num_dev = acc_get_num_devices(acc_device_nvidia)
dev_id = mod(local_rank, num_dev)
call acc_set_device_num(dev_id, acc_device_nvidia)

print *, 'Rank ', local_rank, 'is associated to GPU', dev_id

#endif
...

```

The original CPU-based version of the code exploited three different MPI implementations, which were selected with the input parameter `mpi_opt_level` ranging from 1 to 3. Values respectively related to:

- 1 A blocking operation via `MPI_SENDRECV`;
- 2 A combination of nonblocking `MPI_ISEND/MPI_IRecv` and `MPI_WAITALL`;
- 3 A combination of nonblocking `MPI_ISEND/MPI_IRecv` and `MPI_WAITALL` taking advantage of MPI Derived Data Types (DDT).

At this stage, it is worth clarifying that cases 1 and 2 performed almost equally. However, it is possible to differentiate the two options through GPU porting, as will be explained. As regards the third approach, the related communications in the non-accelerated execution considerably outperformed the other two implementations. In fact, DDT benefits from the ability to automatically detect and move data exclusively associated with Ghost Nodes (GN), thus overcoming the need to script time-demanding loops for the selection of the buffers to be transferred. Nevertheless, the current version of the OpenACC Application Programming Interface (API) is not optimised for dealing with MPI DDT, so neither results nor further discussion will be reported in the present work. Anyhow, to the authors' knowledge, the OpenACC Organisation is going through a solution to update the standard to cope with this issue. Therefore, the data movement through MPI DDT is accelerated as well, following the GPU-porting spirit adopted for the second approach.

As aforementioned, in regular communications, MPI requires the host staging of the data pointers before transfer. The OpenACC directive to perform this task is `!$acc update`, followed by the clause `host(variables list)` or `device(variables list)` depending on the direction of the staging. The variables are updated on the host memory before send occurs and are again made available on the device after receive operation is completed. Thus, the two clauses perform a D2H transfer on the sender side and an H2D movement on the receiver side. These two steps are an evident source of efficiency loss. However, they are required when one needs to work on a GPU-equipped machine that is not set for RDMA. To smooth hardware limits, some effort was spent to hide update processes. In particular, the `async(n)` clause lets an accelerated task execute asynchronously with other local operations until a `wait(n)` clause is met, which, in fact, freezes the remainder of the code if the process is not concluded. Here, the parameter `n` allows for the definition of multiple corresponding asynchronous queues with related independent processes.

Algorithm 4 reports a portion of code from the MPI module, which implements the blocking communication approach within a GPU (Host-based MPI) environment. Here, data are shared between GN sides East and West of the contiguous ranks. Desynchronisation is adopted to hide the host update task: in this way, queue 4 starts the host staging of the eastern side without preventing the execution of queue 5, which has an analogous effect on the western side instead. Thus, the former is concluded before sending the buffer, while the latter can proceed in parallel until the corresponding buffer is to be sent. This logic allows all East-to-West communications to be performed without waiting for the West buffer's host staging, which is a requirement only for West-to-East sharing and can be completed simultaneously with the first MPI_SENDRECV, hence hiding the related update time. Then, GPU communication is completed once the received pointer data are overwritten on the device. The same pattern is adopted for the other directions in the complete subroutine, and all the host staging processes are queued with dedicated threads before the first MPI call.

Listing 4: Fragment of code from the MPI communication module. The selection depicts the data movement of East-West Ghost Nodes, with the blocking implementation and host staging OpenACC directives (for non RDMA-enabled systems).

```
...
!$acc update host(bfr_s_E) async(4)
!$acc update host(bfr_s_W) async(5)
!$acc wait(4)
call MPI_SENDRECV(bfr_s_E, bfr_size_x, dtype, neigh(E), tag+1, &
                  bfr_r_W, bfr_size_x, dtype, neigh(W), tag+1, &
                  comm, status, err)
!$acc update device(bfr_r_W)
!$acc wait(5)
call MPI_SENDRECV(bfr_s_W, bfr_size_x, dtype, neigh(W), tag+2, &
                  bfr_r_E, bfr_size_x, dtype, neigh(E), tag+2, &
                  comm, status, err)
!$acc update device(bfr_r_E)
...
```

Similar considerations hold for the GPU-ported implementation of the nonblocking MPI approach (Algorithm 5). Again, desynchronisation is exploited to hide update host time within send operations. However, in this case, immediate receive calls are independent of the presence of buffers on the system's memory, therefore they can live inside the host staging queues. Conversely, these latter need to be completed before the immediate send task. With this approach, a two-sided communication is accomplished upon a MPI_WAITALL call. This block guarantees that data sharing is successful on both the contiguous ranks before letting the code proceed. For this reason, the device memory update with the received pointers data must follow this operation.

Listing 5: Fragment of code from the MPI communication module. The selection depicts the data movement of East-West Ghost Nodes, with the nonblocking implementation and host staging OpenACC directives (for non RDMA-enabled systems).

```

...
 !$acc update host(bfr_s_E) async(4)
 !$acc update host(bfr_s_W) async(5)
 call MPI_IRecv(bfr_r_W, bfr_size_x, dtype, neigh(W), tag+1, comm, req_xx(2), err)
 call MPI_IRecv(bfr_r_E, bfr_size_x, dtype, neigh(E), tag+2, comm, req_xx(4), err)
 !$acc wait(4)
 call MPI_Isend(bfr_s_E, bfr_size_x, dtype, neigh(E), tag+1, comm, req_xx(1), err)
 !$acc wait(5)
 call MPI_Isend(bfr_s_W, bfr_size_x, dtype, neigh(W), tag+2, comm, req_xx(3), err)
 call MPI_Waitall(size(req_xx), req_xx, MPI_STATUSES_IGNORE, err)
 !$acc update device(bfr_r_W, bfr_r_E)
 ...

```

Due to the direct linking among GPUs' memories on different nodes, the implementation of GPU-aware MPI communications is much more straightforward and prone to higher computational efficiency. URANOS enables this feature by setting the parameter `cuda_aware = .true.` inside the case file. GPU-aware MPI connection within RDMA environment makes it possible to avoid the time spent in staging through the host memory. Consequently, the effort spent on the desynchronization of the update tasks is no longer necessary with this approach. However, for the communication to occur, the code needs to be instructed on the pointers addresses of the data shared through several MPI calls. This is done by enclosing all the MPI instances inside a `!$acc host_data` construct. Thus, pointers to be shared among ranks need to be listed inside the `use_device(variables list)` clause.

It is worth noting that the first two MPI implementations (i.e., `mpi_opt_level` equal to 1 or 2) require the definition of buffers containing the only boundary values of the rank-specific portion of the computational grid. In fact, this condition makes it necessary to define additional loops before and after communications. These have the task of extracting the shared values from the complete nodal list of the computational frame, which the rank will send. Then, the received buffers need to be re-assembled onto the full array for the computation to proceed with the updated values from the neighbor rank. Through desynchronization, these tasks were parallelized in such a way as to hide buffers' building time within MPI calls. This is possible since each buffer accesses different positions on the complete array, which, therefore, can be simultaneously manipulated.

Overcoming these supplementary operations is possible through DDT (i.e., `mpi_opt_level=3`). In this case, the GPU-porting follows the same pattern discussed so far. However, this implementation requires only the complete array to be shared among ranks. As a result, the staging constructs taken from the OpenACC paradigms only apply to the variable containing all the nodal values and no desynchronization is required.

Acceleration performance analysis

The present paragraph reports quantitative information about URANOS parallel performance. The latter is tested on GALILEO100 and MARCONI100 HPC supercomputers, provided by CINECA [8, 9] and on the NVIDIA DGX A100 [52] system.

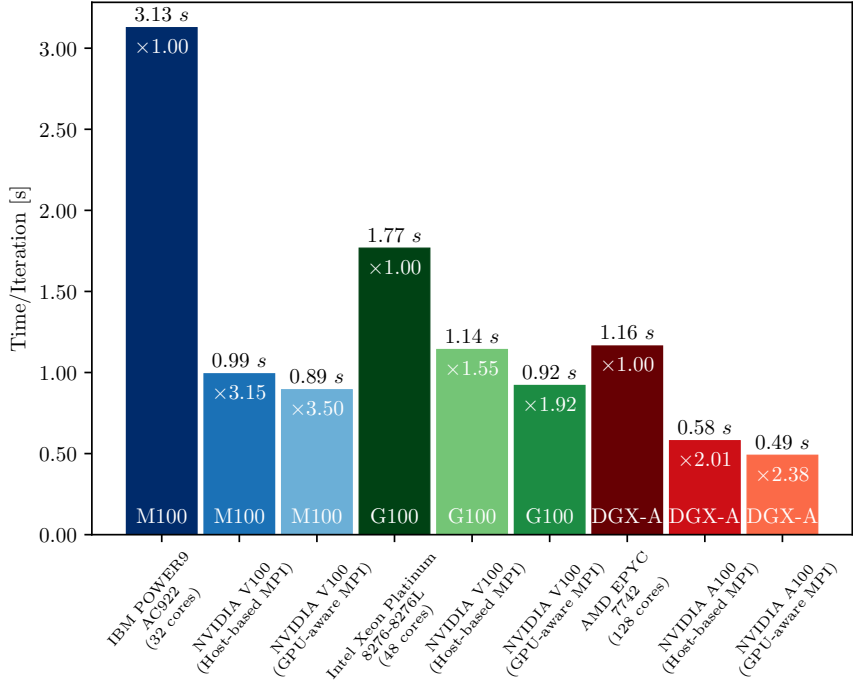


Figure 1: Speed-up results for URANOS, using different HPC architectures. CPU-based runs refer to a single computing node with the MPI parallelization and set the reference for each machine speed-up evaluation. Accelerated results are reported for both GPU-aware MPI and GPU Host-based MPI implementation. Run time values are included for clarity of comparison between different machines’ performance. Machines specific connections are as follows: NVLink 2.0 for both GPU-GPU and CPU-GPU on M100, PCIe3 for both GPU-GPU and CPU-GPU on G100, NVLink 3.0 for GPU-GPU and PCIe4 for CPU-GPU on DGX-A100.

Single CPU-node vs single GPU

A concise evaluation of URANOS performance is presented in Figure 1. Here, a uniform homogeneous $256 \times 256 \times 256$ Cartesian grid is used to evolve a three-dimensional bi-periodic Riemann problem. The test allows for tracking the computational costs of the whole spatial solver, accounting also for the shock-capturing procedures (WENO/TENO) and the shock-detection. The reference unit for CPU calculations is a single node, exploited using MPI parallelization, while for GPUs, the reference is the single card. It is not worthless to be mentioned that a single card running MPI still shares data, when handling periodic boundary conditions. In this event, on GPU-aware-equipped systems, the MPI implementation tends to convert the data sharing into a device-to-device copy. Conversely, on Host-based MPI communications, the connection type between GPUs and CPUs (e.g. NVLink or PCIe) imposes a limit on the transfers.

The speed-up results are strongly dependent on the hardware. In particular, the maximum speed-up is obtained with the MARCONI100 architecture with a $\times 3.5$ acceleration. Furthermore, as expected, Figure 1 shows that using the GPU-aware MPI implementation leads to higher efficiency values. In the context of MPI, the GPU-aware MPI technologies cover all kinds of inter-rank communication: intra-node, inter-node, and Remote Direct Memory Access (RDMA) inter-node communication [39]. Thus, the GPU-aware MPI implementation is more straightforward and efficient than the standard MPI one.

Solver profiling

When working on GPU porting, profiling activities are crucial to visualize kernels' execution and determine the solver's most critical portions concerning the execution time. The present version of URANOS provides a dedicated profiling module, `src/profiling_module.f90`, that acts as an interface for external profiling libraries. The module, in particular, allows any portion of code to be monitored by enclosing it between the `StartProfRange` and `EndProfRange` calls. The final result looks like the following algorithm:

Listing 6: Example of tracking code portions's performance using the URANOS ad-hoc profiling interface.

```
call StartProfRange("some_text")
...
!---- portion of the code to be monitored ----!
...
call EndProfRange
```

Results in the present paper are collected by disposing of the NVIDIA Nsight System [48, 50, 51] and, in particular, using the NVTX API. NVTX is enabled by the used-defined `-DNVTX` compiler option. However, in light of making the solver as neutral as possible with respect to GPU vendors, the profiling module is readily organized to accept other profiling libraries, e.g., rocTX by AMD. When the compiler/profiling tool system that best suits the user's requirements is chosen, these settings are left to the user in the form of comments in the profiling module.

Figure 2 reports the highest URANOS routines speed-up values regarding the average time spent per single iteration. Computations refer to the same test exploited to gather results in Section §Single CPU-node vs single GPU. Again, CPU results are obtained with an entire MARCONI100 compute node, while a single card is used for GPU data collection. Results highlight that the most time-consuming part involves the Navier-Stokes Right-Hand Side (RHS) computation (i.e., `rhsNS`); the latter taking around the $\simeq 95\%$ of the whole iteration. Thus, the speed-up of the Navier-Stokes RHS is comparable to the application's overall acceleration. Furthermore, it is again verifiable that the GPU-aware MPI implementation is more efficient than the classical GPU (Host-based MPI) approach since the MPI buffer sharing (i.e., `mpiBC`) is nearly $\times 10$ accelerated comparing the two methods.

Multi CPU-nodes/GPUs performance

Large computational domains require multiple GPUs in which each MPI process typically manages one graphic card. URANOS parallel performance is evaluated by exploiting the CINECA's MARCONI100 supercomputer, based on IBM Power 9 architecture, coupled with 4 NVIDIA Tesla Volta V100 GPUs per node and equipped with NVLink technology. The HPC-SDK by NVIDIA is used in concert with IBM's Spectrum MPI as internal testing showed this to be optimal. We elected to use the default bindings from Spectrum MPI as this best mimics what is typically done in the user community and no difference was detected in performance with the exception of a single node, 4 GPUs with host-based MPI where a 4% slowdown was detected compared to the optimal bindings.

Figure 3 reports the CPU and GPU parallel performance of code in terms of weak and strong

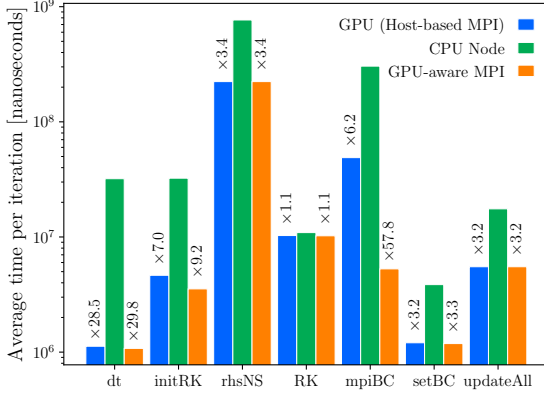


Figure 2: Comparison of highest code-sections acceleration for the GPU-aware MPI (orange) and GPU (Host-based MPI) (blue) implementations over the CPU version (green). Data are collected by exploiting the MARCONI100 architecture. The CPU computation refers to a full computing node while GPU results are gathered with a single card. It is worth mentioning that communications persist even on a single-GPU framework to handle periodic boundary conditions. Different bars pertain to different code sections: 1) time-step computation (*dt*) 2) Runge-Kutta initialization (*initRK*) 3) Navier-Stokes right-hand-side computation (*rhsNS*) 4) Runge-Kutta sub-steps computation (*RK*) 5) MPI buffer sharing (*mpiBC*) 6) physical boundary conditions (*setBC*) 7) update of the auxiliary variables (*updateAll*).

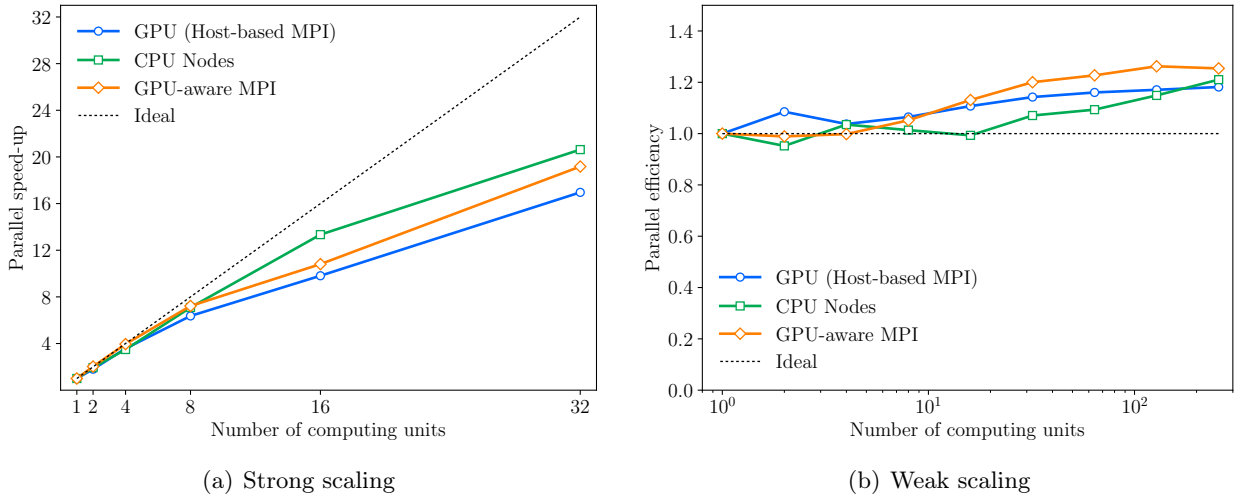


Figure 3: Strong (3(a)) and weak (3(b)) scaling performance of UANOS using the NVIDIA V100 GPU powered cluster MARCONI100. Computing units are entire nodes for CPU results (green lines with squares) and single cards for GPU ones. Orange lines with diamonds refer to a GPU-aware MPI implementation, while blue lines with circles refer to a GPU (Host-based MPI) approach.

scaling. CPU *number of computing units* refers to entire computing nodes while pertaining to single cards for GPU computations. Strong scaling results are gathered by keeping the total number of grid points constant while increasing the computing units. In particular, $N_x \times N_y \times N_z = 512 \times 256 \times 256$ grid points are used. Conversely, weak scaling performance is measured by fixing $N_x \times N_y \times N_z = 256 \times 256 \times 256$ grid points per computing unit. Computations are performed by evolving a three-dimensional bi-periodic Riemann problem as in previous test cases, thus, activating all the solver features. Figure 3(a) shows that a systematic better scaling is recovered for the CPU version of the solver, the latter owing to a strong scaling efficiency of about 60% using 32 compute nodes. Efficiency, instead, is reduced by around 50 % using 32 GPUs. In any case, this result is entirely in line with other open-source solvers available online [4, 12, 69]. It can also be observed that using the GPU-aware MPI implementation slightly enhances the strong scaling efficiency compared to the GPU (Host-based MPI) one. Weak scaling performance, instead, (Fig. 3(b)) shows that the parallel efficiency is very stable for a non-trivial amount of nodes/GPUs and generally never goes under 75%, even with 256 computational units. This value in terms of GPU is by no means trivial. We mention, in fact, that very recent multi-physic simulations, such as the one performed by Succi et al. [63] and Falcucci et al. [25] exploited 512 GPUs for a 10^{11} points grid, obtaining the impressive performance of 0.1 s/iter, i.e. obtaining a factor 10 of acceleration compared to URANOS. However, the performance is obtained in a Lattice-Boltzmann framework that is much more prone to be ported on GPU than the present finite-difference approach.

Solver validation and results discussion

This section reports the validation of URANOS with the GPU implementation using different techniques on extensive wall-flows cases. In particular, we report DNS, WRLES and WMLES results obtained from the simulation of turbulent channel and boundary layer flows, which are the two most representative test cases for wall-bounded flows in a canonical form. The simulation parameters are reported in Table 1 and Table 2, respectively. Additional verifications in terms of error scaling behavior of both convective and viscous terms, 1D and 2D Riemann problems are reported in Appendix .

Turbulent channel flow

We begin by presenting the case of a turbulent channel flow considering a nearly incompressible setup at $M_b = u_b/c_w = 0.1$ and a compressible one at $M_b = 1.5$ for different values of the bulk Reynolds number, i.e., $Re_b = 2\rho_b u_b h / \mu_w$. Here $u_b = 1/(\rho_b V) \int_V \rho u dV$ is the bulk velocity, $\rho_b = 1/V \int_V \rho dV$ is the bulk density while μ_w and c_w are the laminar viscosity and the speed of sound at the wall location, respectively. Table 1 also reports the nominal and the computed friction Reynolds number (Re_τ and Re_τ^* , respectively), where $Re_\tau = \rho_w u_\tau h / \mu_w$, are also available. The computations are carried out in a tridimensional box with size $L_x \times L_y \times L_z = 2\pi h \times 2h \times \pi h$ along the x , y and z coordinates, respectively, being h the channel half-height. A uniform mesh spacing is applied in the wall-parallel directions, whereas, for DNS and WRLES computations, a non-uniform distribution is adopted in the wall-normal direction according to the Gauss' error function [66]. WMLES setups, instead, are discretized with uniform meshes along with the three Cartesian directions. The number of nodes, $N_x \times N_y \times N_z$, the value of the stretching parameter, α , and the corresponding mesh

spacings in inner units (i.e., normalised by the viscous length, δ_ν), $\Delta x^+ \times \Delta y_w^+ \div \Delta y_c^+ \times \Delta z^+$, are reported in Table 1 for all the simulations. The units in the y -direction are reported as a range between the wall (Δy_w^+) and the centerline (Δy_c^+) spacings, respectively. Concerning the boundary conditions, periodicity is enforced in the wall-parallel directions, while a no-slip isothermal condition is imposed for the two walls. The grid spacing is staggered in correspondence with the first and the last cell; thus, the wall coincides with an intermediate node. This process guarantees mass conservation and allows increasing the simulation time-step [43]. The initial condition follows the procedure described in Henningson and Kim [33], which superimposes a vortex pair to the analytical solution of the Poiseuille flow. This strategy promotes an early transition to turbulence. In order to sustain the flow rate in the channel, a forcing term $f_i = \{0, f, 0, 0, fu\}^T$ is added to the RHS of the Navier-Stokes equations. The latter is evaluated at each time step. The process enforces the conservation of the mass flow rate discretely.

The DNS solver is first validated by simulating turbulent channel flows in nearly incompressible and compressible regimes. The former setup consists of a bulk Mach number of $M_b = 0.1$ and a nominal friction Reynolds number of $Re_\tau = 180$, while the latter is representative of a supersonic condition with $M_b = 1.5$ and $Re_\tau = 215$. The SGS model is inactive in both cases since all the energetic turbulent scales are captured with adequate mesh resolution down to the Kolmogorov scale (see Table 1). Figure 4 shows the mean streamwise inner-scaled velocity profile, $u^+ = \tilde{u}/u_\tau$, and density-scaled Reynolds stress components, $\bar{\tau}_{ij}^+ = \widetilde{\rho u_i'' u_j''}/\tau_w$, as a function of the inner-scaled wall distance, $y^+ = y/\delta_\nu$. An excellent agreement with the reference DNS data by Bernardini et al. [3] is observed, and a further comparison between only CPU and GPU approaches reveals an error between the computed friction Reynolds number with the target value of 0.6%. Comparisons between CPU (blue shades) and GPU (green shades) results also confirm accordance down to machine precision and allow us to present solely GPU-accelerated simulations from now on. Figure 5 reports DNS results pertaining to a compressible configuration, whereas to the statistics mentioned above, we also add the mean inner-scaled temperature profile, $T^+ = \tilde{T}/T_w$. Also for this case, results excellently agree with the reference data of Modesti and Pirozzoli [43].

Moving to the LES framework, we present the obtained results for a turbulent channel flow configuration using WRLES, where different SGS models are also compared (WALE [47], MXTS [34] and σ model [60]). Here, we consider an incompressible setup with $M_b = 0.1$ and $Re_\tau = 590$. Figure 6 shows the mean streamwise velocity profile, $u^+ = \tilde{u}/u_\tau$, and density-scaled Reynolds stress components, $\bar{\tau}_{ij}^+ = \widetilde{\rho u_i'' u_j''}/\tau_w$, as a function of the inner-scaled wall distance, y^+ . All SGS models produce results that closely match the reference DNS data by Vreman and Kuerten [67], with the MXTS appearing to perform the best with a 0.3% error on the computed friction Reynolds number, followed by σ and the wall-adapting local eddy-viscosity (WALE) models with a 0.6% error each.

Finally, same statistics are gathered with WMLES in $M_b = 0.1$ and $Re_\tau = 5200$ turbulent channel flow configuration. Figure 7 shows the results that are in very good agreement with DNS data of Lee and Moser [40] far from the wall, showing the model efficiency in correcting the LES field's low resolution in the near-wall region.

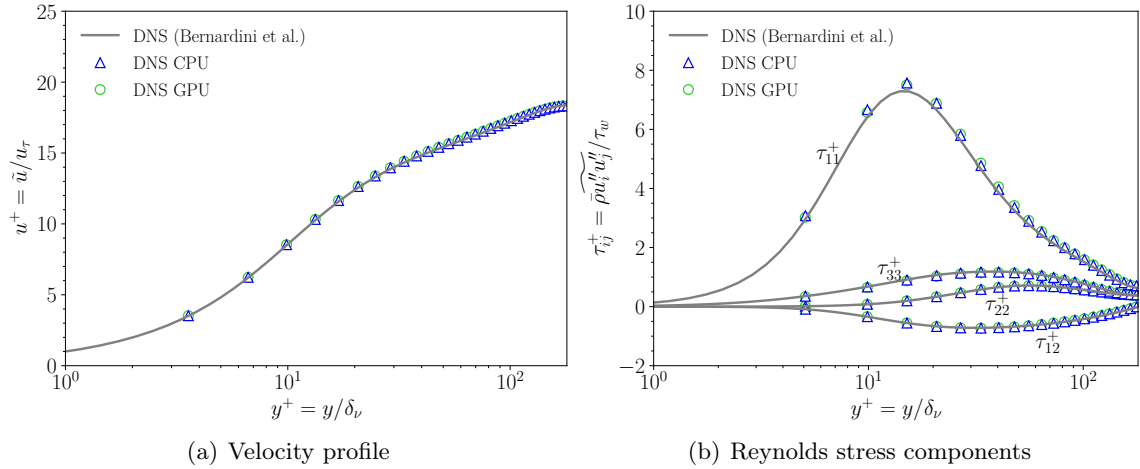


Figure 4: DNS of turbulent channel flow at $M_b = 0.1$ and $Re_\tau = 180$. Distribution of (4(a)) mean velocity profiles and (4(b)) Reynolds stresses as a function of y^+ , compared with reference DNS data by Bernardini et al. [3] (gray lines).

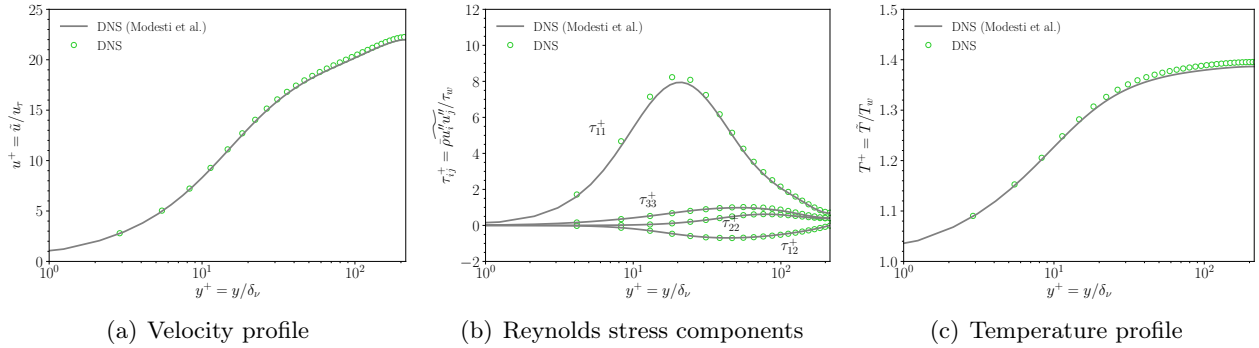


Figure 5: DNS of turbulent channel flow at $M_b = 1.5$ and $Re_\tau = 215$. Distribution of (5(a)) mean velocity profiles, (5(b)) Reynolds stresses and (5(c)) temperature profiles as a function of y^+ , compared with reference DNS data of Modesti and Pirozzoli [43] (gray lines).

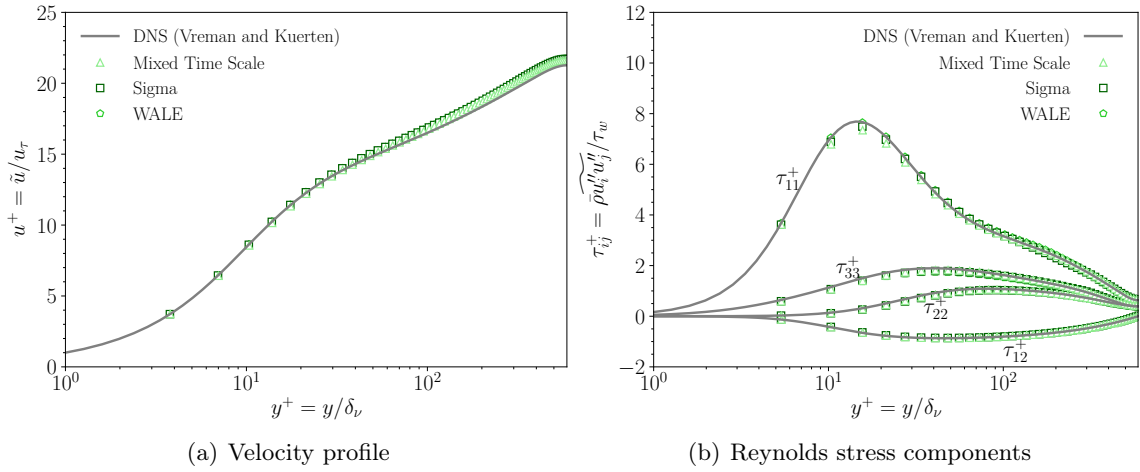


Figure 6: WRLES of turbulent channel flow at $M_b = 0.1$ and $Re_\tau = 590$. Distribution of (6(a)) mean velocity profiles and (6(b)) Reynolds stresses as a function of y^+ , compared with reference DNS data by Vreman and Kuerten [67] (gray lines).

Table 1: Parameters of the turbulent channel flow simulations.

| Case | Approach | SGS model | Re_τ | Re_b | M_b | Re_τ^* | N_x | N_y | N_z | α | Δx^+ | $\Delta y_w^+ \div \Delta y_c^+$ | Δz^+ |
|------------|----------|------------------|-----------|--------|-------|-------------|-------|-------|-------|----------|--------------|----------------------------------|--------------|
| TC01 (CPU) | DNS | - | 180 | 5632 | 0.1 | 179 | 192 | 128 | 192 | 2 | 5.9 | $0.7 \div 3.8$ | 2.9 |
| TC01 (GPU) | DNS | - | 180 | 5632 | 0.1 | 179 | 192 | 128 | 192 | 2 | 5.9 | $0.7 \div 3.8$ | 2.9 |
| TC02 | DNS | - | 215 | 6008 | 1.5 | 218 | 256 | 128 | 128 | 2.4 | 5.3 | $0.32 \div 5.9$ | 5.3 |
| TC03 | WRLES | MXTS | 590 | 22242 | 0.1 | 588 | 96 | 96 | 96 | 3 | 38.6 | $1.2 \div 21.5$ | 19.3 |
| TC03 | WRLES | $\sigma - model$ | 590 | 22242 | 0.1 | 586 | 96 | 96 | 96 | 3 | 38.6 | $1.2 \div 21.5$ | 19.3 |
| TC03 | WRLES | WALE | 590 | 22242 | 0.1 | 586 | 96 | 96 | 96 | 3 | 38.6 | $1.2 \div 21.5$ | 19.3 |
| TC04 | WMLES | WALE | 5200 | 253374 | 0.1 | | 160 | 128 | 80 | | 204 | 41 | 204 |

Table 2: Parameters of the turbulent boundary layer flow simulations

| Case | Approach | SGS model | Re_τ | $Re_{\tau,0}$ | Ma_∞ | N_x | N_y | N_z | Δx^+ | Δy_w^+ | Δz^+ |
|------|----------|-----------|-----------|---------------|-------------|-------|-------|-------|--------------|----------------|--------------|
| BL01 | DNS | - | 250 | 180 | 2 | 2800 | 128 | 600 | 8.0 | 0.5 | 2.5 |
| BL02 | WRLES | WALE | 250 | 180 | 2 | 768 | 128 | 128 | 29.0 | 0.5 | 11.7 |
| BL03 | WMLES | WALE | 1200 | 1000 | 5.86 | 1400 | 200 | 200 | 90 | 30 | 36 |

Turbulent boundary layer flow

We proceed to present the results obtained by simulating turbulent boundary layers in a compressible regime using DNS, WRLES and WMLES techniques. In particular, for the first two cases, we consider a $M_\infty = 2$ setup with an adiabatic wall condition at $Re_\tau = 250$, while for the latter, a hypersonic $M_\infty = 5.86$ regime is addressed and the friction Reynolds number is significantly increased ($Re_\tau = 1200$). For this simulation δ_0 , the incoming boundary layer thickness is selected as the characteristic length. The parameter is computed at the height where the boundary layer recovers the 99% of the free-stream speed. Thus, to each boundary layer station a given friction Reynolds number $Re_\tau = \delta/\delta_\nu$ is associated with, where $\delta_\nu = \mu_w/(\rho_w u_\tau)$, μ_w , ρ_w and u_τ still denoting the viscous length, the laminar wall viscosity, the fluid wall density and the wall friction velocity, respectively. The inflow friction Reynolds number, $Re_{\tau,0} = \delta_0/\delta_\nu$, is enforced as a boundary condition as reported in Table 2. All simulations are carried out using a three-dimensional box of size $L_x \times L_y \times L_z = (90 \times 10 \times 6)\delta_0$, which is long enough to adequately capture the large-scale and intermittent dynamics of turbulent structures avoiding any statistical correlation with the inflow condition. A summary of the simulation parameters is given in Table 2, where the number of points and mesh spacing in viscous units are also reported for each case. As far as the boundary conditions, fully three-dimensional Navier-Stokes Characteristic Boundary Conditions (NSCBC) [41, 59] are imposed at the top and the right boundaries of the domain using both characteristic decomposition and granting the evolution of transverse and viscous terms. This method provides the proper outflow behaviour with a minimal reflection of acoustics waves or injection of spurious oscillations. At the bottom wall, no-slip and non-penetrating conditions are satisfied by setting all velocity components to zero while adiabaticity/isothermality is enforced setting the wall temperature equal to

$$\frac{T_w}{T_\infty} = T_{rat} \left[1 + \frac{r}{2}(\gamma - 1)M_\infty^2 \right] \quad (17)$$

where $r = Pr^{1/3}$ denotes the recovery factor, while T_{rat} denotes the ratio between the wall temperature and the nominal adiabatic temperature. According to the available DNS references, T_{rat} is set equal to 1 and 0.76 for super- and hyper-sonic cases, respectively. The flow is assumed to be

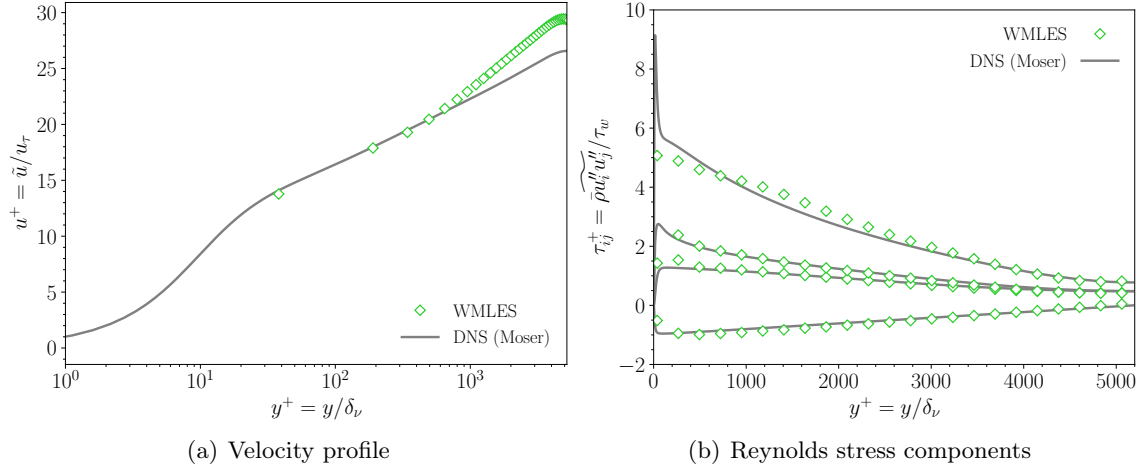


Figure 7: WMLES of turbulent channel flow at $M_b = 0.1$ and $Re_\tau = 5200$. Distribution of (7(a)) mean velocity profiles and (7(b)) Reynolds stresses as a function of y^+ , compared with reference DNS data by Moser et al. [45] (gray lines).

statistically homogeneous in the spanwise direction, and periodic boundary conditions are applied. The inflow condition is implemented accordingly to the synthetic digital filter method originally developed by Klein et al. [38] and later optimized by Kempf et al. [36], where velocity fluctuations are superimposed to a nominal turbulent mean velocity profile. Finally, the computation is initialized by prescribing a fully developed turbulent boundary layer using the Van Driest transformed Musker family profiles [46] and perturbing the initial system with the digital filter approach. Figure 8 shows the mean streamwise inner-scaled velocity profile, $u^+ = \bar{u}/u_\tau$, and density-scaled Reynolds stress components, $\bar{\tau}_{ij}^+ = \bar{\rho}\bar{u}_i''\bar{u}_j''/\tau_w$, as a function of the inner-scaled wall distance, $y^+ = y/\delta_\nu$. We observe an excellent agreement with the reference DNS data by Pirozzoli and Bernardini [58], validating the DNS solver even for supersonic boundary layer flows.

The same reference case is also exploited to compare WRLES solutions, as shown in Figure 9. Here, we observe a good agreement with reference data with only minor deviations on the peak location of the streamwise component of velocity fluctuations. Finally, we validate our WMLES implementation in the extreme conditions of a $M_\infty = 5.86$ hypersonic flow, which is also a test case for the aptness of the implemented shock-capturing scheme. On this note, we used the TENO-A 5 convective scheme, whose performances enhance WMLES computations. Figure 10 show the results for the mean streamwise inner-scaled velocity, the turbulent kinetic energy, $k^+ = \bar{\rho}\bar{u}_i''\bar{u}_i''/\tau_w$, and the mean inner-scaled temperature profiles. Both LES profiles (blue dots) and wall model outputs (orange lines) are reported, which are representative of the exchange between the model and LES domain [15]. An excellent agreement is observed compared to the reference DNS data by Cogo et al. [10] in the mean streamwise velocity and temperature profiles, while deviations in the inner layer are present in the turbulent kinetic energy profile. Nevertheless, the outer layer dynamics are correctly recovered.

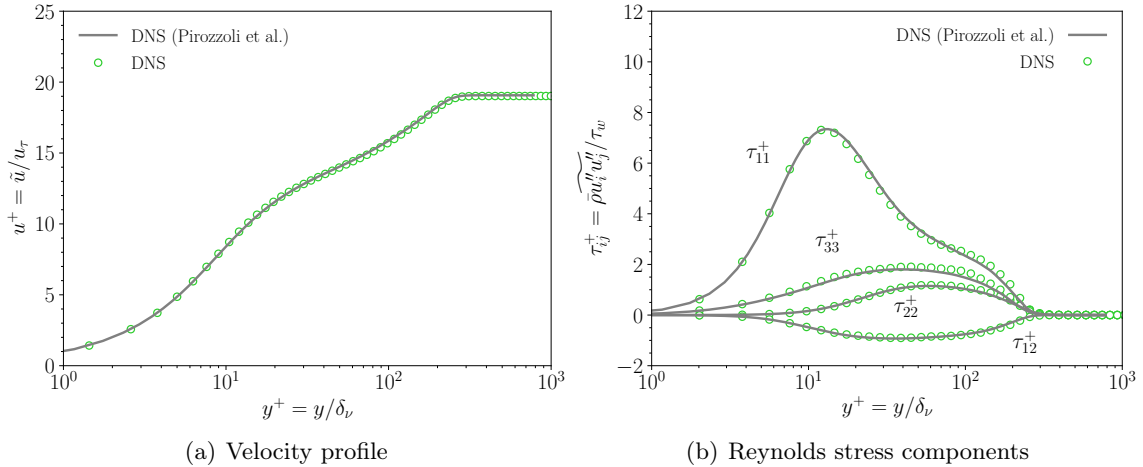


Figure 8: DNS of boundary layer flow at $M_\infty = 2$ and $Re_\tau = 250$. Distribution of (8(a)) mean velocity profiles and (8(b)) Reynolds stresses as a function of y^+ , compared with reference DNS data by Pirozzoli and Bernardini [58] (gray lines).

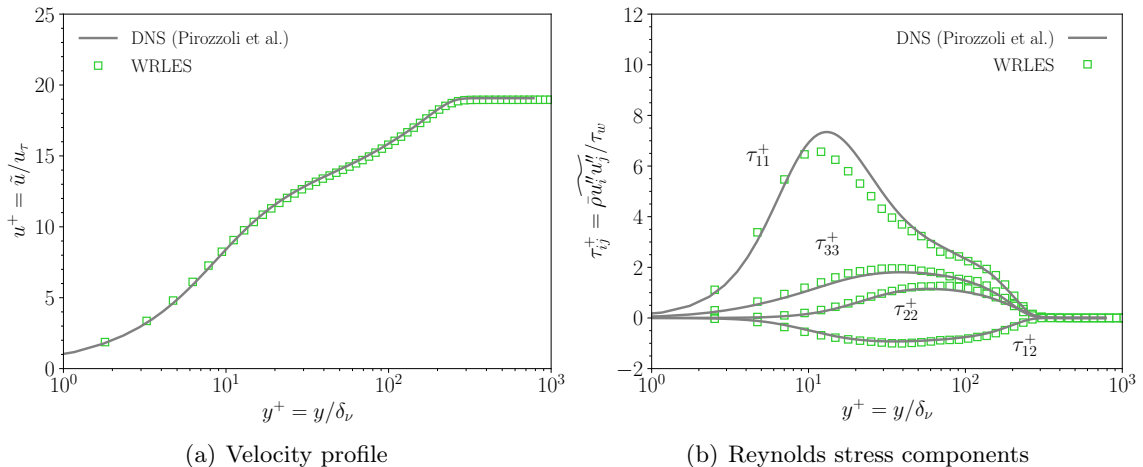


Figure 9: WRLES of boundary layer flow at $M_\infty = 2$ and $Re_\tau = 250$. Distribution of (9(a)) mean velocity profiles and (9(b)) Reynolds stresses as a function of y^+ , compared with reference DNS data by Pirozzoli and Bernardini [58] (gray lines).

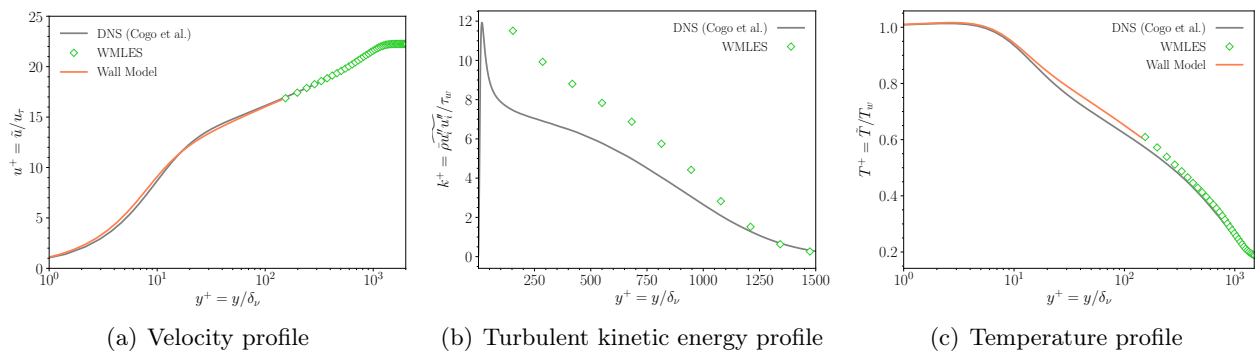


Figure 10: DNS of turbulent boundary layer at $M_b = 5.86$ and $Re_\tau = 1200$. Distribution of (10(a)) mean velocity profiles, (10(b)) Reynolds stresses and (10(c)) temperature profiles as a function of y^+ , compared with reference DNS data of Cogo et al. [10] (gray lines).

Conclusions

We have presented URANOS, an in-house, GPU-enabled, high-resolution, compressible flow solver, which is tailored for wall-bounded flow applications. Specific detail was presented on the solver structure, numerical methods and discretization of the Navier-Stokes system of equations. Particular attention is paid in describing the numerical techniques ranging from variable accuracy order, several advanced shock-capturing procedures, and an ad-hoc treatment of viscous terms.

With the algorithm defined, attention was focused on the performance aspects of the software. The methodology in adopting OpenACC for on-node parallelism on both CPUs and GPUs was detailed showing quantitative performance results. Relevant information is also provided regarding the multiple MPI approaches managed by the code. In total, three different MPI approaches are documented and profiled with both GPU-aware MPI and copy-to-host communication. With this, URANOS' users can select the optimal MPI implementations for the available architecture.

Finally, the work documents quantitative results for the solver's accuracy. In particular, starting from the most basic validations, data are provided for the predictions of the wall-flow dynamic in channel flow and turbulent boundary layer configurations, comparing available reference solutions with present DNS/LES and WMLES results across a broad spectrum of both Reynolds and Mach numbers.

The present software constitutes a flexible and multi-platform fluid dynamic solver that is beyond the limitations of other freely available software. In particular, two characteristics make URANOS a further step in the CFD panorama: i) Since OpenACC is configured as a standard directive-based language extension, URANOS can use contemporary and future GPU-based clusters in a vendor-neutral manner, limiting the tuning process and the refactoring activities concerning the continuous changes and the constantly evolving HPC market. Thus, making the solver an easily maintained, truly open-source, and highly flexible platform, even in light of upcoming GPU technologies. ii) Today, available high-resolution open-source solvers are based on DNS, while URANOS adopts state-of-the-art turbulence modeling strategies in terms of LES strategies and WMLES approaches, positioning the solver as a key starting point for developing more complex physical models targeting engineering applications.

Future developments of the program will include complex (and even moving) geometry treatment to deal with complex engineering-based applications, e.g., [1, 2, 21]. The open-source version of the code is available at the following link: https://gitlab.com/fralusa/uranos_gpu.

Acknowledgments

The authors acknowledge the following institutions for awarding us access to their computational facilities: the "France Genci/CEA" that allows us TGCC Joliot Curie cluster in the framework of the PRACE project 2021240111, the "Consorzio Interuniversitario per il Calcolo Automatico" for granting us access to Marconi100 and Galileo100 in framework of LESToGPU (HP10CFGKSW) and iWMLES (HP10C8RJ5T) projects and the NVIDIA Corporation to dispose us the DGX-A system.

Funding

This research received no specific grant from any funding agency, commercial or not-for-profit sectors.

Declaration of interests

The authors declare no conflict of interest.

Additional solver verifications

The present appendix aims at presenting additional numerical verifications in terms of convective and viscous schemes error scaling and 1D/2D Riemann problems behaviors.

Convective schemes error scaling

As a first step, we measure the error scaling of the convective schemes by comparing numerical solutions to analytical references. In particular, the advection of a single harmonic density wave is used as a test case. The problem's initial conditions read as follows:

$$(\rho, u, v, w, p)_0 = (1 + A \sin(\pi x), u_\infty, 0, 0, 1) \quad (18)$$

and neglecting viscous terms, 1D periodic compressible Navier-Stokes system of equations admits the following solution

$$(\rho, u, v, w, p) = (1 + A \sin(\pi(x - u_\infty t)), u_\infty, 0, 0, 1). \quad (19)$$

Here $A = 0.2$ and $u_\infty = 0.05$, respectively. The p and the ∞ norms are computed by comparing the numerical solution, ρ^* , with the analytical reference according to the following expressions:

$$L_p = \left(\frac{1}{N_x} \sum_{i=1}^{N_x} |\rho_i - \rho_i^*|^p \right)^{1/p} \quad (20a)$$

$$L_\infty = \max_{i=1}^{N_x} |\rho_i - \rho_i^*| \quad (20b)$$

Here N_x denotes the number of grid points while p , the norm order, is set equal to 1 and 2. Error scalings are reported in Figure 11. From the obtained results, all schemes are found scaling with their theoretical order of accuracy, and the outcome remains stable for all the investigated norms. This confirms that the convective discretization methods are adequately implemented.

One dimensional Riemann problems

As a further step two one-dimensional Riemann problems for the Euler equations are here presented. In particular, the Sod and the Shu-Osher *shock tube* problems are considered [35]. Initial conditions are provided by Jiang and Shu [35]: The problems are addressed on a uniform mesh featuring

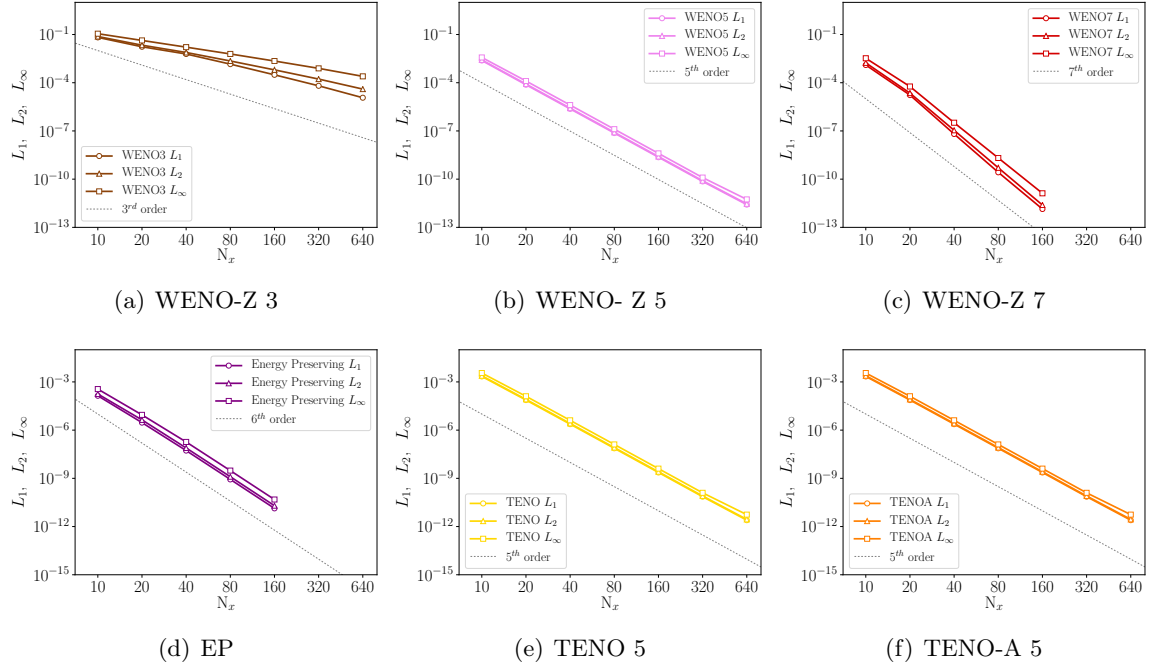


Figure 11: Error scaling on a smooth solution for various convective schemes.

$N_x = 200$ grid points. Extrapolation boundaries are ensured at the left and right limits. The five shock-capturing approaches (i.e., WENO-Z 3/5/7, TENO 5, TENO-A 5) are used to gather the numerical solutions. Comparison to a $N_x = 2000$ points numerical solution is determined. System dynamics is evolved up to $t/t_0 = 2$ and $t/t_0 = 1.3$ time units for the Sod and the Shu-Osher problem, respectively. Figure 12 collect the results of the analysis. In particular, Figs. 12(a) and 12(c) provide the Sod's and the Shu-Osher global scaled density profiles, ρ/ρ_0 , as a function scaled tube axial coordinate, x/L_0 . Enlargements on critical regions are provided in Figs. 12(b) and 12(d). From the obtained results, it can be observed that all shock-capturing methods accurately represent the system dynamics. In particular, a marked dependence on the order of accuracy as well as moving from WENO to TENO is found. Discontinuous and intensively varying portions of the density field (i.e., shocks and high-frequency features) adhere progressively to the reference as the order of accuracy increases.

Two dimensional Riemann problems

A 2D-Riemann problem for Euler equations is additionally addressed to further visualize shock-capturing algorithm accuracy. Similar to the one-dimensional version, the problem consists of initializing a discontinuous solution to the Euler system of equations and displaying the system's behavior through time. By introducing a second dimension, many different configurations and combinations are made feasible and Guo and Shi [31] provide a comprehensive overview of the most

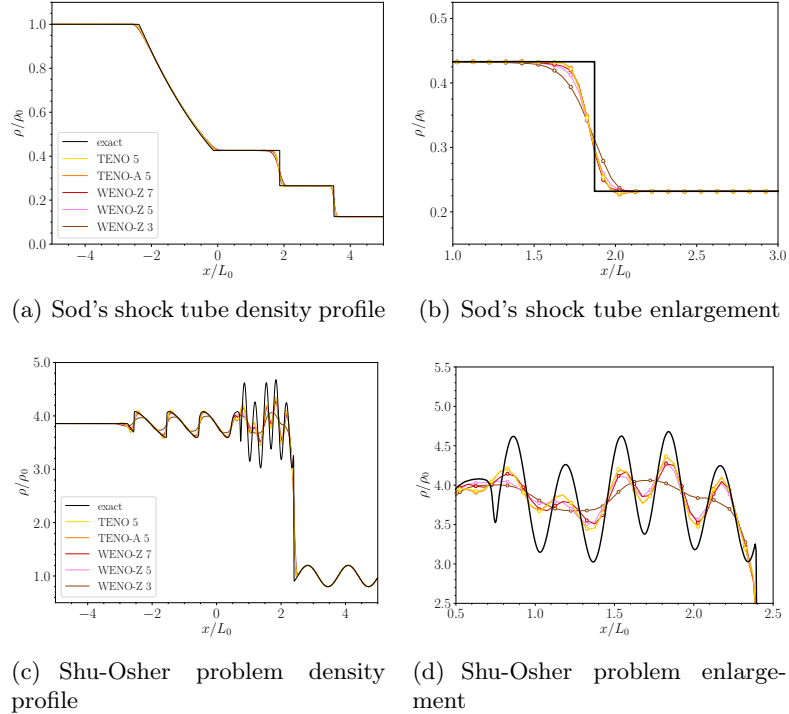


Figure 12: Density profiles for the Sod’s shock tube (12(a)-12(b)) and Shu-Osher problem (12(c)-12(d)). A comparison between the analytical and the numerical solution is presented as a function of convective schemes.

prevalent arrangements. Here we deal with the following *four-quadrants* setup:

$$\begin{pmatrix} \rho \\ u \\ v \\ p \end{pmatrix}_0 = \begin{cases} (1.5000, 0.000, 0.000, 1.500) & \text{if } x > 0, y > 0 \\ (0.5323, 1.206, 0.000, 0.300) & \text{if } x < 0, y > 0 \\ (0.1380, 1.206, 1.206, 0.029) & \text{if } x < 0, y < 0 \\ (0.5323, 0.000, 1.206, 0.300) & \text{if } x > 0, y < 0 \end{cases} \quad (21a)$$

Despite previous tests, the results of two-dimensional Riemann problems are purely qualitative in terms of contours plots and provide distinctions regarding the resolution of shock-capturing schemes. Simulations are performed on uniform grids of size $(L_x \times L_y) = L_0 \times L_0$ length units and featuring in $N_x \times N_y = 1600 \times 1600$ computational nodes. Extrapolation boundaries are employed in all the four edges of the domain, and the solution is advanced in time up $t/t_0 = 0.3$. Results are reported in Figure 13 where the self-similar density field flow structure obtained with WENO-Z 5 (Fig. 13(a)), WENO-Z 7 (Fig. 13(b)), TENO 5 (Fig. 13(c)) and TENO-A 5 (Fig. 13(d)) are reported. Results perfectly fit the qualitative analyzes reported in the literature [31], and again, the effect of the order of accuracy concerning the shock-capturing approaches is shown. In particular, by increasing the accuracy order of WENO methods, as well as going from WENO to TENO implementations, enhanced spectral properties allow for determining additional shear layer instabilities as well as greater detailing of the central plume.

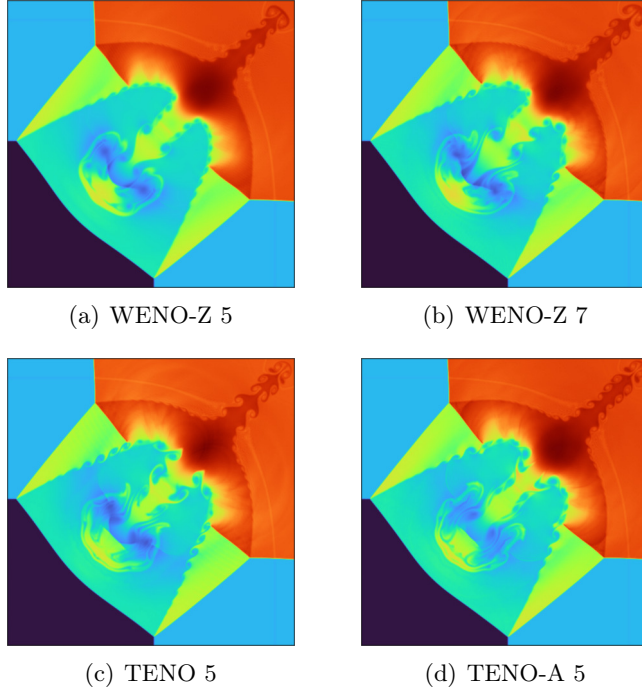


Figure 13: Comparison of the self-similar density field flow structure for the four-quadrants problem as a function of the shock-capturing approach.

Viscous scheme error scaling

A laminar and steady-state Kolmogorov Flow is examined under doubly periodic conditions to quantify the error scaling of viscous components. The problem involves forcing the two-dimensional Navier-Stokes system of equation along with a single Cartesian direction with the following term

$$f(y) = \alpha \sin(\omega ky) \quad (22)$$

Here $\omega = 2\pi/L_y$ is the reduced frequency, k is the wave number, α is the force amplitude, and L_y is the length of the domain along with the y -coordinate. Low-speed and laminar conditions make Navier-Stokes system to reduce to the following equation

$$\frac{d}{dy} \left(\mu \frac{du}{dy} \right) + f(y) = 0 \quad (23)$$

whose analytical solution is expressed as

$$u(y) = \frac{\alpha Re_\infty}{\sqrt{\gamma} Ma_\infty \omega^2 k^2} \sin(\omega ky) \quad (24)$$

The problem is numerically reproduced by simulating the flow dynamics in a square box of size $L_x \times L_y = L_0 \times L_0$. The force amplitude, α , is set to $0.1u_\infty$ while k is set to 4. Laminar conditions are assured by setting the reference $Re_\infty = 10$ and $Ma_\infty = 0.1$, respectively. The computation is carried out until the steady-state convergence of the system.

Five increasingly refined uniform grids are employed to compare the analytical and the numerical solutions. In particular, Figure 14 provides the error scaling of viscous terms for a 2nd, a 4th and

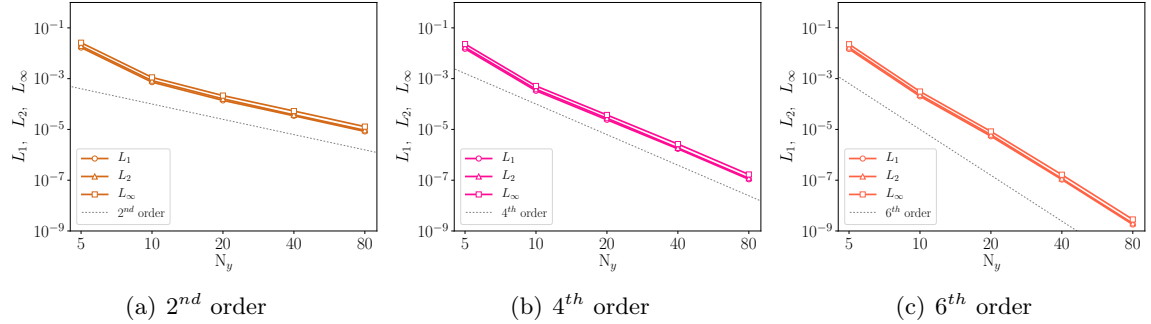


Figure 14: Error scaling on a smooth solution for viscous schemes as a function of the order of accuracy.

a 6^{th} order implementation. Results allow us to state that the viscous components are adequately implemented. Additional details of the method are reported by De Vanna et al. [14].

Bibliography

- [1] Filippo Avanzi, Francesco De Vanna, Yin Ruan, and Ernesto Benini. Design-Assisted of Pitching Aerofoils through Enhanced Identification of Coherent Flow Structures. *Designs*, pages 1–25, 2021. doi: <https://doi.org/10.3390/designs5010011>.
- [2] Filippo Avanzi, Francesco De Vanna, Yin Ruan, and Ernesto Benini. Enhanced identification of coherent structures in the flow evolution of a pitching wing. *AIAA Science and Technology Forum and Exposition, AIAA SciTech Forum 2022*, 2022. doi: 10.2514/6.2022-0182.
- [3] Matteo Bernardini, Sergio Pirozzoli, and Paolo Orlandi. Velocity statistics in turbulent channel flow up to $Re_\tau = 4000$. *J. Fluid Mech.*, 742:171–191, 2014. doi: <https://doi.org/10.1017/jfm.2013.674>.
- [4] Matteo Bernardini, Davide Modesti, Francesco Salvadore, and Sergio Pirozzoli. Streams: a high-fidelity accelerated solver for direct numerical simulation of compressible turbulent flows. *Comput. Phys. Commun.*, 263:107906, 2021. doi: <https://doi.org/10.1016/j.cpc.2021.107906>.
- [5] Marcos Castro, Bruno Costa, and Wai Sun Don. High order weighted essentially non-oscillatory WENO-Z schemes for hyperbolic conservation laws. *J. Comput. Phys.*, 230(5):1766–1792, 2011. doi: <https://doi.org/10.1016/j.jcp.2010.11.028>.
- [6] Dean R Chapman. Computational aerodynamics development and outlook. *AIAA J.*, 17(12):1293–1313, 1979. doi: <https://doi.org/10.2514/3.61311>.
- [7] Haecheon Choi and Parviz Moin. Grid-point requirements for large eddy simulation: Chapman’s estimates revisited. *Phys. Fluids*, 24(1):011702, 2012. doi: <https://doi.org/10.1063/1.3676783>.
- [8] CINECA. Ug3.3: Galileo100 userguide. <https://wiki.u-gov.it/confluence/display/SCAIUS/UG3.3%3A+GALILEO100+UserGuide>, 2022.
- [9] CINECA. Ug3.2: Marconi100 userguide. <https://wiki.u-gov.it/confluence/pages/viewpage.action?pageId=336727645>, 2022.
- [10] Michele Cogo, Francesco Salvadore, Francesco Picano, and Matteo Bernardini. Direct numerical simulation of supersonic and hypersonic turbulent boundary layers at moderate-high reynolds numbers and isothermal wall condition. *J. Fluid Mech.*, 945, 2022. doi: <https://doi.org/10.1017/jfm.2022.574>.
- [11] Gennaro Coppola, Francesco Capuano, Sergio Pirozzoli, and Luigi de Luca. Numerically stable formulations of convective terms for turbulent compressible flows. *J. Comput. Phys.*, 382:86–104, 2019. doi: <https://doi.org/10.1016/j.jcp.2019.01.007>.
- [12] Pedro Costa, Everett Phillips, Luca Brandt, and Massimiliano Fatica. Gpu acceleration of cans for massively-parallel direct numerical simulations of canonical fluid flows. *Comput. Math. with Appl.*, 81:502–511, 2021. doi: <https://doi.org/10.1016/j.camwa.2020.01.002>.

- [13] Francesco De Vanna, Francesco Picano, and Ernesto Benini. A sharp-interface immersed boundary method for moving objects in compressible viscous flows. *Comput. Fluids*, 201:104415, 2020. doi: <https://doi.org/10.1016/j.compfluid.2019.104415>.
- [14] Francesco De Vanna, Alberto Benato, Francesco Picano, and Ernesto Benini. High-order conservative formulation of viscous terms for variable viscosity flows. *Acta Mech.*, 232(6):2115–2133, 2021. doi: <https://doi.org/10.1007/s00707-021-02937-2>.
- [15] Francesco De Vanna, Michele Cogo, Matteo Bernardini, Francesco Picano, and Ernesto Benini. Unified wall-resolved and wall-modeled method for large-eddy simulations of compressible wall-bounded flows. *Phys. Rev. Fluids*, 6(3):034614, 2021. doi: <https://doi.org/10.1103/PhysRevFluids.6.034614>.
- [16] Francesco De Vanna, Michele Cogo, Matteo Bernardini, Francesco Picano, and Ernesto Benini. A wall-modeled/wall-resolved les method for turbulent wall flows. In *14th WCCM-ECCOMAS Congress 2020*, volume 600, 2021. doi: 10.23967/wccm-eccomas.2020.045.
- [17] Francesco De Vanna, Francesco Picano, and Ernesto Benini. Large-eddy-simulations of the unsteady behaviour of a mach 5 hypersonic intake. In *AIAA Scitech 2021 Forum*, page 0858, 2021. doi: <https://doi.org/10.2514/6.2021-0858>.
- [18] Francesco De Vanna, Francesco Picano, Ernesto Benini, and Mark Kenneth Quinn. Large-Eddy Simulations of the Unsteady Behavior of a Hypersonic Intake at Mach 5. *AIAA J*, 59(10), 2021. doi: <https://doi.org/10.2514/1.J060160>.
- [19] Francesco De Vanna, Matteo Bernardini, Francesco Picano, and Ernesto Benini. Wall-modelled and wall-resolved large-eddy simulations of shock-wave/boundary layer interaction. In *AIAA SCITECH 2022 Forum*, page 0484, 2022. doi: <https://doi.org/10.2514/6.2022-0484>.
- [20] Francesco De Vanna, Matteo Bernardini, Francesco Picano, and Ernesto Benini. Wall-modeled les of shock-wave/boundary layer interaction. *Int J Heat Fluid Flow*, 98:109071, 2022. doi: <https://doi.org/10.1016/j.ijheatfluidflow.2022.109071>.
- [21] Francesco De Vanna, Danilo Bof, and Ernesto Benini. Multi-objective rans aerodynamic optimization of a hypersonic intake ramp at mach 5. *Energies*, 15(8):2811, 2022. doi: <https://doi.org/10.3390/en15082811>.
- [22] Francesco De Vanna, Michele Cogo, Matteo Bernardini, Francesco Picano, and Ernesto Benini. A straightforward strategy to unify wr/wmles approaches for compressible wall-bounded flows. In *AIAA SCITECH 2022 Forum*, page 0181, 2022. doi: <https://doi.org/10.2514/6.2022-0181>.
- [23] Francesco De Vanna, Giacomo Baldan, Francesco Picano, and Ernesto Benini. Effect of convective schemes in wall-resolved and wall-modeled les of compressible wall turbulence. *Comput. Fluids*, 250:105710, 2023. doi: <https://doi.org/10.1016/j.compfluid.2022.105710>.
- [24] F Ducros, V Ferrand, Franck Nicoud, C Weber, D Darracq, C Gachereau, and Thierry Poinsot. Large-eddy simulation of the shock/turbulence interaction. *J. Comput. Phys.*, 152(2):517–549, 1999. doi: <https://doi.org/10.1006/jcph.1999.6238>.

- [25] Giacomo Falcucci, Giorgio Amati, Pierluigi Fanelli, Vesselin K Krastev, Giovanni Polverino, Maurizio Porfiri, and Sauro Succi. Extreme flow simulations reveal skeletal adaptations of deep-sea sponges. *Nature*, 595(7868):537–541, 2021. doi: <https://doi.org/10.1038/s41586-021-03658-1>.
- [26] Lin Fu, Xiangyu Y Hu, and Nikolaus A Adams. A family of high-order targeted eno schemes for compressible-fluid simulations. *J. Comput. Phys.*, 305:333–359, 2016. doi: <https://doi.org/10.1016/j.jcp.2015.10.037>.
- [27] Lin Fu, Xiangyu Y Hu, and Nikolaus A Adams. Targeted ENO schemes with tailored resolution property for hyperbolic conservation laws. *J. Comput. Phys.*, 349:97–121, 2017. doi: <https://doi.org/10.1016/j.jcp.2017.07.054>.
- [28] Lin Fu, Xiangyu Y Hu, and Nikolaus A Adams. A new class of adaptive high-order targeted ENO schemes for hyperbolic conservation laws. *J. Comput. Phys.*, 374:724–751, 2018. doi: <https://doi.org/10.1016/j.jcp.2018.07.043>.
- [29] Eric Garnier, Nikolaus Adams, and Pierre Sagaut. *Large eddy simulation for compressible flows*. Springer Science & Business Media, 2009.
- [30] Sigal Gottlieb and Chi-Wang Shu. Total variation diminishing runge-kutta schemes. *Math. Comput.*, 67(221):73–85, 1998. doi: <https://doi.org/10.1090/S0025-5718-98-00913-2>.
- [31] Yan Guo and YuFeng Shi. Seventh order compact-weno scheme for hyperbolic conservation laws. *Comput. Fluids*, 176:193–209, 2018. doi: <https://doi.org/10.1016/j.compfluid.2018.09.006>.
- [32] Arash Hamzehloo, David J Lusher, Sylvain Laizet, and Neil D Sandham. On the performance of WENO/TENO schemes to resolve turbulence in DNS/LES of high-speed compressible flows. *Int. J. Numer. Methods Fluids*, 93(1):176–196, 2021. doi: <https://doi.org/10.1002/fld.4879>.
- [33] Dan S Henningson and John Kim. On turbulent spots in plane poiseuille flow. *J. Fluid Mech.*, 228:183–205, 1991. doi: <https://doi.org/10.1017/S0022112091002677>.
- [34] Masahide Inagaki, Tsuguo Kondoh, and Yasutaka Nagano. A mixed-time-scale sgs model with fixed model-parameters for practical les. *J. Fluids Eng.*, 127(1):1–13, 2005. doi: <https://doi.org/10.1115/1.1852479>.
- [35] Guang-Shan Jiang and Chi-Wang Shu. Efficient implementation of weighted eno schemes. *J. Comput. Phys.*, 126(1):202–228, 1996. doi: <https://doi.org/10.1006/jcph.1996.0130>.
- [36] AM Kempf, S Wysocki, and M Pettit. An efficient, parallel low-storage implementation of Klein’s turbulence generator for LES and DNS. *Comput. Fluids*, 60:58–60, 2012. doi: <https://doi.org/10.1016/j.compfluid.2012.02.027>.
- [37] F.G. Keyes. A summary of viscosity and heat-conduction data for He, A, H₂, O₂, N₂, CO, CO₂, H₂O, and air. *Trans. Am. Soc. Mech. Eng.*, 73(5):589–595, 1951. doi: <https://doi.org/10.1115/1.4016339>.

- [38] Markus Klein, Amsini Sadiki, and Johannes Janicka. A digital filter based generation of inflow data for spatially developing direct numerical or large eddy simulations. *J. Comput. Phys.*, 186(2):652–665, 2003. doi: [https://doi.org/10.1016/S0021-9991\(03\)00090-1](https://doi.org/10.1016/S0021-9991(03)00090-1).
- [39] Jiri Kraus. An introduction to cuda-aware mpi. <https://developer.nvidia.com/blog/introduction-cuda-aware-mpi/>, 2013. NVIDIA Technical Blog.
- [40] Myoungkyu Lee and Robert D Moser. Direct numerical simulation of turbulent channel flow up to $Re_\tau = 5200$. *J. Fluid Mech.*, 774:395–415, 2015. doi: <https://doi.org/10.1017/jfm.2015.268>.
- [41] Guido Lodato, Pascale Domingo, and Luc Vervisch. Three-dimensional boundary conditions for direct and large-eddy simulation of compressible viscous flows. *J. Comput. Phys.*, 227(10):5105–5143, 2008. doi: <https://doi.org/10.1016/j.jcp.2008.01.038>.
- [42] David J Lusher, Satya P Jammy, and Neil D Sandham. Opensbli: Automated code-generation for heterogeneous computing architectures applied to compressible fluid dynamics on structured grids. *Comput. Phys. Commun.*, 267:108063, 2021. doi: <https://doi.org/10.1016/j.cpc.2021.108063>.
- [43] Davide Modesti and Sergio Pirozzoli. Reynolds and mach number effects in compressible turbulent channel flow. *Int. J. Heat Fluid Flow.*, 59:33–49, 2016. doi: <https://doi.org/10.1016/j.ijheatfluidflow.2016.01.007>.
- [44] Davide Modesti and Sergio Pirozzoli. Direct numerical simulation of supersonic pipe flow at moderate reynolds number. *Int. J. Heat Fluid Flow.*, 76:100–112, 2019. doi: <https://doi.org/10.1016/j.ijheatfluidflow.2019.02.001>.
- [45] Robert D Moser, John Kim, and Nagi N Mansour. Direct numerical simulation of turbulent channel flow up to $re_\tau = 590$. *Phys. Fluids*, 11(4):943–945, 1999. doi: <https://doi.org/10.1063/1.869966>.
- [46] AJ Musker. Explicit expression for the smooth wall velocity distribution in a turbulent boundary layer. *AIAA J.*, 17(6):655–657, 1979. doi: <https://doi.org/10.2514/3.61193>.
- [47] Franck Nicoud and Frédéric Ducros. Subgrid-scale stress modelling based on the square of the velocity gradient tensor. *Flow Turbul. Combust.*, 62(3):183–200, 1999. doi: <https://doi.org/10.1023/A:1009995426001>.
- [48] NVIDIA. Nvidia nsight systems. <https://developer.nvidia.com/nsight-systems>.
- [49] NVIDIA. *PGI compilers & TOOLS, OPENACC GETTING STARTED GUIDE*, 2017.
- [50] NVIDIA. *NVIDIA Tools Extension Library (NVTX)*, 2020.
- [51] NVIDIA. *Nsight Systems User Guide*, 2021.
- [52] NVIDIA. Nvidia dgx a100. <https://www.nvidia.com/it-it/data-center/dgx-station-a100/>, 2022.
- [53] OpenACC. <https://www.openacc.org/>, 2022.

- [54] OpenACC-Standard.org. The openacc application programming interface. <https://www.openacc.org/sites/default/files/inline-images/Specification/OpenACC.3.0.pdf>, 2019. Version 3.0.
- [55] Jun Peng, Shengping Liu, Shiya Li, Ke Zhang, and Yiqing Shen. An efficient targeted ENO scheme with local adaptive dissipation for compressible flow simulation. *J. Comput. Phys.*, 425: 109902, 2021. doi: <https://doi.org/10.1016/j.jcp.2020.109902>.
- [56] Sergio Pirozzoli. Generalized conservative approximations of split convective derivative operators. *J. Comput. Phys.*, 229(19):7180–7190, 2010. doi: <https://doi.org/10.1016/j.jcp.2010.06.006>.
- [57] Sergio Pirozzoli. Stabilized non-dissipative approximations of euler equations in generalized curvilinear coordinates. *J. Comput. Phys.*, 230(8):2997–3014, 2011. doi: <https://doi.org/10.1016/j.jcp.2011.01.001>.
- [58] Sergio Pirozzoli and Matteo Bernardini. Turbulence in supersonic boundary layers at moderate reynolds number. *J. Fluid Mech.*, 688:120–168, 2011. doi: <https://doi.org/10.1017/jfm.2011.368>.
- [59] T Poinsot and SK Lele. Boundary conditions for direct simulations of compressible viscous flows. *J. Comput. Phys.*, 101(1):104–129, 1992. doi: [https://doi.org/10.1016/0021-9991\(92\)90046-2](https://doi.org/10.1016/0021-9991(92)90046-2).
- [60] M Rieth, F Proch, OT Stein, MWA Pettit, and AM Kempf. Comparison of the Sigma and Smagorinsky LES models for grid generated turbulence and a channel flow. *Comput. Fluids*, 99:172–181, 2014. doi: <https://doi.org/10.1016/j.compfluid.2014.04.018>.
- [61] Joshua Romero, Jacob Crabbill, JE Watkins, Freddie D Witherden, and Antony Jameson. Zefr: A gpu-accelerated high-order solver for compressible viscous flows using the flux reconstruction method. *Comput. Phys. Commun.*, 250:107169, 2020. doi: <https://doi.org/10.1016/j.cpc.2020.107169>.
- [62] Francesco Salvadore, Matteo Bernardini, and Michela Botti. GPU accelerated flow solver for direct numerical simulation of turbulent flows. *J. Comput. Phys.*, 235:129–142, 2013. doi: <https://doi.org/10.1016/j.jcp.2012.10.012>.
- [63] Sauro Succi, Giorgio Amati, Massimo Bernaschi, Giacomo Falcucci, Marco Lauricella, and Andrea Montessori. Towards exascale lattice boltzmann computing. *Comput. Fluids*, 181: 107–115, 2019. doi: <https://doi.org/10.1016/j.compfluid.2019.01.005>.
- [64] William Sutherland. Lii. the viscosity of gases and molecular force. *The London, Edinburgh, and Dublin Philosophical Magazine and Journal of Science*, 36(223):507–531, 1893. doi: <https://doi.org/10.1080/14786449308620508>.
- [65] H Baya Toda, O Cabrit, G Balarac, S Bose, J Lee, H Choi, and F Nicoud. A subgrid-scale model based on singular values for LES in complex geometries. *Center for Turbulence Research, Proceedings of the Summer Program*, pages 193–202, 2010. URL http://web.stanford.edu/group/ctr/Summer/SP10/3_03_bayatoda.pdf.

- [66] F De Vanna, Francesco Picano, and Ernesto Benini. An immersed boundary method for moving objects in compressible flows. In *ERCOFTAC Workshop Direct and Large Eddy Simulation*, pages 291–296. 2019. doi: https://doi.org/10.1007/978-3-030-42822-8_38.
- [67] AW Vreman and Johannes GM Kuerten. Statistics of spatial derivatives of velocity and pressure in turbulent channel flow. *Phys. Fluids*, 26(8):085103, 2014. doi: <https://doi.org/10.1063/1.4891624>.
- [68] Freddie D Witherden, Antony M Farrington, and Peter E Vincent. Pyfr: An open source framework for solving advection–diffusion type problems on streaming architectures using the flux reconstruction approach. *Comput. Phys. Commun.*, 185(11):3028–3040, 2014. doi: <https://doi.org/10.1016/j.cpc.2014.07.011>.
- [69] Xiaojue Zhu, Everett Phillips, Vamsi Spandan, John Donners, Gregory Ruetsch, Joshua Romero, Rodolfo Ostilla-Mónico, Yantao Yang, Detlef Lohse, Roberto Verzicco, et al. Afid-gpu: a versatile navier–stokes solver for wall-bounded turbulent flows on gpu clusters. *Comput. Phys. Commun.*, 229:199–210, 2018. doi: <https://doi.org/10.1016/j.cpc.2018.03.026>.

Appendix E

Paper V

Inverse velocity transformation wall model for reacting turbulent hypersonic boundary layers

Michele Cogo^{1,2}, Christopher Williams², Kevin Patrick Griffin²,
Francesco Picano^{1,4}, Parviz Moin²

1. Centro di Ateneo di Studi e Attività Spaziali "Giuseppe Colombo" - CISAS,
University of Padova, Padova, PD 35131, Italy,

2. Center for Turbulence Research, Stanford University, Stanford, CA, USA

3. Department of Industrial Engineering, University of Padova, Padova, PD 35131, Italy,

Center for Turbulence Research Annual Research Briefs, 2023

Motivation and objectives

The design of supersonic and hypersonic systems is predicated upon the ability to accurately predict aerothermodynamics loads acting on the surface of the vehicle [2, 4]. At high Mach numbers, the combined presence of shock waves, turbulence, and thermochemical processes affects significantly the performance and structural integrity of the aircraft and its propulsion system [1, 15, 17]. The ability to resolve physical and chemical processes with such heterogeneous spatial and temporal scales, especially near the wall, requires such massive computational resources and suitable numerical tools that only very recently has direct numerical simulation (DNS) become feasible for flat plate boundary layers [7, 16, 18]. In this regard, the development of wall models is essential to mitigate the computational effort for canonical flows and enable simulation of more complex flow configurations of scientific interest.

One of the most employed class of wall models, the equilibrium wall model (EWM), can be derived from the Reynolds-averaged formulation of the Navier–Stokes equations assuming a constant stress layer. In the past decade, significant improvements have been made to provide a suitable formulation of the classical EWM for relatively high Mach numbers and intense wall cooling [3, 12, 13, 19]. More recently, Griffin et al. [11] proposed a near-wall model based on an inverse velocity transformation of Griffin et al. [10] and an algebraic temperature–velocity relation [21]. Their study showed improved results compared to the classical EWM, especially for highly compressible flows with large wall heat fluxes, with the added advantage of needing to solve only one ordinary differential equation (ODE) instead of two.

Notwithstanding the recent developments in high-speed boundary-layer modeling, making the effort to account for high temperature effects in chemically reacting multicomponent mixtures is still rare, owing to the added modeling complexity and lack of availability of reference data. Recently, Muto et al. [14] proposed an extension of the EWM to multicomponent mixtures in chemical equilibrium. Efforts to account for differential diffusion and finite-rate chemistry were later made by Di Renzo and Urzay [6], who conducted an *a priori* study in supersonic channel flows. In particular, this study compared two different mixing length models to estimate the eddy viscosity, finding that the semilocal formulation of the Van Driest damping factor provided the best results. However, large discrepancies with reference data were still present in the prediction of oxygen molar fraction profiles and were attributed to modeling errors of the chemical source term.

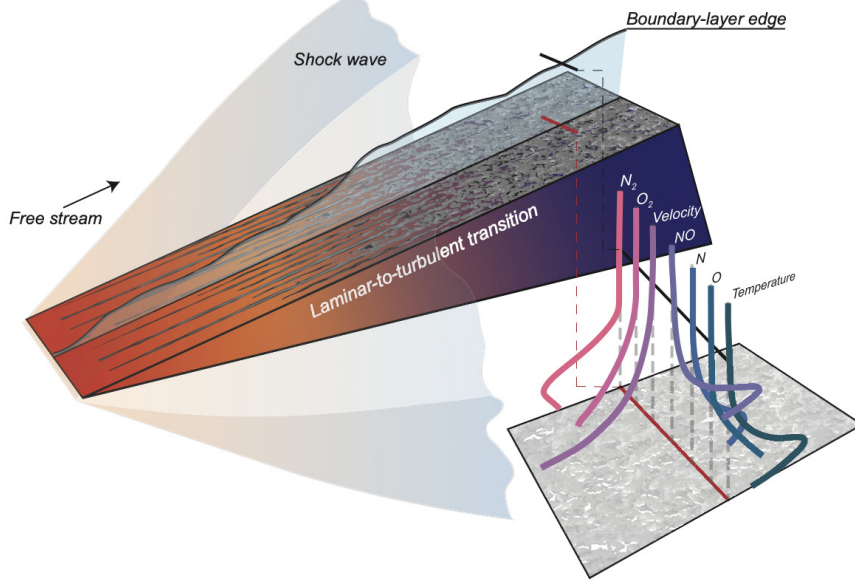


Figure 1: Schematic of a hypersonic flow configuration over a wedge and the underlying variation of flow properties in the turbulent region.

The present study builds on prior work by taking advantage of the novel framework proposed by Griffin et al. [11] (hereafter referred to as the GFM) as a baseline. The model is progressively extended to multicomponent reacting mixtures, accounting for differential diffusion and finite-rate chemistry in a similar fashion to Di Renzo and Urzay [6] and Di Renzo et al. [8]. The accuracy of the present approach, as well the prior model of Di Renzo and Urzay [6], is assessed in an *a priori* sense for the first time in a turbulent reacting boundary layer, using the boundary-layer data of Williams et al. [18]. Five species are included in the present analysis, i.e., $N_s = 5$, namely N_2 , O_2 , NO , N and O , a neutral mixture most representative of dissociation/recombination phenomena for temperatures below 6000 K. A schematic of a flow over a wedge representative of the described configuration is presented in Figure 1.

Wall-model equations

The present model aims to predict the average wall stress, heat flux, and composition of a wall-bounded flow that obeys the compressible Navier–Stokes equations subject to species transport in a chemically reacting mixture of ideal gases. In the classical formulation, the conserved variables consist of the partial densities $\rho_i = \rho Y_i$ of the i -th species in the mixture; the three components of momentum per unit volume ρu , ρv , and ρw ; and the specific stagnation internal energy $e_0 = e + |\mathbf{u}|^2/2$, with e being the specific internal energy of the mixture and \mathbf{u} , the velocity vector. The reader can find a thorough description of the underlying conservation equations and thermochemistry in Williams et al. [18].

In the context of wall modeling, a general formulation of the transport equations is based on the primitive variables \tilde{u} , \tilde{T} , and \tilde{Y}_i , from which the desired wall quantities and mixture properties can be derived. In section §Equilibrium-wall-model equations for a reacting mixture, a summary of the extended EWM proposed by Di Renzo and Urzay [6] is given, and Sections §GFM equations

for a thermally perfect frozen mixture and §Extension of GFM equations for a reacting mixture report the present extension of the GFM. In particular, the former presents a first generalization of the original model to thermally perfect gases with frozen composition, while the latter includes the coupling with the equations of species partial density for reacting flows. Throughout this brief, the superscript $+$ indicates a nondimensionalization by the friction velocity $u_\tau = \sqrt{\tau_w/\rho_w}$, the viscous length scale $\delta_\nu = \mu_w/(u_\tau \rho_w)$, ρ_w ; and μ_w , where τ_w , ρ_w and μ_w are the shear stress, density, and dynamic viscosity evaluated at the wall, respectively.

Equilibrium-wall-model equations for a reacting mixture

The extended EWM for reacting flows of Di Renzo and Urzay [6] is based on the Favre-averaged transport equations simplified with the constant stress layer assumption. The conservation equations for momentum, enthalpy, and species partial density read

$$\begin{aligned} \frac{d}{dy} \left[(\tilde{\mu} + \mu_t) \frac{d\tilde{u}}{dy} \right] &= 0, \\ \frac{d}{dy} \left[\tilde{u} (\tilde{\mu} + \mu_t) \frac{d\tilde{u}}{dy} + \tilde{\lambda} \frac{d\tilde{T}}{dy} + \frac{\mu_t}{Pr_t} \frac{d\tilde{h}}{dy} - \sum_{i=1}^{N_s} \bar{\rho}_i \tilde{V}_{y,i} \tilde{h}_i \right] &= 0, \text{ and} \\ \frac{d}{dy} \left(-\bar{\rho}_i \tilde{V}_i + \frac{\mu_t}{Sc_t} \frac{d\tilde{Y}_i}{dy} \right) + \bar{w}_i &= 0, \quad \text{for } i = 1, \dots, N_s. \end{aligned} \quad (1)$$

The reader can find in Di Renzo and Urzay [6] the definition of mixture properties, wall-normal diffusion velocities \tilde{V}_i , partial specific enthalpies \tilde{h}_i , and production rates \bar{w}_i . Di Renzo and Urzay [6] invoke the laminar closure for the transport of reaction rates, $\bar{w}_i = f(\tilde{T}, \bar{\rho}, \tilde{Y}_i)$, which neglects the fluctuations of each variable and assumes a statistical independence between them. The turbulent Prandtl number Pr_t and the turbulent Schmidt number Sc_t were assumed equal to 0.9.

The eddy viscosity μ_t is computed with a mixing length model, which reads

$$\mu_t = k \bar{\rho} y \sqrt{\frac{\tau_w}{\bar{\rho}}} \left[1 - \exp \left(-\frac{y^*}{A^+} \right) \right]^2, \quad (2)$$

where $A^+ = 17$ and $k = 0.41$. This formulation employs the semilocal-scaled wall-normal coordinate $y^* = y/(\bar{\nu}/\sqrt{\tau_w/\bar{\rho}})$ in the Van Driest damping function, which has been shown to better account for compressibility effects compared to the classical version using y^+ [20].

The set of ODEs of Eq. (1), the extended EWM, and the eddy viscosity model of Eq. (2), will be considered in this study for comparison.

GFM equations for a thermally perfect frozen mixture

The original formulation of the GFM, [11], leverages the compressibility transformation of Griffin et al. [10] and the temperature-velocity relation of Zhang et al. [21] to build a framework which especially targets high-speed flows with strong heat transfer. The proposed model was formulated for calorically perfect gases and showed clear improvements from the classical EWM, better accounting for compressibility and wall-cooling effects, which are relevant for applications in the hypersonic regime. In this section, a preliminary extension of this model is proposed for thermally perfect mixtures with constant composition, meaning that the chemical state is considered frozen (i.e.,

chemical timescales are much larger than fluid dynamics timescales), while the variation of the specific heat with temperature $c_p = f(T)$ is taken into account.

Following the study of Griffin et al. [11], the inverse velocity transformation equation is first considered, which reads as

$$\frac{d\tilde{U}^+}{dy^*} = \left(\frac{1}{\bar{\mu}^+ S_t^+} - \frac{1}{\bar{\mu}^+} + \sqrt{\bar{\rho}^+} \left(1 + \frac{1}{2\bar{\rho}^+} \frac{d\bar{\rho}^+}{dy^+} y^+ - \frac{1}{\bar{\mu}^+} \frac{d\bar{\mu}^+}{dy^+} y^+ \right) \right)^{-1}. \quad (3)$$

In this formulation, the incompressible mean strain rate $S_t^+ = dU^+/dy^+$ can be algebraically computed from the constant property version of the relation $dU/dy = \tau_w/(\mu + \mu_t)$, where μ_t is the eddy viscosity estimated with the classical mixing length model. It is important to note that the evaluation of μ_t is needed only to compute the incompressible mean strain rate, whereas the compressible counterpart is evaluated without assuming any model for the eddy viscosity, which will be relevant later in this section. In the original formulation, the velocity is coupled with the temperature by means of an algebraic law that assumes a quadratic relationship between the two quantities [9, 21]. The relation has been reformulated by Griffin et al. [11] to be exactly consistent with the matching data rather than the edge data (i.e., $h = h_m$ if $U = U_m$, but $h \neq h_e$ when $U = U_e$) to obtain

$$\tilde{T} = \tilde{T}_w + sPr \left(\tilde{T}_r - \tilde{T}_w \right) \frac{\tilde{U}}{\tilde{U}_e} \left(1 - \frac{\tilde{U}}{\tilde{U}_m} \right) + \left(\frac{\tilde{U}}{\tilde{U}_m} \right)^2 \left(\tilde{T}_m - \tilde{T}_w \right), \quad (4)$$

where subscripts $_m$ and $_e$ indicate quantities computed at the matching location and at the edge of the boundary layer, respectively.

In a thermally perfect regime, the more general enthalpy–velocity relation is considered [9], being consistent with the nonlinear relationship between temperature and enthalpy, which reads

$$\tilde{h} = \tilde{h}_w + sPr \left(\tilde{h}_r - \tilde{h}_w \right) \frac{\tilde{U}}{\tilde{U}_e} \left(1 - \frac{\tilde{U}}{\tilde{U}_e} \right) + \left(\frac{\tilde{U}}{\tilde{U}_m} \right)^2 \left(\tilde{h}_e - \tilde{h}_w \right), \quad (5)$$

where s is the Reynolds analogy factor, Pr is the Prandtl number, and $\tilde{h}_r = \tilde{h}_e + r\tilde{U}_e^2/2$ is the recovery enthalpy.

In this relation, the product $sPr = 0.82$ is assumed to be constant and equal to the fitted value of Zhang et al. [21] (also supported by Cogo et al. [5] for cold walls), while the recovery factor is taken as $r = 0.89$. A preliminary assessment of the accuracy of the enthalpy–velocity relation proposed in Eq. (5) is presented in Figure 2, which Griffin et al. [11] also reports the original temperature–velocity relation of Griffin et al. [11]. It is apparent that while the latter clearly deviates from the DNS profile, the former has a very good agreement especially at low speeds (near the wall). In light of similar findings from Passiatore et al. [16], which considered a chemically and thermally out-of-equilibrium mixture, the enthalpy–velocity relationship seems to be relatively robust. Temperature is a nonlinear function of enthalpy and composition, and thus large variations in temperature are observed based on the composition/chemistry modeling.

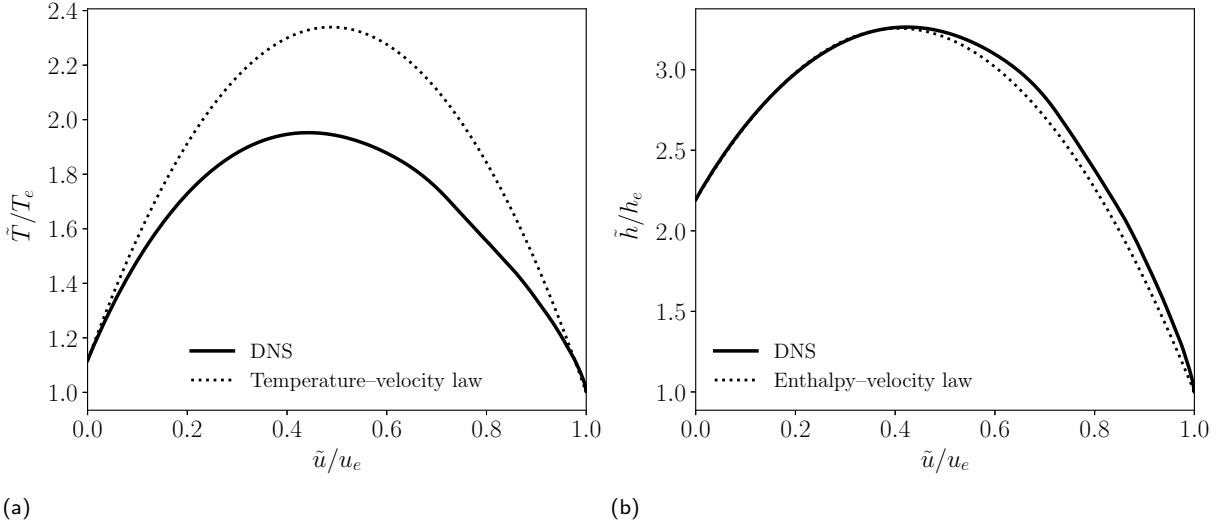


Figure 2: Comparison of the accuracy of algebraic laws for (a) temperature–velocity, Eq. (4), and (b) enthalpy–velocity, Eq. (5). DNS data from Williams et al. [18].

Extension of GFM equations for a reacting mixture

This section further extends the formulation proposed in Section §GFM equations for a thermally perfect frozen mixture to reacting mixtures, accounting for differential diffusion and finite-rate chemistry in a similar fashion to Di Renzo and Urvay [6]. In the present formulation, Eqs. (3)-(5) are coupled to the species partial density equations, yielding the following nonlinear system

$$\begin{aligned} \frac{d\tilde{U}^+}{dy^*} &= \left(\frac{1}{\bar{\mu}^+ S_t^+} - \frac{1}{\bar{\mu}^+} + \sqrt{\bar{\rho}^+} \left(1 + \frac{1}{2\bar{\rho}^+} \frac{d\bar{\rho}^+}{dy^+} y^+ - \frac{1}{\bar{\mu}^+} \frac{d\bar{\mu}^+}{dy^+} y^+ \right) \right)^{-1}, \\ \tilde{h} &= \tilde{h}_w + s \Pr(\tilde{h}_r - \tilde{h}_w) \frac{\tilde{U}}{\tilde{U}_e} \left(1 - \frac{\tilde{U}}{\tilde{U}_e} \right) + \left(\frac{\tilde{U}}{\tilde{U}_m} \right)^2 (\tilde{h}_e - \tilde{h}_w), \text{ and} \\ \frac{d}{dy} \left(-\bar{\rho}_i \tilde{V}_i + \frac{\mu_t}{Sc_t} \frac{d\tilde{Y}_i}{dy} \right) + \bar{w}_i &= 0, \quad \text{for } i = 1, \dots, N_s \end{aligned} \quad (6)$$

where Sc_t is assumed equal to 0.9 and laminar closure is employed to model the chemical reaction rate \bar{w}_i (refer to Section §Equilibrium-wall-model equations for a reacting mixture). A key difference from the prior work of Di Renzo and Urvay [6] is that the eddy viscosity μ_t present in the species equation is not modeled with the semilocal formulation of the mixing length assumption of Eq. (2).

In fact, since the inverse velocity transformation, Eq. (3), relies only on the classical mixing length model for incompressible flows, the eddy viscosity can be directly computed from the compressible mean strain rate $d\tilde{U}^+/dy^*$ by assuming a constant stress layer as

$$\frac{dU^+}{dy^*} \Big|_{GFM} \frac{dy^*}{dy} u_\tau = \frac{\tau_w}{\mu + \mu_t}. \quad (7)$$

This approach directly couples the eddy viscosity model for a given compressible flow to the compressibility transformation under consideration, without having to define a compressible version of the mixing length model to account for the variability of the thermodynamical properties.

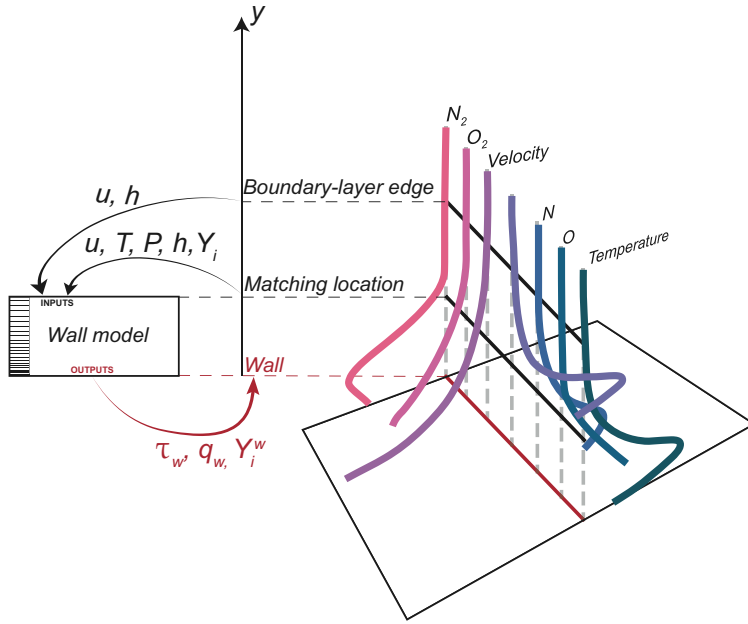


Figure 3: Schematic of a wall model implementation for high-speed turbulent boundary layers with variable composition.

Computational framework

The proposed extension of the GFM consists of the nonlinear system described in Eq. (6), which can be numerically solved from the wall to an arbitrary matching location. In the present analysis, the performance of the model is evaluated in an *a priori* sense, meaning that the thermodynamic state and the streamwise velocity at the matching location are obtained from Favre-averaged DNS data, which are enforced as the outer boundary condition of the problem. At the wall, no-slip, isothermal and non-catalytic conditions are imposed. Finally, values for the streamwise velocity and enthalpy at the boundary-layer edge are required. A schematic of the wall model implementation is reported in Figure 3, which summarizes the inputs and outputs, as well as a qualitative representation of relevant wall-normal profiles.

The numerical solution of the system of equations is obtained following the approach of Di Renzo and Urzay [6], which employed a multivariate Newton solver modified with a line-search algorithm. The equations are discretized on a stretched grid of 150 points using second-order finite differences; a tolerance of 10^{-12} is required to establish convergence. The performance of the extended EWM and GFMs is evaluated using two hypothetical matching locations at $y_m^+ = 15$ and 100. The former is selected near the wall where both models are expected to show a good agreement, while the latter lies in the log layer, $y/\delta_{99} \approx 0.1$, and is placed well beyond the mean temperature peak, a critical feature to reproduce for these type of flows. Here, δ_{99} indicates the local boundary-layer thickness at 99% of the mean streamwise velocity.

Finally, additional results obtained with frozen chemistry are included, meaning that transport equations for species are not carried and the composition is kept constant to the value imposed at the matching location. These results represent a measure of the influence that the coupling with mass fraction profiles has in the prediction of primary quantities of interest (i.e., velocity and temperature).

| Case | $\epsilon_{\tau_w}(\%)$ | $\epsilon_{q_w}(\%)$ | $\epsilon_{Y_{N_2}^w}(\%)$ | $\epsilon_{Y_O^w}(\%)$ |
|--------|-------------------------|----------------------|----------------------------|------------------------|
| EWM015 | 2.4 | 8.3 | 0.04 | -0.03 |
| GFM015 | 0.70 | 1.1 | 0.02 | -0.05 |
| EWM100 | -8.8 | -5.2 | -0.42 | -1.9 |
| GFM100 | -2.4 | -1.2 | -0.35 | -1.4 |

Table 1: *A priori* modeling errors of wall shear stress τ_w , wall heat flux q_w , and major species mass fraction $Y_{N_2}^w$ and Y_O^w at the wall. Errors are reported for both the extended EWM and GFM at matching locations $y_m^+ = 15$ and 100. DNS data from Williams et al. [18].

Results

The present study is based primarily on the reference DNS dataset of Williams et al. [18], which consists of a reacting turbulent hypersonic boundary layer with an edge Mach number of $M_e = 7$ and edge temperature of $T_e = 2700$ K. The selected streamwise location is characterized by a friction Reynolds number of $Re_\tau \equiv \delta_{99}/\delta_\nu = 1161$. The intense thermochemical processes present in this database, and their strong interaction with turbulence, represent a challenging environment that is beneficial to the assessment of the model's accuracy. The reader is referred to Williams et al. [18] for a detailed description of the computational setup and mean-flow statistics.

A first impression of the accuracy of the extended EWM and the extended GFM is given in Figure 4, which reports the inner-scaled velocity u^+ and rescaled temperature T/T_w profiles. Additionally, results obtained with frozen chemistry are included. Analyzing at Figure 4(a,c), it can be noted that all profiles matching at $y^+ = 15$ have a good agreement with reference data. Slight underprediction of the temperature profile is visible for the extended EWM. Quantitative errors in the prediction of the wall shear stress τ_w and wall heat flux q_w are reported in Table 1, where the extended GFM shows clear improvements. A general overview of profiles matching at $y^+ = 100$ shows a consistent improvement of the GFM in the predictions of both velocity and temperature profiles. In particular, compared to the EWM model, smaller deviations from DNS are present in the log-layer intercept of the velocity profile, Figure 4(b), and there is a reduced overestimation of the temperature peak, Figure 4(d). The loss of accuracy due to the frozen chemistry assumption is clearly visible in Figure 4(d), which still shows an improved accuracy of the GFM for these cases. In Figure 4(b), this aspect is less evident and frozen profiles seem to predict slightly better the log-layer intercept. This behavior is attributed to the cancellation of errors and corroborates the idea that velocity profiles are less sensitive to changes in composition in comparison to the temperature.

As discussed in Section 2, the evaluation of the compressible mean strain rate of Eq. (3) not only is relevant to derive the mean velocity profile but also can be leveraged to predict the eddy viscosity without relying on a compressible mixing length model. Figure 5 compares the proposed approach of Eq. (7) with the standard mixing length assumption with the semilocal formulation of Eq. (2) used in the extended EWM, showing an improved agreement with DNS data as the matching location is moved farther from the wall.

Figure 6 reports the profiles of enthalpy \tilde{h}/h_{ref} , Figure 6(a), and the five mass fractions \tilde{Y}_i , Figure 6(b-f). Here, it is worth recalling that enthalpy has a nonlinear dependence with temperature, and is also a function of the local composition. In Figure 6(a), the GFM shows an excellent prediction of the enthalpy profile compared with DNS data, while the EWM exhibits an overprediction in the

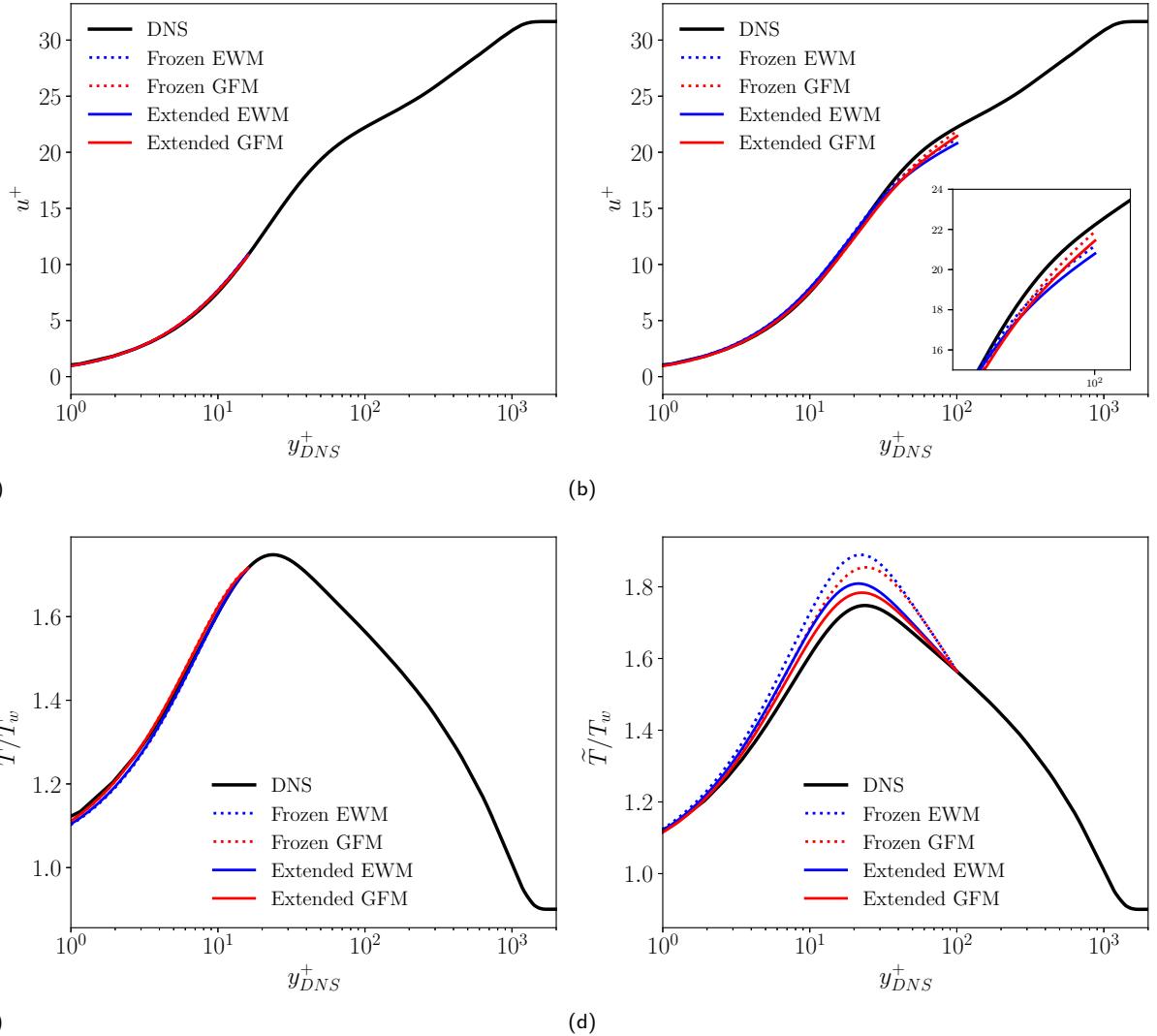


Figure 4: Favre-averaged profiles of (a,b) inner-scaled streamwise velocity u^+ and (c,d) rescaled temperature \tilde{T}/T_w as function of the DNS y^+ . The matching location corresponds to either (a,c) $y_{DNS}^+ = 15$, or (b,d) $y_{DNS}^+ = 100$. DNS data from Williams et al. [18].

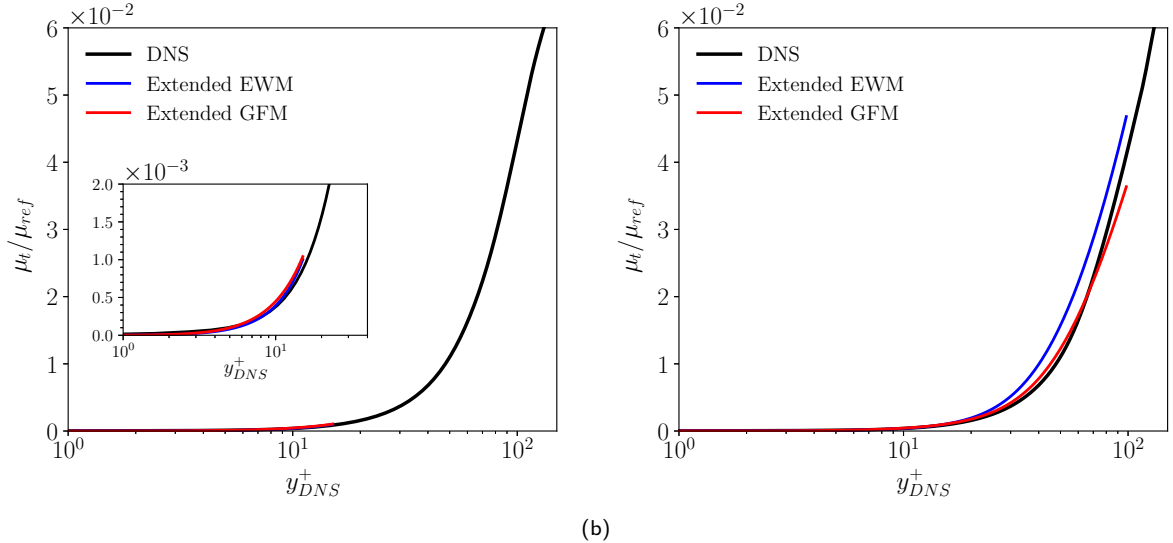


Figure 5: Comparison of the eddy viscosity μ_t profiles as function of y_{DNS}^+ computed with the extended EWM (semilocal mixing length model) of Eq. (2) and the extended GFM of Eq. (7). DNS data refer to the theoretical value of the Boussinesq approximation $-\bar{\rho}\widetilde{u''v''}/(d\bar{u}/dy)$. The matching locations correspond to (a) $y_{DNS}^+ = 15$ and (b) $y_{DNS}^+ = 100$. DNS data from Williams et al. [18].

buffer layer that culminates in the peak region. A considerable loss of accuracy is visible for frozen cases, especially near the wall. This is expected because while DNS values of mass fractions are imposed at the matching location, the correct enthalpy at the wall cannot be retrieved by assuming a constant composition throughout the boundary layer. Figure 6(b-f) shows results on the prediction of mass fraction profiles, namely \tilde{Y}_{N_2} , \tilde{Y}_{O_2} , \tilde{Y}_{NO} , \tilde{Y}_N , and \tilde{Y}_O . A general overview of all profiles shows minimal differences between the EWM and the GFM, the former being slightly better in the prediction of \tilde{Y}_N and the latter showing marginally improved results in all other compounds. However, both models show deviations from DNS data that result in under-/overpredictions of mass fractions at the wall as well as incorrect prediction of gradients at the matching location visible for certain compounds (e.g., see inset of Figure 6(e) for \tilde{Y}_{NO}). It is worth noting that both models progressively approach DNS data when the matching location is between the wall and the temperature peak (not shown). Modeling errors regarding the wall values of \tilde{Y}_{N_2} and \tilde{Y}_O are available in Table 1, as these are the most abundant species in the mixture, while the others species are close to zero at the wall. Although errors at the wall are relatively small, clear differences with DNS profiles can be noted in the predicted gradients at the matching location. The fact that this feature is shared by both models suggests that specific assumptions included in the Favre-averaged equations of species overshadow differences induced by their coupling with other quantities discussed above (\tilde{u} , \tilde{T}).

From the discussion of Williams et al. [18], it is apparent that the laminar closure model for the chemical reaction rate \bar{w}_i has clear shortcomings that become progressively more drastic as the turbulence–chemistry interaction level increase. In particular, accurately accounting for correlated fluctuations in the temperature and partial density fields is fundamental for prediction of the mean chemical production rate throughout the boundary layer, which cannot be predicted only with averaged quantities.

In order to more objectively address the influence of this assumption on both models, Figure

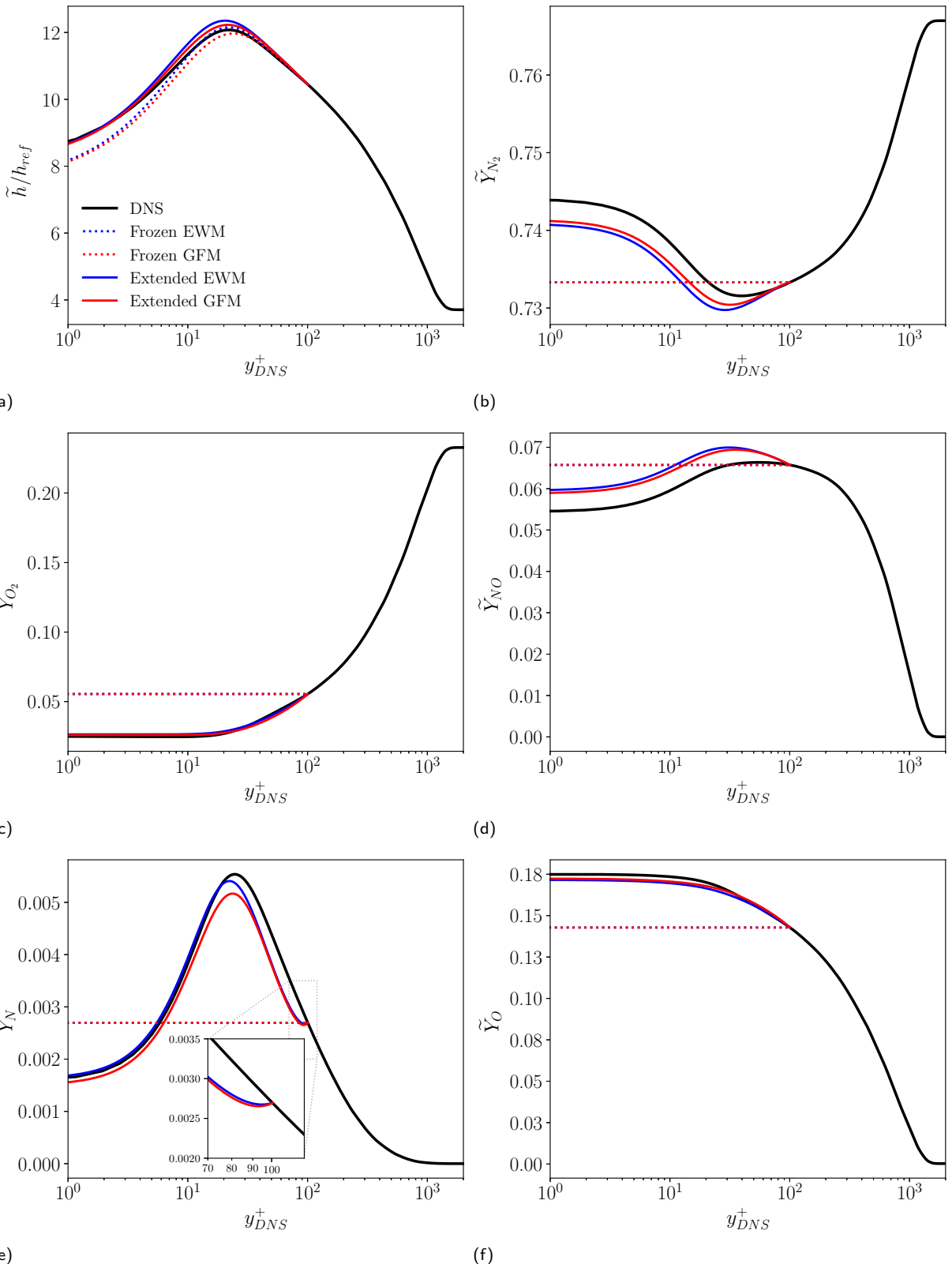


Figure 6: Favre-averaged profiles of (a) rescaled enthalpy \tilde{h}/h_{ref} and (b-f) mass fractions \tilde{Y}_{O_2} , \tilde{Y}_{N_2} , \tilde{Y}_{NO} , \tilde{Y}_N , and \tilde{Y}_O as a function of y_{DNS}^+ . The matching location corresponds to $y_{DNS}^+ = 100$. DNS data from Williams et al. [18].

| Case | ϵ_{τ_w} (%) | ϵ_{q_w} (%) | $\epsilon_{Y_{N_2}^w}$ (%) | $\epsilon_{Y_O^w}$ (%) |
|---------|-------------------------|----------------------|----------------------------|------------------------|
| EWM100* | -8.7 | -5.4 | -0.12 | -2.5 |
| GFM100* | -2.4 | -1.0 | -0.11 | 0.11 |

Table 2: *A priori* modeling errors of wall shear stress τ_w , wall heat flux q_w and species mass fraction $Y_{N_2}^w$ and Y_O^w at the wall. All values refer to cases in which the DNS profile of the chemical reaction rate has been enforced in the solution, $\bar{w}_i = f(y)|_{DNS}$. Errors are reported for both extended EWM and GFM at matching location $y_m^+ = 100$. DNS data from Williams et al. [18].

7 shows the resulting profiles of enthalpy and mass fractions when the DNS profiles of chemical reaction rates are enforced in the solution, $\bar{w}_i = f(y)|_{DNS}$. Here, it is visible how the extended GFM drastically improves the prediction of the correct gradient at the matching location for all species, which are in very good agreement with DNS data. This improvement is shared with the EWM only for certain compounds (\tilde{Y}_{N_2} , \tilde{Y}_{NO}), while for the other species the prediction is actually worse. For these compounds, it is expected that cancellation of errors could play a role because discrepancies with DNS were already small and other modeling assumptions may become relevant. At the wall, the extended GFM shows an excellent agreement with DNS data (see also Table 2), except for \tilde{Y}_N , which may be affected by other modeling errors. It should be noted that the improved behavior of the mass fractions profiles by including $\bar{w}_i = f(y)|_{DNS}$ is not shared with the enthalpy profiles, nor velocity and temperature profiles, which shows almost identical results (not shown). This is also visible in the shear stress and heat flux predictions reported in Table 2, although it is important to note that errors were already relatively low.

Conclusions

This study presents an *a priori* assessment of the accuracy of the extension of the GFM proposed by Griffin et al. [11] to compressible turbulent reacting wall-bounded flows, comparing it with the accuracy of the extended EWM proposed by Di Renzo and Urzay [6]. The variability in the composition of the mixture near the wall is predicted by taking into account differential diffusion and finite-rate chemistry. Both models have been tested for the first time using DNS data from a strongly reacting turbulent boundary layer [18], which provides an essential reference given the enhanced turbulence–chemistry interaction in place. The extended GFM shows improved results when predicting the Favre-averaged wall-normal profiles of inner-scaled velocity u^+ , rescaled temperature \tilde{T}/T_w , and enthalpy \tilde{h}/h_{ref} . This is reflected in the smaller modeling errors of wall shear stress τ_w , wall heat flux q_w , and most abundant species mass fractions \tilde{Y}_{N_2} and \tilde{Y}_O , which are all below 3%.

The prediction of wall-normal profiles of mass fractions is comparable in both models, showing deviations from DNS especially in the prediction of wall-normal gradients at the matching location. These features are attributed to the absence of turbulence–chemistry interaction modeling in the prediction of the chemical reaction term \bar{w} , which overshadows the respective model’s differences on the predictions of the mean temperature and velocity profiles. This is confirmed by enforcing the DNS profiles of \bar{w} to both models, which clearly improves the overall estimate of composition for the extended GFM.

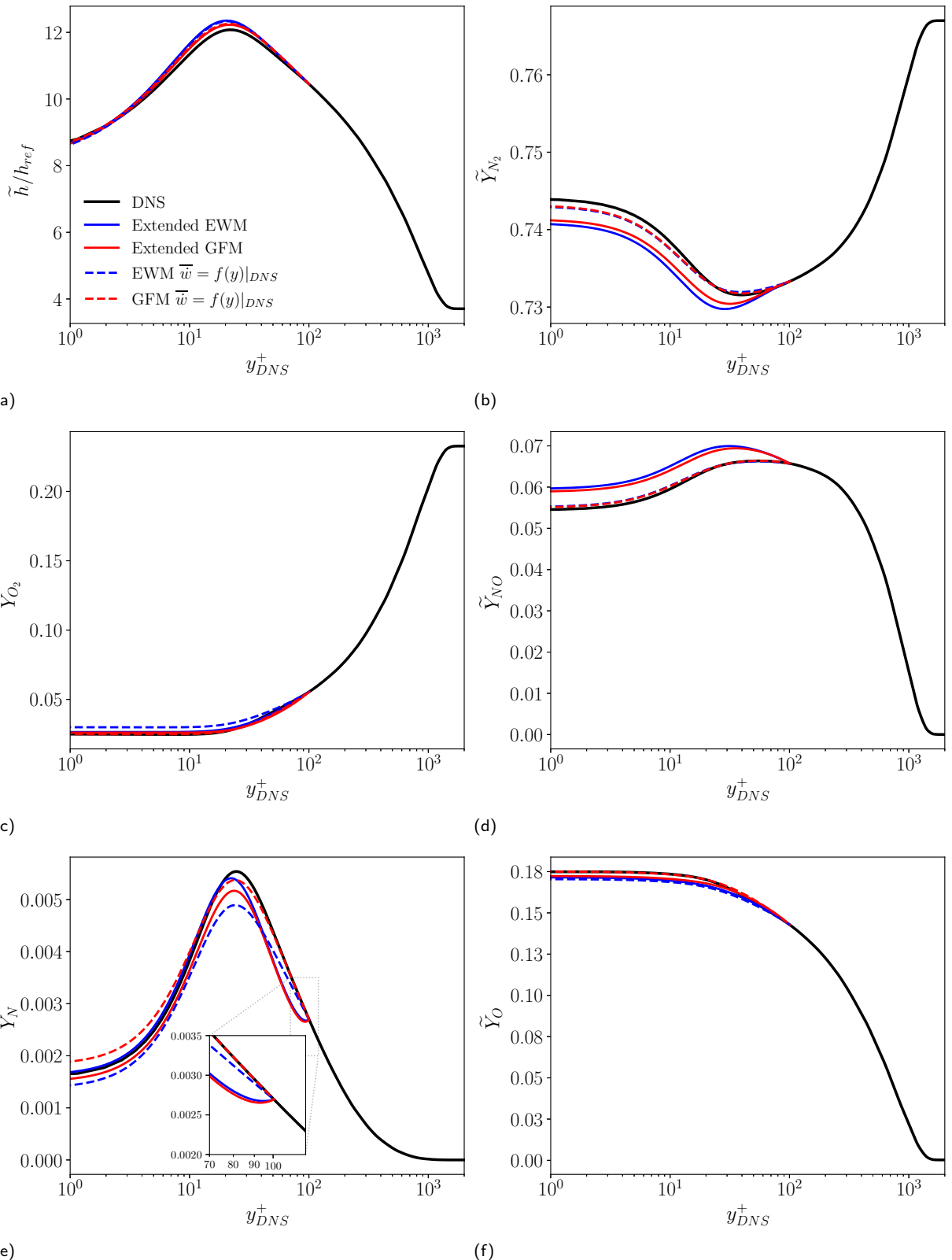


Figure 7: Favre-averaged profiles of (a) rescaled enthalpy \tilde{h}/h_{ref} and (b-f) mass fractions \tilde{Y}_{O_2} , \tilde{Y}_{N_2} , \tilde{Y}_{NO} , and \tilde{Y}_N as a function of y_{DNS}^+ . The matching location corresponds to $y_{DNS}^+ = 100$. DNS data from Williams et al. [18].

Acknowledgments

M.C. is supported by the Franklin P. and Caroline M. Johnson Fellowship in the School of Engineering Fund at Stanford University, Fulbright Italy, Zegna Founder's Scholarship and Fondazione Cassa di Risparmio di Padova e Rovigo. C.T.W. acknowledges support by the National Science Foundation Graduate Research Fellowship Program under Grant No. DGE-2146755. K.P.G. is supported by the Exascale Computing Project (Grant17-SC-20SC). The authors thank Dr. Mario Di Renzo for his support on the computational framework and Dr. Donatella Passiatore for the critical review of this manuscript.

This work was authored in part by the National Renewable Energy Laboratory, operated by Alliance for Sustainable Energy, LLC, for the U.S. Department of Energy (DOE) under Contract No. DEAC3608GO28308. The views expressed in the article do not necessarily represent the views of the DOE or the U.S. Government. The U.S. Government retains and the publisher, by accepting the article for publication, acknowledges that the U.S. Government retains a nonexclusive, paid-up, irrevocable, worldwide license to publish or reproduce the published form of this work or allow others to do so, for the U.S. Government purposes.

Bibliography

- [1] J. D. Anderson. *Hypersonic and High-temperature Gas Dynamics*. AIAA education series. American Institute of Aeronautics and Astronautics, 2006. ISBN 9781563477805.
- [2] John J Bertin and Russell M Cummings. Critical hypersonic aerothermodynamic phenomena. *Annu. Rev. Fluid Mech.*, 38(1):129–157, 2006.
- [3] Sanjeeb T Bose and George Ilhwan Park. Wall-modeled large-eddy simulation for complex turbulent flows. *Annual review of fluid mechanics*, 50(1):535–561, 2018.
- [4] Graham V. Candler. Rate Effects in Hypersonic Flows. *Annu. Rev. Fluid Mech.*, 51(September 2018):379–402, 2019. ISSN 00664189. doi: 10.1146/annurev-fluid-010518-040258.
- [5] Michele Cogo, Umberto Baù, Mauro Chinappi, Matteo Bernardini, and Francesco Picano. Assessment of heat transfer and mach number effects on high-speed turbulent boundary layers. *Journal of Fluid Mechanics*, 974:A10, 2023.
- [6] M Di Renzo and J Urzay. An a priori study of the accuracy of an equilibrium wall model for dissociating air in supersonic channel flows. *Annual Research Briefs, Center for Turbulence Research*, pages 29–40, 2019.
- [7] M. Di Renzo and J. Urzay. Direct numerical simulation of a hypersonic transitional boundary layer at suborbital enthalpies. *J. Fluid Mech.*, 912:A29, 2021. doi: 10.1017/jfm.2020.1144. URL <http://dx.doi.org/10.1017/jfm.2020.1144>.
- [8] Mario Di Renzo, Lin Fu, and Javier Urzay. Htr solver: An open-source exascale-oriented task-based multi-gpu high-order code for hypersonic aerothermodynamics. *Computer Physics Communications*, 255:107262, 2020.
- [9] L. Duan and M.P. Martin. Direct numerical simulation of hypersonic turbulent boundary layers. Part 4. Effect of high enthalpy. *J. Fluid Mech.*, 684:25–59, 2011.
- [10] K. P. Griffin, L. Fu, and P. Moin. Velocity transformation for compressible wall-bounded turbulent flows with and without heat transfer. *P. Natl. Acad. Sci USA*, 118(34), 2021.
- [11] Kevin P Griffin, Lin Fu, and Parviz Moin. Near-wall model for compressible turbulent boundary layers based on an inverse velocity transformation. *Journal of Fluid Mechanics*, 970:A36, 2023.
- [12] Prahladh S Iyer and Mujeeb R Malik. Analysis of the equilibrium wall model for high-speed turbulent flows. *Physical Review Fluids*, 4(7):074604, 2019.
- [13] S. Kawai and J. Larsson. A dynamic wall model for large-eddy simulation of high reynolds number compressible flows. *CTR Annu. Res. Briefs*, 2:5–37, 2010.
- [14] Daiki Muto, Yu Daimon, Taro Shimizu, and Hideyo Negishi. An equilibrium wall model for reacting turbulent flows with heat transfer. *International Journal of Heat and Mass Transfer*, 141:1187–1195, 2019.
- [15] Chul Park. Nonequilibrium hypersonic aerothermodynamics. 1989.

- [16] D. Passiatore, L. Sciacovelli, P. Cinnella, and G. Pascazio. Thermochemical non-equilibrium effects in turbulent hypersonic boundary layers. *J. Fluid Mech.*, 941, 2022.
- [17] J. Urzay. Supersonic combustion in air-breathing propulsion systems for hypersonic flight. *Annu. Rev. Fluid Mech.*, 50:593–627, 2018.
- [18] C. T. Williams, Di Renzo M., and Moin P. Direct simulation of turbulence-chemistry interaction in a strongly reacting turbulent hypersonic boundary layer. *Annual Research Briefs*, 2023.
- [19] X. I.A. Yang, J. Urzay, S. Bose, and P. Moin. Aerodynamic heating in wall-modeled large-eddy simulation of high-speed flows. *AIAA J.*, 56(2):731–742, 2018. ISSN 00011452. doi: 10.2514/1.J056240.
- [20] Xiang IA Yang and Yu Lv. A semi-locally scaled eddy viscosity formulation for les wall models and flows at high speeds. *Theoretical and Computational Fluid Dynamics*, 32(5):617–627, 2018.
- [21] Y. S. Zhang, W. T. Bi, F. Hussain, and Z. S. She. A generalized Reynolds analogy for compressible wall-bounded turbulent flows. *J. Fluid Mech.*, 739:392–420, 2014.